Modelling Ultrafast Two-Dimensional Spectroscopy of Vibronic Systems using non-Markovian Hierarchical Equations of Motion.

A thesis submitted by

DALE GREEN

in partial fulfilment of the requirements for
the degree of Doctor of Philosophy.

UNIVERSITY OF EAST ANGLIA
SCHOOL OF CHEMISTRY

January 2020

Abstract

Two-dimensional spectroscopy utilises a series of ultrafast optical interactions to create excited populations and track the decay of resulting wavepackets. This enables the study of the potential energy surfaces of complex chemical and biological systems, including the rates of relaxation between states and the dephasing of ensembles. But the inherent complexity of the condensed phase, associated with the vast degrees of freedom and disorder, presents significant challenges in modelling such photophysical processes. In particular, the similarity in relaxation timescale of the system and its surrounding environment provides the opportunity for feedback of information, introducing memory effects which have a major impact on the spectral lineshape. The shape and duration of the applied laser pulses also leads to filtering effects, such that spectra of complex systems can easily be misinterpreted. In this research, theoretical models for the simulation of two-dimensional electronic spectroscopy of vibronic systems are developed in both the underdamped and overdamped limits, using the hierarchical equations of motion to account for non-Markovian memory effects. Firstly, an investigation into the origins of spectral broadening from the perspective of quantum information theory finds that underdamped environments involve greater non-Markovian effects, but also that increased inhomogeneous broadening in overdamped environments is correlated with greater measurable non-Markovianity. The role of the laser spectrum is then demonstrated through spectral filtering of the coherence pathways of a vibronic zinc-porphyrin monomer. Changes in the 2D spectra on formation of delocalized exciton states in vibronic dimers are then examined in terms of a series of perylene bisimide homodimers, where the electronic coupling is controlled by increasing the monomer separation distance. Finally, an analysis of vibrational relaxation within a vibronic heterodimer, combined with selective laser excitation, demonstrates the full capability of the model by simulating energy transfer within an excitonic aggregate involving both system and environmental vibrational motion.

Contents

Abstract **2**

List of Figures **5**

List of Tables **10**

Acknowledgements **11**

Publications **12**

1 Introduction **13**

2 Theoretical Methods **20**
2.1 Open Quantum Systems and Markovianity 20
2.1.1 Closed Quantum Systems 20
2.1.2 Open Quantum Systems 22
2.1.3 Markovianity 25
2.1.4 External Forces 29
2.2 Components of the Hamiltonian 31
2.2.1 System Hamiltonian 31
2.2.1.1 Vibronic Monomer 31
2.2.1.2 Electronically Coupled Aggregates 36
2.2.1.3 Vibronic Dimer 39
2.2.2 Bath Interaction 43
2.2.2.1 Interaction Hamiltonian 43
2.2.2.2 Bath Coupling Operators 44
2.2.2.3 Spectral Densities 46
2.2.3 Field Interaction 49
2.2.3.1 Interaction Hamiltonian 49
2.2.3.2 Dipole Moment Operator 50
2.3 Non-Markovian Quantum Dynamics 52
2.3.1 Master Equations 52
2.3.2 Hierarchical Equations of Motion 53
2.3.2.1 Overdamped 55
2.3.2.2 Underdamped 58
2.3.2.3 Arbitrary Spectral Density 61
2.3.3 Implementation 64

2.4 Theory of Spectroscopy 64
2.4.1 Polarization 65
2.4.2 First Order Linear Spectroscopy 67
2.4.3 Third Order Photon Echo Spectroscopy 70
2.4.3.1 Polarization and Response function 70
2.4.3.2 Equation-of-Motion Phase-Matching Approach . . 76
2.4.3.3 2D Spectra 79

3 Analysis of Spectral Lineshape 83
3.1 System vs. Bath Vibrations 83
3.2 Limits of the Lineshape 87
3.3 Quantifying Non-Markovianity and Its Effect on Spectral Lineshape 92

4 Spectral Filtering of a Vibronic Monomer 102
4.1 Zinc-Porphyrin Monomer and Laser Spectra 102
4.2 Liouville Pathway Analysis 104
4.3 Filtered Spectra 111

5 Application to Vibronic Dimers 117
5.1 Coupling Limits 117
5.2 Perylene Bisimide Homodimers 121
5.3 Energy Transfer in a Vibronic Heterodimer 135

6 Conclusion 141

Appendices 145

A Notation and Symbols 145

B Further Theory 147
B.1 Wavepacket Projection 147
B.2 Site Basis Vibronic Dimer Hamiltonian 147
B.3 EOM-PMA Generating Functions 149

C Computational Implementation 152
C.1 HEOM Dynamics Packages 152
C.2 2D Spectroscopy Software 153
C.3 Fourth Order Runge-Kutta Integration 156
C.4 Fourier Transform and Normalisation Procedures 157

Acronyms 158

Bibliography 160

List of Figures

2.1.1 The importance of memory in Markovian vs. non-Markovian evolution. 26
2.1.2 The trace distance, $D(\rho_1, \rho_2)$, for a two-level-system initially in its ground state (outer) compared with its excited state (inner) decreases as the excited state population relaxes, following the decrease in distinguishability. 28
2.1.3 A solution of perylene bisimide in toluene interacting with the electric field of a laser pulse as an open quantum system. 30
2.2.1 Potential energy surface of a vibronic system with two electronic states coupled to the jth vibrational mode. 32
2.2.2 Site basis state populations and wavepacket projection of the excited electronic state with initial population in (top) site basis state $|e, 0\rangle$ and (bottom) lowest vibronic state, when $\Delta_0 > 0$. . . 35
2.2.3 Transformation of the vibronic monomer Hamiltonian from the site to vibronic basis alters the wavefunction coefficients without a change in state energy, as long as the reorganisation energy is included. 36
2.2.4 Energy level diagram for formation of a J-aggregate. 38
2.2.5 Relative orientation of monomer transition dipole moments for H- and J-aggregates. 38
2.2.6 Energy level diagram of the composite site basis states for the jth mode of a vibronic homodimer. 41
2.2.7 Formation of exciton states in a H-aggregate in the strong coupling limit. 42
2.2.8 Formation of exciton states in a H-aggregate in the weak coupling limit. 42
2.2.9 Modulation of the fundamental transition frequency of the system, ω_{eg}^0, as a result of coupling to the bath. 47
2.2.10 (a) Underdamped spectral density, $J_{\mathrm{U}}(\omega)$, and (b) corresponding correlation function, $L_{\mathrm{U}}(t)$, for a Brownian oscillator with $\tilde{\omega}_0 = 600\,\mathrm{cm}^{-1}$ and $\tilde{\gamma} = 120\,\mathrm{cm}^{-1}$, with (c) the overdamped spectral density, $J_{\mathrm{O}}(\omega)$, and (d) correlation function, $L_{\mathrm{O}}(t)$, obtained on increasing the damping to $\tilde{\gamma} = 3600\,\mathrm{cm}^{-1}$. 49

2.3.1 Hierarchy diagram for a single overdamped bath with $\tilde{\eta} = 500\,\mathrm{cm}^{-1}$, $\tilde{\Lambda} = 100\,\mathrm{cm}^{-1}$ and $\tilde{\xi} = 1000\,\mathrm{cm}^{-1}$ at $78\,\mathrm{K}$, such that there are three Matsubara axes. 58
2.3.2 Hierarchy diagram for a single underdamped bath with $\tilde{\omega}_0 = 600\,\mathrm{cm}^{-1}$, $\tilde{\eta} = 500\,\mathrm{cm}^{-1}$, $\tilde{\gamma} = 150\,\mathrm{cm}^{-1}$ and $\tilde{\xi} = 600\,\mathrm{cm}^{-1}$ at $78\,\mathrm{K}$, such that there are three Matsubara dimensions. 60
2.3.3 Markovian vs. Non-Markovian evolution in terms of the HEOM for an arbitrary spectral density. 63
2.4.1 The four double-sided Feynman diagrams of the linear response. 69
2.4.2 Timeline of interactions in 2D photon echo spectroscopy, showing the waiting times between field envelopes (black) and emission of the third order polarization, $P^{(3)}(t)$, in the rephasing direction (blue). 70
2.4.3 Double-sided Feynman diagrams for the third order non-linear response, where pathways are labelled as R_x, $x = 1, \ldots, 4$ using the 2DES convention and as $R_x^\star$, $x = 1, \ldots, 6$ using the 2DIR convention. 73
2.4.4 Third order polarization and 2D spectra in the impulsive limit for a two-level-system with significant inhomogeneous broadening. 82

3.1.1 The limits of damping in terms of the system-bath boundary. . . 84
3.1.2 Linear absorption spectra for a two-level-system coupled to a vibration (a) within the system degrees of freedom broadened by an overdamped bath and (b) within the bath degrees of freedom as an underdamped Brownian oscillator. 85
3.1.3 Absorptive 2D spectra for a two-level-system coupled to a vibration (a) within the system degrees of freedom broadened by an overdamped bath and (b) within the bath degrees of freedom as an underdamped Brownian oscillator. 87
3.2.1 Linear absorption spectra for a two-level-system coupled to an underdamped Brownian oscillator with $\tilde{\omega}_0 = 600\,\mathrm{cm}^{-1}$ and fixed reorganisation energy, varying (a) γ and (b) temperature. . 88
3.2.2 Linear absorption spectra for a two-level-system coupled to an overdamped bath with fixed reorganisation energy and varying (a) Λ and (b) temperature. 89
3.2.3 Absorptive 2D spectra for a two-level-system coupled to an overdamped bath for a range of $\Delta\tau_c$ up to $T = 400\,\mathrm{fs}$, each normalised to their respective maxima at $T = 0\,\mathrm{fs}$. 90
3.2.4 Ellipticity of the overdamped 2D spectra in figure 3.2.3, excluding $\Delta\tau_c = 0.1$, for $T = 0 - 500\,\mathrm{fs}$, sampled at $10\,\mathrm{fs}$ intervals. 91

3.2.5 Linear absorption spectrum for a two-level-system coupled to an overdamped bath with $\Delta\tau_c = 1.0$, calculated using the ASD-HEOM terminated at the first (1st) and second (2nd) layers. . . 92
3.3.1 (Top) Trace distance, $D(\rho_1, \rho_2)$, and (bottom) cumulative integration of the positive flux, with maximum equal to $\mathcal{N}$, for each of the damping strengths in table 3.1. 94
3.3.2 Postive flux of the trace distance shown in figure 3.3.1, for each of the damping strengths in table 3.1. 95
3.3.3 Calculated linear absorption spectra for each of the damping strengths in table 3.1. 97
3.3.4 Absorptive 2D spectra for population times $T = 0 - 300\,\mathrm{fs}$ for the $\tilde{\gamma} = 300\,\mathrm{cm}^{-1}$ underdamped bath, labelled $\gamma < \omega_0$, and the three overdamped baths, identified by their $\Delta\tau_c$ values, as per table 3.1, normalised to the maximum of $\Delta\tau_c = 0.64$ at $T = 0\,\mathrm{fs}$. 99
3.3.5 Ellipticity, E, of the absorptive 2D spectra against the measured non-Markovianity, $\mathcal{N}$, for the three overdamped baths, identified by their $\Delta\tau_c$ values, for (left) $T = 0, 50$ and $100\,\mathrm{fs}$ and (right) $T = 0 - 400\,\mathrm{fs}$, sampled at $10\,\mathrm{fs}$ intervals. 100

4.1.1 Molecular structure (left) and linear absorption spectrum (right) of the 5,15-bisalkynyl zinc-porphyrin monomer. 103
4.1.2 Calculated (σ_A) and experimental (Measured) linear absorption spectra with centred and shifted laser spectra. 104
4.2.1 Rephasing population pathways. 105
4.2.2 Non-rephasing population pathways. 106
4.2.3 Rephasing coherence pathways. 107
4.2.4 Non-rephasing coherence pathways. 108
4.2.5 Unfiltered peak location key diagrams. 109
4.2.6 Example of a filtered pathway drawn on the vibronic PES and as a double-sided Feynman diagram. 110
4.2.7 Filtered peak location key diagrams for the blue-shifted laser, as in figure 4.2.5. 110
4.3.1 Rephasing spectra at $T = 100$, 200 and $500\,\mathrm{fs}$ for (top) centred and (bottom) blue-shifted laser spectra, each normalised to their maximum along the population time, T, respectively. . . . 111
4.3.2 Non-rephasing spectra at $T = 100$, 200 and $500\,\mathrm{fs}$ for (top) centred and (bottom) blue-shifted laser spectra, each normalised to their maximum along the population time, T, respectively. 111

4.3.3 (a) Rephasing spectrum (real) at $T = 120\,\mathrm{fs}$ for the centred laser spectrum, normalised to the maximum amplitude within the total $1\,\mathrm{ps}$ of population time, with coordinates a, b and c labelled. (b) Trace of the rephasing (real) amplitude for the three coordinates in (a), including fit of an exponential decay for each. (c) Residual for each coordinate in (a) after subtraction of any exponential decay, with labelled phase shift between a and b/c, arbitrarily offset for clarity. (d) FFT spectra for the residuals in (c). 112
4.3.4 (1) Calculated and (2) experimental amplitude spectra for the centred laser spectrum. 114
4.3.5 (1) Calculated and (2) experimental amplitude spectra for the blue-shifted laser spectrum. 115

5.1.1 Site basis vibronic homodimer potential energy surface. 118
5.1.2 Exciton basis vibronic homodimer potential energy surface for a H-aggregate in the strong coupling limit. 119
5.1.3 Exciton basis vibronic homodimer potential energy surface for a H-aggregate in the weak coupling limit. 119
5.1.4 (a) Linear absorption spectra for J-aggregate homodimers in the strong and weak coupling limits as well as the monomer spectrum from figure 3.1.2 (a), and the corresponding absorptive 2D spectra at $T = 0\,\mathrm{fs}$ for the homodimers in the (b) strong and (c) weak coupling limits. 120
5.2.1 (Left) Structure of PBI monomer with transition dipole moment magnitude and orientation. (Right) Calculated (σ_A) and experimental (Measured) linear absorption spectra of the PBI monomer, also showing the relative intensity of the vibronic transitions contributing to the first peak. 122
5.2.2 Potential energy surface of the two-mode PBI monomer. 123
5.2.3 Absorptive 2D spectra of the two-mode PBI monomer for $T = 0 - 200\,\mathrm{fs}$ at intervals of $50\,\mathrm{fs}$, normalised to the maximum at $T = 0\,\mathrm{fs}$. 124
5.2.4 (a) Residual of the rephasing (real) amplitude for the coordinate ($\tilde{\nu}_\tau = 18\,939\,\mathrm{cm}^{-1}$, $\tilde{\nu}_t = 18\,939\,\mathrm{cm}^{-1}$), sampled every $5\,\mathrm{fs}$, after subtraction of an exponential decay with a lifetime of $142\,\mathrm{fs}$. (b) FFT power spectrum of the residual in (a), identifying peaks corresponding to ω_0 and ω_1. 124
5.2.5 Amplitude spectra for the two-mode PBI monomer. 125
5.2.6 (a) Energy level diagram for the two-mode PBI monomer and (b) example negative non-rephasing coherence pathway. 126

5.2.7 (Left) Molecular structure and monomer separation distance for D0 and D1 dimers. (Right) Measured linear absorption spectra for M, D0 and D1. 128
5.2.8 Experimental (top) and calculated (bottom) absorptive 2D spectra for M (left), D0 (middle) and D1 (right) at $T = 100\,\mathrm{fs}$. . 129
5.2.9 Calculated linear absorption spectra, σ_A, for two-mode M, D0 and D1 PBI systems, as well as the measured spectra for M and D0. 131
5.2.10 Absorptive 2D spectra for the D0 homodimer, where the constituent monomers are coupled to either the $\tilde{\omega}_0 = 231\,\mathrm{cm}^{-1}$ or $\tilde{\omega}_1 = 550\,\mathrm{cm}^{-1}$ vibrational mode only, for $T = 0 - 200\,\mathrm{fs}$ at intervals of $50\,\mathrm{fs}$, normalised to the maximum at $T = 0\,\mathrm{fs}$. 132
5.2.11 Absorptive 2D spectra for the two-mode D0 homodimer at $T = 0$, 50 and $100\,\mathrm{fs}$, normalised to the maximum at $T = 0\,\mathrm{fs}$. 133
5.2.12 Absorptive 2D spectra for the two-mode D1 homodimer at $T = 0$, 50 and $100\,\mathrm{fs}$, normalised to the maximum at $T = 0\,\mathrm{fs}$. 133
5.2.13 Absorptive 2D spectra for the D1 homodimer, where the constituent monomers are coupled to either the $\tilde{\omega}_0 = 231\,\mathrm{cm}^{-1}$ or $\tilde{\omega}_1 = 550\,\mathrm{cm}^{-1}$ vibrational mode only, for $T = 0 - 200\,\mathrm{fs}$ at intervals of $50\,\mathrm{fs}$, normalised to the maximum at $T = 0\,\mathrm{fs}$. 134
5.3.1 Energy level diagram showing the singly excited states of the vibronic heterodimer. 136
5.3.2 (Left) Calculated linear absorption spectrum, σ_A, of the vibronic heterodimer with laser spectrum overlaid. (Right) Normalised absorptive 2D spectrum at $T = 50\,\mathrm{fs}$. 137
5.3.3 Absorptive 2D spectra for the vibronic heterodimer at $T = 50, 100, 200, 300, 400$ and $500\,\mathrm{fs}$, normalised to the maximum along the population time, T. 138
5.3.4 (a) Exciton basis and (b) equivalent composite site basis state populations for the vibronic heterodimer initialised with the entire population in $|\Psi_9^E\rangle$. (c) Summing the site basis populations corresponding to excitation of monomer A versus B demonstrates ca. 20% excitation energy transfer from A to B over $500\,\mathrm{fs}$. 139

C.1.1 Flowchart for HEOM dynamics packages. 153
C.2.1 Main windows of the 2D spectroscopy software. 154
C.2.2 Flowchart for 2D spectroscopy calculations. 155

List of Tables

3.1 Damping strengths, dissipation rates and correlation times used, for $\tilde{\eta} = 20\,\mathrm{cm}^{-1}$ such that $\tilde{\Delta} = 91.33\,\mathrm{cm}^{-1}$ at $300\,\mathrm{K}$. $\Delta\tau_c$ given for overdamped environments only. 93

3.2 Measured $\mathcal{N}$ and linear absorption spectrum FWHM for each damping strength in table 3.1, where $\tilde{\eta} = 20\,\mathrm{cm}^{-1}$, such that $\tilde{\Delta} = 91.33\,\mathrm{cm}^{-1}$ at $300\,\mathrm{K}$ for all cases. $\Delta\tau_c$ given for overdamped environments only. 96

4.1 Symbol key for Liouville pathways. 109

A.1 Summary of mathematical notation. 145

A.2 Review of parameters. 146

Acknowledgements

The research presented in this thesis was completed using the High Performance Computing Cluster supported by the Research and Specialist Computing Support service at UEA. I wish to express my gratitude to all the members of this team for enabling my demanding calculations and always providing cheerful assistance when needed. I would also like to thank the wonderful staff at UEA and all my colleagues for their support throughout my PhD.

Specifically, I am grateful to Professor Ismael A. Heisler for his guidance regarding the spectroscopy element of the research and for being a patient and encouraging secondary supervisor before moving to pastures new. My thanks also to Professor Stephen R. Meech for taking over as secondary supervisor. I must also thank Dr Arend G. Dijkstra, Dr Franco Valduga De-Almeida Camargo and Professor R. Guy Woolley for their insight and expertise, I am hugely grateful for our collaborative work.

Similarly, I wish to express my gratitude to Dr Mathew D. Williams and Dr Kayn A. Forbes for our countless conversations which have maintained my motivation and enthusiasm, to the project students who have worked with my software or me personally, and to my fellow research students for their encouragement. In particular I thank Ben S. Humphries, with whom I have spent many hours unravelling the meaning of non-Markovianity, and Giovanni Bressan, for his experimental expertise. I also thank the multiple generations of UEA Music Society members whom I have conducted and performed with over the years. My musical endeavours have undoubtedly preserved my sanity and nothing restores the cheerfulness of a weary soul better than producing good music with good friends.

My eternal gratitude goes to my supervisor, Dr Garth A. Jones, who has always found time for me, excited to see what I have made and full of new ideas for us to explore. His enduring support and guidance has carried me through the relentless onslaught of challenges and frustrations and I shall be forever grateful for the opportunities presented to me.

Finally, I thank my family, who have survived my weekly lectures and have given me the strength to continue my education to this level. I am incredibly fortunate to have the selfless and limitless support of my family and they share in my every success.

Publications

Research undertaken as part of this thesis resulted in the following publications:

1. Green, D.; V. A. Camargo, F.; Heisler, I. A.; Dijkstra, A. G.; Jones, G. A. Spectral Filtering as a Tool for Two-Dimensional Spectroscopy: A Theoretical Model. *J. Phys. Chem. A* **2018**, *122* (30), 6206–6213.

2. Bressan, G.; Green, D.; Chan, Y.; Bulman Page, P. C.; Jones, G. A.; Meech, S. R.; Heisler, I. A. One- to Two-Exciton Transitions in Perylene Bisimide Dimer Revealed by Two-Dimensional Electronic Spectroscopy. *J. Phys. Chem. A* **2019**, *123* (8), 1594–1601.

3. Green, D.; Humphries, B. S.; Dijkstra, A. G.; Jones, G. A. Quantifying Non-Markovianity in Underdamped versus Overdamped Environments and Its Effect on Spectral Lineshape. *J. Chem. Phys.* **2019**, *151* (17), 174112.

1 Introduction

The development of new technologies, which take inspiration from chemical and physical processes in natural systems, requires careful consideration of the timescales of molecular motion and the dissemination of energy. Ultrafast spectroscopy probes these timescales with a femtosecond resolution to observe the vibrational motion of molecules and reveal details of their electronic structure.[1–3] But, in the condensed phase, interactions with neighbouring molecules in the environment of the probed system introduce dissipation and dephasing, which lead to broadening of the peaks, ultimately determining the spectral lineshape.[4,5] A description of the environment is, therefore, obtained from this broadening, which is a dynamical effect controlled by the rate at which the system returns to equilibrium relative to that of the environment. These rates control the flow of information between the system and its environment, such that the system is influenced by a finite history of states, corresponding to its *memory*.[6,7] In the Markovian limit, the absence of memory enables the dynamics of the system to be modelled by simple time-local master equations. But, for a finite memory, non-Markovian effects require more complex time non-local methods to correctly account for the feedback of information from the environment to the system.[8,9] Interpreting the wealth of information contained within the spectral lineshape, regarding both the quantum system and its environment, therefore requires a detailed understanding of such memory effects and all the timescales involved in the dynamics.

Two-dimensional optical spectroscopy (2DOS) correlates the excitation and emission frequencies of Liouville pathways, which track the changing state of the system as it interacts with the electric fields of three laser pulses.[1,10–12] As the delay between interactions is increased, the appearance and oscillation of peaks provides information of the structure of the system, whilst changes in lineshape yield details of the environmental interactions.[3,13,14] For complex systems with congested linear spectra, any broadening from environmental interactions further obscures the detail, such that 2DOS provides a means of differentiating Liouville pathways into peaks across the correlation spectra and revealing any coupling between states.[2,4,15] Oscillations in the amplitude of spectra on increasing the waiting time between field interactions are a result of *coherence* pathways, involving the superposition of states, enabling the study of

quantum mechanical effects within the system dynamics.[16–18] The rephasing ability of two-dimensional photon echo techniques also projects inhomogeneous broadening due to static disorder onto the diagonal of the correlation spectra, such that electronic dephasing times are easily determined from the homogeneous anti-diagonal lineshape.[3,19] Analysis of the spectral lineshape reveals the timescale of the environmental dynamics through the decay of the associated correlation function.[1,19,20] But, restriction of the excitation frequency by the finite width of the laser spectrum leads to filtering of Liouville pathways and distortion of spectral lineshape,[21–23] where pulse overlap effects may also produce misleading oscillatory features.[24]

Experimental methods for 2DOS are being developed using frequencies across the electromagnetic spectrum,[25] including 2D infrared spectroscopy (2DIR), which probes vibrational structure,[26] and 2D electronic spectroscopy (2DES), which uses ultraviolet/visible (UV/vis) sources to investigate electronic structure and any electronic-vibrational, or *vibronic*, coupling.[11,27] Individually tuning the spectrum of each laser pulse enables the isolation of particular coherence pathways in two-colour 2DES,[3,28,29] with similar refinement achieved by employing polarised laser pulses[30–32] and chiral 2D spectroscopy.[33] The combination of UV/vis and infrared frequencies in 2D electronic-vibrational spectroscopy (2DEV) and 2D vibrational-electronic spectroscopy (2DVE) provides direct insight into the coupling between electronic and vibrational degrees of freedom.[19,34,35] 2DEV has been applied to light-harvesting complexes[36,37] and molecular dimers,[38] where analysis of the lineshape reveals correlations in the fluctuations of the electronic and vibrational frequencies due to coupling to the environment.[39,40] 2DES has found application in the study of exciton states in quantum wells[41,42] and quantum dots,[43–46] and any vibrational coupling in these systems.[47,48] Similarly, 2DES has been used to investigate the role of vibrations in singlet fission,[49] in the development of molecular logic gates,[50,51] and for studies of reaction dynamics for light-induced chemical changes, such as the photoisomerization of molecules.[52–59]

In particular, 2DES has been used to examine the remarkable quantum efficiency of light-harvesting complexes, caused by the electronic coupling of pigment chromophores into a delocalized excitonic system within the protein structure.[60–62] 2DES of the Fenna-Mathews-Olson (FMO) bacteriochlorophyll *a* protein of green sulfur bacteria exhibited cross peaks which identified specific relaxation pathways through the delocalized excitonic system.[63–68] This suggested that electronic coherence had an important role in the relaxation mechanism which produced such efficient light-harvesting. The potential application of long-lived electronic coherence in novel solar harvesting technologies created much excitement and a surge in publications on this topic.[69,70] Electronic coherences with unexpectedly long dephasing times,

ranging from hundreds of femtoseconds to a picosecond, were measured experimentally,[71–73] supported by studies using polarised pulses to remove the vibrational contributions.[74,75] But, as electronic dephasing is typically rapid, $< 100\,\mathrm{fs}$, whilst vibrational coherences are known to be much longer lived, ca. $1\,\mathrm{ps}$, significant doubt in these observations endured and the ability to distinguish electronic from vibrational coherences became a key objective.[76–78] It was soon identified that exciton-vibrational coupling had a significant role in these systems,[30,79–85] and was responsible for the enhanced rate of excitation energy transfer (EET) in the light-harvesting complexes of cryptophyte algae.[86] But, as the observation of these coherences was mainly achieved at cryogenic temperatures, the need for further studies using physiological conditions was recognised in order to confirm the coherent mechanism.[87]

The surge in experimental work was supported by substantial development of theoretical models for these systems. Evidence for long-lived electronic coherence at physiological temperatures was achieved by fully accounting for the range of environmental timescales using hierarchically coupled equations of motion.[88] Again, it was found that accounting for coupled vibrational modes was essential for recreating the experimental results, where vibronic models for molecular aggregates reproduced oscillating spectral features,[89,90] and verified the distinction of vibrational versus electronic coherences.[91,92] Since then, many model systems based on dimers of organic dye molecules and larger molecular aggregates have been used to investigate evidence of both vibrational and electronic coupling in 2DES.[93–103] Organic dye molecules and macrocycles such as cyanines[91,98,104] and porphyrins,[22,105] as well as chromophores such as chlorophyll,[28,106,107] have been extensively studied to explore the function of coherences in biological complexes.

Compared with the original adiabatic models, which solved for the electronic coupling and then considered the vibrational modes separately, simultaneously accounting for electronic and vibrational coupling within the system Hamiltonian results in quenching of the electronic coupling within molecular aggregates.[108–110] Using this nonadiabatic model for a vibronic dimer, Tiwari *et al.* showed that EET is driven by anticorrelated vibrations, leading to enhancement of vibrational coherences on the ground electronic state.[111–113] Supported by similar models, this suggested that the long-lived coherences observed in 2DES of light-harvesting systems originate from the vibrational degrees of freedom more than the electronic.[114] It was further shown that whilst vibronic coupling can prolong inter-exciton coherence, its lifetime is comparable to the electronic dephasing time and also that ground state vibrational coherences have strong contributions at the same peak locations as the expected electronic coherences.[95] Similarly, it was found that resonance between the vibrational frequency and the splitting of exciton states in model

heterodimers leads to an enhancement of the rate of EET, again emphasising the importance of vibrations in these systems.[69,115–118] Environmental effects have also been considered, where it is suggested that static disorder and inhomogeneous broadening have a role in prolonging the lifetime of observed coherences.[119] But it is regularly reported that the desirable quantum effects are irrelevant at physiological temperatures, where exciton-vibrational coherences are rapidly destroyed by electronic dephasing.[120–122] Concerns regarding the finite width of the laser spectrum leading to distortion of the 2D spectra and misinterpretation of ground and excited state coherences have also been justified by these models.[104,123,124]

The observation of long-lived electronic coherences has now been refuted, where models which fully account for the ground electronic state and correlated vibrations in the molecular aggregates attribute the beatings to ground state vibrational coherences or mixed electronic-vibrational coherences on the excited state.[14,125–128] The contribution of incoherent EET is also considered as equally, if not more relevant, than the coherent mechanism.[129,130] Despite this, the potential for the development of novel technologies inspires continued research into the role of quantum coherence in EET within light-harvesting complexes.[131,132] Recent work even suggests a transformation from electronic $\rightarrow$ vibronic $\rightarrow$ vibrational dynamics is involved in the excited state of molecular aggregates with static disorder.[133]

Successful models for 2DES therefore require an accurate account of the electronic and vibrational coupling within the system, as well as the environmental and field interactions. When considering both the system and the environment, there are too many degrees of freedom for a full quantum mechanical treatment. But, the environmental interaction can be simplified using an open quantum system approach, where the quantum system interacts with a bath of harmonic oscillators described by a spectral density.[8,134] 2DES enables characterisation of the system-bath correlation function, which follows fluctuations in the transition frequencies of the system due to interaction with the bath modes.[135,136] Experimental lineshapes are well reproduced using a stochastic theory which derives spectral lineshape from model forms of the system-bath correlation function.[137] From such a treatment comes analytical methods such as the popular multimode Brownian oscillator (MBO) model, where the system-bath interaction is calculated using the perturbative cumulant expansion.[1,138–141] As this approach determines the optical response functions using correlation functions of the energy gap fluctuations, a finite history is accounted for, such that non-Markovian memory effects are included despite the perturbative method.[142]

Alternative dynamical methods are based upon the path integral approach of Caldeira and Leggett.[143] Fluctuations in the quantum system caused by coupling to a stochastic bath are accounted for by extending a Langevin equation for Brownian motion to the quantum regime, where a friction term and a term for a random driving force are regulated by the fluctuation-dissipation theorem.[144,145] The non-perturbative Nakajima-Zwanzig projection operator technique then produces a time non-local, integro-differential master equation, which contains a memory kernel through which non-Markovian effects enter the dynamics, dependent on the shape of the spectral density.[8,146,147] But solving time non-local equations presents a significant challenge and simplifying approximations, including the Born approximation to enforce weak system-bath coupling and the Markov approximation to return to a time-local form, result in more tractable perturbative methods, such as Redfield theory.[142,148]

Kubo and Tanimura have also presented an alternative solution which reformed the path integral approach into the time-local hierarchical equations of motion (HEOM).[9,146,149] In its earliest form, the HEOM method was derived from factorised initial conditions, where the system and bath are uncorrelated, restricted to Gaussian-Markovian noise and the high temperature limit.[150] But it was quickly shown by Tanimura *et al.* that the HEOM method is suitable for coloured, non-Markovian noise, strong system-bath coupling at low temperatures and correlated initial conditions, such that it presents a numerically exact solution for the full range of bath coupling strengths and timescales.[151–154] Different approaches to the decomposition of the spectral density have resulted in several variations of the HEOM for studies where the electronic states of the system are coupled to vibrational modes. These correspond to different limits of the damping strength, including undamped methods where the vibration is in the system,[155] overdamped for weakly coupled bath vibrations,[156,157] underdamped for strongly coupled bath vibrations,[158] and combinations of the above.[159] HEOM methods have been applied to a range of linear and non-linear optical spectroscopies, including 2DIR, where multiple vibrational modes are coupled to the same or different thermal baths with the potential for correlated bath interactions.[149,160,161] The facility of the HEOM for modelling spectroscopy comes from the ability to propagate bath correlations across field interactions and fully account for non-Markovian effects.[156] HEOM methods have also been used in studies of electron transfer[162] and the entanglement of qubits,[163,164] as well as the light-harvesting complexes and excitonic molecular aggregates.[157,165–168] Modern models combine the nonadiabatic vibronic dimer Hamiltonian with HEOM methods for separate baths responsible for electronic dephasing and vibrational relaxation.[169]

2DES involves a third order polarization generated by convolution of the three electric fields with the molecular response function, which describes the evolution of the system and its interaction with the environment.[26,140] Methods such as the MBO model, which involve a perturbative expansion in the system-field interaction, have seen great success in reproducing experimental lineshapes.[1,89,136,170] But the perturbative method requires the system-field interaction to be weak and complications such as finite pulse width and pulse overlap effects, as well as competing processes such as EET in larger systems, require the incorporation of additional terms into the response function, decreasing the efficiency of these models.[142] In contrast, non-perturbative methods avoid any simplifying approximations and are capable of accounting for any strength system-field coupling and all time-ordering effects.[171] Non-perturbative approaches calculate the third order polarization for all phase combinations of the incident fields and then extract the phase-matched direction of 2DES as post-processing.[124,172,173] But this is computationally intensive and only adds to the demands of the system-bath interaction.[142,174]

An alternative quantum dynamical method is the equation-of-motion phase-matching approach (EOM-PMA) developed by Gelin *et al.*[175] This involves propagation of a set of auxiliary density matrices to obtain the third order polarization in the phase-matched direction.[174] Although derived using a perturbative expansion and thus restricted to the weak field limit, explicit definition of the laser pulses within the EOM-PMA accounts for all finite pulse effects, as in the non-perturbative methods, but only for the phase-matched direction, avoiding the expensive post-processing. The EOM-PMA has been generalised to any number of field interactions[176] and has also been translated for wavefunction based methods.[177] It has been used in 2DES studies of FMO,[178] conical intersections[179] and for the investigation of finite pulse effects in excitonic and vibronic systems.[180,181] The design of the EOM-PMA allows it to be combined with a variety of dynamical methods for the system-bath interaction, including Redfield approaches for Markovian baths[174,175,180] and non-Markovian methods, including time non-local master equations[98,142,182,183] and the HEOM.[184,185] Combination of the EOM-PMA with the HEOM produces a formidable model, which accounts for finite pulse effects in addition to the exact, non-perturbative open quantum system dynamics.[186]

In this thesis, a multipurpose model is developed for the 2DES of vibronic systems, including non-Markovian and finite pulse effects. This is achieved by implementation of the vibronic Hamiltonian for monomer and dimer systems into quantum dynamical simulations which combine the HEOM with the EOM-PMA. Theoretical methods are presented in chapter 2, beginning with a review of the theory of open quantum systems and Markovianity in section 2.1. Components of the total Hamiltonian are then discussed in section 2.2, in terms

of the vibronic system and its interactions with the harmonic bath and the external electric fields. The hierarchical equations of motion are then derived in different limits of the phenomenological damping in section 2.3 and the theory of spectroscopy is summarised in section 2.4, describing separate methods for the calculation of 2D spectra, with or without a laser spectrum of finite width. The following chapters then present applications of the model which have featured in recent publications and any subsequent advances. In chapter 3, the capability of the model is demonstrated through a comparison of the spectral lineshape obtained using approaches where the vibration is contained within the system or bath degrees of freedom, followed by an investigation of the measurable non-Markovianity in different damping limits. Then, the origins of peaks in 2DES are explored through an analysis of the Liouville pathways for a vibronic zinc-porphyrin monomer in chapter 4, where the finite width of the laser spectrum is used to selectively filter pathways and remove spectral features. The model is then pushed to its computational limits in chapter 5, where the 2DES of vibronic dimers is discussed in different limits of the electronic and vibronic coupling in section 5.1. Simulations for a series of perylene bisimide homodimers then demonstrate the effect of decreased electronic coupling strength in J-aggregates on the appearance of excited state absorption peaks in section 5.2. Finally, all features of the model are employed in section 5.3 for the 2DES of a model heterodimer system, designed such that selective excitation using the finite width of the laser spectrum, combined with rapid vibrational relaxation, demonstrates evidence of EET between monomers as the waiting time increases.

2 Theoretical Methods

Details of the theoretical methods used in this thesis are presented in this chapter. A general description of open quantum system methods and Markovianity is followed by details of the total Hamiltonian, separated into the system, bath and field components. Non-Markovian quantum dynamical methods are then discussed, presenting the hierarchical equations of motion (HEOM) methods used, before reviewing the theory of spectroscopy.

2.1 Open Quantum Systems and Markovianity

This section presents an overview of the models developed in this thesis by introducing the key concepts of open quantum systems and Markovianity. Open quantum system models separate a quantum system from its environment, such that the degrees of freedom requiring a full quantum mechanical treatment are reduced. The quantum system is then evolved including the interaction with an infinite thermal bath to account for dephasing and the dissipation of energy into the environment. A quantum mechanical interpretation of Markovianity then provides a framework which describes the memory of the system in terms of the flow of information between the system and bath. Measures from quantum information theory can then be used to quantify the degree of non-Markovianity within the dynamics and illustrate the role of non-Markovian memory effects within these models.

2.1.1 Closed Quantum Systems

A complete description of a quantum system is given by the time dependent wavefunction, $|\Psi(t)\rangle$, from which the expectation values of all physical observables are obtained. The evolution of the quantum system is determined by the Schrödinger equation,

$$i\hbar\tfrac{\mathrm{d}}{\mathrm{d}t}\left|\Psi(t)\right\rangle = \mathsf{H}(t)\left|\Psi(t)\right\rangle, \tag{2.1.1}$$

where $\hbar = \frac{h}{2\pi}$ is the reduced Planck's constant, $i = \sqrt{-1}$ and $\mathsf{H}(t)$ is the Hamiltonian operator for a closed system. In this way, a closed system defines a completely isolated volume of space with all degrees of freedom defined within $\mathsf{H}(t)$.

A state at t_0 is transformed over a period of time, t, using the unitary time-evolution operator,

$$|\Psi(t)\rangle = U(t, t_0)\,|\Psi(t_0)\rangle\,, \tag{2.1.2}$$

where,

$$U(t, t_0) = \mathsf{T}_{\leftarrow} \exp\left(-\frac{i}{\hbar}\int_{t_0}^{t} \mathrm{d}s\, \mathsf{H}(s)\right). \tag{2.1.3}$$

The integral accounts for the time dependence of the Hamiltonian and $\mathsf{T}_{\leftarrow}$ is the chronological (forward) time-ordering operator.[8]

For condensed phase models involving ensembles of molecules, it becomes useful to adopt the density operator formalism to account for mixed states. The density operator is given by,

$$\rho(t) = \sum_k p_k\,|\Psi_k(t)\rangle\langle\Psi_k(t)|\,, \tag{2.1.4}$$

where each state of a molecule, $|\Psi_k\rangle$, is occupied with the probability, p_k such that $\sum_k p_k = 1$.[187] When a single $p_k = 1$, the density operator is in a *pure* state. Statistical mixtures of pure states then produce *mixed* states, with the purity condition given by $\rho^2 = \rho$. The density operator equally extends to mixtures of mixed states as,[187]

$$\rho(t) = \sum_{jk} p_j p_{jk}\,|\Psi_{jk}(t)\rangle\langle\Psi_{jk}(t)| = \sum_j p_j \rho_j, \tag{2.1.5}$$

where $\rho_j(t) = \sum_k p_{jk}\,|\Psi_{jk}(t)\rangle\langle\Psi_{jk}(t)|$, enabling the density operator to follow the population of the entire ensemble of molecules within the closed system. This enables the state space of the Hamiltonian to be defined in terms of the energy levels of a single molecule, with the generality of the density operator able to describe a statistical ensemble of the order of several moles.

The diagonal elements of the density operator, *populations*, correspond to probabilities identifying the proportion of the ensemble occupying each state, such that $\rho(t)$ has a trace of unity and is a positive operator, with all eigenvalues ≥ 0. The off-diagonal elements are *coherences*, which identify that the system is in a *superposition* of basis states, $|\Psi_k\rangle$, when non-zero. The density matrix of a closed system evolves as,

$$\rho(t) = U(t, t_0)\rho(t_0)U^{\dagger}(t, t_0), \tag{2.1.6}$$

for which the equation of motion is the Liouville-von Neumann equation,

$$\frac{\mathrm{d}}{\mathrm{d}t}\rho(t) = \mathcal{L}(t)\rho(t) = -i[\mathsf{H}(t), \rho(t)] = -i(\mathsf{H}(t)\rho(t) - \rho(t)\mathsf{H}(t)), \tag{2.1.7}$$

where $\mathcal{L}(t)$ is the Liouville superoperator and square brackets denote the commutator.[8] On integration, the density matrix after some time, t, is obtained from the initial state $\rho(t_0)$ as,

$$\rho(t) = \mathsf{T}_{\leftarrow} \exp\left(\int_{t_0}^{t} \mathrm{d}s\mathcal{L}(s)\right)\rho(t_0). \tag{2.1.8}$$

With the time dependence confined to the states, this definition corresponds to the Schrödinger picture of quantum mechanics. An alternative involving the time dependence transferred to within the operators is known as the Heisenberg picture. These are limiting cases of the more general interaction picture, where a Hamiltonian describing the interaction of two components is separated as,[8]

$$\mathsf{H}(t) = \mathsf{H}_0 + \mathsf{H}_{\mathrm{I}}(t). \tag{2.1.9}$$

H_0 is time independent, containing the sum of the contributing Hamiltonians assuming no interaction, whilst $\mathsf{H}_{\mathrm{I}}(t)$ contains all of the time dependent interaction terms. The interaction picture is used in the theory of open quantum systems, section 2.1.2, and spectroscopy, section 2.4.1, as the closed system dynamics are separated into the interaction of a reduced system with its environment and any external fields.

2.1.2 Open Quantum Systems

In the theory of open quantum systems, the sealed volume of space is separated into the system of interest and its environment.[7,8] The system and environment are coupled such that neither evolution is free of the other. This is identical to the concept of *entanglement*, though this name is avoided in this work due to its primary association with quantum computation and qubits, which are not discussed.[187]

The total Hamiltonian is now,

$$\mathsf{H}(t) = \mathsf{H}_{\mathrm{S}} \otimes \mathrm{I}_{\mathrm{B}} + \mathrm{I}_{\mathrm{S}} \otimes \mathsf{H}_{\mathrm{B}} + \mathsf{H}_{\mathrm{SB}}(t), \tag{2.1.10}$$

where H_m and I_m, $m \in \{\mathrm{S}, \mathrm{B}\}$, are respectively the Hamiltonian and identity operator for the system or bath degrees of freedom and $\mathsf{H}_{\mathrm{SB}}(t)$ is the time dependent interaction term.[8] The total Hamiltonian involves a composite Hilbert space constructed from the tensor product of the system and

environment degrees of freedom, $\mathcal{H}_{\text{SB}} = \mathcal{H}_{\text{S}} \otimes \mathcal{H}_{\text{B}}$, each of which can be retrieved via use of a partial trace such that the reduced operator of the system $\rho_{\text{S}}(t) = \mathbf{Tr}_{\text{B}}\rho(t)$. From eq. 2.1.6, the evolution of the reduced density operator is thus,[8]

$$\rho_{\text{S}}(t) = \mathbf{Tr}_{\text{B}}\left(U(t,t_0)\rho(t_0)U^{\dagger}(t,t_0)\right). \tag{2.1.11}$$

Enforcing the condition of separability, such that the initial states of the system and bath are uncorrelated, the total state at t_0 is the tensor product of the system and bath states,[7]

$$\rho(t_0) = \rho_{\text{S}}(t_0) \otimes \rho_{\text{B}}(t_0). \tag{2.1.12}$$

Further applying the Born approximation, where the system-bath interaction is sufficiently weak that the state of the bath does not deviate significantly from thermal equilibrium and the time dependence of the bath can be ignored, the evolution of the reduced system density operator becomes,

$$\rho_{\text{S}}(t) = \Phi(t)\rho_{\text{S}}(t_0) = \mathbf{Tr}_{\text{B}}\left(U(t,t_0)(\rho_{\text{S}}(t_0) \otimes \rho_{\text{B}})U^{\dagger}(t,t_0)\right), \tag{2.1.13}$$

where $\Phi(t)$ defines a linear map within the reduced system's state space of density matrices, $\mathcal{S}(\mathcal{H}_{\text{S}})$.[8] The significance of $\Phi(t)$ is that it maps the reduced system state $\rho_{\text{S}}(t_0)$ to $\rho_{\text{S}}(t)$, accounting for the bath interaction correctly, but operating only on the state space of the reduced system.

For a clear distinction from the unitary evolution of the total density operator, $\Phi(t)$ is known as a quantum *dynamical map*, which is trace, Hermiticity and positivity preserving for operators such as the density operator. A Hermitian operator is positive if all its eigenvalues are positive, an essential property for probability distributions such as the density operator.[7] The condition of positivity for a dynamical map then requires that positive operators be transformed to other positive operators, ensuring that physical states, with non-negative probabilities, are transformed to other physical states. The condition of complete positivity asserts this to be true for the total degrees of freedom, including the traced bath states.[7,68] In the language of quantum information theory, a completely positive map corresponds to a *quantum channel*, equivalent to any evolution of the density operator where these conditions are met.[187,188]

Breuer *et al.* define an environment with infinite degrees of freedom, corresponding to a continuum of modes, as a *reservoir*, termed a *bath* when allowed to achieve thermal equilibrium.[7,8] In this thesis, the environment is always considered as a continuum of modes at a defined temperature, such that the terms *environment* and *bath* are used interchangeably. In fully accounting for the bath interaction, the theory of open quantum systems upholds the laws of thermodynamics whilst only propagating the degrees of freedom of the

reduced system, making it a powerful method for modelling phenomena in the condensed phase.

The affect of the bath is to introduce damping into the evolution of the reduced system. This is analogous to classical Langevin equations where stochastic Brownian motion is hindered and interrupted by a frictional force.[134] In terms of modelling spectroscopy, there are two main types of damping, as defined in traditional models for Nuclear Magnetic Resonance (NMR) spectroscopy.[189] These are T_1 type dissipation, where energy is transferred from the system to the bath, corresponding to relaxation of the system, and T_2^* type dephasing, which causes decoherence of superposition states.[26,149] Dephasing is hugely significant in spectroscopy as excitation by a broadband laser pulse typically transfers population to multiple excited states, creating a superposition which evolves with time as a *wavepacket*. Dephasing of the wavepacket causes the signal to decay, introducing uncertainty in the involved transition frequencies, ultimately resulting in spectral broadening.

The amount of damping is determined by the relevant correlation functions, introduced formally in section 2.2.2.3, where the controlling factor is the timescale of bath relaxation. This defines the time required for the bath to return to its equilibrium state after some perturbation, such as the promotion of solute molecules to an excited electronic state, encouraging the reorganisation of surrounding solvent molecules into a more stabilising arrangement. Considering the evolution of the system as discrete steps in time, when the timescale of bath relaxation is fast compared with the relaxation of the system, the bath always reachieves equilibrium between steps. This causes the system-bath interaction to be effectively constant from the perspective of the system and the state of the bath to have negligible influence on the evolution of the system. However, when the system and bath relaxation have similar timescales, the bath does not fully equilibrate between time steps and thus the state of the bath may have a significant impact on the evolution of the system. In this case, a finite history of the state of the system and bath must be taken into account to correctly predict the evolution of the system. The role of the finite history is interpreted as an effect of *memory* within the dynamics.[7,9]

In the limit where the bath has no memory of previous states due to the rapid return to equilibrium, dynamical maps can be combined according to the semigroup property,

$$\Phi(t_1)\Phi(t_2) = \Phi(t_1 + t_2), \tag{2.1.14}$$

for t_1, $t_2 \geq 0$. The set of dynamical maps $\Phi(t)$, $t \geq 0$, which obey this property is called a *quantum dynamical semigroup*.[8,190] This implies the dynamical maps

can be written in exponential form,

$$\Phi(t) = \exp\left(\mathcal{L}t\right), \tag{2.1.15}$$

where $\mathcal{L}$ is the *generator*, analogous to the Liouville superoperator introduced previously, but now generalised for the equation of motion of an open quantum system, typically in Lindblad form, introduced in section 2.3.1. For time dependent generators, the dynamical map becomes the *propagator*,[8]

$$G(t, t_0) = \mathsf{T}_{\leftarrow} \exp\left(\int_{t_0}^{t} \mathrm{d}s\mathcal{L}(s)\right), \tag{2.1.16}$$

with,

$$G(t, t_1)G(t_1, t_0) = G(t, t_0). \tag{2.1.17}$$

The ability to combine propagators in this way defines a *divisible* dynamical map.[191] Divisibility implies that propagation over a period of time can be portioned into independent evolutions, with no adjoining memory. Divisible dynamical maps therefore obey the Markov property and are Markovian.[6,190]

2.1.3 Markovianity

In classical probability theory, the Markov property dictates that the next state of a system is entirely determined by the current state, independent of its history.[7,191] Therefore, describing the evolution of a system as a series of discrete points in space and time, for a Markovian process, the probabilities which govern the next set of coordinates for each element within a distribution are entirely determined by the current coordinates. This means that previous states have no influence and the master equation is time-local, involving no memory. Consequently, any scenario which does not obey this condition is non-Markovian and the memory of previous states has an important role in the evolution of the system. This is summarised in figure 2.1.1, which follows the trajectory of some system along a coordinate, indicating the importance of previous states in determining the current state as a quantifiable memory for both Markovian and non-Markovian cases. This shows how a finite history of states is involved in non-Markovian evolution, implying a time non-local master equation.

This is the definition of classical Markovianity, which is related to the notion of quantum Markovianity, but cannot be the same due to the challenges of measurement in quantum systems. In quantum mechanics, accurate probabilities for the total state of the system and bath cannot be determined for every discrete moment in time, as the action of measurement collapses the wavefunction, destroying any system-bath correlations which may have

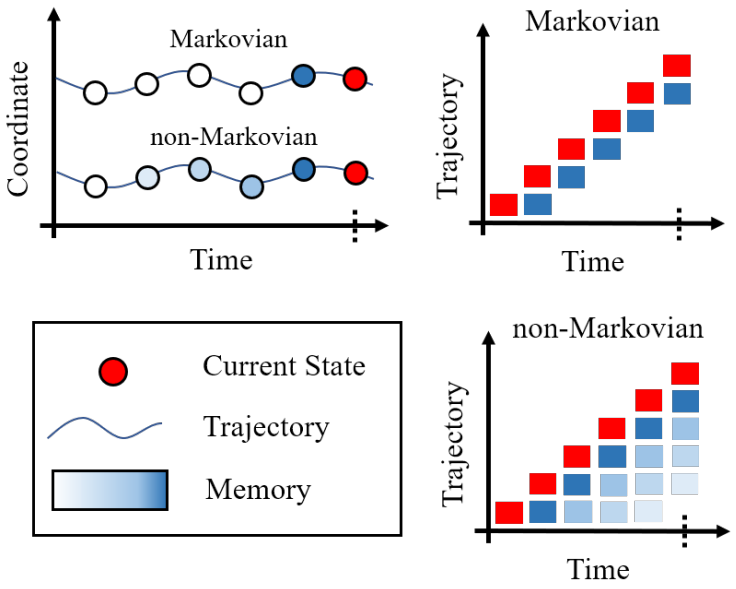

Figure 2.1.1: The importance of memory in Markovian vs. non-Markovian evolution. As the system progresses along a trajectory, the influence of a previous state in determining the current state is indicated by its memory. In a Markovian evolution, for each time step, the current state is entirely determined by the preceding state. Conversely, on reaching the time step indicated by the dashed line, a non-Markovian evolution involves a finite history of previous states.

influenced future steps as an effect of memory. Therefore, a workable definition of quantum Markovianity must originate from the state of the reduced system alone, readily obtained through state tomographic measurements.[7] Quantum Markovianity is defined via an analysis of the flow of information between the system and bath.

The amount of information held regarding a system is quantified in terms of its entropy, which is a measure of uncertainty and disorder. It is logical to associate more ordered systems of lower entropy with large amounts of information, such that increasing entropy for more disordered systems represents a loss of information and an increase in ambiguity regarding the state, energy and position *et cetera*. For quantum systems, the Von Neumann entropy is measured as,

$$S(\rho) = -k_{\mathrm{B}}\mathbf{Tr}\left(\rho \ln \rho\right), \tag{2.1.18}$$

based upon the classical Shannon entropy.[8,187,192] The entropy of a pure state is zero as maximum information is available. For a set of distinct states, this corresponds to one state being occupied, whilst all others are unoccupied. The entropy of mixed states is thus greater than zero as the ambiguity increases regarding the configuration of the ensemble population amongst several states. Maximum entropy corresponds to uniform occupation of all available states, leading to maximum ambiguity.

For composite systems, $\mathcal{H}_{\mathrm{AB}} = \mathcal{H}_{\mathrm{A}} \otimes \mathcal{H}_{\mathrm{B}}$, such as open quantum systems, the subadditivity condition,

$$S(\rho_{\mathrm{AB}}) \leq S(\rho_{\mathrm{A}}) + S(\rho_{\mathrm{B}}), \tag{2.1.19}$$

describes how correlations between subsystems A and B reduce the entropy by providing additional information compared with uncorrelated states, where the above would be equal.[187] This demonstrates how the destruction of system-bath correlations leads to a loss of information and an increase in entropy. Entropy is also a concave functional,

$$S\left(\sum_j p_j \rho_j\right) \geq \sum_j p_j S(\rho_j), \tag{2.1.20}$$

such that the entropy of a mixture of states is higher than the entropy of the constituent states, given that the states ρ_j are not identical.[8,187]

A *distance measure* then enables a comparison of the flow of information in different quantum channels. Two classical probability distributions can be compared at one moment in time using the static distance measure of the *trace distance*.[187] This extends to the quantum regime for a pair of states, ρ_1 and ρ_2, such that the trace distance is defined as,[6,191,193]

$$D(\rho_1, \rho_2) = \tfrac{1}{2}\mathbf{Tr}|\rho_1 - \rho_2|, \tag{2.1.21}$$

where $|\mathsf{A}| = \sqrt{\mathsf{A}^\dagger \mathsf{A}}$, as the positive square root.[187]

The trace distance provides a quantifiable *distinguishability* of the two systems as a continuous scale between identical states, $\rho_1 = \rho_2$, where $D(\rho_1, \rho_2) = 0$ and orthogonal states where $D(\rho_1, \rho_2) = 1$.[7,187] Density matrices are orthogonal if their supports are orthogonal, where the *support* is the subspace of eigenvectors with non-zero eigenvalues. Likewise, identical density matrices have parallel supports. Figure 2.1.2 shows the decay of the trace distance for a two-level-system with orthogonal initial conditions. The nested pie charts show the populations of the ground (g) and excited (e) states at specific times, where the outer (inner) chart corresponds to an initial population entirely in its ground (excited) state. As the excited population of the inner system relaxes over time, its ground state population increases, leading to a decrease in distinguishability between the two systems, resulting in a decrease in the trace distance.

The *contraction of the trace distance* by trace preserving, positive dynamical maps then forces,

$$D(\rho_1(t), \rho_2(t)) \leq D(\rho_1(t_0), \rho_2(t_0)), \tag{2.1.22}$$

as the system states ρ_1 and ρ_2 become less distinguishable over time due to the

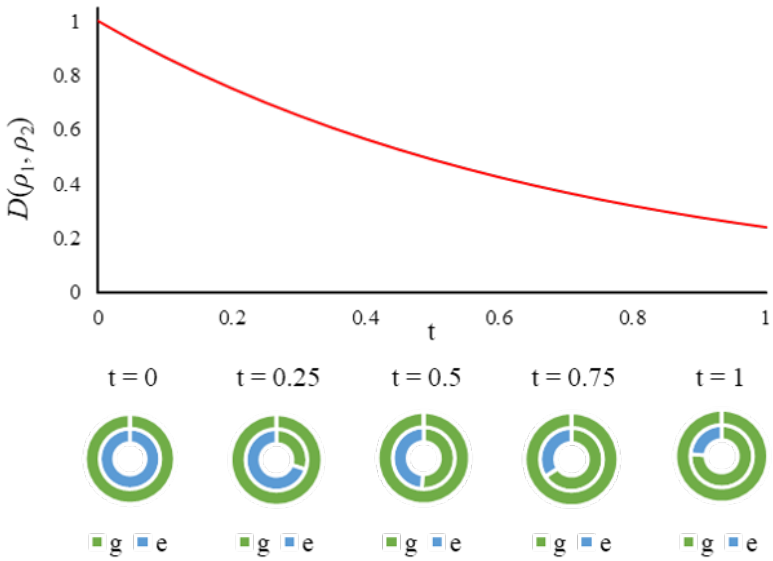

Figure 2.1.2: The trace distance, $D(\rho_1, \rho_2)$, for a two-level-system initially in its ground state (outer) compared with its excited state (inner) decreases as the excited state population relaxes, following the decrease in distinguishability. Reprinted from reference 194, with the permission of AIP Publishing.

increase in entropy of each system.[7,190] As decreasing distinguishability corresponds to the monotonic loss of information regarding the states ρ_1 and ρ_2, Breuer, Laine and Piilo interpret this decrease as the transfer of information from the system to the bath, such that the entropy of the reduced system increases whilst the entropy of the bath decreases.[6,190] The increase in information of the bath manifests as either a change of state within the bath degrees of freedom or the formation of additional system-bath correlations.[7]

By extension, the contraction of the trace distance further applies to divisible dynamical maps in a quantum dynamical semigroup, such that a continuous reduction in distinguishability is also associated with the Markov property. Therefore, if the conditions for a quantum dynamical semigroup are met, the evolution must be Markovian, where a Markovian evolution corresponds to the monotonic loss of information from the system to the bath.[6,9,188,191] This immediately presents the alternative non-Markovian scenario for non-divisible dynamical maps, where an increase in the trace distance, equivalent to an increase in distinguishability, corresponds to the transfer of information from the bath to the system. This description therefore gives a much clearer definition of memory as the ability for information transferred to the bath to feedback into the system, involving the build up of system-bath correlations over some finite history.[7]

Breuer, Laine and Piilo (BLP) then use this description to define a measure of non-Markovianity. First, the flux of information transfer is calculated as the

gradient of the trace distance,[195]

$$\sigma = \frac{\mathrm{d}}{\mathrm{d}t} D(\rho_1(t), \rho_2(t)). \tag{2.1.23}$$

Integration of the positive flux, $\sigma > 0$, then measures the amount of information returned to the system through non-Markovian feedback,[6,190,193,196,197]

$$\mathcal{N} = \max_{\rho_{1,2}} \int_{\sigma>0} \sigma(t)\, \mathrm{d}t. \tag{2.1.24}$$

The value of $\mathcal{N}$ therefore corresponds to the total information transferred from the bath to the system, quantifying the *degree of non-Markovianity*. This provides a means of comparison for the role of non-Markovian effects within open quantum system dynamics. Maximum non-Markovianity is achieved for orthogonal initial states, whilst $\mathcal{N} = 0$ identifies a Markovian process.[190] This measure is used in section 3.3 to investigate the role of non-Markovian effects in determining spectral lineshape in different limits of the bath damping.

2.1.4 External Forces

For simulations of optical spectroscopy, the open quantum system is exposed to the external electric field of an incident laser. A full description of the interaction of system molecules with an electromagnetic field is given by the extremely rigorous theory of quantum electrodynamics (QED).[198] Similar to the theory of open quantum systems, this adds terms into the total Hamiltonian representing the energy of the field, H_F, and the time dependent system-field interaction, $\mathsf{H}_\mathrm{SF}(t)$. By ignoring spontaneous processes and assuming sufficient intensity to obtain coherent states of the electromagnetic field, the semi-classical perspective can be adopted, which accounts for the interaction component only.[199] The semi-classical approximation involves adding the time dependent system-field interaction term, $\mathsf{H}_\mathrm{SF}(t)$, to the Hamiltonian of the reduced system, H_S, within the generator, $\mathcal{L}$, in eq. 2.1.16.

Simulations in this thesis therefore represent a scenario as in figure 2.1.3, where a solution of perylene bisimide in toluene is probed by a series of laser pulses (see section 5.2). The perylene bisimide molecules are the system and the presence of the toluene provides an environment which is the bath. The electric field of the laser interacts with the system, placing the perylene bisimide molecules in a superposition of excited states. The damping influence of the bath then causes the resulting excited state wavepacket to dephase and the extra energy to dissipate into the bath over the following picoseconds. If the timescales of system and bath relaxation are similar, the feedback of information from the bath to the system provides a memory of previous states, requiring

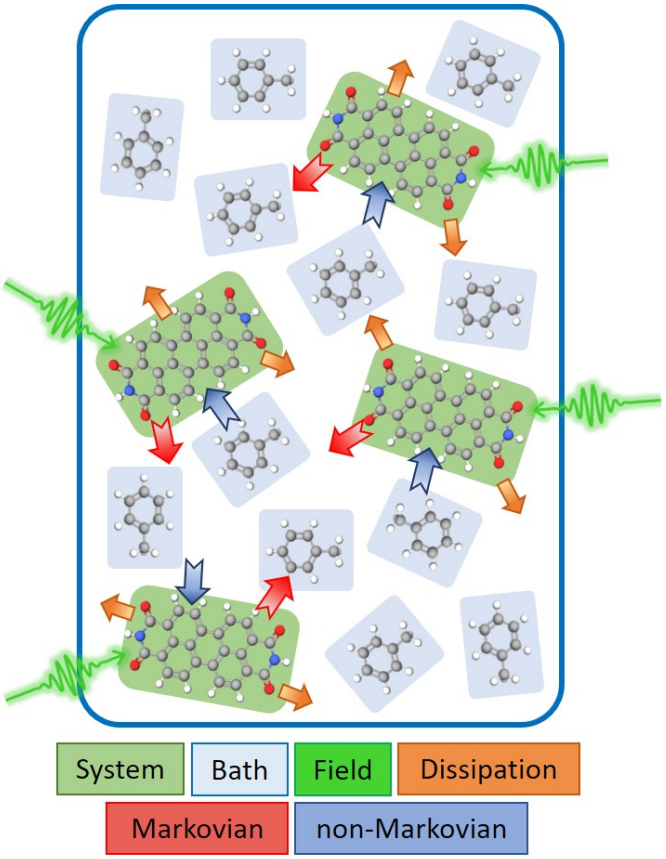

Figure 2.1.3: A solution of perylene bisimide in toluene interacting with the electric field of a laser pulse as an open quantum system. The laser excites the system (solute) which leads to dissipation of energy into the bath (solvent). The monotonic loss of information from the system to the bath is Markovian such that the feedback of information from the bath to the system is non-Markovian.

non-Markovian methods to obtain realistic simulations. As the resolution of time-resolved spectroscopic methods improves, currently on the order of attoseconds for X-ray methods,[200] the ability to correctly account for non-Markovian effects becomes ever more pertinent.

Having introduced the progression from closed to open quantum system dynamics and the distinction of the reduced system from its bath and any external forces, section 2.2 goes on to define the components of the Hamiltonian in detail. The definition of Markovianity presented in this section is applied throughout this thesis, where the quantum information theory perspective is used to interpret the results of chapter 3.

2.2 Components of the Hamiltonian

In this section, the displaced harmonic oscillator model is used to define the reduced system Hamiltonians for vibronic monomers and dimers, including a description of useful basis transformations. The spectral densities and bath coupling operators involved in the system-bath interaction for these systems are then introduced, followed by definition of the dipole moment operator, involved in the system-field interaction.

2.2.1 System Hamiltonian

2.2.1.1 Vibronic Monomer

For a system with two electronic states, where the ground state, $\mathbf{S}_0$, is denoted by $|g\rangle$, and the first excited state, $\mathbf{S}_1$, by $|e\rangle$, the Hamiltonian is,

$$\mathsf{H}_{\mathrm{M}}^{S} = |g\rangle\mathsf{h}_g\langle g| + |e\rangle\mathsf{h}_e\langle e|\,, \tag{2.2.1}$$

where h_i, $i = g, e$ are the nuclear Hamiltonians for the vibrational contribution,

$$\mathsf{h}_g = \sum_j \left(\frac{\mathsf{p}_j^2}{2m_j} + \tfrac{1}{2}m_j\omega_j^2\mathsf{q}_j^2\right), \tag{2.2.2}$$

$$\mathsf{h}_e = \hbar\omega_{eg}^0 + \sum_j \left(\frac{\mathsf{p}_j^2}{2m_j} + \tfrac{1}{2}m_j\omega_j^2(\mathsf{q}_j - d_j)^2\right), \tag{2.2.3}$$

and m_j, p_j and q_j are respectively the mass, the momentum and the coordinate of the jth vibrational mode, with frequency ω_j.[1] This defines the Hamiltonian of a vibronic monomer, identified by subscript M, focusing on the dominant electronic and vibrational contributions and ignoring any translational or rotational terms. Each vibrational mode is approximated as a harmonic oscillator, independently coupled to the electronic degrees of freedom, where d_j is the displacement of the minima of the ground, V_g, and excited state, V_e, potential energy surfaces along the coordinate q_j, and $\hbar\omega_{eg}^0$ is the transition energy between the lowest vibrational levels of the two electronic states. The potential energy surface (PES) for a vibronic monomer is shown in figure 2.2.1. Each vibrational mode couples to the electronic degrees of freedom linearly upon excitation, with no change in the reduced mass or frequency of the mode, where the displacement accounts for a change in the equilibrium geometry of the excited electronic state compared with that of the ground state.[17,110]

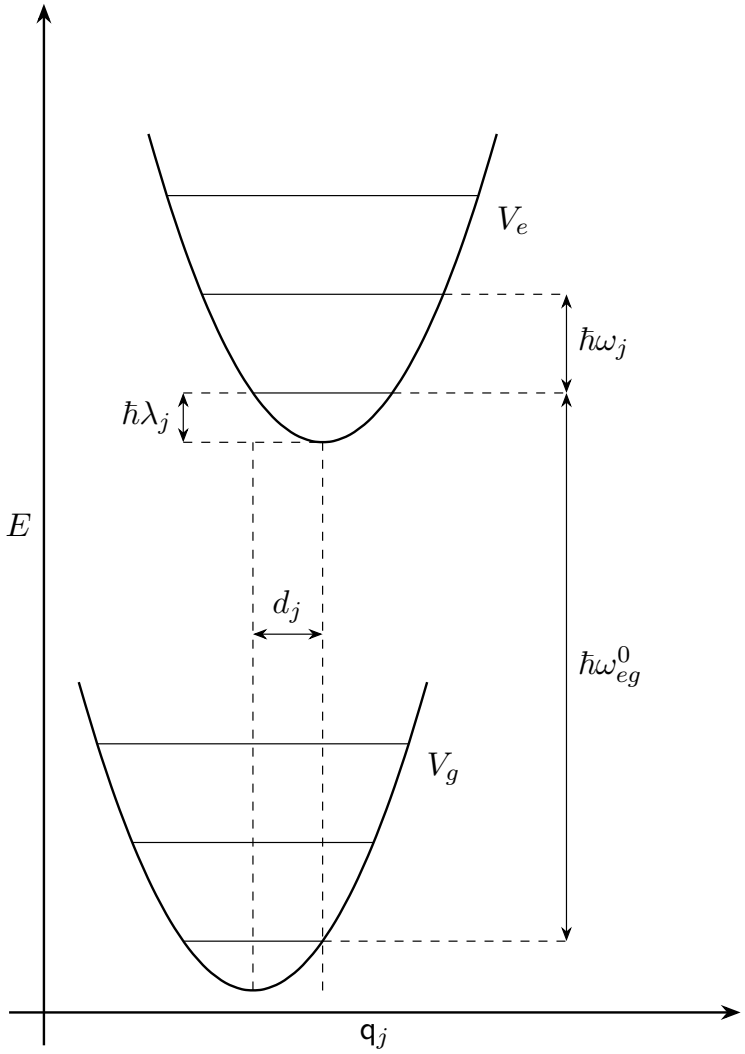

Figure 2.2.1: Potential energy surface of a vibronic system with two electronic states coupled to the jth vibrational mode.

Switching to a dimensionless coordinate system independent of the reduced mass,[1]

$$\mathsf{P}_j = \left(\sqrt{\hbar m_j \omega_j}\right)^{-1} \mathsf{p}_j, \tag{2.2.4}$$

$$\mathsf{Q}_j = \left(\sqrt{\frac{m_j \omega_j}{\hbar}}\right) \mathsf{q}_j, \tag{2.2.5}$$

$$\Delta_j = \left(\sqrt{\frac{m_j \omega_j}{\hbar}}\right) d_j, \tag{2.2.6}$$

the nuclear Hamiltonians are expressed in the occupation number representation as,

$$\mathsf{h}_g = \sum_j \hbar\omega_j \left(\mathsf{b}_j^\dagger \mathsf{b}_j + \tfrac{1}{2}\right), \tag{2.2.7}$$

$$\mathsf{h}_e = \hbar(\omega^0_{eg} + \lambda) + \sum_j \hbar\omega_j \left(\mathsf{b}_j^\dagger \mathsf{b}_j - \frac{\Delta_j}{\sqrt{2}}(\mathsf{b}_j + \mathsf{b}_j^\dagger) + \tfrac{1}{2}\right), \tag{2.2.8}$$

where the second quantized form creation, $\mathsf{b}_j^\dagger$, and annihilation, b_j, operators are,[180,186]

$$\mathsf{b}_j^\dagger = \sqrt{\frac{m_j\omega_j}{2\hbar}}\left(\mathsf{q}_j - \frac{i}{m_j\omega_j}\mathsf{p}_j\right) = \frac{1}{\sqrt{2}}\left(\mathsf{Q}_j - i\mathsf{P}_j\right), \tag{2.2.9}$$

$$\mathsf{b}_j = \sqrt{\frac{m_j\omega_j}{2\hbar}}\left(\mathsf{q}_j + \frac{i}{m_j\omega_j}\mathsf{p}_j\right) = \frac{1}{\sqrt{2}}\left(\mathsf{Q}_j + i\mathsf{P}_j\right), \tag{2.2.10}$$

and obey the boson commutation relation,

$$[\mathsf{b}_j, \mathsf{b}_k^\dagger] = \delta_{jk}. \tag{2.2.11}$$

For N vibrational modes, the nuclear contribution to the system Hamiltonian consists of the orthonormal vectors,

$$|n\rangle = |\nu_0\nu_1\ldots\nu_{N-1}\rangle, \tag{2.2.12}$$

corresponding to the tensor product of the subspace of each mode, where $|\nu_j\rangle$ are eigenstates of the number operator for the jth mode,

$$\mathsf{b}_j^\dagger\mathsf{b}_j|\nu_j\rangle = \nu_j|\nu_j\rangle, \tag{2.2.13}$$

and,

$$\mathsf{b}_j|n\rangle = \sqrt{\nu_j}|\nu_0\ldots\nu_j - 1,\ldots\nu_{N-1}\rangle, \tag{2.2.14}$$

$$\mathsf{b}_j^\dagger|n\rangle = \sqrt{\nu_j+1}|\nu_0\ldots\nu_j + 1,\ldots\nu_{N-1}\rangle. \tag{2.2.15}$$

The vibrational Hamiltonian for the ground electronic state, h_g, is diagonal in this basis, $\mathsf{h}_g|n\rangle = E_n|n\rangle$, with energies,

$$E_n = \sum_j^N \hbar\omega_j(\nu_j + \tfrac{1}{2}), \tag{2.2.16}$$

whereas the excited state vibrational Hamiltonian, h_e, contains off-diagonal elements $\propto(\mathsf{b}_j + \mathsf{b}_j^\dagger)$.

Combination with the electronic degrees of freedom via a tensor product gives the full monomer wavefunction in the *site* basis, indicated by superscript *S*,

$$|\Psi_{\mathrm{M}}^S\rangle = |\alpha\rangle\otimes|n\rangle = |\alpha, n\rangle, \tag{2.2.17}$$

where $\alpha = g, e$. This invokes the Born-Oppenheimer approximation, stating that there is no coupling of the electronic and vibrational motion in this basis, other than the explicitly introduced off-diagonal terms described above.[1,201]

The strength of the electronic and vibrational coupling is governed by the excited state displacement of each mode, often reported as the Huang-Rhys parameter, S_j,[1,109]

$$S_j = \tfrac{1}{2}\Delta_j^2 = \frac{m\omega_j d_j^2}{2\hbar}, \tag{2.2.18}$$

which results in the total reorganisation energy, $\hbar\lambda$, where,

$$\lambda = \sum_j \lambda_j = \sum_j S_j \omega_j. \tag{2.2.19}$$

The Huang-Rhys parameter is calculated from the overlap of the ground and excited state vibrational wavefunctions according to,

$$S_j = \frac{|\langle e, 1_j | g, 0_j\rangle|^2}{|\langle e, 0_j | g, 0_j\rangle|^2}, \tag{2.2.20}$$

where the shorthand $|n\rangle = |0_0, 0_1, \ldots, \nu_j, \ldots, 0_{N-1}\rangle = |\nu_j\rangle$ is used to identify the vibrational quantum number of the jth mode, where all other modes are in the ground state, and the overlap integrals, $|\langle e, n|g, 0\rangle|^2$, are the Franck-Condon factors.[109,202]

For a monomer with the electronic singlet states,

$$\mathbf{S}_0 = |g\rangle = \begin{pmatrix} 1 \\ 0 \end{pmatrix}; \qquad \mathbf{S}_1 = |e\rangle = \begin{pmatrix} 0 \\ 1 \end{pmatrix} \tag{2.2.21}$$

coupled to a vibrational mode with two vibrational levels, the monomer Hamiltonian is,

$$\mathsf{H}_{\mathrm{M}}^{S} = \begin{pmatrix} \frac{1}{2}\hbar\omega_0 & 0 & 0 & 0 \\ 0 & \frac{3}{2}\hbar\omega_0 & 0 & 0 \\ 0 & 0 & \hbar\omega_{eg}^0 + \hbar\lambda + \frac{1}{2}\hbar\omega_0 & -\hbar\omega_0\frac{\Delta_0}{\sqrt{2}} \\ 0 & 0 & -\hbar\omega_0\frac{\Delta_0}{\sqrt{2}} & \hbar\omega_{eg}^0 + \hbar\lambda + \frac{3}{2}\hbar\omega_0 \end{pmatrix}. \tag{2.2.22}$$

In the site basis, this corresponds to the electronic excited state becoming delocalized across the vibrational levels due to the excited state displacement, Δ_0, such that population forced into the state $|e, 0\rangle$ disperses to other vibrational levels over time, forming a wavepacket from the resulting superposition. This is shown in figure 2.2.2 (top), with details of the wavepacket projection provided in Appendix B.1, page 147.

When the excited state displacement is non-zero, the eigenstates of the site basis Hamiltonian correspond to a new set of *vibronic* states, identified by a superscript V, with eigenvalues ϵ_k,

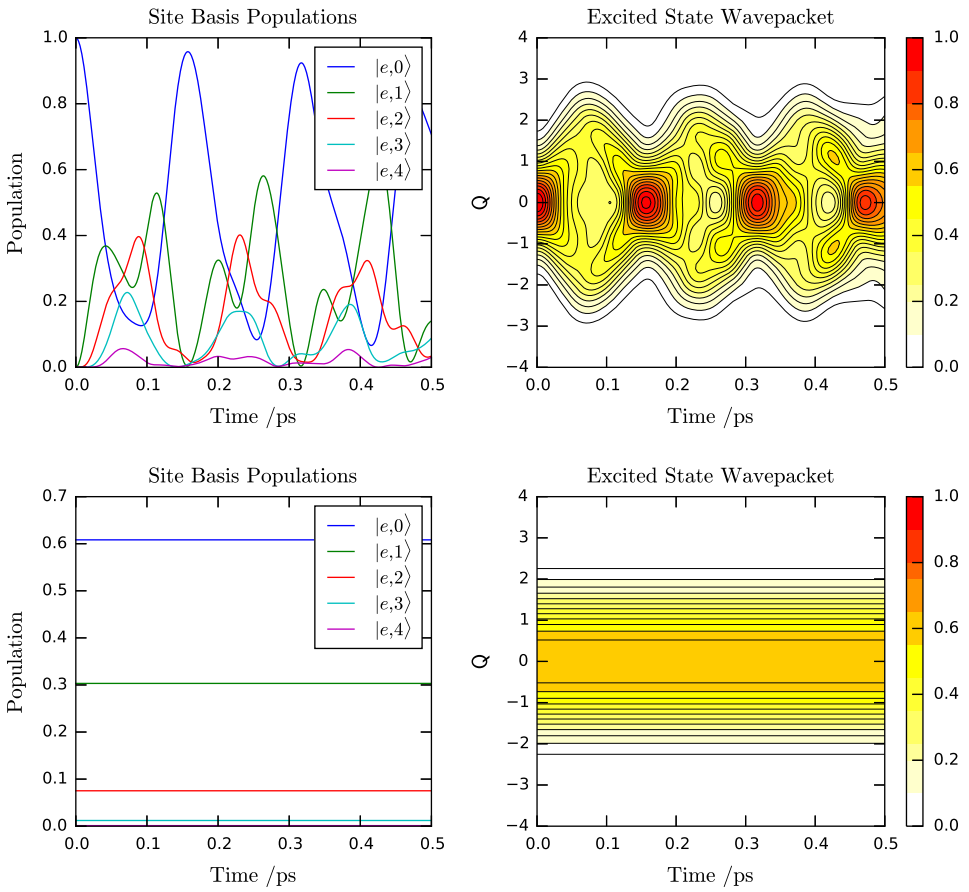

Figure 2.2.2: Site basis state populations and wavepacket projection of the excited electronic state with initial population in (top) site basis state $|e,0\rangle$ and (bottom) lowest vibronic state, when $\Delta_0 > 0$. The superposition associated with the (bottom) vibronic state corresponds to an eigenstate of the system Hamiltonian such that the wavepacket is stationary. Further details are provided in Appendix B.1.

$$\mathsf{H}_{\mathrm{M}}^{S} = \sum_{k} \epsilon_k \left|\Psi_{\mathrm{M},k}^{V}\right\rangle\!\left\langle\Psi_{\mathrm{M},k}^{V}\right| . \tag{2.2.23}$$

Vibronic states are stationary, as shown by 2.2.2 (bottom), and represent the adiabatic basis of molecular states which is detected experimentally.

The site basis Hamiltonian, $\mathsf{H}_{\mathrm{M}}^{S}$, is transformed to the vibronic basis Hamiltonian, $\mathsf{H}_{\mathrm{M}}^{V}$, through diagonalization with the unitary transformation matrix, $\mathsf{U}_{\mathrm{M}}^{VS}$, calculated from the equivalent site and vibronic basis wavefunctions.[203]

$$\mathsf{H}_{\mathrm{M}}^{V} = (\mathsf{U}_{\mathrm{M}}^{VS})^{\dagger}\mathsf{H}_{\mathrm{M}}^{S}\mathsf{U}_{\mathrm{M}}^{VS} = \sum_{k} \epsilon_k \left|\Psi_{\mathrm{M},k}^{S}\right\rangle\!\left\langle\Psi_{\mathrm{M},k}^{S}\right| , \tag{2.2.24}$$

where,

$$\mathsf{U}_{\mathrm{M}}^{VS} = \sum_{k} \left|\Psi_{\mathrm{M},k}^{V}\right\rangle\!\left\langle\Psi_{\mathrm{M},k}^{S}\right| . \tag{2.2.25}$$

Any operator is readily transformed back and forth between these bases using $\mathsf{A}^V = (\mathsf{U}^{VS})^\dagger \mathsf{A}^S \mathsf{U}^{VS}$.

Transformation to the vibronic Hamiltonian alters the wavefunction coefficients without a change in the eigenvalues, as long as the reorganisation energy is included in the diagonal elements of h_e, as in eq. 2.2.8. Some models, such as that used by Ottiger *et al.*, neglect this term and suffer a stabilisation of the eigenvalues in the vibronic basis.[109,110]

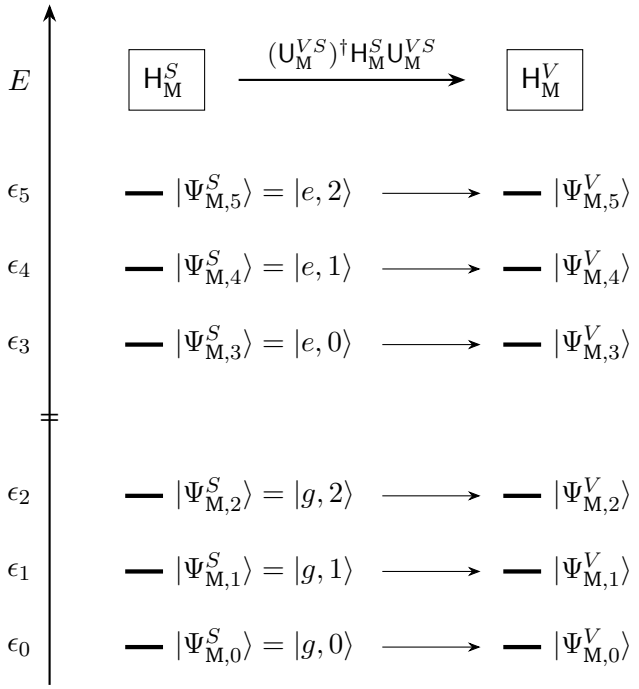

Figure 2.2.3: Transformation of the vibronic monomer Hamiltonian from the site to vibronic basis alters the wavefunction coefficients without a change in state energy, as long as the reorganisation energy is included.

Numerical diagonalization requires a sufficiently large number of vibrational levels to be included to avoid truncation errors.[167] In this work, diagonalization of a vibronic monomer is completed including vibrational levels up to $\nu_j = 9$, before a reduced number are extracted for use in the intensive spectroscopy calculations.

2.2.1.2 Electronically Coupled Aggregates

The proximity of molecules in the condensed phase enables the transfer of electronic energy from a donor to an acceptor via electronic coupling. At the longest range, this corresponds to radiative transfer via emission and absorption of a photon of light, but at shorter range, radiationless mechanisms dominate, leading to excitonic structures.[82,204,205] Radiationless energy transfer involves a Coulombic, dipole-dipole interaction, modelled using Förster theory, as well as a

shorter range quantum mechanical exchange interaction caused by wavefunction overlap of the donor and acceptor species, described by Dexter theory.[205,206] In terms of the Coulombic interaction, Förster theory provides a quasi-classical rate equation for the incoherent transfer of energy from the donor to the acceptor.[93,103,207] But, controversially, the observation of oscillating features in 2DES suggests a coherent mechanism is also involved, enhancing the rate of EET through quantum mechanical effects, requiring models which account for the formation of spatially delocalized exciton states.[125,126,208,209]

For aggregates formed by the packing of molecules or the covalent bonding of monomer units, the intermolecular electronic coupling is described using the Kasha model, which adopts the point dipole approximation to describe the formation of Frenkel excitons.[206,210] The electronic coupling, J, of the transition dipole moments of monomer A and monomer B, $\boldsymbol{\mu}_{\mathrm{A/B}}$, is given by the Förster coupling equation,

$$J = \frac{\boldsymbol{\mu}_{\mathrm{A}} \cdot \boldsymbol{\mu}_{\mathrm{B}} - 3(\boldsymbol{\mu}_{\mathrm{A}} \cdot \hat{\mathbf{R}})(\boldsymbol{\mu}_{\mathrm{B}} \cdot \hat{\mathbf{R}})}{4\pi\varepsilon_r\varepsilon_0 R^3}, \tag{2.2.26}$$

where $\mathbf{R} = R\hat{\mathbf{R}}$ is the displacement vector separating the monomers, ε_0 is the vacuum permittivity and ε_r is the relative permittivity of the solvent.[206] The transition dipole moments involved are introduced in more detail in section 2.2.3.2.

The electronic coupling combines the monomer excited states, $|e\rangle$, into two exciton states delocalized across the monomer units, separated in energy by $2J$. The in-phase, symmetric combination of local monomer states strengthens the transition dipole moment, producing an optically bright state, $|e^+\rangle$, whilst the out-of-phase, antisymmetric combination results in cancellation of the transition dipole moment, producing the dark state, $|e^-\rangle$.[206] This is depicted in figure 2.2.4, where the doubly excited state, $|f\rangle$, is also shown, neglecting the exciton-exciton interaction which causes a minor shift in the transition frequencies involved, without any effect on the observed beatings of the exciton states in 2DES.[211]

The position and orientation of the monomer transition dipole moments results in two types of aggregate, as shown in figure 2.2.5.[206] J-aggregates are formed when the transition dipole moments are arranged “head-to-tail”, such that the electronic coupling is negative, $J < 0$, and the bright, symmetric exciton state is lower in energy than the dark, antisymmetric state. J-aggregates are identified by a red shift of the linear absorption spectrum and an increase in radiative decay rate compared with the monomer species, as rapid relaxation to the lower exciton, with an already strengthened transition dipole moment, reinforces the fluorescing population. For larger aggregates, this leads to the phenomenon of superradiance.[206] H-aggregates are formed when the transition

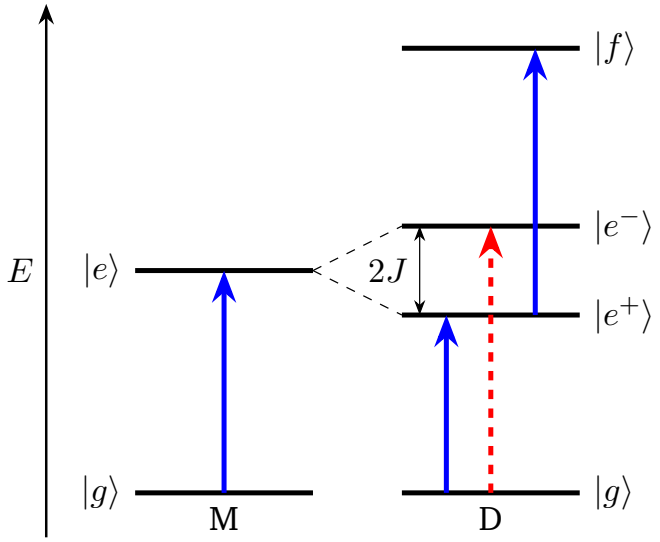

Figure 2.2.4: Energy level diagram for formation of a J-aggregate. The electronic coupling of monomers, M, forms two exciton states, $|e^+\rangle$ and $|e^-\rangle$, separated by $2J$ and a doubly excited state, $|f\rangle$. Allowed transitions are shown by solid blue arrows and forbidden transitions by dashed red arrows.

dipole moments are arranged "sibe-by-side", such that the electronic coupling is positive, $J > 0$, and the bright, symmetric exciton state is higher in energy than the dark, antisymmetric state. This results in a blue shift of the linear absorption spectrum and a decrease in fluorescence, where alternative internal conversion and intersystem crossing mechanisms dominate for higher energy states.[205,206,212,213]

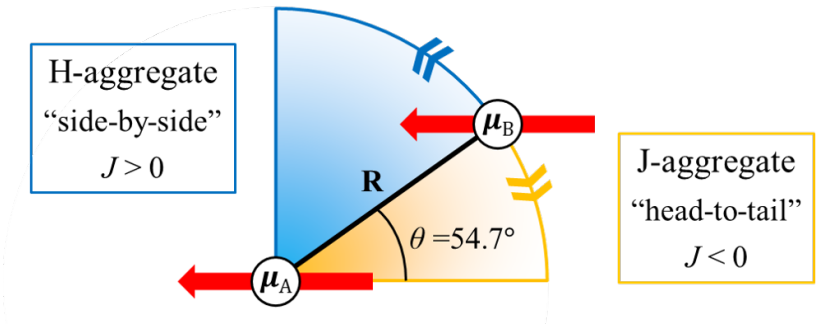

Figure 2.2.5: Relative orientation of monomer transition dipole moments for H- and J-aggregates. For fixed R and parallel transition dipole moments, increasing θ from $0°$ (collinear) to $90°$ results in transition from a J- to H-aggregate, with the boundary at $\theta = 54.7°$.

Modern adaptations of the Kasha model, accounting for charge transfer states and Dexter exchange interactions, have reproduced the conventional behaviour for very different aggregate geometries.[205,206] However, the Kasha model does not account for molecular vibrations, where the adiabatic approximation in Förster theory breaks down, and as the debate concerning the role of vibrations in EET continues, more rigorous models for the electronic coupling of vibronic

systems are needed.[111,113]

2.2.1.3 Vibronic Dimer

Accounting for the vibrational degrees of freedom in an electronically coupled dimer requires construction of a composite Hilbert space containing the vibronic states of both monomer units. Continuing from section 2.2.1.1, the site basis wavefunctions for a vibronic dimer involve the tensor product of the monomer states,

$$|\Psi_{\mathrm{D}}^{S}\rangle = |\alpha_{\mathrm{A}}, n_{\mathrm{A}}\rangle \otimes |\alpha_{\mathrm{B}}, n_{\mathrm{B}}\rangle = |\alpha_{\mathrm{A}}, n_{\mathrm{A}}, \alpha_{\mathrm{B}}, n_{\mathrm{B}}\rangle\,, \tag{2.2.27}$$

where again α denotes the electronic state whilst n is the state of N vibrational modes. Subscript D is used to identify the dimer subspace, where A and B represent the separate monomers. The site basis dimer Hamiltonian is then,

$$\begin{aligned} \mathsf{H}_{\mathrm{D}}^{S} \;=\; & \mathsf{H}_{\mathrm{MA}}^{S} \otimes \mathrm{I}_{\mathrm{MB}} + \mathrm{I}_{\mathrm{MA}} \otimes \mathsf{H}_{\mathrm{MB}}^{S} \\ & + J \sum_{n_{\mathrm{A}}, n_{\mathrm{B}}} \left(|e, n_{\mathrm{A}}, g, n_{\mathrm{B}}\rangle\langle g, n_{\mathrm{A}}, e, n_{\mathrm{B}}| + |g, n_{\mathrm{A}}, e, n_{\mathrm{B}}\rangle\langle e, n_{\mathrm{A}}, g, n_{\mathrm{B}}| \right), \end{aligned} \tag{2.2.28}$$

where I_{M} is the identity operator over the entire monomer degrees of freedom.[98,111,114,128] This sums the Hamiltonians of the two monomers and incorporates the electronic coupling between states with equivalent vibrational quanta, where the electronic excitation exchanges between the two monomers.[114,206] Therefore, the site basis dimer Hamiltonian contains off-diagonal terms for both the vibrational and electronic couplings, in a basis which spans all the vibrational levels of the doubly ground electronic state, $|g, n_{\mathrm{A}}, g, n_{\mathrm{B}}\rangle$, the singly excited electronic states, $|e, n_{\mathrm{A}}, g, n_{\mathrm{B}}\rangle$ and $|g, n_{\mathrm{A}}, e, n_{\mathrm{B}}\rangle$, and the doubly excited electronic state, $|e, n_{\mathrm{A}}, e, n_{\mathrm{B}}\rangle$. An example $\mathsf{H}_{\mathrm{D}}^{S}$ is presented in matrix form in Appendix B.2, page 147.

Diagonalization of the site basis dimer Hamiltonian into the *exciton* basis, identified by superscript E, simultaneously accounts for the vibrational and electronic couplings, such that the vibronic states of each monomer are delocalized across an excitonic dimer system as described in section 2.2.1.2.

$$\mathsf{H}_{\mathrm{D}}^{E} = (\mathsf{U}_{\mathrm{D}}^{ES})^{\dagger} \mathsf{H}_{\mathrm{D}}^{S} \mathsf{U}_{\mathrm{D}}^{ES}, \tag{2.2.29}$$

where,

$$\mathsf{U}_{\mathrm{D}}^{ES} = \sum_{k} |\Psi_{\mathrm{D},k}^{E}\rangle\langle\Psi_{\mathrm{D},k}^{S}|\,, \tag{2.2.30}$$

and $|\Psi_{\mathrm{D},k}^{E}\rangle$ are the eigenstates of the site basis dimer Hamiltonian, $\mathsf{H}_{\mathrm{D}}^{S}$,

$$\mathsf{H}_{\mathrm{D}}^{S} = \sum_{k} \epsilon_k |\Psi_{\mathrm{D},k}^{E}\rangle\langle\Psi_{\mathrm{D},k}^{E}|\,. \tag{2.2.31}$$

This corresponds to the general case, suitable for the vibronic homodimers and heterodimers used in this thesis, which accounts for the full electronic and vibrational degrees of freedom of the system, including the vibrational levels of the doubly ground state. The composite site basis for a vibronic homodimer is shown in figure 2.2.6. The tensor product of the monomer states dramatically increases the size of the system Hamiltonian from $(2(\nu+1)^N)^2$ elements in $\mathsf{H}_{\mathrm{M}}^S$ to $(2(\nu+1)^N)^4$ in $\mathsf{H}_{\mathrm{D}}^S$, where N is the number of vibrational modes and ν is the vibrational quantum number of the highest vibrational level included for each mode. To combat this, it is common to ignore any states where the electronic ground state has excited vibrational modes, reducing the composite site basis states in figure 2.2.6 to a single doubly ground state, $|\Psi_0\rangle$, and the vibronic states where monomer A is excited, $|\Psi_\nu^A\rangle$, or monomer B is excited, $|\Psi_\nu^B\rangle$.

The reduced number of states is useful to describe the limits of the electronic and vibrational couplings in this model, which easily extend to the full composite basis. Using the shorthand for the singly excited vibronic states in figure 2.2.6, the symmetric $(+)$ and antisymmetric $(-)$ exciton states are calculated as the linear combination of site basis wavefunctions, respectively,[109]

$$|\Psi_\nu^{\pm}\rangle = \frac{|\Psi_\nu^{\mathrm{A}}\rangle \pm |\Psi_\nu^{\mathrm{B}}\rangle}{\sqrt{2}}. \tag{2.2.32}$$

Ottiger *et al.* then explain that incorporation of the vibrational modes leads to a quenching of the electronic coupling by the Franck-Condon factors, from the expected J of eq. 2.2.26 to,[109]

$$J_{\mathrm{vib}} = J\langle\Psi_\nu^A|\Psi_0\rangle\langle\Psi_\nu^B|\Psi_0\rangle. \tag{2.2.33}$$

As a result, strong vibrational coupling significantly weakens the electronic coupling, producing two limiting cases:

Strong Coupling Limit

When there is little or no vibrational coupling, $\Delta_j \to 0$, minimal excited state displacement causes the Franck-Condon factors for purely electronic transitions, with no change in vibrational quanta, to tend to unity, i.e. $\langle\Psi_0^A|\Psi_0\rangle \to 1$, whilst those for all vibronic transitions tend to zero, $\langle\Psi_\nu^A|\Psi_0\rangle \to 0$ for $\nu > 0$, such that the electronic coupling is not quenched. This corresponds to the *strong coupling limit*, which refers to the strength of the electronic interaction relative to the vibrational coupling, $\hbar\lambda_j < J$, and produces the expected Davydov splitting of $2J$ between exciton states, as in figure 2.2.4.[110,214]

An energy level diagram for a H-aggregate in the strong coupling limit is given in figure 2.2.7. This shows, as described in section 2.2.1.2, that the bright, symmetric exciton is higher in energy for H-aggregates, where the strong

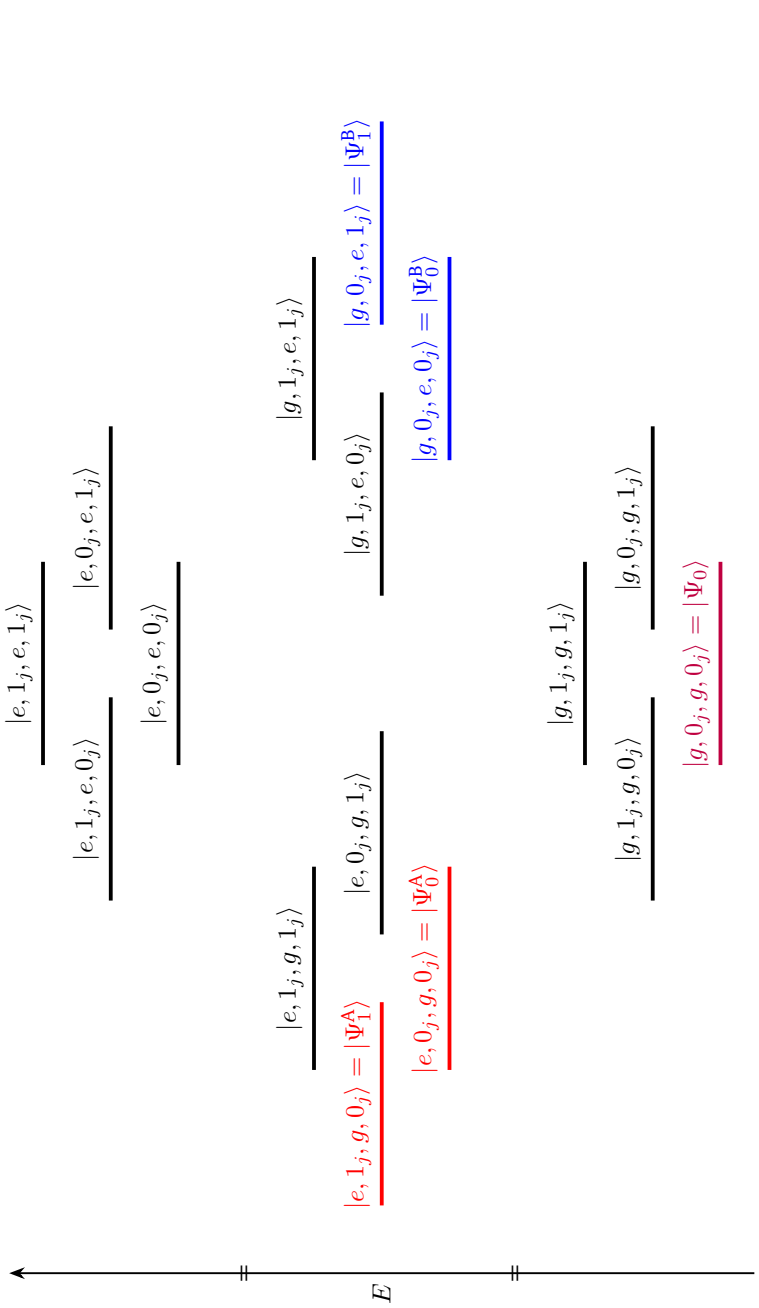

Figure 2.2.6: Energy level diagram of the composite site basis states for the jth mode of a vibronic homodimer. The ground and singly excited states not including any vibrational excitation in the electronic ground state are highlighted and assigned a shorthand, as used in the text.

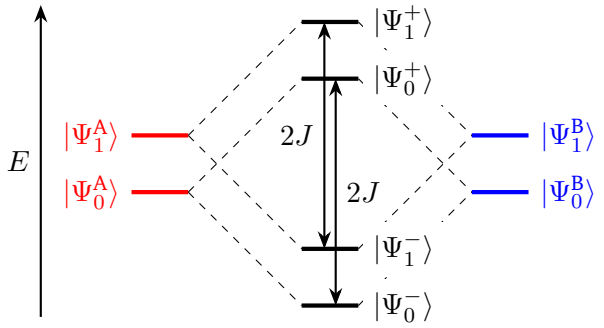

Figure 2.2.7: Formation of exciton states in a H-aggregate in the strong coupling limit.

coupling limit results in the vibronic levels associated with each exciton state being grouped together in bands. Evidence for this grouping has been presented by Ottiger *et al.*, where isotopic substitution was used to break the inversion symmetry enough to enable the forbidden transition to the lower, antisymmetric exciton state.[109]

Weak Coupling Limit

On increasing the vibrational coupling, the excited state displacement increases such that all Franck-Condon factors become fractional and non-zero. This corresponds to the *weak coupling limit*, $\hbar\lambda_j > J$, where the electronic coupling is significantly quenched.[109,110] As shown in figure 2.2.8, in this limit, the much smaller splitting between exciton states of $2J_{\text{vib}}$ results in the vibronic progression of the monomer separating into pairs of exciton states, again demonstrated by Ottiger's isotopic substitution experiment.[109]

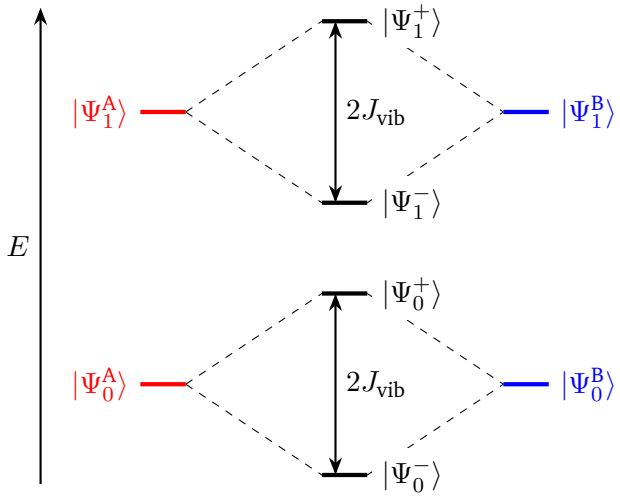

Figure 2.2.8: Formation of exciton states in a H-aggregate in the weak coupling limit. The red and blue levels have the same energy as in figure 2.2.7, demonstrating the difference in coupling strength.

As discussed in chapter 1, correctly accounting for molecular vibrations in electronically coupled aggregates presents a significant but hugely relevant challenge, as a step towards understanding efficient EET in light-harvesting systems. The vibronic dimer Hamiltonian presented here is used in chapter 5 to demonstrate the formation of exciton states in simple homodimers using 2DES and then discuss EET within a heterodimer in terms of relaxation between the vibronic exciton states. This completes the definition of the reduced system Hamiltonians used in this thesis. Section 2.2.2 moves on to a description of the system-bath interaction.

2.2.2 Bath Interaction

2.2.2.1 Interaction Hamiltonian

The system is embedded in a solvent or protein environment such that its Brownian motion is subject to a stochastic force. The classical Langevin equation is extended to the quantum regime using the popular Caldeira-Leggett model, where the system-bath interaction is sufficiently weak that the environment is generalised to an infinite assembly of harmonic oscillators, assuming a continuous spectrum of noise.[143] The total Hamiltonian is split into that of the system and an interaction term,

$$\mathsf{H} = \mathsf{H}_\mathrm{S} + \mathsf{H}_\mathrm{I}, \tag{2.2.34}$$

where,[8,9,134,149]

$$\begin{aligned} \mathsf{H}_\mathrm{I} &= \sum_{n,\upsilon} \left[\frac{\mathsf{p}_{n,\upsilon}^2}{2m_{n,\upsilon}} + \tfrac{1}{2} m_{n,\upsilon}\omega_{n,\upsilon}^2 \left(\mathsf{x}_{n,\upsilon} - \frac{g_{n,\upsilon}\mathsf{B}_n}{m_{n,\upsilon}\omega_{n,\upsilon}^2} \right)^2 \right] \\ &= \sum_{n,\upsilon} \left[\frac{\mathsf{p}_{n,\upsilon}^2}{2m_{n,\upsilon}} + \tfrac{1}{2} m_{n,\upsilon}\omega_{n,\upsilon}^2 \mathsf{x}_{n,\upsilon}^2 - g_{n,\upsilon}\mathsf{x}_{n,\upsilon}\mathsf{B}_n + \frac{g_{n,\upsilon}^2\mathsf{B}_n^2}{2m_{n,\upsilon}\omega_{n,\upsilon}^2} \right]. \end{aligned} \tag{2.2.35}$$

The environment is divided into separate baths, indexed n, each containing a continuum of harmonic modes, indexed υ, of mass, $m_{n,\upsilon}$, frequency, $\omega_{n,\upsilon}$, momentum, $\mathsf{p}_{n,\upsilon}$ and coordinate $\mathsf{x}_{n,\upsilon}$. The system is coupled to each bath mode with strength $g_{n,\upsilon}$, where B_n are system operators defining the action of the bath.

It is clear that H_I contains three components. The bath Hamiltonian is given by the sum of harmonic oscillators,

$$\mathsf{H}_\mathrm{B} = \sum_{n,\upsilon} \left[\frac{\mathsf{p}_{n,\upsilon}^2}{2m_{n,\upsilon}} + \tfrac{1}{2} m_{n,\upsilon}\omega_{n,\upsilon}^2 \mathsf{x}_{n,\upsilon}^2 \right], \tag{2.2.36}$$

the system-bath interaction couples the system operator, B_n, to the bath coordinates, $\mathsf{x}_{n,\upsilon}$, with strength, $g_{n,\upsilon}$,

$$\mathsf{H}_{\mathrm{SB}} = -\sum_{n,\upsilon} g_{n,\upsilon}\mathsf{x}_{n,\upsilon}\mathsf{B}_n, \tag{2.2.37}$$

and the final term acts as a correction to the system potential, proportional to the strength of bath coupling squared,

$$\mathsf{H}_{\mathrm{Sc}} = \sum_{n,\upsilon} \frac{g_{n,\upsilon}^2}{2m_{n,\upsilon}\omega_{n,\upsilon}^2}\mathsf{B}_n^2 = \sum_n \eta_n \mathsf{B}_n^2. \tag{2.2.38}$$

This is equivalent to the reorganisation energy of the vibrational modes included in the system Hamiltonian in section 2.2.1.1. The distribution of coupling strengths defines the spectral density of each bath,[8,134,149]

$$J_n(\omega) = \pi \sum_{\upsilon} \frac{g_{n,\upsilon}^2}{2m_{n,\upsilon}\omega_{n,\upsilon}}\delta(\omega - \omega_{n,\upsilon}), \tag{2.2.39}$$

from which the total reorganisation energy for each bath is calculated as,[68]

$$\eta_n = \frac{1}{\pi}\int_0^\infty \frac{J_n(\omega)}{\omega}\mathrm{d}\omega. \tag{2.2.40}$$

2.2.2.2 Bath Coupling Operators

The electronic and vibrational degrees of freedom of the system couple to the environment differently, such that it is logical to distinguish their interactions as separate baths, indexed n. The electronic environment, identified as $n = 1$, accounts for electrostatic interactions between the system molecules and fluctuating charges in the surrounding protein structure or solvent environment.[122] This affects the electronic excited states of the system such that the bath coupling operators for the electronic environment are,

$$\mathsf{B}_{1,\mathrm{M}}^S = \sum_n |e,n\rangle\langle e,n|\,, \tag{2.2.41}$$

for a monomer and,

$$\begin{aligned}\mathsf{B}_{1,\mathrm{D}}^S \quad = \quad & \sum_{n_\mathrm{A},n_\mathrm{B}} \left(|g,n_\mathrm{A},e,n_\mathrm{B}\rangle\langle g,n_\mathrm{A},e,n_\mathrm{B}| + |e,n_\mathrm{A},g,n_\mathrm{B}\rangle\langle e,n_\mathrm{A},g,n_\mathrm{B}|\right. \\ & \left. +2\,|e,n_\mathrm{A},e,n_\mathrm{B}\rangle\langle e,n_\mathrm{A},e,n_\mathrm{B}|\right),\end{aligned} \tag{2.2.42}$$

for a dimer. These are diagonal operators through which the stochastic bath motion causes the transition frequencies between electronic states to fluctuate, leading to T_2^* pure dephasing, as described in section 2.1.2.

The phonon environment, indexed as $n = 2$, corresponds to a continuum of bath modes, where disruption to the vibrational motion of the system due to the protein structure or solvent molecules leads to both dissipation and dephasing. Incorporation of the phonon bath accounts for relaxation within the vibrational modes of the system, representing processes such as intramolecular vibrational relaxation (IVR). However, relaxation in these models corresponds to the transfer of energy from the system into the bath modes, which is different from the redistribution amongst system modes involved in IVR processes, hence the more general term *vibrational relaxation* is used throughout this work. This does not mean that IVR processes are discounted in these models, just that the system modes to which energy is transferred are considered part of the bath degrees of freedom.

The bath coupling operators for the phonon environment are, in the site basis,

$$\mathsf{B}^{S}_{2,\mathrm{M}} = \mathrm{I}_{\mathrm{el}} \otimes \sum_{j} \mathsf{Q}_j = \mathrm{I}_{\mathrm{el}} \otimes \sum_{j} \left[\frac{\mathsf{b}_j + \mathsf{b}_j^{\dagger}}{\sqrt{2}} \right], \tag{2.2.43}$$

for a monomer, where $\mathrm{I}_{\mathrm{el}} = \sum_{\alpha} |\alpha\rangle\langle\alpha|$, $\alpha = g, e$ is the identity operator over the electronic degrees of freedom, and,

$$\mathsf{B}^{S}_{2,\mathrm{D}} = \mathsf{B}^{S}_{2,\mathrm{MA}} \otimes \mathrm{I}_{\mathrm{MB}} + \mathrm{I}_{\mathrm{MA}} \otimes \mathsf{B}^{S}_{2,\mathrm{MB}}, \tag{2.2.44}$$

for a dimer.[8,122,134] This corresponds to a direct coupling of the coordinates of the system vibrational modes, Q_j, and those of the bath oscillators, $\mathsf{x}_{2,\upsilon}$, for each electronic state, as in eq. 2.2.37. Tanimura explains that this linear-linear, LL, coupling results in both longitudinal, T_1, and transversal, T_2, vibrational relaxation.[5,149] Additional T_2^* pure dephasing due to the phonon environment can be incorporated through the introduction of higher order quadratic terms in the bath operator, resulting in a square-linear, SL, coupling $\propto g_{2,\upsilon}\mathsf{x}_{2,\upsilon}\mathsf{Q}_j^2$; though this is neglected in most models and hence not included in eq. 2.2.43.

As in section 2.2.1, the bath coupling operators for the phonon environment are transformed into the vibronic and exciton bases using the unitary transformations,

$$\mathsf{B}^{V}_{2,\mathrm{M}} = (\mathsf{U}^{VS}_{\mathrm{M}})^{\dagger}\mathsf{B}^{S}_{2,\mathrm{M}}\mathsf{U}^{VS}_{\mathrm{M}}, \tag{2.2.45}$$

$$\mathsf{B}^{E}_{2,\mathrm{D}} = (\mathsf{U}^{ES}_{\mathrm{D}})^{\dagger}\mathsf{B}^{S}_{2,\mathrm{D}}\mathsf{U}^{ES}_{\mathrm{D}}, \tag{2.2.46}$$

where the bath coupling operators for the electronic environment, B_1, are positive diagonal operators and do not change under this transformation.

Fluorescence and phosphorescence processes, corresponding to relaxation between electronic states caused by spontaneous emission, can also be included by addition of a third bath with a coupling operator equivalent to the dipole

moment operator.[186] But as the timescales of such luminescence are significantly longer than dephasing and vibrational relaxation processes, typically nanoseconds or slower versus femtoseconds, luminescence does not feature in this thesis.

2.2.2.3 Spectral Densities

Assuming a continuum of harmonic modes for each bath allows the discrete form of the spectral density, $J_n(\omega)$, in equation 2.2.39 to be approximated with a continuous analytical form. It is possible to measure the spectral density of the environment experimentally,[136,215] but realistic behaviours are achieved using a variety of mathematical functions, based upon a phenomenological damping parameter, γ, which controls the friction of the bath.

The shape of the spectral density defines the time dependence of the system-bath interaction through the system-bath correlation function,[1,149,151,158]

$$L_n(t) = \frac{\hbar}{\pi}\int_0^\infty \mathrm{d}\omega J_n(\omega)\left(\coth\left(\frac{\beta\hbar\omega}{2}\right)\cos\omega t - i\sin\omega t\right). \tag{2.2.47}$$

This governs the interaction in accordance with the fluctuation-dissipation theorem, where the real component corresponds to thermal fluctuations and the imaginary component causes dissipation.[216]

The timescale for decay of the correlation function defines the *correlation time*, τ_c, equivalent to the time taken for the bath to return to equilibrium after perturbation.[1,26,217] As discussed in section 2.1.3, short correlation times compared with the relaxation timescale of the system are associated with the Markovian limit, whilst commensurate timescales suggest the involvement of non-Markovian memory effects. For discrete spectral densities, involving only a small number of modes, the regular oscillation of the bath periodically restores the coherence of the reduced system, introducing the recurrence time, τ_R. As the number of bath modes increases, the recurrence time also increases, becoming sufficiently longer than the relaxation timescale of the system for continuous spectral densities that it can be disregarded, unless the spectral density is highly structured, featuring particularly strong coupling to select modes, such that the periodic motion remains.[9]

In general, chemical and biological systems in the condensed phase have Ohmic spectral densities of the form,

$$J_n(\omega) = \eta_n \omega e^{-\frac{\omega}{\omega_c}}, \tag{2.2.48}$$

proportional to the coupling strength, η_n, and an exponential decay controlled

by the cutoff frequency, ω_c.[9,122,179] Super-Ohmic and sub-Ohmic variations of this density are also used, involving greater and lower powers of ω respectively, with the latter finding application in solid state dynamics.[7,68,134] Ohmic spectral densities are primarily considered as Markovian as the corresponding correlation functions decay with a constant rate, but non-Markovian effects are also involved, particularly as the coupling strength increases.[149,218]

Employing an improved cutoff, the ubiquitous Lorentz-Drude or Debye form of the Ohmic spectral density,

$$J_n(\omega) = 2\eta_n \frac{\omega \Lambda_n}{\omega^2 + \Lambda_n^2}, \tag{2.2.49}$$

concentrates the coupling strength at lower frequency modes, with a peak at $\omega = \Lambda$, where $\Lambda^{-1} = \tau_c$.[8,216,217] The system-bath coupling strength is temperature dependent according to,[1]

$$\eta_n = \frac{\hbar \Delta_n^2}{2 k_{\mathrm{B}} T}, \tag{2.2.50}$$

where k_{B} is the Boltzmann constant and the temperature, T, is constant for all baths. As discussed in section 2.2.2.2, bath induced dephasing is a result of electrostatic interactions between the system and environment molecules causing the potential energy surface of the electronically excited states to fluctuate. This causes the transition frequencies of the system to deviate from their equilibrium value, ω_{eg}^0, over time,[1,4,27]

$$\omega_{eg}^0(t) = \omega_{eg}^0 + \delta\omega(t), \tag{2.2.51}$$

where Δ_n is the amplitude of these fluctuations, a measure of their spread, as shown in figure 2.2.9. Note the distinction from the dimensionless excited state displacement, Δ_j, in section 2.2.1.1, which is clear through context and the loss of subscript n for the fluctuation amplitude in discussions involving a single bath.

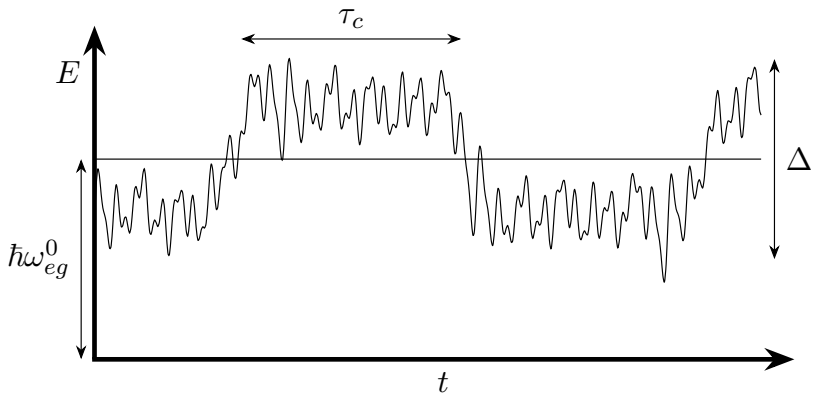

Figure 2.2.9: Modulation of the fundamental transition frequency of the system, ω_{eg}^0, as a result of coupling to the bath. The amplitude of the fluctuations is measured by Δ, with the correlation time $\tau_c = \Lambda^{-1}$.

The autocorrelation function of the deviation of the transition frequencies is therefore equivalent to the system-bath correlation function, capturing the behaviour of the entire ensemble. Assuming Gaussian-Markov statistics, involving a normal distribution of frequencies and a short correlation time, the correlation function has the form,[1,149,150]

$$\langle \delta\omega(t)\delta\omega(0)\rangle = \Delta^2 \exp\left(-\frac{t}{\tau_c}\right), \tag{2.2.52}$$

dominated by an exponential decay which smoothly restores equilibrium. This corresponds to an *overdamped* environment, where the relative sizes of Δ and τ_c produce the homogeneous and inhomogeneous limits, which are discussed at length in the context of the results in chapter 3. An overdamped spectral density is typically used to apply an inhomogeneity to the system, reflecting the differences in the system-bath interaction across the ensemble.[149,159,219]

Alternatively, the spectral density can be highly structured, where there is much stronger coupling to certain bath modes, which are only weakly damped. Structured spectral densities are modelled as an *underdamped* Brownian oscillator, with the form,[1,158]

$$J_n(\omega) = \frac{2\eta_n\gamma_n\omega_{0n}^2\omega}{(\omega_{0n}^2-\omega^2)^2+\gamma_n^2\omega^2}. \tag{2.2.53}$$

This involves a canonical transformation, which takes a strongly coupled system mode of frequency ω_0, which is itself weakly coupled to a bath with a Drude spectral density, and transfers it into the bath degrees of freedom.[159,162,216] This is demonstrated in the analysis of spectral lineshape in section 3.1. An underdamped spectral density has a strong peak at ω_0, which is broadened to some extent by the damping parameter, γ. An example underdamped spectral density is shown in figure 2.2.10 (a). The presence of the strong peak in the spectral density causes the correlation function to oscillate as it decays, shown in figure 2.2.10 (b).

The bath motion is formally underdamped when $\gamma \ll \omega_0$, producing prominent oscillations in the correlation function which have a significant effect on the system dynamics. On increasing the damping to the overdamped limit, where $\gamma \gg \omega_0$, the correlation function decays much more rapidly, such that the oscillating component is removed and the Drude form is regained,[1,138] where,

$$\Lambda = \frac{\omega_0^2}{\gamma} = \frac{1}{\tau_c}. \tag{2.2.54}$$

The return to Drude form is shown by the overdamped spectral density in figure 2.2.10 (c), where the corresponding correlation function in figure 2.2.10 (d) shows the exponential decay of eq. 2.2.52.

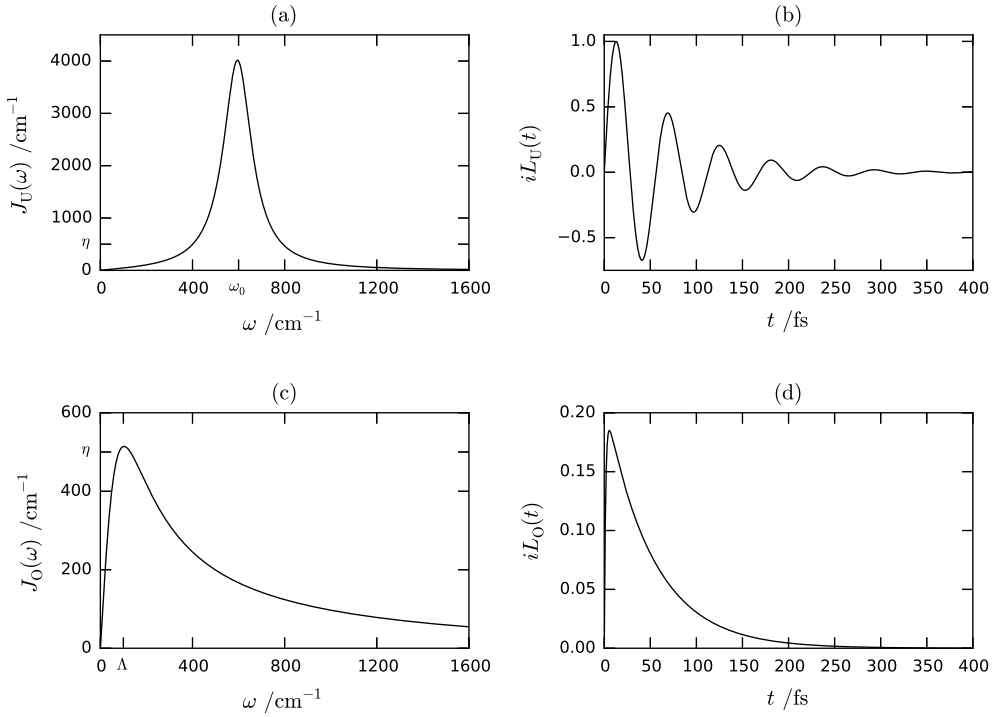

Figure 2.2.10: (a) Underdamped spectral density, $J_{\mathrm{U}}(\omega)$, and (b) corresponding correlation function, $L_{\mathrm{U}}(t)$, for a Brownian oscillator with $\tilde{\omega}_0 = 600\,\mathrm{cm}^{-1}$ and $\tilde{\gamma} = 120\,\mathrm{cm}^{-1}$, with (c) the overdamped spectral density, $J_{\mathrm{O}}(\omega)$, and (d) correlation function, $L_{\mathrm{O}}(t)$, obtained on increasing the damping to $\tilde{\gamma} = 3600\,\mathrm{cm}^{-1}$.

Modelling the environment as a series of underdamped modes maintains a description of the damped vibrational motion without the need to include the vibrational degrees of freedom explicitly within the system Hamiltonian. But the additional complexity in the bath degrees of freedom impacts on the dynamical methods used, as discussed in section 2.3. Underdamped environmental modes also have an important role in the description of protein environments, where highly structured spectral densities are commonplace.[120,166,168,220] With a complete description of the system-bath interaction, section 2.2.3 defines the interaction of the reduced system with external electric fields.

2.2.3 Field Interaction

2.2.3.1 Interaction Hamiltonian

Adopting the semi-classical approximation, the effect of an external electromagnetic field is incorporated via the time dependent system-field interaction Hamiltonian,[1,27]

$$\mathsf{H}_{\mathrm{SF}}(t) = -\hat{\mu} \cdot \mathcal{E}(\mathbf{r}, t), \tag{2.2.55}$$

which couples the total electric field, $\mathcal{E}(\mathbf{r},t)$, to the dipole moment operator of the system, $\hat{\mu}$. The oscillating electric field is defined in space, $\mathbf{r}$, and time, t, as a series of m pulses,

$$\mathcal{E}(\mathbf{r},t) = \sum_m \hat{\mathbf{e}}_m \left(\chi_m E'(t-\tau_m)\exp(-i\omega_m t + i\mathbf{k}_m\cdot\mathbf{r}) + c.c.\right), \tag{2.2.56}$$

with circular frequency, $\omega_m = 2\pi\nu_m$, wavevector, $\mathbf{k}_m$, of magnitude $|\mathbf{k}_m| = \omega/c$, and field strength χ_m, in $\mathrm{V\,m^{-1}}$.[171,175,181] The unit vector $\hat{\mathbf{e}}_m$ defines the polarization of each pulse.[12,184] The field envelope, $E'(t-\tau_m)$, is assumed to be Gaussian, centred at τ_m,

$$E'(t-\tau_m) = \exp\left(\frac{-(t-\tau_m)^2}{2\varsigma^2}\right), \tag{2.2.57}$$

with full-width-half-maximum (FWHM) $\tau_p = 2\sqrt{2\ln 2}\varsigma$ in the time domain, equivalent to $\tilde{\nu}_p = 4\ln 2/\pi c\tau_p$ in the frequency domain. Shorter laser pulses result in a broader spectrum of frequencies, such that the *impulsive limit*, where the field envelope is a delta function of time, corresponds to a flat, white, laser spectrum.[221,222]

2.2.3.2 Dipole Moment Operator

Optical transitions between system states are mediated by the transition electric dipole moment,

$$\boldsymbol{\mu}_{fi} = \mu_{fi}\hat{\mathbf{d}}_{fi}, \tag{2.2.58}$$

a Cartesian vector of magnitude μ, where the unit vector $\hat{\mathbf{d}}$ represents the separation of the initial, i, and final, f, eigenstates involved within the transition.[4] Maximum interaction is assumed such that the electric field of each pulse is perfectly aligned with the transition dipole moment, $\hat{\mathbf{e}}_m = \hat{\mathbf{d}}_{fi}$, and the vector nature of these quantities can be ignored.[1]

The dipole moment operator, $\hat{\mu}$, combines $\boldsymbol{\mu}_{fi}$ with a matrix component within the Hilbert space of the system, which is determined by the selection rules. Diagonal elements define any permanent dipoles associated with the system states, caused by an uneven distribution of electron density, whilst off-diagonal elements correspond to the transition dipole moments between system states. Enforcing the dipole approximation, valid when the wavelength of the electromagnetic radiation is larger than the size of the quantum system such that it is subject to an oscillating uniform field, each molecule is considered a point dipole, neglecting any higher order multipolar terms.[1,198] Permanent dipoles are not involved in any of the systems featured in this thesis.

Considering the electronic states only, a monomer with an allowed transition between the ground and excited states has the dipole moment operator,

$$\hat{\mu}^S_{\text{el,M}} = \boldsymbol{\mu}_{eg} \left(|g\rangle\langle e| + |e\rangle\langle g| \right). \tag{2.2.59}$$

For a vibronic monomer, this dipole moment operator is expanded over the identity operator of the vibrational states, $\mathrm{I}_{\text{vib}} = \sum_n |n\rangle\langle n|$, giving, in the site basis,[98]

$$\begin{aligned} \hat{\mu}^S_{\text{M}} &= \boldsymbol{\mu}_{eg} \left(|g\rangle\langle e| \otimes \sum_n |n\rangle\langle n| + |e\rangle\langle g| \otimes \sum_n |n\rangle\langle n| \right) \\ &= \boldsymbol{\mu}_{eg} \sum_n \left(|g,n\rangle\langle e,n| + |e,n\rangle\langle g,n| \right). \end{aligned} \tag{2.2.60}$$

This contains non-zero off-diagonal elements that connect equivalent vibrational levels of the two electronic states, describing purely electronic transitions.

Transformation to the *vibronic* basis using the same unitary matrix as for the system Hamiltonian, eq. 2.2.25,

$$\hat{\mu}^V_{\text{M}} = (\mathsf{U}^{VS}_{\text{M}})^\dagger \hat{\mu}^S_{\text{M}} \mathsf{U}^{VS}_{\text{M}}, \tag{2.2.61}$$

increases the number of non-zero off-diagonal elements, where the displacement of the excited state potential energy surface results in non-zero wavefunction overlap for a greater range of transitions, including vibronic overtones and hot bands. Individual transition dipole moments are calculated as,[98]

$$\mu^V_{\text{M},kl} = \langle \Psi^V_{\text{M},k} | \, \hat{\mu}^S_{\text{M}} \, | \Psi^V_{\text{M},l} \rangle = \sum_n \left(\langle \Psi^V_{\text{M},k} | g,n \rangle \langle e,n | \Psi^V_{\text{M},l} \rangle + \langle \Psi^V_{\text{M},k} | e,n \rangle \langle g,n | \Psi^V_{\text{M},l} \rangle \right). \tag{2.2.62}$$

The dipole moment operator for a vibronic dimer is obtained by the tensor sum of the two monomer dipole moments,

$$\hat{\mu}^S_{\text{D}} = \left(\hat{\mu}^S_{\text{MA}} \otimes \mathrm{I}_{\text{MB}} + \mathrm{I}_{\text{MA}} \otimes \hat{\mu}^S_{\text{MB}} \right), \tag{2.2.63}$$

and is equally transformed to the exciton basis as,

$$\hat{\mu}^E_{\text{D}} = (\mathsf{U}^{ES}_{\text{D}})^\dagger \hat{\mu}^S_{\text{D}} \mathsf{U}^{ES}_{\text{D}}. \tag{2.2.64}$$

The displacement and relative orientation of the two monomer dipole moments determines the electronic coupling, as discussed in section 2.2.1.2, and can be exploited in experiments employing polarised pulses to isolate vibronic signatures.[30–32] However, the formation of J-aggregates discussed in chapter 5 is restricted to a collinear arrangement of monomer dipole moments to model a series of covalently bonded perylene bisimide homodimers.

The definition of the system Hamiltonian for vibronic monomers and dimers presented in this section, accompanied by their interaction with overdamped and underdamped baths and external electric fields through their respective dipole moment operators, provides a complete open quantum system model, as described in section 2.1. The propagation of these systems through time is then performed using the quantum dynamical methods presented in section 2.3.

2.3 Non-Markovian Quantum Dynamics

The equation of motion for the reduced density operator of the system is solved using a range of methods, dependent on the requirements of the system-bath interaction. Beginning with a brief description of Markovian approaches, this section presents the non-Markovian hierarchical equations of motion (HEOM) for environments with overdamped, underdamped and arbitrary spectral densities. Primary features of the computational implementation used in this research are then introduced, with greater detail of the software developed available in Appendix C.

2.3.1 Master Equations

From section 2.1.2, the evolution of the reduced density operator of the system is determined by the propagator, $G(t, t_0)$, which accounts for the interaction with the bath within the generator, $\mathcal{L}(t)$, eq. 2.1.16. The master equation of the reduced system has the general form,[66,182]

$$\dot{\rho}_{\mathsf{S}}(t) = \mathcal{L}(t)\rho_{\mathsf{S}}(t) = -\frac{i}{\hbar}\left[\mathsf{H}_{\mathsf{S}} + \mathsf{H}_{\mathsf{SF}}(t), \rho_{\mathsf{S}}(t)\right] + \mathsf{D}(\rho_{\mathsf{S}}(t)), \tag{2.3.1}$$

where $\dot{\rho}(t) = \frac{\mathrm{d}}{\mathrm{d}t}\rho(t)$ and $\mathsf{D}(\rho(t))$ is the relaxation superoperator which controls the interaction with the bath. Here, the optional system-field interaction has also been included as an addition to the system Hamiltonian within the commutator.

Enforcing the Markov approximation for weak system-bath coupling and rapid bath relaxation compared with that of the system, the relaxation superoperator is expressed in Lindblad form as,

$$\dot{\rho}_{\mathsf{S}}(t) = -\frac{i}{\hbar}\left[\mathsf{H}_{\mathsf{S}}, \rho_{\mathsf{S}}(t)\right] + \sum_k \kappa_k \left[\mathsf{C}_k \rho_{\mathsf{S}}(t) \mathsf{C}_k^\dagger - \frac{1}{2}\left\{\mathsf{C}_k^\dagger \mathsf{C}_k, \rho_{\mathsf{S}}(t)\right\}\right], \tag{2.3.2}$$

where $\{\mathsf{C}, \rho\}$ denotes the anti-commutator.[66,223] The Lindblad operators, C_k, introduce dissipation and dephasing at a constant rate, κ_k, such that the master equation is time-local and Markovian.[224] The Lindblad master equation

represents a quantum dynamical semigroup and is thus favourably trace and positivity preserving.[225] However, this master equation is not generally applicable. In order to achieve this form, additional terms may be required in the system Hamiltonian, or the Lindblad operators may need to undergo several transformations to accurately incorporate any renormalisation due to the system-bath coupling, such as the Lamb-shift.[8,66,224] Tanimura also warns that in converting to Lindblad form and enforcing certain assumptions, the observed dynamics can become unphysical, even if complete positivity is preserved.[159]

Time-local Lindblad master equations can be derived without enforcing the Markov approximation, resulting in time dependent rate constants, $\kappa_k(t)$. However, complete positivity is preserved only if these constants are positive throughout the evolution, where negative values indicate non-Markovian dynamics, corresponding to the return of information from the bath to the system.[6,9,195] Similar time-local approaches include the Redfield master equation methods, which have been applied to electron transfer, energy transfer and 2D spectroscopy simulations.[93,148,174,175,180] This perturbative method accounts for dephasing and vibrational relaxation through the Redfield-tensor, a relaxation superoperator involving a Markovian master equation of the form in eq. 2.3.1.[148,156]

Non-Markovian methods generally employ time non-local master equations, involving direct reference to previous time steps within a memory kernel, in the form of the system-bath correlation function.[8,9,147] Several non-Markovian methods have been developed, ranging from the original Nakajima-Zwanzig[8] and time non-local master equations,[82,98,142,146,182,183] through to recent methods such as the time-evolving matrix product operator (TEMPO) algorithm.[226] The most accurate solutions use the Feynman-Vernon path-integral formalism to produce non-perturbative methods yielding numerically exact evolutions, such as the hierarchical equations of motion (HEOM).[149,151,156] The accuracy of such models is held in such high regard that they are often employed as a basis of comparison for approximate methods.[217,227]

2.3.2 Hierarchical Equations of Motion

Combining stochastic theory with the path integral method of Caldeira and Leggett for the interaction of a quantum system with a Markovian bath, Kubo and Tanimura derived a hierarchy of equations of motion capable of accounting for the non-Markovian effects of an extended range of correlation times, beyond the capabilities of perturbative methods.[68,149–151,156,228] Further developments, including the addition of terms for improved stability for strong system-bath

coupling at low temperatures and the use of non-Ohmic spectral densities leading to pronounced non-Markovian effects, have produced a popular method for modelling the dephasing and dissipation of open quantum systems involving overdamped and underdamped vibrational motion.[151,152,154,158]

The path integral formalism of Feynman and Vernon describes the evolution of the system by considering all available *paths* between two points and weighting the contribution of each with its classical action.[229] The evolution is calculated by summing over all possible paths, where every pair of paths is coupled by an *influence functional*.[134] The influence functional accounts for long-range interactions, enabling this approach to go beyond the weak-coupling limit of the system-bath interaction and correctly incorporate non-Markovian effects associated with coloured noise.[9,149]

From the system-bath interaction Hamiltonian of eq. 2.2.35, the evolution of the reduced density operator is written as a double path integral,[149]

$$\begin{aligned}\rho_{\mathrm{S}}(\mathsf{Q},\mathsf{Q}';t) \;=\; & \int \mathcal{D}[\mathsf{Q}(\tau)] \int \mathcal{D}[\mathsf{Q}'(\tau)] \int \mathrm{d}\mathsf{Q}_0 \int \mathrm{d}\mathsf{Q}_0' \rho_{\mathrm{S}}(\mathsf{Q}_0,\mathsf{Q}_0')\rho_{\mathrm{C}}(\mathsf{Q},\mathsf{Q}',t;\mathsf{Q}_0,\mathsf{Q}_0') \\ & \times \exp\left\{\frac{i}{\hbar}S_{\mathrm{S}}[\mathsf{Q};t]\right\} F(\mathsf{Q},\mathsf{Q}';t) \exp\left\{-\frac{i}{\hbar}S_{\mathrm{S}}[\mathsf{Q}';t]\right\}, \qquad (2.3.3)\end{aligned}$$

which propagates from the initial time t_0 to t the paths $\mathsf{Q}(t_0) = \mathsf{Q}_0$ to $\mathsf{Q}(t) = \mathsf{Q}$ and $\mathsf{Q}'(t_0) = \mathsf{Q}_0'$ to $\mathsf{Q}'(t) = \mathsf{Q}'$, such that $\rho_{\mathrm{S}}(\mathsf{Q}_0,\mathsf{Q}_0')$ is the initial state of the system. A single path integral corresponds to an amplitude such that the double path integral, involving the complex conjugate of the action in the second path, yields a probability, here in the form of the density operator.[229] Any initial correlations of the system and bath are defined in $\rho_{\mathrm{C}}(\mathsf{Q},\mathsf{Q}',t;\mathsf{Q}_0,\mathsf{Q}_0')$, which is equal to unity for factorised initial conditions under the Born approximation. $S_{\mathrm{S}}[\mathsf{Q};t]$ defines the action of the system for the path Q,[165] and the effect of the bath is introduced via the Feynman-Vernon influence functional,[149,151]

$$\begin{aligned}F(\mathsf{Q},\mathsf{Q}';t) \;=\; & \exp\left\{\left(-\frac{i}{\hbar}\right)^2 \int_{t_0}^{t} \mathrm{d}\tau \mathsf{B}^{\times}(\mathsf{Q},\mathsf{Q}';\tau) \qquad (2.3.4)\right. \\ & \left. \times \int_{t_0}^{\tau} \mathrm{d}\tau' \left[L_2(\tau-\tau')\mathsf{B}^{\times}(\mathsf{Q},\mathsf{Q}';\tau') - iL_1(\tau-\tau')\mathsf{B}^{\circ}(\mathsf{Q},\mathsf{Q}';\tau')\right]\right\},\end{aligned}$$

for the system-bath correlation function,

$$L(t) = L_2(t) - iL_1(t), \qquad (2.3.5)$$

where,

$$L_1(t) \;=\; \frac{\hbar}{\pi}\int_0^{\infty} \mathrm{d}\omega J(\omega)\sin(\omega t), \qquad (2.3.6)$$

$$L_2(t) \;=\; \frac{\hbar}{\pi}\int_0^{\infty} \mathrm{d}\omega J(\omega)\coth\left(\frac{\beta\hbar\omega}{2}\right)\cos(\omega t), \qquad (2.3.7)$$

for the spectral density, $J(\omega)$, of the form in eq. 2.2.39. Within the influence functional,

$$\mathsf{B}^{\times}(\mathsf{Q},\mathsf{Q}';\tau) = \mathsf{B}(\mathsf{Q}(\tau)) - \mathsf{B}(\mathsf{Q}'(\tau)), \tag{2.3.8}$$

$$\mathsf{B}^{\circ}(\mathsf{Q},\mathsf{Q}';\tau) = \mathsf{B}(\mathsf{Q}(\tau)) + \mathsf{B}(\mathsf{Q}'(\tau)). \tag{2.3.9}$$

The influence functional accounts for the interaction of the paths in the period t_0 to t, incorporating the correlation function as a memory kernel. This gives an exact, non-perturbative solution suitable for the full range of bath timescales, accounting for all non-Markovian effects. Differentiation of the influence functional and input of an approximate analytic form for the spectral density then enables derivation of the equations of motion for a hierarchy of auxiliary density operators (ADOs).[150–152,165] Similar expansions are involved in the derivation of the stochastic Liouville equation[149] and stochastic Schrödinger equations.[9] As the HEOM are derived from the spectral density, different forms are needed for different limits of the bath damping, as introduced in section 2.2.2.3.

2.3.2.1 Overdamped

Recalling from section 2.2.2.1 that the bath is modelled as an assembly of harmonic oscillators separated into $n = 1, \ldots, N$ baths, the total spectral density is,

$$J(\omega) = \sum_{n=1}^{N} J_n(\omega), \tag{2.3.10}$$

and the total bath coupling operator,

$$\mathsf{B} = \sum_{n=1}^{N} \mathsf{B}_n, \tag{2.3.11}$$

where the inverse temperature, $\beta = (k_{\mathrm{B}}T)^{-1}$, is assumed the same for all baths.

For an overdamped environment, the spectral density is approximated as the Lorentz-Drude form,

$$J_n(\omega) = 2\eta_n \frac{\omega\Lambda_n}{\omega^2 + \Lambda_n^2}, \tag{2.3.12}$$

where η_n is the reorganisation energy of the bath and Λ^{-1} the correlation time. Solving eq. 2.2.47 via contour integration then gives the system-bath correlation

function as the sum of exponential terms,[1,151,165]

$$\begin{aligned} L_n(t) &= \eta_n\Lambda_n\left(\cot\left(\frac{\hbar\beta\Lambda_n}{2}\right)-i\right)e^{-\Lambda_n t}+\sum_{k=1}^{M}\frac{4\eta_n\Lambda_n\nu_{nk}}{\hbar\beta(\nu_{nk}^2-\Lambda_n^2)}e^{-\nu_{nk}t} \\ &= \sum_{k=0}^{M}c_{nk}e^{-\nu_{nk}t}, \end{aligned} \tag{2.3.13}$$

expressed in terms of the Matsubara frequencies, $\nu_{nk}; k = 0, 1, 2, ..., M$, and the coefficients, c_{nk}, given by,

$$\nu_{n0} = \Lambda_n, \tag{2.3.14}$$

$$\nu_{nk} = \frac{2\pi k}{\hbar\beta}, \tag{2.3.15}$$

$$c_{n0} = \eta_n\Lambda_n\left(\cot\left(\frac{\hbar\beta\Lambda_n}{2}\right)-i\right), \tag{2.3.16}$$

$$c_{nk} = \frac{4\eta_n\Lambda_n}{\hbar\beta}\left(\frac{\nu_{nk}}{\nu_{nk}^2-\Lambda_n^2}\right). \tag{2.3.17}$$

Entering this correlation function into the influence functional of eq. 2.3.4, a hierarchy of equations of motion is derived for the auxiliary density operators (ADOs), $\rho_{\mathbf{j}}$, as,[194,216]

$$\begin{aligned} \dot{\rho}_{\mathbf{j}}(t) &= -\left(\frac{i}{\hbar}\mathsf{H}_{\mathsf{S}}^{\times}+\sum_{n=1}^{N}\sum_{k=0}^{M}j_{nk}\nu_{nk}\right)\rho_{\mathbf{j}}(t)-i\sum_{n=1}^{N}\sum_{k=0}^{M}\mathsf{B}_n^{\times}\rho_{j_{nk}^{+}}(t) \\ &\quad -i\sum_{n=1}^{N}\sum_{k=0}^{M}j_{nk}\left(c_{nk}\mathsf{B}_n\rho_{j_{nk}^{-}}(t)-c_{nk}^{*}\rho_{j_{nk}^{-}}(t)\mathsf{B}_n\right) \\ &\quad -\sum_{n=1}^{N}\left(\frac{2\eta_n}{\hbar\beta\Lambda_n}-\eta_n\cot\left(\frac{\hbar\beta\Lambda_n}{2}\right)-\sum_{k=1}^{M}\frac{c_{nk}}{\nu_{nk}}\right)\mathsf{B}_n^{\times}\mathsf{B}_n^{\times}\rho_{\mathbf{j}}(t), \end{aligned} \tag{2.3.18}$$

where $\mathsf{H}_{\mathsf{S}}^{\times}\rho = [\mathsf{H}_{\mathsf{S}}, \rho]$ denotes the commutator of the system Hamiltonian and the density matrix. Each ADO is uniquely identified by the $N(M+1)$-dimensional vector $\mathbf{j} = (j_{10}, \ldots, j_{nk}, \ldots, j_{NM})$, where each element, j_{nk}, is the integer multiplier of the corresponding Matsubara frequency for that ADO. The reduced density operator of the system corresponds to $\rho_{\mathbf{0}}$, where all elements of $\mathbf{j}$ are equal to zero.

The first term in eq. 2.3.18 describes the evolution of the reduced system and multiples of Matsubara frequencies which represent the existence of a number of bath phonons. The HEOM method accounts for the system-bath interaction as the transfer of phonons between the system and the bath.[149,151] By propagating a series of ADOs, representing different arrangements of bath phonons, the HEOM accounts for a history of interactions such that non-Markovian effects are automatically included. The ADOs are interconnected via the terms involving

the $\mathbf{j}^{\pm} = (j_{10}, \ldots, j_{nk} \pm 1, \ldots, j_{NM})$ vectors. The second term in eq. 2.3.18, involving elements of $\mathbf{j}^{+}$, corresponds to creation of bath phonons as they are emitted from the system into the bath, resulting from the imaginary part of the correlation function associated with dissipation. The third term in eq. 2.3.18, involving elements of $\mathbf{j}^{-}$, corresponds to annihilation of bath phonons as they are reabsorbed by the system, caused by the real part of the correlation function associated with thermal fluctuations. The final term in eq. 2.3.18, involving the double commutator of the bath operator, is a low temperature correction term developed by Ishizaki and Tanimura which assists with the convergence of the HEOM under strong coupling by reducing the number of Matsubara frequencies required.[152]

Such a hierarchy must therefore be terminated in terms of the number of Matsubara frequencies for each bath and the maximum value of j_{nk}, henceforth referred to as the depth of the hierarchy. Here, the efficient termination criterion of Dijkstra and Prokhorenko is used, in which a convergence parameter, ξ, is selected to be the Markovian limit.[216] Any evolution involving frequencies greater than this parameter is too rapid to be affected by non-Markovian feedback and the equation of motion for such ADOs is approximated to a simpler form. The convergence parameter determines the number of Matsubara frequencies via,

$$\frac{2(M+1)\pi}{\hbar\beta} > \xi, \tag{2.3.19}$$

and the hierarchy depth according to,

$$\sum_{n=1}^{N}\sum_{k=0}^{M} j_{nk}\nu_{nk} > \xi. \tag{2.3.20}$$

This termination criterion is suitable as long as ξ is significantly larger than the rate of bath relaxation. Unless stated otherwise, a default of $\xi = 10\Lambda_n$ is adopted in this thesis, where Λ_n is the larger of $n = 1, 2$. Terminating ADOs are propagated according to the approximation,

$$\dot{\rho}_{\mathbf{j}}(t) \simeq -\frac{i}{\hbar}\mathsf{H}_{\mathsf{S}}^{\times}\rho_{\mathbf{j}}(t), \tag{2.3.21}$$

which returns to the Liouville-von Neumann form, ignoring any further influence from the bath.

An example hierarchy for an overdamped bath is presented in figure 2.3.1, where ADOs are depicted as spheres in a lattice structure, with each ν_{nk} considered a separate axis. The first ADO beyond ξ in each axis is assigned as a terminator such that the overall hierarchy defines a sealed volume, within which non-Markovian memory effects are fully accounted for.

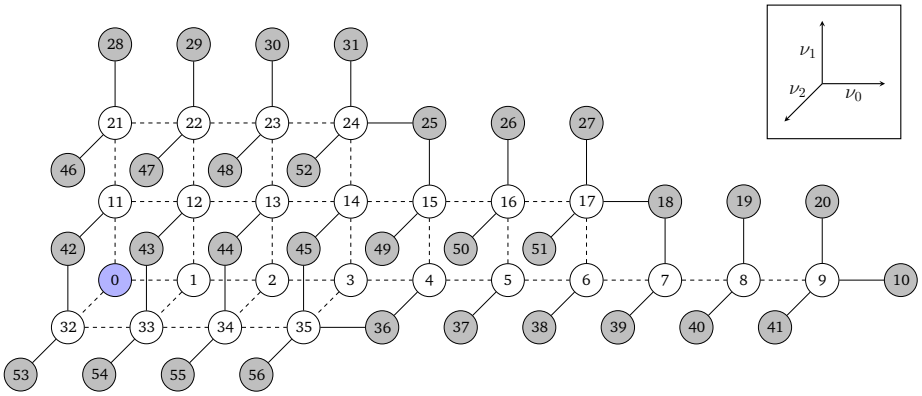

Figure 2.3.1: Hierarchy diagram for a single overdamped bath with $\tilde{\eta} = 500\,\mathrm{cm}^{-1}$, $\tilde{\Lambda} = 100\,\mathrm{cm}^{-1}$ and $\tilde{\xi} = 1000\,\mathrm{cm}^{-1}$ at 78 K, such that there are three Matsubara axes. Each sphere represents a density operator where the reduced density matrix of the system is blue, normal ADOs are white and terminating ADOs are grey.

Compared with alternative termination methods which truncated all Matsubara axes to an identical depth,[152] the criterion used here is significantly more efficient as it terminates axes involving larger ν_{nk} more quickly, without any loss in accuracy.[194]

2.3.2.2 Underdamped

Similarly, for an underdamped environment with the spectral density,

$$J_n(\omega) = \frac{2\eta_n\gamma_n\omega_{0n}^2\omega}{(\omega_{0n}^2-\omega^2)^2+\gamma_n^2\omega^2}, \tag{2.3.22}$$

of section 2.2.2.3, solving eq. 2.2.47 and separating the real and imaginary parts as in eq. 2.3.5 gives,[158,162]

$$L_{1n}(t) = \frac{\hbar\eta_n\omega_{0n}^2}{2i\zeta_n}\left(e^{-(\gamma_n/2-i\zeta_n)t}-e^{-(\gamma_n/2+i\zeta_n)t}\right), \tag{2.3.23}$$

$$\begin{aligned} L_{2n}(t) = {} & \frac{\hbar\eta_n\omega_{0n}^2}{2\zeta_n}e^{-(\gamma_n/2-i\zeta_n)t}\coth\left(\frac{\hbar\beta}{2}\left(\zeta_n+i\frac{\gamma_n}{2}\right)\right) \\ & -\frac{\hbar\eta_n\omega_{0n}^2}{2\zeta_n}e^{-(\gamma_n/2+i\zeta_n)t}\coth\left(\frac{\hbar\beta}{2}\left(-\zeta_n+i\frac{\gamma_n}{2}\right)\right) \\ & -\frac{4\eta_n\gamma_n\omega_{0n}^2}{\hbar\beta}\sum_{k=1}^{\infty}\frac{\nu_k}{(\omega_{0n}^2+\nu_k^2)^2-\gamma_n^2\nu_k^2}e^{-\nu_k t}, \end{aligned} \tag{2.3.24}$$

where $\zeta_n = \sqrt{\omega_{0n}^2-\frac{\gamma_n^2}{4}}$ when $\gamma_n < 2\omega_{0n}$ and $\nu_k = \frac{2\pi k}{\hbar\beta}$ are the Matsubara frequencies. The correlation function is again the sum of exponential terms, eq.

2.3.13, with frequencies ν_{nk} and coefficients, c_{nk}, where,

$$\begin{aligned}
\nu_{n0} &= \frac{\gamma_n}{2} - i\zeta_n, && (2.3.25)\\
\nu_{n1} &= \frac{\gamma_n}{2} + i\zeta_n, && (2.3.26)\\
\nu_{nk} &= \frac{2\pi(k-1)}{\hbar\beta}, && (2.3.27)\\
c_{n0} &= \frac{\hbar\eta_n\omega_{0n}^2}{2\zeta_n}\left\{\coth\left(\frac{\hbar\beta}{2}\left(\zeta_n + i\frac{\gamma_n}{2}\right)\right) - 1\right\}, && (2.3.28)\\
c_{n1} &= -\frac{\hbar\eta_n\omega_{0n}^2}{2\zeta_n}\left\{\coth\left(\frac{\hbar\beta}{2}\left(-\zeta_n + i\frac{\gamma_n}{2}\right)\right) - 1\right\}\\
&= \frac{\hbar\eta_n\omega_{0n}^2}{2\zeta_n}\left\{1 - \coth\left(\frac{\hbar\beta}{2}\left(-\zeta_n + i\frac{\gamma_n}{2}\right)\right)\right\}, && (2.3.29)\\
c_{nk} &= -\frac{4\eta_n\gamma_n\omega_{0n}^2}{\hbar\beta}\frac{\nu_{nk}}{(\omega_{0n}^2 + \nu_{nk}^2)^2 - \gamma_n^2\nu_{nk}^2}. && (2.3.30)
\end{aligned}$$

The equation of motion for the hierarchy of ADOs is then,[194]

$$\begin{aligned}
\dot{\rho}_{\mathbf{j}}(t) &= -\left(\frac{i}{\hbar}\mathsf{H}_{\mathsf{S}}^{\times} + \sum_{n=1}^{N}\sum_{k=0}^{M} j_{nk}\nu_{nk} - \sum_{n=1}^{N}\sum_{k=M}^{\infty}\mathsf{B}_n^{\times}\Psi_{nk}\right)\rho_{\mathbf{j}}(t)\\
&\quad + \sum_{n=1}^{N}\sum_{k=0}^{M}\mathsf{B}_n^{\times}\rho_{j_{nk}^+}(t) + \sum_{n=1}^{N} j_{n0}\Theta_n^-\rho_{j_{n0}^-}(t) + \sum_{n=1}^{N} j_{n1}\Theta_n^+\rho_{j_{n1}^-}(t)\\
&\quad + \sum_{n=1}^{N}\sum_{k=2}^{M} j_{nk}\nu_{nk}\Psi_{nk}\rho_{j_{nk}^-}(t), && (2.3.31)
\end{aligned}$$

where,

$$\begin{aligned}
\Psi_{nk} &= \frac{4\eta_n}{\hbar\beta}\frac{\gamma_n\omega_{0n}^2}{(\omega_{0n}^2 + \nu_{nk}^2)^2 - \gamma_n^2\nu_{nk}^2}\mathsf{B}_n^{\times}, && (2.3.32)\\
\Theta_n^{\pm} &= \frac{\eta_n\omega_{0n}^2}{2\zeta_n}\left\{\mp\mathsf{B}_n^{\circ} \pm \coth\left(\frac{\hbar\beta}{2}\left(\mp\zeta_n + i\frac{\gamma_n}{2}\right)\right)\mathsf{B}_n^{\times}\right\}, && (2.3.33)
\end{aligned}$$

and $\mathsf{B}_n^{\times}\rho = [\mathsf{B}_n, \rho]$ denotes the commutator of the bath coupling operator and the density matrix and $\mathsf{B}_n^{\circ}\rho = \{\mathsf{B}_n, \rho\}$ the anti-commutator. The ADOs are again characterised by the $N(M+1)$-dimensional vectors $\mathbf{j}$ and $\mathbf{j}^{\pm}$, with the terms of eq. 2.3.31 interpreted in terms of the creation and annihilation of bath phonons as for the overdamped case, but where the complex Matsubara frequencies ν_{n0} and ν_{n1} introduce additional terms involving $\Theta_n^{\pm}$.

The underdamped hierarchy is again terminated using ξ as the Markovian limit, with the number of Matsubara frequencies determined by eq. 2.3.19. The hierarchy depth is truncated according to,

$$\sum_{n=1}^{N}\sum_{k=0}^{M} j_{nk}|\mathbf{Re}(\nu_{nk})| > \xi, \qquad (2.3.34)$$

accounting for the complex frequencies. Terminating ADOs are propagated using the approximation,[162]

$$\dot{\rho}_{\mathbf{j}}(t) \simeq -\left(\frac{i}{\hbar}\mathsf{H}_{\mathsf{S}}^{\times} + i\sum_{n=1}^{N}(j_{n0}-j_{n1})\zeta_n - \sum_{n=1}^{N}\sum_{k=M}^{\infty}\mathsf{B}_n^{\times}\Psi_{nk}\right)\rho_{\mathbf{j}}(t), \tag{2.3.35}$$

where the sum to infinity is truncated with a sufficiently high value when implemented numerically.

An example underdamped hierarchy is presented in figure 2.3.2, again demonstrating a sealed volume. However, compared with the overdamped example in figure 2.3.1, the differences in ν_{n0} and ν_{n1} result in the first two axes having equal depth, such that the underdamped HEOM involves many more ADOs than the overdamped case, increasing computational complexity.

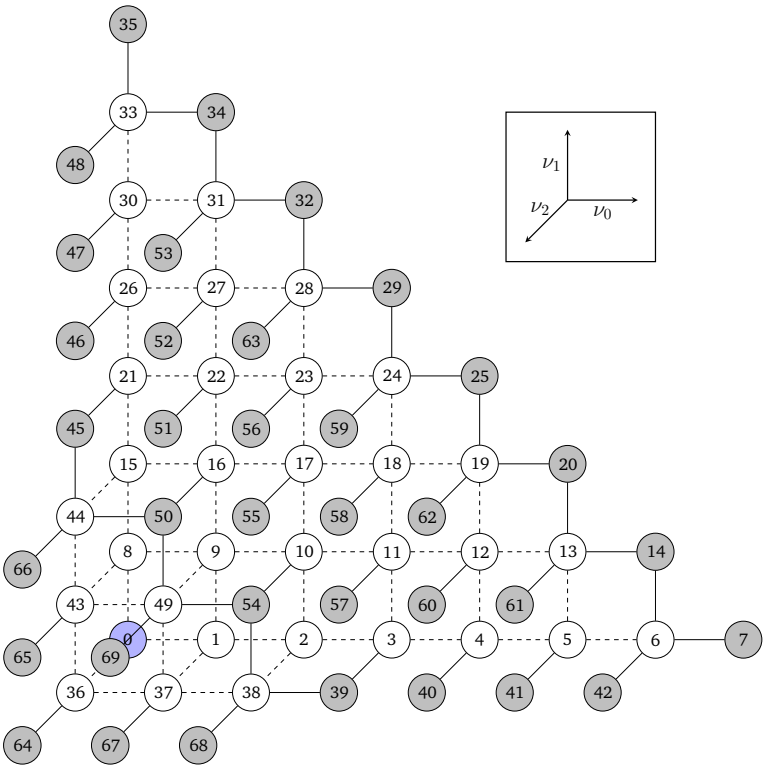

Figure 2.3.2: Hierarchy diagram for a single underdamped bath with $\tilde{\omega}_0 = 600\,\mathrm{cm}^{-1}$, $\tilde{\eta} = 500\,\mathrm{cm}^{-1}$, $\tilde{\gamma} = 150\,\mathrm{cm}^{-1}$ and $\tilde{\xi} = 600\,\mathrm{cm}^{-1}$ at $78\,\mathrm{K}$, such that there are three Matsubara dimensions. Each sphere represents a density operator where the reduced density matrix of the system is blue, normal ADOs are white and terminating ADOs are grey.

As the spectral density of eq. 2.3.22 reproduces the Drude form on increasing the damping to the overdamped limit, when $\gamma_n \gg \omega_{0n}$, this HEOM is also suitable for the overdamped case, with $\zeta_n = i\sqrt{\frac{\gamma_n^2}{4} - \omega_{0n}^2}$. However, it is insufficiently stable in the critical region of $\gamma_n \approx \omega_{0n}$ and the additional computational requirements of the underdamped HEOM means the HEOM of section 2.3.2.1 is preferable for overdamped environments.

2.3.2.3 Arbitrary Spectral Density

The HEOM presented in sections 2.3.2.1 and 2.3.2.2 correspond to modern methods, derived from specific forms of the spectral density and efficiently terminated. These find broad application in the literature and have even been combined to account for systems simultaneously coupled to both overdamped and underdamped environments.[159] But an alternative form is also presented in one of the original articles by Tanimura which accounts for an arbitrary spectral density.[151] In this case the equation of motion is presented as the integro-differential equation,

$$\begin{aligned}\dot{\rho}_{\mathsf{S}}(t;\omega_1,\omega_2,\ldots,\omega_m) &= -\left[\frac{i}{\hbar}\mathsf{H}_{\mathsf{S}}^{\times}+i\sum_{j=1}^{m}\omega_j\right]\rho_{\mathsf{S}}(t;\omega_1,\omega_2,\ldots,\omega_m)\\ &\quad -i\int_{-\infty}^{+\infty}\mathrm{d}\omega_{m+1}\mathsf{B}^{\times}\rho_{\mathsf{S}}(t;\omega_1,\omega_2,\ldots,\omega_{m+1})\\ &\quad -i\sum_{k=1}^{m-1}\Theta(\omega_k)\rho_{\mathsf{S}}(t;\omega_1,\omega_2,\ldots,\omega_{k-1},\omega_{k+1},\ldots,\omega_m)\\ &\quad -i\Theta(\omega_m)\rho_{\mathsf{S}}(t;\omega_1,\omega_2,\ldots,\omega_{m-1}),\end{aligned} \tag{2.3.36}$$

where,

$$\Theta(\omega)=J(\omega)\left[\coth\left[\frac{\beta\hbar\omega}{2}\right]\mathsf{B}^{\times}+\mathsf{B}^{\circ}\right], \tag{2.3.37}$$

written in terms of the total spectral density, eq. 2.3.10, and bath coupling operator, eq. 2.3.11. This defines a series of auxiliary density matrices, $\rho_{\mathsf{S}}(t;\omega_1,\omega_2,\ldots,\omega_m)$, representing the simultaneous evolution of the reduced system and m bath phonons of frequencies ω_m, where the reduced density operator of the system corresponds to the case in the absence of phonons, $\rho_{\mathsf{S}}(t)$. This generates a series of layers connecting the evolution of different numbers of bath phonons. The more direct involvement of the phonon frequencies in this formulation provides a more accessible physical interpretation of the HEOM method and usefully demonstrates the origins of the terms involved in the more abstract HEOM presented in previous sections.

The equation of motion for the reduced density operator of the system, corresponding to the top or zeroth layer, is,

$$\dot{\rho}_{\mathsf{S}}(t)=-\frac{i}{\hbar}\mathsf{H}_{\mathsf{S}}^{\times}\rho_{\mathsf{S}}(t)-i\int_{-\infty}^{+\infty}\mathrm{d}\omega_1\mathsf{B}^{\times}\rho_{\mathsf{S}}(t;\omega_1), \tag{2.3.38}$$

which involves the usual Liouville-von Neumann term plus an integral representing the creation of a single phonon of frequency ω_1. The evolution of

this auxiliary, the first layer, then involves additional terms,

$$\begin{aligned}\dot{\rho}_{\mathsf{S}}(t;\omega_1) &= -\left[\frac{i}{\hbar}\mathsf{H}_{\mathsf{S}}^{\times}+i\omega_1\right]\rho_{\mathsf{S}}(t;\omega_1)-i\int_{-\infty}^{+\infty}\mathrm{d}\omega_2\mathsf{B}^{\times}\rho_{\mathsf{S}}(t;\omega_1,\omega_2)\\ &\quad -i\Theta(\omega_1)\rho_{\mathsf{S}}(t). \end{aligned} \tag{2.3.39}$$

The first term evolves the reduced system plus the bath phonon of frequency ω_1, whilst the second integrates over a second frequency, representing the creation of a second bath phonon through system dissipation. The third term then accounts for annihilation of the first bath phonon, as it is reabsorbed by the system, corresponding to the thermal fluctuations of the bath through $\Theta(\omega_1)$.

This pattern then continues for the auxiliary with two bath phonons, the second layer, as,

$$\begin{aligned}\dot{\rho}_{\mathsf{S}}(t;\omega_1,\omega_2) &= -\left[\frac{i}{\hbar}\mathsf{H}_{\mathsf{S}}^{\times}+i(\omega_1+\omega_2)\right]\rho_{\mathsf{S}}(t;\omega_1,\omega_2)\\ &\quad -i\int_{-\infty}^{+\infty}\mathrm{d}\omega_3\mathsf{B}^{\times}\rho_{\mathsf{S}}(t;\omega_1,\omega_2,\omega_3)\\ &\quad -i\Theta(\omega_2)\rho_{\mathsf{S}}(t;\omega_1)-i\Theta(\omega_1)\rho_{\mathsf{S}}(t;\omega_2), \end{aligned} \tag{2.3.40}$$

which contains terms annihilating either of the present bath phonons, coupled to the auxiliary describing the evolution with the remaining phonon. This continues to the third layer,

$$\begin{aligned}\dot{\rho}_{\mathsf{S}}(t;\omega_1,\omega_2,\omega_3) &= -\left[\frac{i}{\hbar}\mathsf{H}_{\mathsf{S}}^{\times}+i(\omega_1+\omega_2+\omega_3)\right]\rho_{\mathsf{S}}(t;\omega_1,\omega_2,\omega_3)\\ &\quad -i\int_{-\infty}^{+\infty}\mathrm{d}\omega_4\mathsf{B}^{\times}\rho_{\mathsf{S}}(t;\omega_1,\omega_2,\omega_3,\omega_4)-i\Theta(\omega_3)\rho_{\mathsf{S}}(t;\omega_1,\omega_2)\\ &\quad -i\Theta(\omega_1)\rho_{\mathsf{S}}(t;\omega_2,\omega_3)-i\Theta(\omega_2)\rho_{\mathsf{S}}(t;\omega_1,\omega_3), \end{aligned} \tag{2.3.41}$$

interpreted in an identical manner, and so on, infinitely.

This interpretation nicely demonstrates the ability of HEOM methods to incorporate non-Markovian effects. Interaction of the system and bath through $\mathsf{B}^{\times}$ creates bath phonons, which are then propagated alongside the reduced system within the auxiliaries. This accounts for the transfer of information from the system to the bath and its storage within the bath degrees of freedom. Then, dependent on the timescales of bath relaxation as defined in the spectral density, these phonons will either dissipate further throughout the bath degrees of freedom, never to influence the system again, corresponding to a Markovian evolution, or be reabsorbed by the system after some period through $\Theta(\omega)$, creating a feedback of information, introducing non-Markovian effects. This is summarised in figure 2.3.3. In this way, the HEOM account for all possible sequences of interactions and the creation and annihilation of bath phonons of any frequency in any order, accurately modelling the dynamics of the system in

a broad range of conditions. This is described by an elegant diagrammatic method presented by Tanimura in reference 151 in terms of a continued fraction form of the hierarchy.

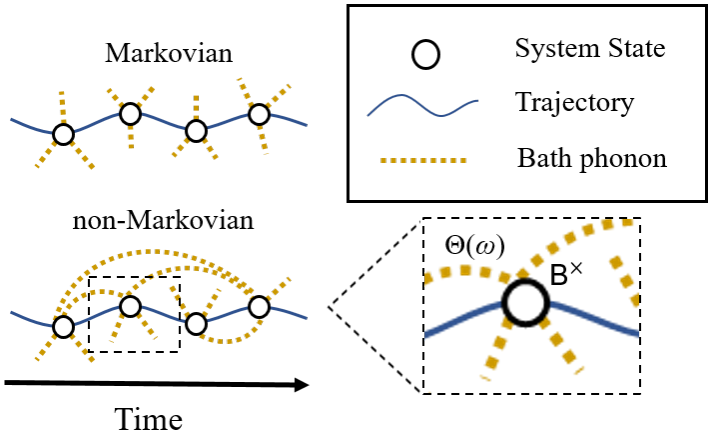

Figure 2.3.3: Markovian vs. Non-Markovian evolution in terms of the HEOM for an arbitrary spectral density (ASD-HEOM).

The ability to evolve the dynamics of the system with an arbitrary spectral density makes this a powerful and desirable method for the study of environments with highly structured spectral densities and the origins of non-Markovian effects. However, it is incredibly costly to implement computationally because of the large dependence on phonon frequencies. Discretizing the spectral density to W frequencies, the mth layer involves W^m auxiliaries, each with dimensions of the reduced density operator, which itself is large in the case of the vibronic dimers discussed in section 2.2.1.3. Within a few layers, the computational requirements quickly become impractical. This hierarchy must also be terminated by again defining the Markovian limit in terms of a certain number of simultaneously propagating bath phonons. This is achieved by removal of the term involving the integral of the auxiliary corresponding to the first layer beyond the Markovian limit. But, in the knowledge that the HEOM methods presented previously involve hierarchy depths ranging from tens to hundreds of ADOs in each Matsubara axis, propagating a suitable number of layers is unfeasible.

For this thesis, the HEOM with an arbitrary spectral density (henceforth abbreviated as ASD-HEOM) has been implemented up to the second layer and is used in the analysis of spectral lineshape in chapter 3. However, due to its substantial demand for computational resources, the ASD-HEOM is primarily used as a guide for the physical interpretation of more efficient modern methods, as discussed in this section.

2.3.3 Implementation

For this research, the HEOM methods described above have been developed into convenient Python classes which integrate with efficient FORTRAN algorithms, as described in Appendix C.1, page 152. Integration of the equations of motion is completed using Fourth Order Runge-Kutta (RK4) methods, detailed in appendix C.3, with a step size of fifty attoseconds.

With the system Hamiltonian and bath coupling operators defined as in section 2.2, the initial density matrix is prepared for either a vibronic monomer or dimer as, for example,

$$\rho_{\mathrm{D}}^{E} = \sum_{k} P_k \left|\Psi_{\mathrm{D,k}}^{S}\right\rangle\left\langle\Psi_{\mathrm{D,k}}^{S}\right|, \tag{2.3.42}$$

where the initial population of each state is Boltzmann weighted,

$$P_k = \frac{\exp\left(-\frac{\epsilon_k}{k_{\mathrm{B}}T}\right)}{Z}, \tag{2.3.43}$$

and Z is the canonical partition function,

$$Z = \sum_{k} \exp\left(-\frac{\epsilon_k}{k_{\mathrm{B}}T}\right) = \mathbf{Tr}\left(\exp\left(-\frac{\mathsf{H}_{\mathrm{D}}^{E}}{k_{\mathrm{B}}T}\right)\right). \tag{2.3.44}$$

This corresponds to factorised initial conditions where the system and bath are uncorrelated. As described by Tanimura, initial system-bath correlations are then established by propagation of the HEOM for a few picoseconds prior to the main simulation.[153] Simulations can be performed in the site, vibronic or exciton basis as long as all operators involved are consistent in that basis.

With a clear understanding of how the HEOM account for non-Markovian effects within open quantum system dynamics, section 2.4 discusses different approaches for application of the overdamped and underdamped HEOM methods to the theory of spectroscopy.

2.4 Theory of Spectroscopy

Beginning with a description of the macroscopic polarization, this section describes the response function formalism for linear and 2D photon echo spectroscopy. The equation-of-motion phase-matching approach (EOM-PMA) for simulation of 2DES involving laser spectra with a finite width is also described, before a discussion of how to interpret 2D spectra is presented.

2.4.1 Polarization

Let us begin by considering a molecular description of spectroscopy. The oscillating electric field of an incident laser couples to the transition dipole moment of the irradiated molecules, following the system-field interaction Hamiltonian in eq. 2.2.55. When the frequency of the oscillating field resonates with a transition frequency between two quantized levels of a molecule's electronic structure connected with a non-zero transition dipole moment, an energy conserving absorption occurs, transferring the molecule to an excited state as a photon is annihilated. As the laser spectrum has a finite width, several resonant transitions occur simultaneously across an ensemble, creating a wavepacket involving the superposition of multiple exited states, each with a distribution of frequencies due to the stochastic bath interactions. The electric field causes the molecules to oscillate in phase, creating a non-equilibrium charge distribution which endures after the electric field is removed, known as the *macroscopic polarization*.[26] This polarization is the physical observable of spectroscopy which our models must reproduce.[219] As each individual molecule is affected by its local environment differently, after interaction with the electric field the oscillations rapidly become out of phase, resulting in decay of the macroscopic polarization via dephasing, as the ensemble returns to its equilibrium distribution.[26]

The *macroscopic polarization* is calculated as the expectation value of the dipole moment operator and density matrix, reflecting Maxwell's equations for the field produced by oscillating charges,[1,26,140]

$$P = \mathbf{Tr}(\hat{\mu}\rho) = \langle\hat{\mu}\rho\rangle. \tag{2.4.1}$$

Components of the polarization are then separated as a perturbative expansion with respect to the number of coupled electric fields, where $P^{(1)}$ is the linear polarization resulting from interaction with a single electric field, and all higher order terms are classified as non-linear,[1,230]

$$P = P^{(1)} + P^{(2)} + P^{(3)} + \dots. \tag{2.4.2}$$

This requires that the field be sufficiently strong that it can be treated classically, whilst remaining weak enough that the eigenstates of the system are unaffected and the interaction can be treated perturbatively, $\mathsf{H}_{\mathrm{SF}}(t) \ll \mathsf{H}_{\mathrm{S}}$, as described in section 2.1.4.[26]

Temporarily neglecting the spatial component of the field, the polarization is

therefore,[27,141,222]

$$P^{(m)}(t) = \int_0^\infty \mathrm{d}t_m \int_0^\infty \mathrm{d}t_{m-1} \ldots \int_0^\infty \mathrm{d}t_1 \mathcal{E}(t-t_m)\mathcal{E}(t-t_m-t_{m-1})\ldots \\ \times \mathcal{E}(t-t_m-\ldots-t_1)R^{(m)}(t_m,\ldots,t_1), \quad (2.4.3)$$

the convolution of m electric fields with the *molecular response function*,[26]

$$R^{(m)}(t_m,\ldots,t_1) = \\ -\left(-\frac{i}{\hbar}\right)^m \langle\hat{\mu}(t_m+\ldots+t_1)[\hat{\mu}(t_{m-1}+\ldots+t_1),\ldots[\hat{\mu}(0),\rho(-\infty)]\ldots]\rangle. \quad (2.4.4)$$

The molecular response function is the desirable quantity which contains information of the structure of the system and its interaction with the environment. Here, $\rho(-\infty)$ corresponds to the reduced density matrix of the system at its equilibrium configuration before interaction with the electric fields and t_m are time intervals between the field interactions, discussed in more detail in section 2.4.3. The molecular response function is interpreted as the free evolution of the system in between each field interaction, accomplished by the commutator of the interaction picture dipole moment operator,

$$\hat{\mu}(t) = G(t,t_0)\hat{\mu}, \quad (2.4.5)$$

which in the absence of any system-bath interaction simplifies to,

$$\hat{\mu}(t) = e^{\frac{i}{\hbar}\mathsf{H_S}(t-t_0)}\hat{\mu}e^{-\frac{i}{\hbar}\mathsf{H_S}(t-t_0)}. \quad (2.4.6)$$

Therefore, the interaction picture dipole moment operator for a vibronic monomer in the site basis, eq. 2.2.60, is,

$$\hat{\mu}^S_{\mathrm{M}}(t) = \boldsymbol{\mu}_{eg}\left(e^{-i\omega_{eg}t}\,|g\rangle\langle e| + e^{i\omega_{eg}t}\,|e\rangle\langle g|\right)\otimes \mathrm{I}_{\mathrm{vib}}, \quad (2.4.7)$$

where $\omega_{eg} = (E_e - E_g)/\hbar$ is the transition frequency between the ground and excited electronic state and $\mathrm{I}_{\mathrm{vib}}$ is the identity operator over the nuclear degrees of freedom of the system.

Symmetry determines that only odd powers of m result in a non-zero polarization for isotropic media, producing first and third order responses corresponding to linear and 2D photon echo spectroscopy.[1,26] Fifth and higher order experiments are presented in the literature, but are not discussed here.[27,149]

2.4.2 First Order Linear Spectroscopy

For linear spectroscopy, the first order polarization is a convolution of a single electric field, $\mathcal{E}(t-t_1)$ from eq. 2.2.56, and the first order molecular response function, $R^{(1)}(t_1)$,[26]

$$P^{(1)}(t) = \int_0^\infty \mathrm{d}t\, \mathcal{E}(t-t_1) R^{(1)}(t_1), \tag{2.4.8}$$

where,

$$R^{(1)}(t_1) = \frac{i}{\hbar}\langle \hat{\mu}(t_1)[\hat{\mu}(0), \rho(-\infty)]\rangle, \tag{2.4.9}$$

and $\rho(-\infty)$ corresponds to the density operator in its equilibrium state, accounting for correlated initial conditions as described in section 2.3.2.

The first order response function is interpreted, from right to left, as the initial interaction of the system with the electric field at $t_0 = 0$, followed by the propagation of some time before emission of the polarization through eq. 2.4.1 at t_1.[149] The first order response function has two terms,

$$R^{(1)}(t_1) = \frac{i}{\hbar}(\langle \hat{\mu}(t_1)\hat{\mu}(0)\rho(-\infty)\rangle - \langle \rho(-\infty)\hat{\mu}(0)\hat{\mu}(t_1)\rangle), \tag{2.4.10}$$

where the *invariance of the trace* allows the two dipole moment operators to be rearranged such that they act on either side of the density matrix.[26] Each term corresponds to a *Liouville pathway*, which follows the change in state of the system over time.[1]

Simplifying to a consideration of the electronic degrees of freedom only and assuming the equilibrium density matrix has the entire population in the ground state, $\rho(-\infty) = |g\rangle\langle g|$, operation of the dipole moment operator with the ket side of the density matrix generates the *coherence* $\hat{\mu}(0)\rho(-\infty) \propto |e\rangle\langle g|$, whilst operation with the bra side gives $\rho(-\infty)\hat{\mu}(0) \propto |g\rangle\langle e|$. Each coherence corresponds to the existence of a superposition of system states, associated with a particular off-diagonal element of the density operator. Then, in the absence of any system-bath coupling, after some time, the second operation of the dipole moment returns the system to the ground state population with the trace,

$$\langle \hat{\mu}(t_1)\hat{\mu}(0)\rho(-\infty)\rangle = \mu_{eg}^2 e^{-i\omega_{eg}t_1}, \tag{2.4.11}$$

$$\langle \rho(-\infty)\hat{\mu}(0)\hat{\mu}(t_1)\rangle = \mu_{eg}^2 e^{i\omega_{eg}t_1}. \tag{2.4.12}$$

From eq. 2.2.56, the real-valued electric field is separated into two complex contributions,

$$\mathcal{E}(t) \propto E'(t)(e^{-i\omega t} + e^{i\omega t}) = E(t) + E^*(t), \tag{2.4.13}$$

again neglecting the spatial contribution and introducing the convention

$E(t) = E'(t)e^{-i\omega t}$, with its complex conjugate $E^*(t) = E'(t)e^{i\omega t}$.[26] Both Liouville pathways interact with each complex part of the field such that the first order polarization has four terms,

$$\begin{aligned} P^{(1)}(t) &= \int_0^\infty \mathrm{d}t_1 (E(t-t_1) + E^*(t-t_1)) R^{(1)}(t_1) \\ &= \int_0^\infty \mathrm{d}t_1 \frac{i}{\hbar} \big(\langle \hat{\mu}(t_1)\hat{\mu}(0)\rho(-\infty)\rangle E(t-t_1) \\ &\quad + \langle \hat{\mu}(t_1)\hat{\mu}(0)\rho(-\infty)\rangle E^*(t-t_1) \\ &\quad - \langle \rho(-\infty)\hat{\mu}(0)\hat{\mu}(t_1)\rangle E(t-t_1) \\ &\quad - \langle \rho(-\infty)\hat{\mu}(0)\hat{\mu}(t_1)\rangle E^*(t-t_1) \big), \end{aligned} \tag{2.4.14}$$

where inserting the results of the trace gives,

$$\begin{aligned} P^{(1)}(t) = \frac{i}{\hbar}\mu_{eg}^2 e^{-i\omega t} \int_0^\infty \mathrm{d}t_1 E'(t-t_1) \left(e^{i(\omega-\omega_{eg})t_1} - e^{i(\omega+\omega_{eg})t_1} \right) \\ + \frac{i}{\hbar}\mu_{eg}^2 e^{i\omega t} \int_0^\infty \mathrm{d}t_1 E'(t-t_1) \left(e^{-i(\omega+\omega_{eg})t_1} - e^{-i(\omega-\omega_{eg})t_1} \right). \end{aligned} \tag{2.4.15}$$

On setting the laser frequency resonant with the transition between electronic states, $\omega = \omega_{eg}$, it is clear that two of the exponential terms within the integral disappear, with the remaining two exponential terms corresponding to rapid oscillations, $\propto 2\omega_{eg}$. Adopting the *rotating wave approximation* (RWA), the rapidly oscillating terms are neglected, as integrating over a rapidly oscillating function results in significant cancellation, such that their contribution to the integral becomes negligible.[230] The two remaining resonant pathways result from the $\langle \hat{\mu}(t_1)\hat{\mu}(0)\rho(-\infty)\rangle E(t-t_1)$ term and its complex conjugate, $\langle \rho(-\infty)\hat{\mu}(0)\hat{\mu}(t_1)\rangle E^*(t-t_1)$, which correspond to the same physical process.[26]

The identification of pathways which survive the RWA is efficiently achieved using double-sided Feynman diagrams, with the four pathways of the linear response displayed in figure 2.4.1.[26] In these diagrams, the solid lines represent the ket (left) and bra (right) of the density matrix as time passes vertically. The state of the density matrix is labelled for all time as either a *population*, with equivalent ket and bra states, $|i\rangle\langle i|$, or a *coherence*, with inequivalent ket and bra, $|i\rangle\langle j|$, $i \neq j$, corresponding to a superpositions of states. The state is changed by the instantaneous field interactions which occur at the dashed lines, separated by the labelled time intervals. In more sophisticated diagrams, the state can also change during these time intervals, representing relaxation and energy transfer processes that occur between laser interactions.[231,232] The solid arrows represent the oscillating electric field, where $E(t)$ corresponds to an arrow pointing towards the ket, and $E^*(t)$ an arrow towards the bra. In all diagrams the final dashed arrow corresponds to emission via eq. 2.4.1.[26] The diagrams in figure 2.4.1 immediately show that only (a) and (c) survive the rotating wave approximation as they correspond to an intuitive physical picture

of absorption and then emission of the ket and bra, respectively.

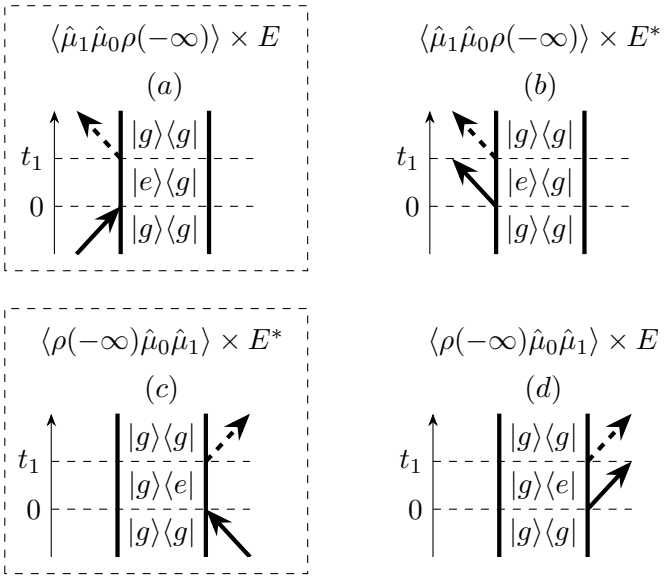

Figure 2.4.1: The four double-sided Feynman diagrams of the linear response. Diagrams in dashed boxes, (a) and (c), survive the rotating wave approximation.

Reintroducing the system-bath interaction, the first order molecular response function is expressed in the Schrödinger picture as,

$$R^{(1)}(t_1) = \frac{i}{\hbar}\mathbf{Tr}\left(\hat{\mu}G(t_1,t_0)\hat{\mu}^{\times}\rho(-\infty)\right), \tag{2.4.16}$$

where $G(t_1,t_0)$ is the propagator which transforms the system from time t_0 to time t_1, eq. 2.1.16.[149] The software developed in this research uses this form, which directly links with the HEOM dynamics presented in section 2.3.

The linear absorption spectrum is then obtained as the Fourier transform of the emitted signal. In this semi-classical theory, the emitted field is 90° phase shifted compared with the macroscopic polarization, $\propto iP(t)$, such that destructive interference diminishes the signal, hence referred to as *absorption*, consistent with the quantum mechanical interpretation.[26] The desired information of the system in the molecular response function is obscured by convolution with the envelope of the electric field. Enforcing the *impulsive limit*, where the field envelope is a delta function of time, $E'(t) = \delta(t)$, the polarization is equivalent to the molecular response function, and the linear absorption spectrum is given by,[1,26]

$$\sigma_A(\omega) = \int_0^{\infty} \mathrm{d}t e^{i\omega t} i R^{(1)}(t). \tag{2.4.17}$$

Note that restricting the trace in eq. 2.4.16 to the ground electronic state avoids duplication of the spectrum at negative frequencies. All linear spectra in this thesis are calculated in the impulsive limit to show all allowed transitions.

2.4.3 Third Order Photon Echo Spectroscopy

2.4.3.1 Polarization and Response function

2D photon echo spectroscopy is a four-wave-mixing technique in which an ultrafast laser pulse is separated into three phase-locked portions. These portions are then typically presented to the sample in a square BOXCARS geometry with controllable delay times such that a fourth signal, the photon echo signal corresponding to the third order polarization, is emitted in the phase-matched direction.[3,10,11,26,141] The photon echo signal is detected using heterodyne methods in which it is superimposed on an additional, much stronger waveform also propagated in the phase-matched direction, known as the Local Oscillator (LO).[4,25,222] Heterodyne methods have a vastly improved signal-noise ratio compared with standard homodyne detection methods, which record the emitted photon echo signal directly.[1]

The third order polarization is thus the convolution of three electric fields with the third order molecular response function, $R^{(3)}(t_1, t_2, t_3)$,[89,141]

$$P^{(3)}_{\mathbf{k}_s}(\tau, T, t) = \int_0^\infty \mathrm{d}t_1 \int_0^\infty \mathrm{d}t_2 \int_0^\infty \mathrm{d}t_3\, \mathcal{E}(t - t_1 - t_2 - t_3) \times \mathcal{E}(t - t_2 - t_3)\mathcal{E}(t - t_3)R^{(3)}(t_1, t_2, t_3). \quad (2.4.18)$$

The response function is defined as non-zero when $t_1, t_2, t_3 \geq 0$, such that the polarization is only produced once all three laser interactions have taken place, reflecting causality.[26,141]

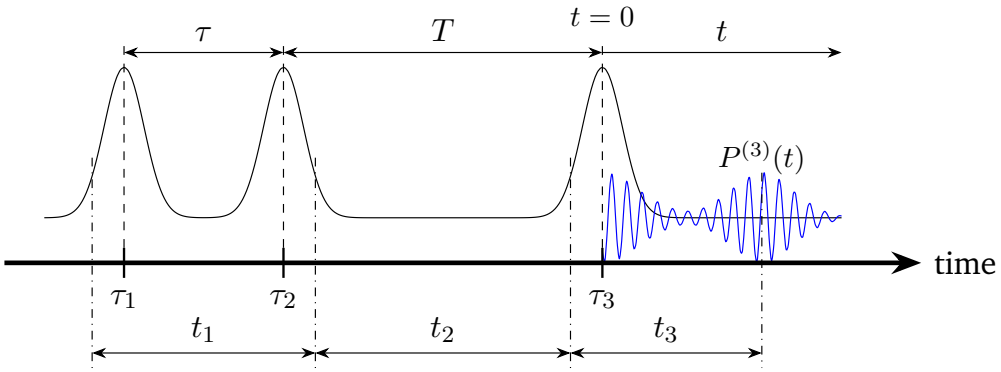

Figure 2.4.2: Timeline of interactions in 2D photon echo spectroscopy, showing the waiting times between field envelopes (black) and emission of the third order polarization, $P^{(3)}(t)$, in the rephasing direction (blue).

The timeline of system-field interactions in a photon echo measurement is presented in figure 2.4.2. This shows the three Gaussian envelopes and generation of the third order polarization.[21] The centres of the Gaussian pulse envelopes are labelled as τ_m, $m = 1, 2, 3$, in accordance with eq. 2.2.56, where

the first and second field envelopes are separated by the coherence time, τ, and the second and third by the population time, T. The centre of the third pulse is defined as $t = 0$ such that the oscillating polarization emerges for $t \geq 0$. The polarization at t is a result of the instantaneous system-field interaction events at the intervals $t_1 + t_2 + t_3$, $t_2 + t_3$ and t_3 earlier, which may occur at any time within the pulse envelopes.[10,141] In the impulsive limit, where $E'(t) = \delta(t)$, $\tau = t_1$, $T = t_2$ and $t = t_3$, and the three interactions are well separated in time such that their order is certain. The possibility of multiple interactions with each field produces a series of non-linear polarizations, emitted in different directions determined by the combination of the wavevectors involved.[26] Aligning the LO with the desired phase-matched direction, $\mathbf{k}_s$, allows a particular direction to be isolated. Beyond the impulsive limit, the overlap of envelopes with a finite width introduces uncertainty as to the order of the interactions, such that the Liouville pathways involved with each direction are less well defined.[24]

A single interaction with each of the three fields, where the interactions are ordered t_1 followed by t_2 followed by t_3, produces a third order polarization in the *rephasing*,

$$\mathbf{k}_s = -\mathbf{k}_1 + \mathbf{k}_2 + \mathbf{k}_3, \tag{2.4.19}$$

and the *non-rephasing*,

$$\mathbf{k}_s = \mathbf{k}_1 - \mathbf{k}_2 + \mathbf{k}_3, \tag{2.4.20}$$

directions.[11,181] Conveniently, in swapping the order with which the first two fields arrive at the sample, equivalent to a negative coherence time, $\tau < 0$, the non-rephasing signal is produced in the rephasing direction.[12,24] This knowledge enables both signals to be measured in a single scan without any change in experimental setup and is also applied in the finite pulse simulations in section 2.4.3.2.

The total third order molecular response function,[26]

$$\begin{aligned} R^{(3)}(t_3, t_2, t_1) &= -\frac{i}{\hbar^3}\langle\hat{\mu}(t_3 + t_2 + t_1)[\hat{\mu}(t_2 + t_1), [\hat{\mu}(t_1), [\hat{\mu}(t_0), \rho(-\infty)]]]\rangle \\ &= -\frac{i}{\hbar^3}\langle\hat{\mu}_3[\hat{\mu}_2, [\hat{\mu}_1, [\hat{\mu}_0, \rho(-\infty)]]]\rangle, \end{aligned} \tag{2.4.21}$$

is interpreted in the same manner as the first order response function, eq. 2.4.16, from right to left, as the instantaneous interaction of the first electric field, followed by the propagation of time in which the system and bath evolve in the absence of any field, then the next interaction and propagation, and the third, before finally the emission of the third order polarization following equation 2.4.1. Here a shorthand is introduced where the subscript of the interaction picture dipole moment operator corresponds to the final time interval involved, again enforcing the causality that the interactions occur in the order t_1 before t_2 and then t_3. The triple commutator results in eight terms,

which form four complex conjugate pairs,

$$\begin{aligned} R^{(3)}(t_3,t_2,t_1) &= -\frac{i}{\hbar^3}\big(\langle\hat{\mu}_3\hat{\mu}_0\hat{\rho}(-\infty)\hat{\mu}_1\hat{\mu}_2\rangle - \langle\hat{\mu}_2\hat{\mu}_1\hat{\rho}(-\infty)\hat{\mu}_0\hat{\mu}_3\rangle \\ &\quad +\langle\hat{\mu}_3\hat{\mu}_1\hat{\rho}(-\infty)\hat{\mu}_0\hat{\mu}_2\rangle - \langle\hat{\mu}_2\hat{\mu}_0\hat{\rho}(-\infty)\hat{\mu}_1\hat{\mu}_3\rangle \\ &\quad +\langle\hat{\mu}_3\hat{\mu}_2\hat{\rho}(-\infty)\hat{\mu}_0\hat{\mu}_1\rangle - \langle\hat{\mu}_1\hat{\mu}_0\hat{\rho}(-\infty)\hat{\mu}_2\hat{\mu}_3\rangle \\ &\quad +\langle\hat{\mu}_3\hat{\mu}_2\hat{\mu}_1\hat{\mu}_0\hat{\rho}(-\infty)\rangle - \langle\hat{\rho}(-\infty)\hat{\mu}_0\hat{\mu}_1\hat{\mu}_2\hat{\mu}_3\rangle\big). \end{aligned} \quad (2.4.22)$$

Using the convention in which the final interaction, $\hat{\mu}_3$, acts on the ket, this identifies four Liouville pathways, which are labelled using the 2DES convention as,

$$R^{(3)}(t_3,t_2,t_1) \propto R_1 + R_1^* + R_2 + R_2^* + R_3 + R_3^* + R_4 + R_4^*, \quad (2.4.23)$$

where,

$$R_1 = \langle\hat{\mu}_3\hat{\mu}_0\hat{\rho}(-\infty)\hat{\mu}_1\hat{\mu}_2\rangle, \quad (2.4.24)$$

$$R_2 = \langle\hat{\mu}_3\hat{\mu}_1\hat{\rho}(-\infty)\hat{\mu}_0\hat{\mu}_2\rangle, \quad (2.4.25)$$

$$R_3 = \langle\hat{\mu}_3\hat{\mu}_2\hat{\rho}(-\infty)\hat{\mu}_0\hat{\mu}_1\rangle, \quad (2.4.26)$$

$$R_4 = \langle\hat{\mu}_3\hat{\mu}_2\hat{\mu}_1\hat{\mu}_0\hat{\rho}(-\infty)\rangle. \quad (2.4.27)$$

As for the first order response, the temporal component of the total electric field is expanded into three complex pairs, where $E(t) = E'(t)e^{-i\omega t}$, as,

$$\mathcal{E}(t) \propto E_1(t) + E_1^*(t) + E_2(t) + E_2^*(t) + E_3(t) + E_3^*(t). \quad (2.4.28)$$

This identifies six components to the third order electric field, which results in $6\times 6\times 6\times 4 = 864$ possible Feynman diagrams for the four pathways. But, assuming non-overlapping pulses and time ordering such that the first interaction, $\hat{\mu}_0$, is due to E_1, the second, $\hat{\mu}_1$, is due to E_2 and the third, $\hat{\mu}_2$, is due to E_3, the number of pathways is reduced to $2\times 2\times 2\times 4 = 32$.[233] For a two level system, only four of these 32 diagrams describe resonant interactions which survive the RWA, as described in section 2.4.2, one for each R_x. These are shown in figure 2.4.3 where the transition frequency involved with each interaction is also included in the diagrams.[1,26]

The sequence of field interactions defines whether the pathways are rephasing or non-rephasing, according to eqs. 2.4.19 and 2.4.20, respectively, where a positive wavevector directs the arrow towards the ket and a negative towards the bra. The first field interaction, acting on the ket for non-rephasing and the bra for rephasing, generates a coherence and the second a population, hence the naming of their corresponding time intervals. The third creates another coherence, before the polarization is emitted, corresponding to the final dashed

Figure 2.4.3: Double-sided Feynman diagrams for the third order non-linear response, where pathways are labelled as R_x, $x = 1, \ldots, 4$ using the 2DES convention and as $R_x^\star$, $x = 1, \ldots, 6$ using the 2DIR convention.

arrow which returns the system to a ground state population. Pathways R_1 and R_2 involve an excited state population during the population time, t_2, such that they are assigned as *stimulated emission* (SE) pathways, whereas pathways R_3 and R_4 have a ground state population and are assigned as *ground state bleach* (GSB). Using the convention for the sign of the third order response function in eq. 2.4.4, both of these pathways correspond to positive peaks in the final spectrum.

Importantly, the rephasing pathways, R_2 and R_3, involve opposite coherences, first $|g\rangle\langle e|$ and then $|e\rangle\langle g|$. In the interaction picture, these evolve with opposite frequencies, as in eq. 2.4.7, such that an inhomogeneous distribution of frequencies which becomes out of phase over some period in the coherence $|g\rangle\langle e|$, will return to being in phase when placed into the $|e\rangle\langle g|$ coherence for the same duration. This revival in the polarization at $\tau = t$ gives the *rephasing* pathways their name and corresponds to the photon echo, equivalent to spin echo techniques in NMR spectroscopy.[12,26] As the non-rephasing pathways involve the same $|e\rangle\langle g|$ coherence during both intervals t_1 and t_3, there is no such revival in the polarization and an inhomogeneous distribution progresses further out of phase.

If the system being probed has additional excited states, two additional pathways survive the RWA, involving *excited state absorption* (ESA). This is common in 2D infrared spectroscopy (2DIR), which induces transitions between vibrational levels with infrared frequencies rather than between electronic states with UV/visible frequencies. The classification of pathways is different within the 2DIR convention and these labels are indicated $R_x^\star$ in figure 2.4.3.[26] The excited state absorption pathways, $R_3^\star$ and $R_6^\star$, involve absorption of the ket from the excited state population to an additional state $|f\rangle$ and for the sign convention in eq. 2.4.4, this additional absorption results in these pathways contributing peaks of an opposite, negative sign in the 2D spectra.

An extensive analysis of the Feynman diagrams for vibronic systems is presented in chapter 4, using the 2DES convention for a monomer with two electronic states. The addition of vibrational levels results in vibronic coherences existing during the population time, leading to oscillating peaks. Extension to vibronic dimers in chapter 5 then introduces ESA pathways as the sequence of interactions involve transitions between singly and doubly excited electronic states.

The bath has an important role at each stage of these third order diagrams. When the system is placed into a coherence, the stochastic bath interactions lead to the dephasing of excited state wavepackets, which causes the polarization to decay. During the population time, dissipation within the system in terms of vibrational relaxation and luminescence again reduce the polarization, whilst

dynamic changes in the state of the system between field interactions introduce additional Liouville pathways which can dominate the spectra at long waiting times. The ability to capture the complexity of these competing processes in addition to the information obtained about the structure of the system itself is one of the reasons why 2DES is such a valuable technique.

As for the linear response, the third order response function is expressed in the Schrödinger picture as,[2,149]

$$R^{(3)}(t_3,t_2,t_1) = -\frac{i}{\hbar^3}\mathbf{Tr}\left(\hat{\mu}G(t_3+t_2+t_1,t_2+t_1)\hat{\mu}^{\times}G(t_2+t_1,t_1)\right.$$
$$\left.\hat{\mu}^{\times}G(t_1,t_0)\hat{\mu}^{\times}\rho(-\infty)\right). \quad (2.4.29)$$

By distinguishing the raising (absorption), $\hat{\mu}_+$, and lowering (emission), $\hat{\mu}_-$, contributions to the dipole moment operator, the rephasing and non-rephasing contributions to the total response function are separated into,[156,161]

$$R_{\mathrm{R}}(t_1,t_2,t_3) = -\mathbf{Tr}\left(\hat{\mu}G(t_3+t_2+t_1,t_2+t_1)\frac{i}{\hbar}\hat{\mu}_+^{\times}G(t_2+t_1,t_1)\right.$$
$$\left.\frac{i}{\hbar}\hat{\mu}_+^{\times}G(t_1,t_0)\frac{i}{\hbar}\hat{\mu}_-^{\times}\rho(-\infty)\right), \quad (2.4.30)$$

and,

$$R_{\mathrm{NR}}(t_1,t_2,t_3) = -\mathbf{Tr}\left(\hat{\mu}G(t_3+t_2+t_1,t_2+t_1)\frac{i}{\hbar}\hat{\mu}_+^{\times}G(t_2+t_1,t_1)\right.$$
$$\left.\frac{i}{\hbar}\hat{\mu}_-^{\times}G(t_1,t_0)\frac{i}{\hbar}\hat{\mu}_+^{\times}\rho(-\infty)\right), \quad (2.4.31)$$

respectively. In this thesis, all 2D spectra calculated in the impulsive limit are produced by solving the response function in these forms using the HEOM dynamics described in section 2.3. The field interactions are accounted for by applying the commutators to all ADOs of the hierarchy before resuming propagation, such that system-bath correlations are maintained and the resulting spectra include all non-Markovian effects.[156,159,161] Calculation of the spectra then proceeds as discussed in section 2.4.3.3, exchanging the polarization for the response function, as in the calculation of the linear absorption spectrum.

2D spectra are calculated in the impulsive limit in chapters 3 and 5 to concentrate on the effect of the system-bath coupling. However, as discussed in chapter 1, finite pulse effects can have a major impact, leading to distortion of the lineshape and obscuring spectral features, particularly at early times due to the overlap of pulses.[24,184] Finite pulse effects are accounted for using the equation-of-motion phase-matching approach.

2.4.3.2 Equation-of-Motion Phase-Matching Approach

Avoiding the perturbative expansion of the polarization in eq. 2.4.3, the equation-of-motion phase-matching approach (EOM-PMA) incorporates an explicit definition of the external electric fields into a dynamical method for the calculation of 2D spectra including finite pulse effects.[98,175,178,181] Whereas fully non-perturbative solutions calculate the total third order polarization for all phase combinations, propagation of a number of auxiliaries in the EOM-PMA isolates the Liouville pathways in the phase-matched direction only, avoiding costly post-processing.[142,172,174] However, use of the Taylor expansions involved enforces the weak field approximation, such that the EOM-PMA provides an extension to the response function method, but cannot account for strong system-field interactions for which fully non-perturbative methods are necessary.[182]

The total electric field of the incident laser is defined as per equation 2.2.56, with the interaction Hamiltonian separated into the contributions of the three Gaussian portions, $V_m(t)$, as,

$$\begin{aligned} \mathsf{H}_{\mathrm{SF}}(t) &= -\hat{\mu}\mathcal{E}(\mathbf{r},t) \\ &= -\sum_{m=1}^{3} \exp(i\mathbf{k}_m \cdot \mathbf{r}) V_m(t) + c.c., \end{aligned} \tag{2.4.32}$$

where,

$$V_m(t) = \left(\hat{\mu}\chi_m E'_m(t-\tau_m)\exp(-i\omega_m t)\right), \tag{2.4.33}$$

with all parameters as defined in section 2.2.3.[174,175] In the knowledge that the rephasing and non-rephasing signals are produced in the phase-matched direction, $\mathbf{k}_s$, after a single interaction with each of the three fields, it is expected that Liouville pathways in the rephasing direction involve a master equation of the form,

$$\mathcal{L}_1\rho_1(t) = -\frac{i}{\hbar}[\mathsf{H}_{\mathsf{S}} - V_1(t) - V_2^{\dagger}(t) - V_3^{\dagger}(t), \rho_1(t)], \tag{2.4.34}$$

where the system-field interaction Hamiltonian is expressed in terms of the three $V_m(t)$ and the bath coupling has been ignored from eq. 2.3.1. Here, the use of adjoints for $V_2^{\dagger}(t)$ and $V_3^{\dagger}(t)$ enforces the appropriate sign on the wavevectors for the rephasing direction, in accordance with eq. 2.4.19.

In this way, the non-Hermitian auxiliary $\rho_1(t)$ accounts for a number of Liouville pathways, including the rephasing and non-rephasing contributions, as well as multiple other non-linear signals. Gelin *et al.* then consider the dependence of $\rho_1(t)$ with respect to each laser field in terms of the generating

function $\rho_1(\lambda_1, \lambda_2, \lambda_3; t)$, written as the Taylor series,[174,175]

$$\rho_1(\lambda_1, \lambda_2, \lambda_3; t) = \sum_{i,j,k=0}^{\infty} \lambda_1^i \lambda_2^j \lambda_3^k \rho_1^{i,j,k}(t), \tag{2.4.35}$$

where i, j, k represent the number of interactions between the system and the three fields. For example, two interactions between the system and the first field is represented by λ_1^2, whilst zero interactions between the system and the third field is represented by λ_3^0. The rephasing and non-rephasing Liouville pathways are therefore associated with the $\rho_1^{111}(t)$ contribution, which is isolated by combining eight generating functions, where the interaction with each field is sequentially removed,[175]

$$\begin{aligned} \lambda_1\lambda_2\lambda_3\rho_1^{111}(t) \quad = \quad & \rho_1(\lambda_1, \lambda_2, \lambda_3; t) + \rho_1(\lambda_1, 0, 0; t) - \rho_1(\lambda_1, 0, \lambda_3; t) \\ & -\rho_1(\lambda_1, \lambda_2, 0; t) - \rho_1(0, \lambda_2, \lambda_3; t) - \rho_1(0, 0, 0; t) \\ & +\rho_1(0, 0, \lambda_3; t) + \rho_1(0, \lambda_2, 0; t) \\ & +O(\lambda_1^i \lambda_2^j \lambda_3^k),\ i + j + k > 3. \end{aligned} \tag{2.4.36}$$

Each of the generating functions and the above summation are presented in full in appendix B.3, page 149.

Each generating function corresponds to a master equation of the form of eq. 2.4.34, such that there are eight auxiliaries,

$$\rho_1 = \rho_1(\lambda_1, \lambda_2, \lambda_3; t), \tag{2.4.37}$$
$$\rho_2 = \rho_1(\lambda_1, \lambda_2, 0; t), \tag{2.4.38}$$
$$\rho_3 = \rho_1(\lambda_1, 0, \lambda_3; t), \tag{2.4.39}$$
$$\rho_4 = \rho_1(\lambda_1, 0, 0; t), \tag{2.4.40}$$
$$\rho_5 = \rho_1(0, \lambda_2, \lambda_3; t), \tag{2.4.41}$$
$$\rho_6 = \rho_1(0, \lambda_2, 0; t), \tag{2.4.42}$$
$$\rho_7 = \rho_1(0, 0, \lambda_3; t), \tag{2.4.43}$$
$$\rho_8 = \rho_1(0, 0, 0; t), \tag{2.4.44}$$

with the generators,[142,175]

$$\mathcal{L}_1\rho_1(t) = -\frac{i}{\hbar}\left[\mathsf{H_S} - V_1(t) - V_2^\dagger(t) - V_3^\dagger(t), \rho_1(t)\right], \quad (2.4.45)$$

$$\mathcal{L}_2\rho_2(t) = -\frac{i}{\hbar}\left[\mathsf{H_S} - V_1(t) - V_2^\dagger(t), \rho_2(t)\right], \quad (2.4.46)$$

$$\mathcal{L}_3\rho_3(t) = -\frac{i}{\hbar}\left[\mathsf{H_S} - V_1(t) - V_3^\dagger(t), \rho_3(t)\right], \quad (2.4.47)$$

$$\mathcal{L}_4\rho_4(t) = -\frac{i}{\hbar}\left[\mathsf{H_S} - V_1(t), \rho_4(t)\right], \quad (2.4.48)$$

$$\mathcal{L}_5\rho_5(t) = -\frac{i}{\hbar}\left[\mathsf{H_S} - V_2^\dagger(t) - V_3^\dagger(t), \rho_5(t)\right], \quad (2.4.49)$$

$$\mathcal{L}_6\rho_6(t) = -\frac{i}{\hbar}\left[\mathsf{H_S} - V_2^\dagger(t), \rho_6(t)\right], \quad (2.4.50)$$

$$\mathcal{L}_7\rho_7(t) = -\frac{i}{\hbar}\left[\mathsf{H_S} - V_3^\dagger(t), \rho_7(t)\right], \quad (2.4.51)$$

$$\mathcal{L}_8\rho_8(t) = -\frac{i}{\hbar}\left[\mathsf{H_S}, \rho_8(t)\right]. \quad (2.4.52)$$

Combination of the evolved auxiliary states according to eq. 2.4.36 then allows calculation of the third order polarization in the phase-matched direction as the expectation value of the dipole moment operator as usual,

$$P^{(3)}_{\mathbf{k}_s}(\tau, T, t) = \exp(i\mathbf{k}_s \cdot \mathbf{r})\mathbf{Tr}\big(\hat{\mu}\left(\rho_1(t) - \rho_2(t) - \rho_3(t) + \rho_4(t) - \rho_5(t) + \rho_6(t) + \rho_7(t)\right)\big) + c.c., \quad (2.4.53)$$

where $\rho_8(t)$ is ignored as its generator is independent of the laser fields, eq. 2.4.52, equivalent to the propagation of the initial ground state population, which does not contribute to the macroscopic polarization, $\mathbf{Tr}(\hat{\mu}\rho_8(t)) = 0$.[175] The complex conjugate ($c.c.$) accounts for the complementary set of Feynman diagrams.

Whether the rephasing or non-rephasing signals are produced in the phase-matched direction is determined by the time ordering of the pulses and the exponential phase factor, $\exp(i\mathbf{k}_s \cdot \mathbf{r})$. As in experimental methods, positive coherence times correspond to the rephasing signal whilst negative coherence times, $\tau < 0$, exchange the order of the first two field interactions such that the non-rephasing signal is produced. The corresponding phase factors are calculated by considering the temporal phase difference in the fields as they arrive at the sample, equivalent to the spatial phase difference. Considering the wavefront as it travels from source to sample, the pulse sequence in figure 2.4.2 suggests,

$$\mathbf{k_1} \cdot \mathbf{r} = \omega(\tau_1), \quad (2.4.54)$$

$$\mathbf{k_2} \cdot \mathbf{r} = \omega(\tau_1 + \tau), \quad (2.4.55)$$

$$\mathbf{k_3} \cdot \mathbf{r} = \omega(\tau_1 + \tau + T), \quad (2.4.56)$$

where τ_1 is the time from the beginning of the simulation to the centre of the first laser pulse. The exponential phase factor for the rephasing signal is therefore,

$$\exp(i\mathbf{k}_s \cdot \mathbf{r}) = \exp(i(-\mathbf{k_1} + \mathbf{k_2} + \mathbf{k_3}) \cdot \mathbf{r}) = \exp(i\omega(\tau_1 + 2\tau + T)), \quad (2.4.57)$$

with the non-rephasing phase factor given by,

$$\exp(i\mathbf{k}_s \cdot \mathbf{r}) = \exp(i(\mathbf{k_1} - \mathbf{k_2} + \mathbf{k_3}) \cdot \mathbf{r}) = \exp(i\omega(\tau_1 + T)). \quad (2.4.58)$$

Propagation of each of the seven generators in eqs. 2.4.45 - 2.4.52 using the HEOM described in section 2.3 therefore provides a method for calculation of the third order polarization for any open quantum system in the rephasing and non-rephasing directions, fully accounting for finite pulse effects.[184] However, the propagation of a full hierarchy of ADOs for each of these seven auxiliaries adds significant additional complexity to the already intensive calculations. The number of auxiliaries can be reduced to three by enforcing the RWA on the system Hamiltonian and dipole moment operator, but here all seven are used to ensure generality of the model.[142,174] The EOM-PMA is used in chapter 4 to demonstrate spectral filtering of a vibronic monomer and in chapter 5 for the selective excitation of a vibronic heterodimer.

2.4.3.3 2D Spectra

2D spectra are then calculated as the double Fourier transform of the third order polarization with respect to τ and t as,

$$S_{\mathrm{R}}(\omega_\tau, T, \omega_t) = \int_0^\infty \mathrm{d}t \int_0^\infty \mathrm{d}\tau e^{-i\omega_\tau \tau} e^{i\omega_t t} i P^{(3)}_{\mathrm{R}}(\tau, T, t), \quad (2.4.59)$$

for the rephasing and,

$$S_{\mathrm{NR}}(\omega_\tau, T, \omega_t) = \int_0^\infty \mathrm{d}t \int_0^\infty \mathrm{d}\tau e^{i\omega_\tau \tau} e^{i\omega_t t} i P^{(3)}_{\mathrm{NR}}(\tau, T, t), \quad (2.4.60)$$

for the non-rephasing components.[116,141,183,184] Note that the sign of the transform with respect to τ is different for the rephasing and non-rephasing components, reflecting the change in the time ordering of the pulses. On performing a forward transform of the third order polarization in both the τ and t axes, the rephasing signal appears in the $(\mp\omega_\tau, \pm\omega_t)$ quadrants whilst the non-rephasing is found in the $(\pm\omega_\tau, \pm\omega_t)$ quadrants.[4,26] An inverse transform in τ for the rephasing polarization thus produces both spectra in the positive quadrant, avoiding any confusion involving axes labelled with negative frequencies, as used in some of the literature.

The ω_τ and ω_t axes are then read as the excitation and emission frequencies, respectively, with each spectrum presented for a single population time, T.[2,3,128] The excitation frequency, ω_τ, corresponds to the first system-field interaction and thus the frequency of the first (bottom) solid arrow in the third order double-sided Feynman diagrams. The emission frequency, ω_t, corresponds to the final interaction and thus to the frequency of the final (top) dashed arrow in the Feynman diagrams. As discussed by Hamm and Zanni, the rephasing and non-rephasing spectra have both absorptive (real) and dispersive (imaginary) contributions.[26] Therefore it is common to sum these signals to display the purely absorptive spectrum,[156,159,184]

$$S_{\mathrm{A}} = \mathbf{Re}(S_{\mathrm{R}} + S_{\mathrm{NR}}). \tag{2.4.61}$$

2D spectra contain both diagonal and off-diagonal peaks, where peaks on the diagonal correspond to the transitions identified in the linear absorption spectrum, whilst off-diagonal peaks are a result of the excitation and emission frequencies being unequal due to changes in the state of the system caused by the intermediate field interactions. The intensity of peaks originating from pathways where the system is in a population state during the population time, T, known as *population pathways*, decays exponentially due to dephasing and relaxation. The intensity of peaks involving coherences during the population time, *coherence pathways*, oscillates at the frequency of the energy gap between the states involved in the coherence.[65] This is the spectral manifestation of quantum beating.[73,181] A third Fourier transform with respect to the population time enables greater analysis of the coherence pathways, as is discussed at length in chapter 4.

The location and oscillation of peaks provides information of the structure of the system, whilst the lineshape gives details of the bath, in terms of homogeneous and inhomogeneous broadening.[3,10] Unlike linear spectroscopy where these types of broadening are projected onto a single axis, in 2D spectroscopy, inhomogeneous broadening appears as an elongation along the diagonal, whilst the anti-diagonal width is the result of purely homogeneous broadening.[4,140] *Note that throughout this thesis, anti-diagonal refers to the anti-correlated cross section of a specific peak, not necessarily through the origin.* Homogeneous broadening is any broadening common to all system molecules, such as the lifetime broadening caused by the decaying excited state introducing uncertainty regarding the exact transition frequency of the system, resulting in a Lorentzian lineshape.[199,219] Inhomogeneous broadening is any broadening relating to ensemble effects, such as a Gaussian distribution of different transition frequencies for an ensemble of system molecules due to conformational freedom or differing solvent environments.[149,230] As discussed

in section 2.4.3.1, the rephasing Liouville pathways involve opposite coherences, such that an initially dephasing distribution is encouraged to re-phase, instigating a revival in the polarization along $\tau = t$. Upon Fourier transform, this creates a stronger peak which is elongated along the diagonal in the rephasing spectrum compared with the non-rephasing spectrum, such that the elongation remains in the absorptive spectrum when summed.[183] Figure 2.4.4 shows the macroscopic polarization for the rephasing and non-rephasing pathways, Fourier transform to their respective spectra and their summation into the absorptive spectrum, where the inhomogeneous and homogeneous broadening are labelled. These example spectra correspond to a two-level-system with significant inhomogeneous broadening, calculated in the impulsive limit.

As the population time increases, elongation about the diagonal due to inhomogeneous broadening diminishes due to *spectral diffusion* resulting from the decay of system-bath correlations.[20,26,234] The loss of correlations reduces the revival in polarization, such that the rephasing and non-rephasing signals have equivalent intensity and the opposing twists in the spectra (rephasing with positive intensity along the diagonal and non-rephasing with positive along the anti-diagonal) create a more symmetrical peak when summed in the absorptive. This is discussed in greater detail along with the implications of non-Markovianity for spectral lineshape in chapter 3.

In this chapter, a definition of non-Markovianity in quantum systems and an overview of open quantum system dynamics progressed into details of the system and interaction Hamiltonians for vibronic monomers and dimers. Non-Markovian quantum dynamical methods were then derived from the system-bath correlation function for both underdamped and overdamped environments, before the theory of spectroscopy was derived from the system-field interaction. Methods are presented for the simulation of linear and 2D photon echo spectra in the impulsive limit via direct calculation of the appropriate molecular response function, as well as the alternative EOM-PMA for 2DES using laser spectra of finite width. An introductory description of spectral lineshape and the Liouville pathways involved demonstrates how to interpret 2D spectra, providing a foundation for the analysis in subsequent chapters. The theoretical methods discussed here provide a general model for the 2DES of vibronic systems which is assessed in terms of the spectral lineshape and bath interaction in chapter 3, the role of the finite laser spectrum in chapter 4 and its application to excitonic dimer systems in chapter 5.

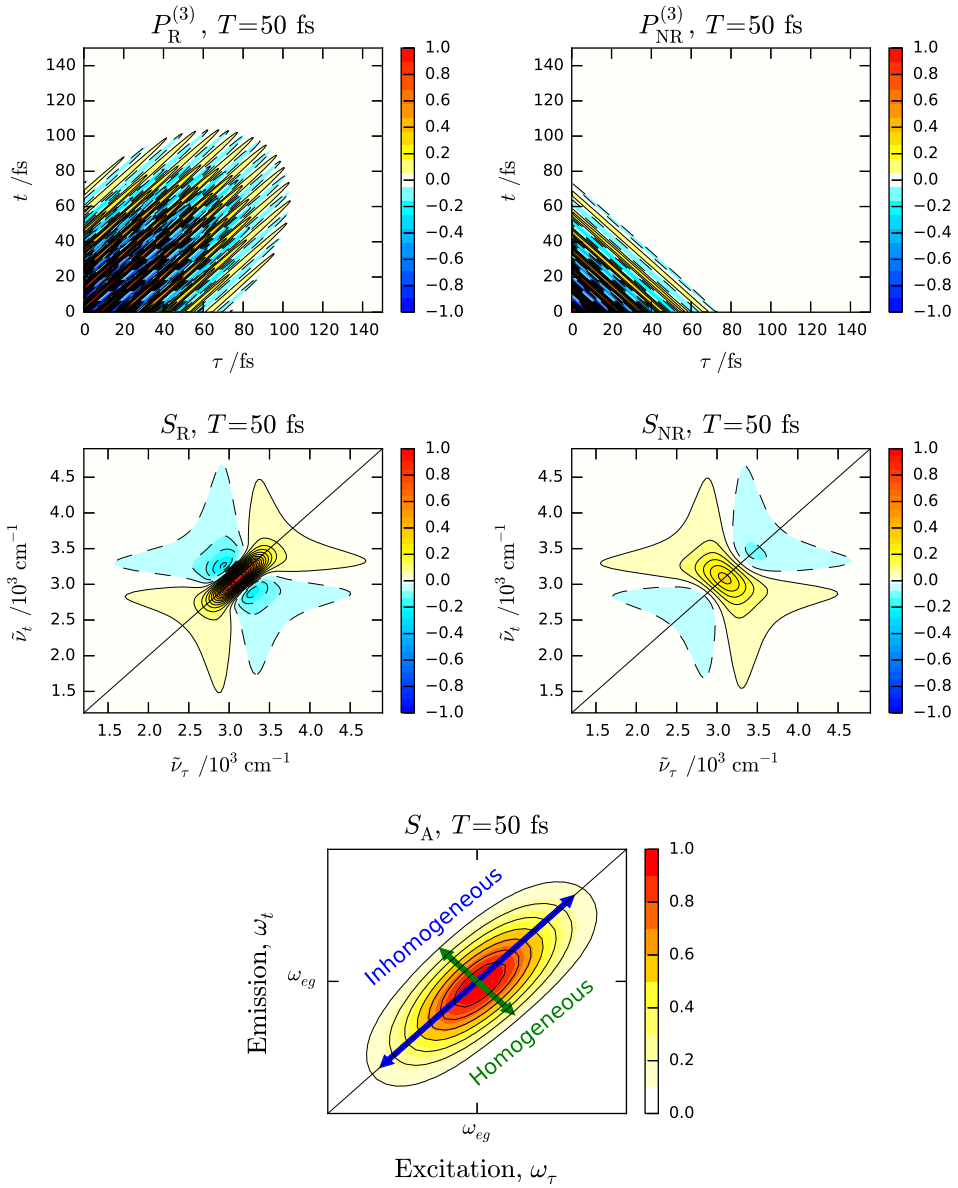

Figure 2.4.4: Third order polarization and 2D spectra in the impulsive limit for a two-level-system with significant inhomogeneous broadening. The non-rephasing polarization and spectrum are normalised to the maximum of the equivalent rephasing signal to demonstrate how the elongation of the rephasing spectrum endures into the absorptive spectrum when summed with the non-rephasing.

3 Analysis of Spectral Lineshape

From here onwards, the results of this research are presented, beginning with a demonstration of the versatility of the models in terms of the range of conditions for which spectral lineshapes can be produced. The measurable non-Markovianity associated with the different damping limits of the bath and its effect on the spectral lineshape are then discussed, as reported by us in reference 194.

3.1 System vs. Bath Vibrations

In section 2.2, it was shown how to construct the system Hamiltonian for a vibronic monomer, and in section 2.3, how to evolve this system in the presence of an overdamped or an underdamped bath. This establishes a versatile model which can be used to simulate a broad range of scenarios, dependent on where the boundary between the system and the bath is defined and the amount of damping. The differences in location of the vibrational mode relative to the system-bath boundary for the undamped, overdamped and underdamped scenarios are shown in figure 3.1.1.

Let us first consider the scenario where the electronic degrees of freedom of the system are coupled to a single vibrational mode which is evolved in the absence of a bath; figure 3.1.1 (a). Acknowledging that spectral lineshape is dominated by the rapid dephasing interaction rather than slower dissipative electronic/vibrational relaxation, in this case the system is undamped, such that the macroscopic polarization decays very slowly over a period of nanoseconds as the electronic excited state relaxes. The corresponding linear absorption spectrum shows a vibronic progression of sharp Lorentzian peaks, with width limited by the lifetime of the electronic excited state. The vibronic progression is produced in accordance with the Franck-Condon principle, where the nuclear degrees of freedom are unchanged during electronic transitions, such that the ground state wavefunction undergoes a *vertical* transition with respect to Q_j, onto the displaced excited state.[202,235] The intensity of each transition is determined by the overlap of the ground and excited state wavefunctions, described by the Franck-Condon factors introduced in section 2.2.1.1.[236]

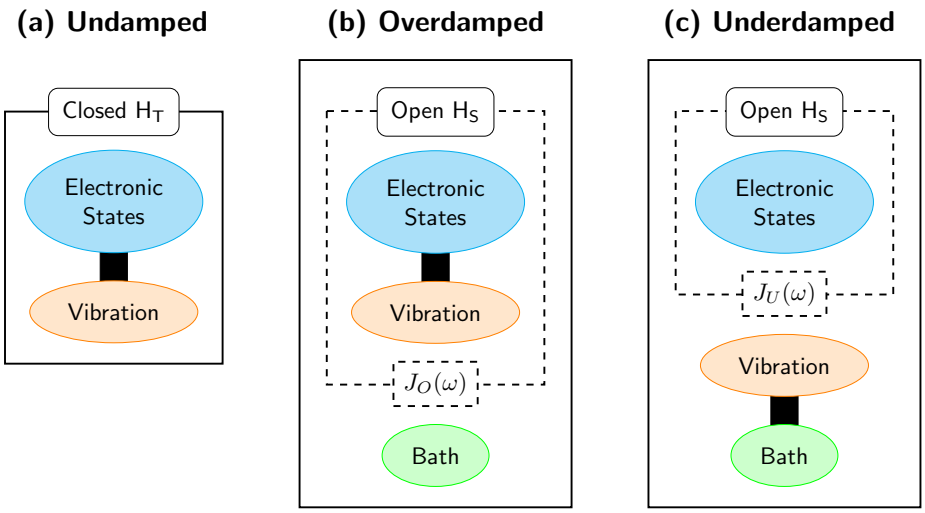

Figure 3.1.1: The limits of damping in terms of the system-bath boundary. In (a) the absence of any bath interaction defines a closed system which is undamped. In (b), the vibrational levels are defined within the system Hamiltonian, which is coupled to an overdamped bath with a Lorentz-Drude spectral density as an open quantum system. In (c), a canonical transformation moves the vibrational mode into the bath degrees of freedom such that the system Hamiltonian contains the electronic states only, with the bath interaction modelled as an underdamped Brownian Oscillator.

On addition of an overdamped bath for electronic dephasing, figure 3.1.1 (b), the macroscopic polarization decays much more rapidly over a few hundred femtoseconds and the peaks are significantly broadened. In this case, the broadening is applied to each vibronic peak, with the correlation time of the bath dictating the lineshape, as discussed in section 3.2. Alternatively, the system-bath boundary can be shifted using a canonical transformation to subsume the vibrational mode into the bath degrees of freedom, leaving the electronic states coupled to a bath in the form of an underdamped Brownian oscillator, introduced in section 2.2.2.3; figure 3.1.1 (c). In this case, the vibrational levels are no longer included in the system Hamiltonian and the external laser field can only induce purely electronic transitions. However, a vibronic progression may still emerge in the linear absorption spectrum due to the oscillations in the system-bath correlation function caused by strong coupling to the underdamped mode. As discussed in section 2.2.2.3, the underdamped Brownian oscillator approach is versatile as increasing the damping returns the spectral density to the Lorentz-Drude overdamped form, leaving the electronic states of the system coupled to a single overdamped bath. This presents a variety of options for modelling a system strongly coupled to a vibrational mode. More complex scenarios can also be conceived, where the electronic states of the system are coupled to multiple vibrational modes, each

potentially damped by a different overdamped bath, or where some or all are defined as underdamped modes.[155,159]

Figure 3.1.2 shows a comparison of the linear absorption spectra for a system where the vibrational degrees of freedom for a single strongly coupled mode are included in the system Hamiltonian in (a) and in the bath degrees of freedom in (b). For figure 3.1.2 (a), the system Hamiltonian is defined as a vibronic monomer, eq. 2.2.1, with the electronic transition frequency $\tilde{\omega}_{eg}^{0} = 15\,000\,\mathrm{cm}^{-1}$, mode frequency $\tilde{\omega}_0 = 600\,\mathrm{cm}^{-1}$ and dimensionless excited state displacement $\Delta_0 = 1$ such that $\tilde{\lambda}_0 = 300\,\mathrm{cm}^{-1}$. Note that throughout this thesis the tilde is used to indicate conversion to wavenumbers, equivalent to multiplication by $(2\pi c)^{-1}$ for angular frequencies or c^{-1} for linear frequencies. The number of vibrational levels included in the Hamiltonian is truncated at $\nu_0 = 5$, where ν_0 is the vibrational quantum number for the 0th mode. This gives a Huang-Rhys factor sufficiently small that the most intense peak corresponds to the fundamental transition frequency, with a clear vibronic progression of peaks at higher energy, separated by the mode frequency. Weak peaks at lower energy than the fundamental transition indicate hot bands resulting from a small vibrationally excited population in the ground electronic state. Each peak is broadened due to coupling to an overdamped bath through the dephasing operator $\mathsf{B}_{1,\mathrm{M}}$, eq. 2.2.41, with bath reorganisation energy $\tilde{\eta}_1 = 20\,\mathrm{cm}^{-1}$ and dephasing rate $\tilde{\Lambda}_1 = 40\,\mathrm{cm}^{-1}$ at $298\,\mathrm{K}$. The Markovian limit is set at $\tilde{\xi} = 1000\,\mathrm{cm}^{-1}$ such that there are 51 ADOs in the overdamped hierarchy.

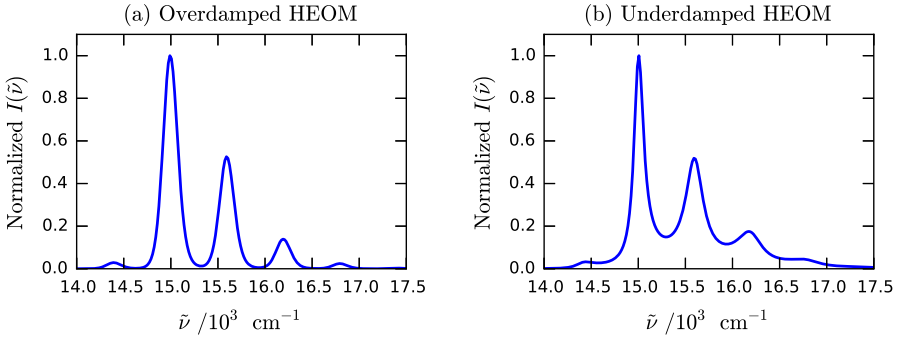

Figure 3.1.2: Linear absorption spectra for a two-level-system coupled to a vibration (a) within the system degrees of freedom broadened by an overdamped bath and (b) within the bath degrees of freedom as an underdamped Brownian oscillator.

For figure 3.1.2 (b), the system is defined in terms of the electronic states only, as a two-level-system (TLS) with a ground, $|g\rangle$, and an excited state, $|e\rangle$, and the Hamiltonian,

$$\mathsf{H}_{\mathrm{S}} = -\frac{\hbar\omega_{eg}}{2}\sigma_z, \tag{3.1.1}$$

where ω_{eg} is the same as in figure 3.1.2 (a). The bath is defined as an underdamped Brownian oscillator with an equivalent coupling operator to

figure 3.1.2 (a) of $\mathsf{B}_1 = |e\rangle\langle e|$ and the same mode frequency, $\tilde{\omega}_{0,1} = 600\,\mathrm{cm}^{-1}$, but with $\tilde{\eta}_1 = 500\,\mathrm{cm}^{-1}$ and $\gamma_1 = 100\,\mathrm{cm}^{-1}$ at $298\,\mathrm{K}$. The same Markovian limit as in figure 3.1.2 (a) results in an underdamped hierarchy containing 482 ADOs, where the increase in the number of ADOs significantly increases computation time. Both spectra are calculated with correlated initial conditions, as detailed in section 2.4.2, where the dipole moment is $\hat{\mu}_{\mathrm{M}}$, from eq. 2.2.60, in figure 3.1.2 (a) and $\hat{\mu} = \boldsymbol{\mu}_{eg}\sigma_x$ for figure 3.1.2 (b), with magnitude $\mu_{eg} = 11\,\mathrm{D}$. Despite the vibrational mode being incorporated into the bath degrees of freedom, figure 3.1.2 (b) shows a similar vibronic progression to figure 3.1.2 (a), with the broadening of the peaks now determined directly by the damping parameter γ_1. Notice that in order to achieve similar intensity for the vibronic progression in figure 3.1.2 (b) as in figure 3.1.2 (a) the reorganisation energy η_1 was increased from λ_0. This emphasises how in figure 3.1.2 (a) the undamped vibronic progression of the system mode is broadened by the bath, but in figure 3.1.2 (b) the vibronic progression emerges from the bath motion, in competition with the damping.

The corresponding absorptive 2D spectra for these scenarios are presented in figure 3.1.3, shown for population times of $T = 0, 80$ and $200\,\mathrm{fs}$, calculated from the response function in the impulsive limit, as in section 2.4.3.1. The spectra in both figure 3.1.3 (a) and (b) clearly show a series of peaks separated by the mode frequency, which modulate in intensity for increasing population time, caused by coupling to the vibrational mode. This again shows how vibronic peaks are equally produced with the vibration in the bath or the system degrees of freedom. However, there is a striking difference in the lineshapes in figure 3.1.3 (a) compared with figure 3.1.3 (b), highlighting the fundamental differences between these approaches, which are less obvious in the linear spectra. In figure 3.1.3 (a), the peaks have an elongation about the diagonal at early times, which diminishes as the population time increases, demonstrating a decaying correlation between excitation and emission frequencies corresponding to inhomogeneous broadening. Whereas in figure 3.1.3 (b), every peak is a 2D Lorentzian, showing no correlation between the excitation and emission frequencies. This relates to differences in the flow of information between the system and bath within the different damping limits, which is discussed in section 3.3. Note that the negative regions of these spectra are due to the unequal intensities of the rephasing and non-rephasing components, as discussed in section 2.4.3.3, and the number of contours used. The monomer systems described in this chapter are incapable of excited state absorption pathways. A discussion of the origins of peaks in 2D spectra is left for the analysis presented in chapter 4.

For more complex systems such as vibronic dimers, the increase in computational demand for propagation of an underdamped hierarchy, due to

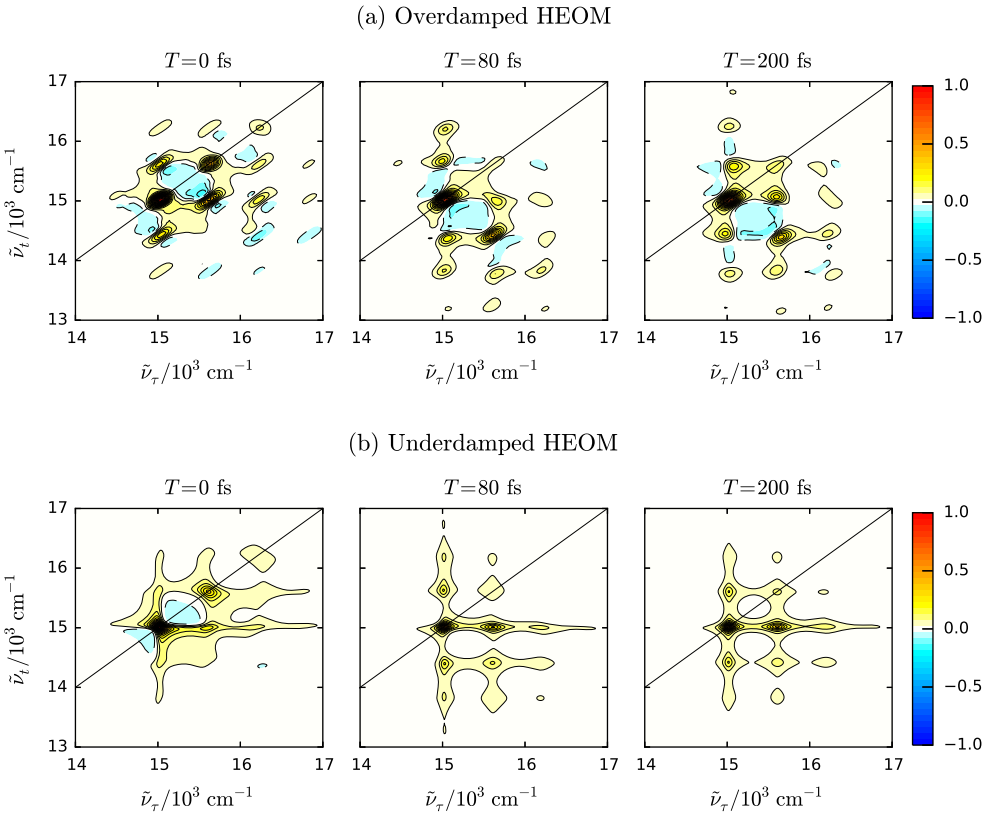

Figure 3.1.3: Absorptive 2D spectra for a two-level-system coupled to a vibration (a) within the system degrees of freedom broadened by an overdamped bath and (b) within the bath degrees of freedom as an underdamped Brownian oscillator.

the increase in the number of ADOs, can be offset by the reduction in the dimensions of the quantum system on transferring the vibrational degrees of freedom into the bath. Similarly, issues concerning truncation of the number of vibrational levels accounted for within the system Hamiltonian are avoided. However, an accurate analysis of the vibronic eigenstates of molecular aggregates requires the vibrational degrees of freedom to be included in the system Hamiltonian.[111] The vibronic dimer models in chapter 5 therefore employ the approach where the vibrational levels are included within the system Hamiltonian, with spectral broadening resulting from coupling to an overdamped bath.

3.2 Limits of the Lineshape

In order to better understand the implications of including the vibration within the system vs. the bath, let us limit the system Hamiltonian to the electronic degrees of freedom only in both cases and compare the lineshape under different bath conditions. The linear absorption spectra for the TLS defined in

section 3.1 coupled to an underdamped Brownian oscillator of frequency ω_0 with fixed reorganisation energy, but varied damping strength and temperature are shown in figure 3.2.1, where $\mathsf{B} = |e\rangle\langle e|$, $\tilde{\xi} = 2000\,\mathrm{cm}^{-1}$ and all other parameters are as labelled. Here, the subscript $n = 1$ is neglected from all bath parameters as the system is coupled to a single bath for electronic dephasing. As in figure 3.1.2 (b), this shows a clear vibronic progression, where increasing the damping strength, γ, decreases the intensity and broadens the peaks. Stronger damping increases the rate of dephasing, producing a greater range of transition frequencies present within the ensemble, broadening the peaks. Similarly, decreasing the temperature increases the intensity and narrows the peaks as the bath motion slows and the range of transition frequencies decreases. Note that, here, a mode frequency of $\tilde{\omega}_0 = 600\,\mathrm{cm}^{-1}$ was used to ensure all cases were formally underdamped, with $\gamma \ll \omega_0$, as discussed in section 2.3.2.2, and how this results in each peak maintaining a Lorentzian shape throughout this range of conditions.

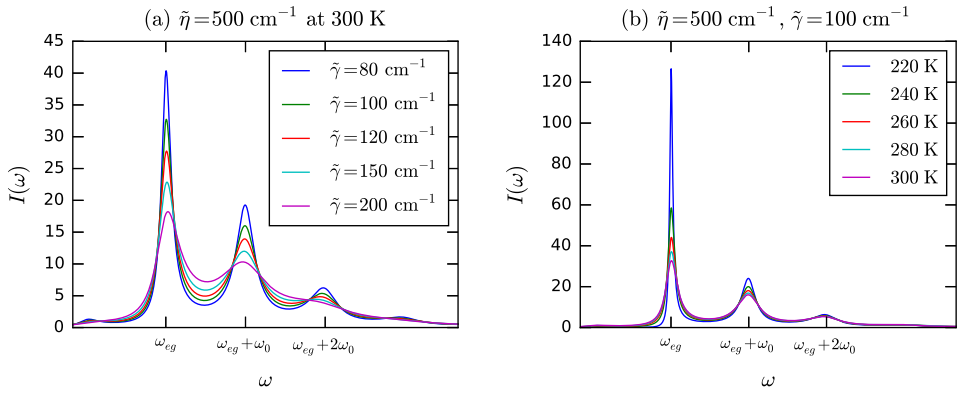

Figure 3.2.1: Linear absorption spectra for a two-level-system coupled to an underdamped Brownian oscillator with $\tilde{\omega}_0 = 600\,\mathrm{cm}^{-1}$ and fixed reorganisation energy, varying (a) γ and (b) temperature.

For an overdamped bath, changing the rate of dephasing, Λ, produces two additional limits, identified by the dimensionless parameter $\Delta\tau_c$.[26] As introduced in section 2.2.2.3, for an overdamped spectral density, the reorganisation energy and temperature are related to the fluctuation amplitude, Δ, via,

$$\eta = \frac{\hbar\Delta^2}{2k_\mathrm{B}T}, \qquad \text{(2.2.50 revisited)}$$

where Δ is a measure of the range of transition frequencies across the ensemble due to the stochastic bath interactions. The time taken for the bath to return to equilibrium after perturbation is defined as the correlation time, $\tau_c = \Lambda^{-1}$, the inverse of the dephasing rate. Figure 3.2.2 shows the linear absorption spectra for an equivalent TLS coupled to a single overdamped bath with parameters as labelled plus $\mathsf{B} = |e\rangle\langle e| - |g\rangle\langle g| = -\sigma_z$ and $\tilde{\Lambda} = 870, 183, 91, 18.25, 9.13\,\mathrm{cm}^{-1}$ such that $\Delta\tau_c = 0.1, 0.5, 1, 5, 10$, respectively, with $\tilde{\xi} = 2000\,\mathrm{cm}^{-1}$. For fast

correlation times compared with the fluctuation amplitude, the *homogeneous limit* emerges, identified by $\Delta\tau_c \ll 1$. Here, the almost instantaneous return of the bath to equilibrium, compared with the slower timescale of system relaxation, produces an identical system-bath interaction across the ensemble, resulting in an averaging which corresponds to the motional narrowing limit.[149] In the homogeneous limit, the linear absorption spectrum shows a sharp Lorentzian peak at the electronic transition frequency, as in figure 3.2.2 (a), for $\Delta\tau_c = 0.1$. At the other extreme, where $\Delta\tau_c \gg 1$ and the correlation times are much longer compared with the fluctuation amplitude, the slow return to equilibrium of the bath allows the full distribution of transition frequencies in the ensemble to be sampled, producing a Gaussian lineshape associated with the *inhomogeneous limit*. Figure 3.2.2 (a) shows the transition from a Lorentzian to a Gaussian lineshape as $\Delta\tau_c$ increases, where the maximum of the Gaussian peak in the inhomogeneous limit is also blue-shifted from the electronic transition frequency due to the Stokes shift.[1,137] Figure 3.2.2 (b) also shows that decreasing the temperature results in a narrower Gaussian lineshape for an inhomogeneously broadened peak with $\Delta\tau_c = 5$, related to the decrease in Δ from eq. 2.2.50.

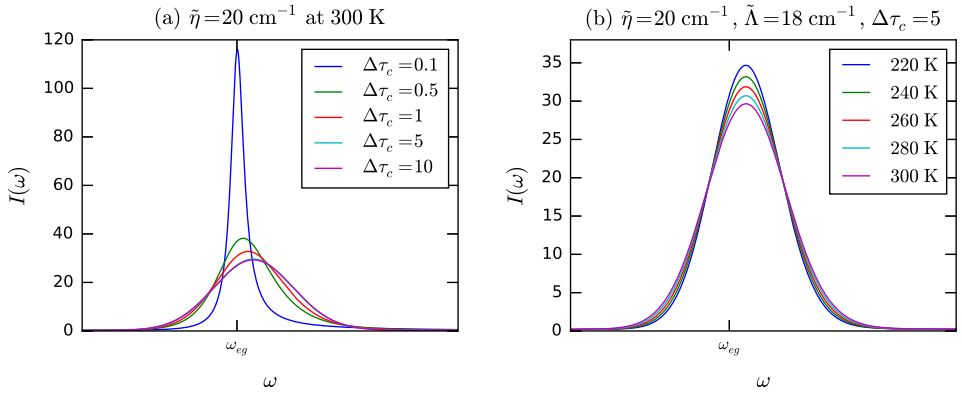

Figure 3.2.2: Linear absorption spectra for a two-level-system coupled to an overdamped bath with fixed reorganisation energy and varying (a) Λ and (b) temperature.

The homogeneous and inhomogeneous limits produce significant differences in the lineshape of 2D spectra, as shown in figure 3.2.3. As discussed in section 2.4.3.3, in the inhomogeneous limit, the slow decay of the system-bath correlation function yields a static distribution of transition frequencies which result in a revival of the polarization in rephasing pathways. This reinforces the rephasing signal such that the diagonal of the absorptive spectrum is elongated into a Gaussian by the sum of Lorentzian peaks, showing a correlation between the excitation and emission frequencies for the normal distribution of transition frequencies.[3,4] As the population time increases and the system-bath correlation function decays with lifetime, τ_c, these correlations are lost and the elongation

diminishes, resulting in a more symmetrical peak dominated by the anti-diagonal, homogeneous linewidth.[20,26,237] However, in the homogeneous limit, such as $\Delta\tau_c = 0.1$, motional narrowing creates a sharp 2D Lorentzian which does not change with population time. Therefore, the elongation of the peak for $\Delta\tau_c = 0.5$ at $T = 0\,\mathrm{fs}$ in figure 3.2.3 indicates a small amount of inhomogeneous broadening remains even for $\Delta\tau_c < 1$, though any correlations decay within $100\,\mathrm{fs}$. Again, the small negative regions at $T = 0\,\mathrm{fs}$ in figure 3.2.3 are a result of the much stronger rephasing signal being insufficiently cancelled by the weaker non-rephasing signal on summation at early population times.

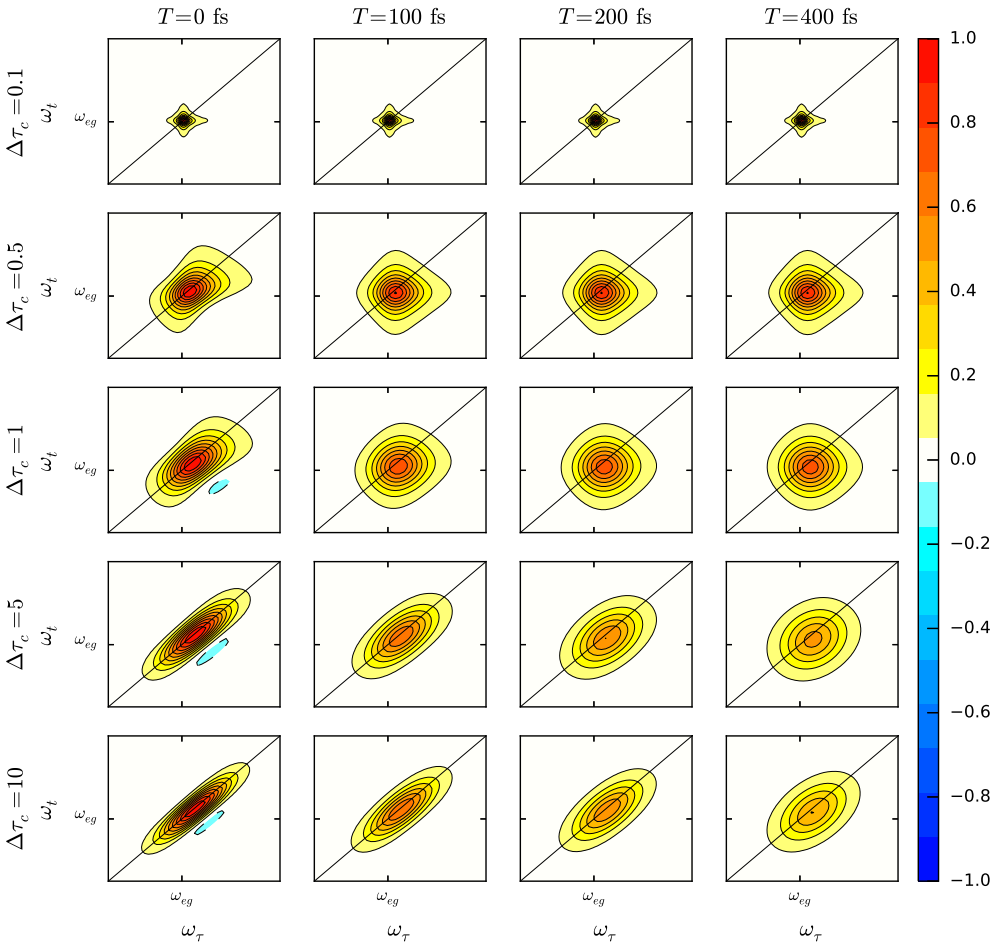

Figure 3.2.3: Absorptive 2D spectra for a two-level-system coupled to an overdamped bath for a range of $\Delta\tau_c$ up to $T = 400\,\mathrm{fs}$, each normalised to their respective maxima at $T = 0\,\mathrm{fs}$.

The loss of the inhomogeneous elongation corresponds to the process of *spectral diffusion*, which describes the decay of the system-bath correlation function, measured by the *ellipticity* of the peaks in the 2D spectra. The ellipticity, E, compares the width of a Gaussian fitted to the diagonal of the peak, ς_D, with that of the anti-diagonal, ς_A and is an exact measure of the

system-bath correlation function,[23,234,238]

$$E = \frac{\varsigma_{\mathrm{D}}^2 - \varsigma_{\mathrm{A}}^2}{\varsigma_{\mathrm{D}}^2 + \varsigma_{\mathrm{A}}^2}. \tag{3.2.1}$$

Figure 3.2.4 shows the ellipticity of the 2D spectra in figure 3.2.3, excluding those in the homogeneous limit of $\Delta\tau_c = 0.1$. This clearly demonstrates the exponential decay in the correlation function for an overdamped bath, expected from the stochastic theory in eq. 2.2.52, where decreasing the correlation time, reducing $\Delta\tau_c$, results in a more rapid decay of the correlation function.

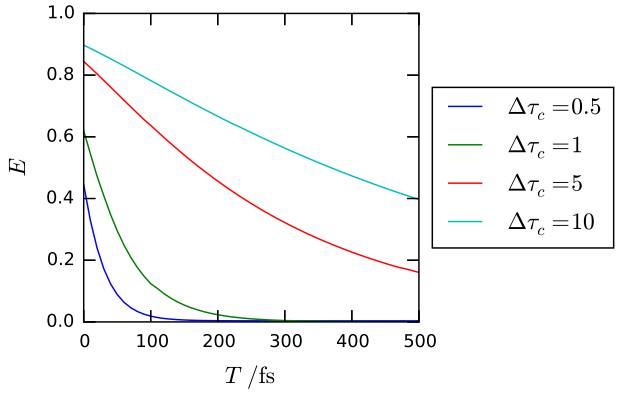

Figure 3.2.4: Ellipticity of the overdamped 2D spectra in figure 3.2.3, excluding $\Delta\tau_c = 0.1$, for $T = 0 - 500\,\mathrm{fs}$, sampled at $10\,\mathrm{fs}$ intervals.

To further investigate the origins of inhomogeneous broadening, linear absorption spectra for the TLS coupled to an overdamped bath with $\Delta\tau_c = 1.0$ were also calculated using the HEOM for an arbitrary spectral density (ASD-HEOM) presented in section 2.3.2.3, under identical conditions as that of figure 3.2.2 (a). Due to the significant increase in computational complexity, spectra were only calculated for the first and second layers, presented in figure 3.2.5. Interestingly, figure 3.2.5 shows a splitting pattern in the spectra, where the first layer produces a doublet and the second layer, a triplet, in stark contrast to the almost Gaussian profile of $\Delta\tau_c = 1.0$ in figure 3.2.2 (a). In the absence of any vibrational modes within the system Hamiltonian, this splitting must result from the bath interaction. Recalling that each layer represents the interaction of a number of phonons with the system, these spectra suggest that each additional phonon would further split the peak, such that a sufficiently large number of layers would reproduce the smooth profile in figure 3.2.2 (a). This suggests that realistic spectra could be produced using the ASD-HEOM, if the number of layers was dramatically increased. But, in the knowledge that the HEOM spectra of figure 3.2.2 are produced with Matsubara axes that typically extend to a depth greater than $j_{1k} = 10$, this is currently infeasible. However, these spectra demonstrate that implementation of the ASD-HEOM has significant potential if it can be scaled up appropriately and, importantly, that inhomogeneous

broadening is intrinsically linked to the number of phonon interactions between the system and the bath. This implies that non-Markovian effects have a crucial role in determining spectral lineshape.

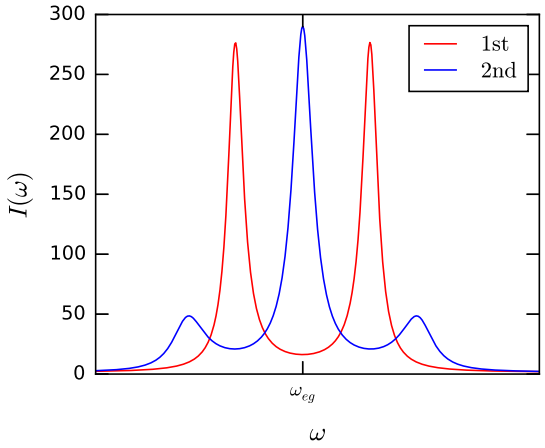

Figure 3.2.5: Linear absorption spectrum for a two-level-system coupled to an overdamped bath with $\Delta\tau_c = 1.0$, calculated using the ASD-HEOM terminated at the first (1st) and second (2nd) layers.

3.3 Quantifying Non-Markovianity and Its Effect on Spectral Lineshape

To investigate the extent to which non-Markovianity influences spectral lineshape, the BLP measure, as defined in section 2.1.3, is applied to a set of bath conditions that span the underdamped and overdamped limits. The results are then compared with the linear and 2DES lineshape calculated under the same conditions to identify trends which link spectral features with the underlying non-Markovian effects. Here, the system Hamiltonian is again restricted to the electronic degrees of freedom only as a TLS in eq. 3.1.1, where $\tilde{\omega}_{eg} = 3000\,\mathrm{cm}^{-1}$ and the dipole moment operator $\hat{\mu} = \sigma_x$. A single vibrational mode of frequency $\tilde{\omega}_0 = 500\,\mathrm{cm}^{-1}$ is transformed into the bath degrees of freedom such that the system is coupled to an underdamped Brownian oscillator when $\gamma \ll \omega_0$, propagated using the HEOM in eq. 2.3.31, or a single overdamped bath when the damping is increased such that $\gamma \gg \omega_0$, propagated using the HEOM in eq. 2.3.18. The system couples to the bath through the operator,

$$\mathsf{B} = \sigma_x - \frac{\sigma_z}{2}, \tag{3.3.1}$$

accounting for both dephasing, σ_z, and dissipation, σ_x processes.[26,156,164] Again the subscript $n = 1$ is neglected from the bath parameters in this section as the system is coupled to a single bath.

For this investigation, the reorganisation energy of the bath is fixed at $\tilde{\eta} = 20\,\mathrm{cm}^{-1}$, such that $\tilde{\Delta} = 91.33\,\mathrm{cm}^{-1}$ at $300\,\mathrm{K}$, resulting in a Huang-Rhys factor of $S = \eta/\omega_0 = 0.04$ and a very small excited state displacement. The range of damping strengths used are presented in table 3.1, along with their respective dissipation rates, Λ, correlation times, τ_c, and $\Delta\tau_c$ values for the overdamped baths. These values were selected so that both underdamped and overdamped baths, including the homogeneous and inhomogeneous limits, are accessed by changing the damping strength alone. Increasing the strength of the damping slows the system-bath interactions, increasing the correlation time and decreasing the rate of dissipation. On increasing γ in this way, the environment transitions from the underdamped, to the homogeneous overdamped and finally to the inhomogeneous overdamped limits, as shown in table 3.1.

$\tilde{\gamma}\,/\mathrm{cm}^{-1}$	$\Lambda(2\pi)^{-1}\,/\mathrm{fs}^{-1}$	$\tau_c\,/\mathrm{fs}$	$\Delta\tau_c$
50	0.150	7	-
300	0.025	40	-
1750	0.004	234	0.64
2750	0.003	367	1.00
8200	0.001	1094	3.00

Table 3.1: Damping strengths, dissipation rates and correlation times used, for $\tilde{\eta} = 20\,\mathrm{cm}^{-1}$ such that $\tilde{\Delta} = 91.33\,\mathrm{cm}^{-1}$ at $300\,\mathrm{K}$. $\Delta\tau_c$ given for overdamped environments only. Reprinted from reference 194, with the permission of AIP Publishing.

The degree of non-Markovianity, $\mathcal{N}$, is calculated for each damping strength by comparing the dynamics of the system with and without excitation due to a single Gaussian laser pulse. The reduced density operator of the system is initialised in the ground electronic state,

$$\rho(t=0) = |g\rangle\langle g| = \begin{pmatrix} 1 & 0 \\ 0 & 0 \end{pmatrix}, \tag{3.3.2}$$

and is then propagated for $2.05\,\mathrm{ps}$ to establish system-bath correlations, with the HEOM convergence parameter set sufficiently large at $\tilde{\xi} = 5000\,\mathrm{cm}^{-1}$. Using the semi-classical approximation for a real laser field as in section 2.2.3.1, the system-field interaction is added into the system Hamiltonian during the evolution, with the pulse centred at $\tau_m = 2\,\mathrm{ps}$. After the field envelope returns to zero and the pulse has ended, the ADOs are propagated for an additional $2\,\mathrm{ps}$, producing the states used in the trace distance calculations. Identical laser pulses are used for all bath conditions, set resonant with the transition frequency of the system, ω_{eg}, with $\chi = 10^3\,\mathrm{V\,m}^{-1}$. Simulations with identical bath conditions but different laser FWHM produce the two series of states for which the trace distance are calculated, where ρ_1 corresponds to no excitation, with a FWHM of $0\,\mathrm{fs}$, and ρ_2 involves a significant excited population, resulting from a FWHM of $20\,\mathrm{fs}$.

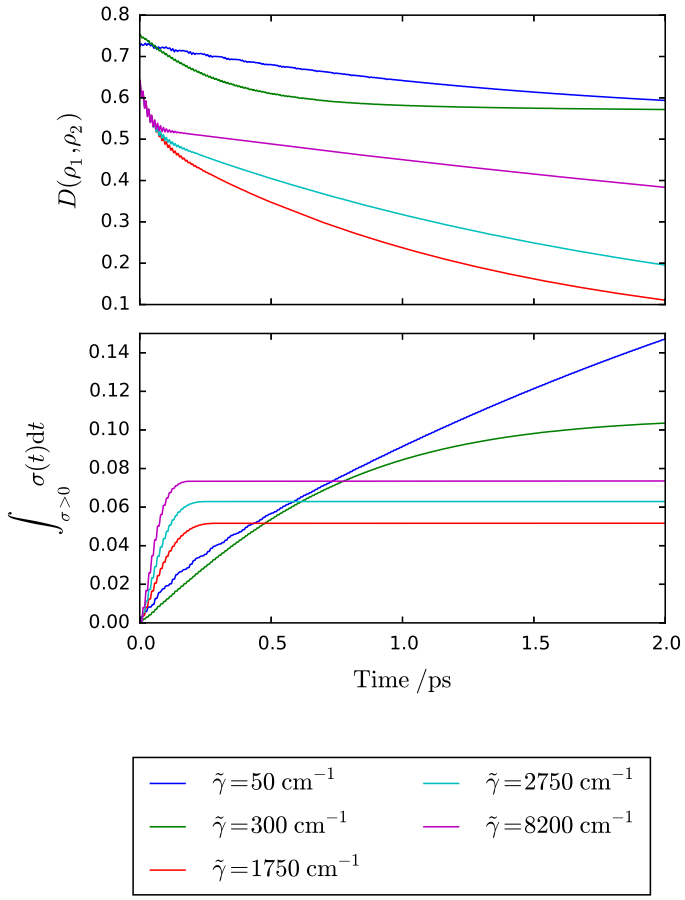

Figure 3.3.1: (Top) Trace distance, $D(\rho_1, \rho_2)$, and (bottom) cumulative integration of the positive flux, with maximum equal to $\mathcal{N}$, for each of the damping strengths in table 3.1. Reprinted from reference 194, with the permission of AIP Publishing.

Figure 3.3.1 (top) shows the trace distance, $D(\rho_1, \rho_2)$, for the range of damping strengths presented in table 3.1, where figure 3.3.1 (bottom) is the cumulative integration of the positive flux, with maximum equal to $\mathcal{N}$, eq. 2.1.24. Emulating figure 2.1.2, as the excited population of ρ_2 dissipates energy to the bath and the ground state population increases, ρ_1 and ρ_2 become less distinguishable and the trace distance decreases. This produces the overall negative gradient observed for $D(\rho_1, \rho_2)$ in figure 3.3.1 (top), but the decaying oscillations also identify a period of non-Markovian feedback in each case. Figure 3.3.2 shows the positive flux, $\sigma > 0$, of the trace distance for each damping strength. As discussed in section 2.1.3, positive flux corresponds to the non-Markovian return of information from the bath to the system, which is integrated to obtain $\mathcal{N}$.

Figures 3.3.1 and 3.3.2 show that the slower decrease in the trace distance for the underdamped baths of $\tilde{\gamma} = 50\,\mathrm{cm}^{-1}$ and $\tilde{\gamma} = 300\,\mathrm{cm}^{-1}$ is accompanied by small, but long-lived oscillations which provide a prolonged feedback of information from the bath to the system. As the integrated flux for $\tilde{\gamma} = 300\,\mathrm{cm}^{-1}$ in figure 3.3.1 (bottom) approaches a plateau within $2\,\mathrm{ps}$, whilst that of

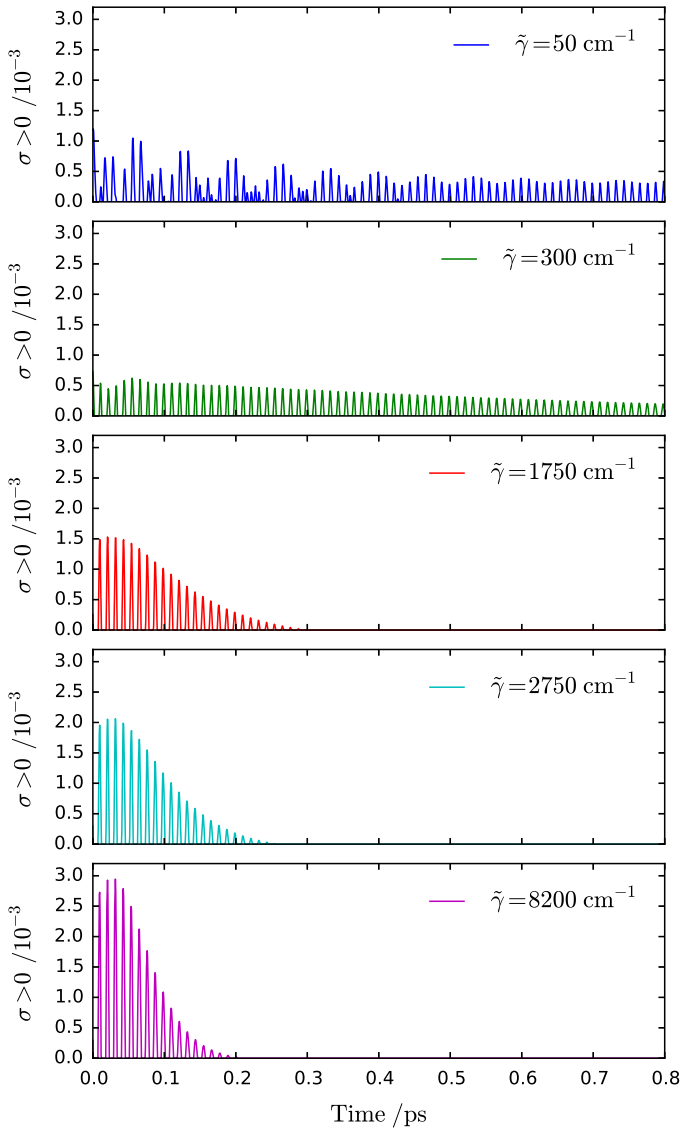

Figure 3.3.2: Postive flux of the trace distance shown in figure 3.3.1, for each of the damping strengths in table 3.1. Reprinted from reference 194, with the permission of AIP Publishing.

$\tilde{\gamma} = 50\,\mathrm{cm}^{-1}$ is still increasing, these results suggest that the maximum measurable non-Markovianity for underdamped baths is obtained gradually over several picoseconds, where increasing the damping strength decreases $\mathcal{N}$. For the weakest damping, $\tilde{\gamma} = 50\,\mathrm{cm}^{-1}$, figure 3.3.2 shows the underdamped oscillations superimposed in the positive flux. However, on increasing the damping to the overdamped limit, the oscillations in the trace distance are much larger and rapidly decay within the first few hundred femtoseconds. This describes an immediate feedback of information from the bath to the system, followed by irreversible Markovian transfer from the system to the bath. This is consistent with the rapid reorganisation of solvent molecules upon excitation of the solute, followed by relaxation of the excited state, which is the intended behaviour for an overdamped bath in these models. Furthermore, in contrast to

the underdamped baths, as the damping strength increases from $\tilde{\gamma} = 1750\,\mathrm{cm}^{-1}$ to $\tilde{\gamma} = 8200\,\mathrm{cm}^{-1}$, the measured non-Markovianity $\mathcal{N}$ also increases, achieving a plateau in the integrated flux in a shorter time. This suggests the inhomogeneous overdamped bath with $\tilde{\gamma} = 8200\,\mathrm{cm}^{-1}$ is associated with much greater non-Markovian feedback than the homogeneous overdamped bath with $\tilde{\gamma} = 1750\,\mathrm{cm}^{-1}$.

Figure 3.3.1 displays two major trends. Firstly, increasing the damping strength results in the maximum non-Markovianity being obtained in a shorter time. This is seen in figure 3.3.2 by the more rapid decay of positive information flux for the overdamped baths with greater damping strength. Secondly, that the magnitude of maximum non-Markovianity, $\mathcal{N}$, displays a more complex trend. Figure 3.3.1 shows that $\mathcal{N}$ is largest in the underdamped limit due to prolonged recurrence of information from the bath back into the system. Increasing the damping then leads to a decrease in $\mathcal{N}$ whilst the bath remains in the underdamped limit. But, interestingly, once the damping is increased such that the bath is overdamped, figure 3.3.1 shows that $\mathcal{N}$ increases as the damping, and thus $\Delta\tau_c$, increases, demonstrating greater non-Markovian feedback in inhomogeneous compared with homogeneous baths. This reveals the importance of non-Markovian effects in slow, inhomogeneous environments, but also suggests that even greater non-Markovian effects are involved in underdamped environments, where the total contribution requires significantly longer to develop. The measured values of $\mathcal{N}$ after $2\,\mathrm{ps}$ are presented in table 3.2.

$\tilde{\gamma}\,/\mathrm{cm}^{-1}$	$\Delta\tau_c$	$\mathcal{N}$	FWHM $(\pm 1)\,/\mathrm{cm}^{-1}$
50	-	0.147	4
300	-	0.104	19
1750	0.64	0.052	110
2750	1.00	0.063	144
8200	3.00	0.074	196

Table 3.2: Measured $\mathcal{N}$ and linear absorption spectrum FWHM for each damping strength in table 3.1, where $\tilde{\eta} = 20\,\mathrm{cm}^{-1}$, such that $\tilde{\Delta} = 91.33\,\mathrm{cm}^{-1}$ at $300\,\mathrm{K}$ for all cases. $\Delta\tau_c$ given for overdamped environments only. Reprinted from reference 194, with the permission of AIP Publishing.

These trends in the measurable non-Markovianity are directly related to the spectral lineshape in linear and 2D spectroscopy. Linear and 2D spectra for each of the damping strengths in table 3.1 were calculated from the molecular response function in the impulsive limit, with correlated initial conditions, as described in section 2.4. The linear absorption spectra are presented in figure 3.3.3. The $\tilde{\gamma} = 50\,\mathrm{cm}^{-1}$ underdamped bath shows a sharp peak at the fundamental transition frequency, $\tilde{\omega}_{eg}$, with a vibronic peak at $\tilde{\omega}_{eg} + \tilde{\omega}_0$, which is significantly less intense due to the small Huang-Rhys factor of $S = 0.04$. On

increasing the damping to $\tilde{\gamma} = 300\,\mathrm{cm}^{-1}$, the fundamental peak broadens with a substantial loss of intensity and the vibronic peak vanishes.

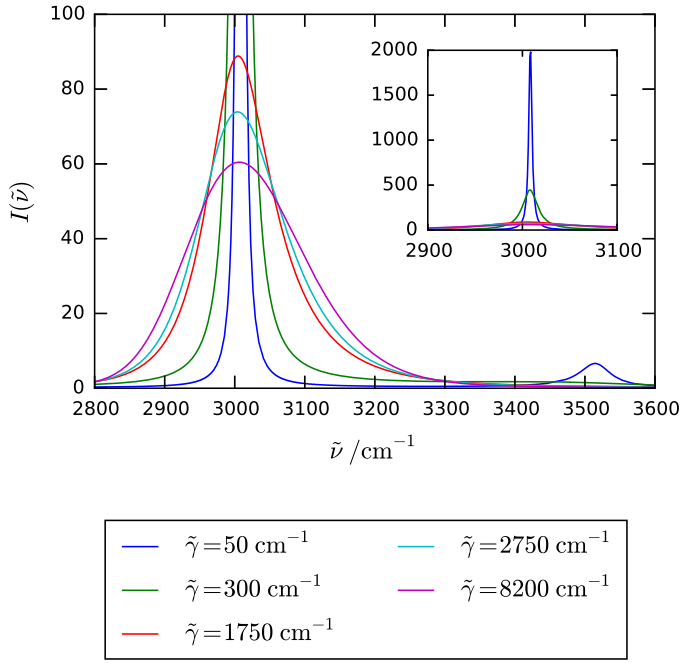

Figure 3.3.3: Calculated linear absorption spectra for each of the damping strengths in table 3.1. Reprinted from reference 194, with the permission of AIP Publishing.

The appearance of the vibronic peak is related to the prolonged non-Markovian feedback for underdamped baths, shown by the long-lived oscillations in the trace distance in figure 3.3.1. As the vibrational mode has been formally subsumed within the bath degrees of freedom through the canonical transformation, the appearance of the vibronic peak indicates that the prolonged, reversible transfer of information between the system and the bath, facilitated by weak damping, enables spectroscopy to probe the bath modes as well as the system. Therefore, as the damping increases and the feedback of information is reduced, the vibronic peak becomes less intense, until it is ultimately removed from the spectrum.

As the damping increases and the bath becomes overdamped, the intensity of the fundamental peak decreases further and the peak broadens from the homogeneous to the inhomogeneous limits. The FWHM of the fundamental peak for each damping strength is also listed in table 3.2. In the high temperature limit, $k_{\mathrm{B}}T \gg \hbar\Lambda$, applicable to each of the overdamped baths defined in this section, the absorption spectrum for a homogeneous bath, $\Delta\tau_c \ll 1$, has the Lorentzian profile,

$$I(\omega) = \frac{\Gamma}{(\omega - \omega_{eg})^2 + \Gamma^2}, \tag{3.3.3}$$

with FWHM of $2\Gamma = 2\Delta^2\tau_c$.[1,137] For $\tilde{\gamma} = 1750\,\mathrm{cm}^{-1}$ with $\Delta\tau_c = 0.64$, this

predicts a FWHM of $116\,\mathrm{cm}^{-1}$, which agrees with the measured FWHM in table 3.2, where the difference suggests that $\Delta\tau_c$ is too large in this case to fit the ideal homogeneous lineshape. Equally, an inhomogeneous bath, $\Delta\tau_c \gg 1$, produces an absorption spectrum with the Gaussian profile,

$$I(\omega) = (2\pi\Delta^2)^{-\frac{1}{2}} \exp\left[-\frac{(\omega-\omega_{eg})^2}{2\Delta^2}\right], \tag{3.3.4}$$

with FWHM of $2\sqrt{2\ln 2}\Delta$, directly proportional to the fluctuation amplitude.[1,137,239] The measured FWHM for the inhomogeneous $\tilde{\gamma} = 8200\,\mathrm{cm}^{-1}$ with $\Delta\tau_c = 3.00$ demonstrates progress towards this limit of $215\,\mathrm{cm}^{-1}$.

As mentioned previously, in the inhomogeneous limit, long correlation times cause the bath motion to be effectively static with respect to the timescale of system relaxation, such that the Gaussian profile of the linear absorption spectrum resembles the normal distribution of transition frequencies present across the ensemble due to the stochastic bath interactions. With all localised inhomogeneities contributing to the lineshape, this suggests that maximum knowledge of the bath degrees of freedom is obtained. In contrast, the short correlation times of the homogeneous limit result in identical interactions of the system and bath across the ensemble, leading to an averaging which loses this detail and produces the motional narrowing limit.[149] This agrees with the trends observed for the overdamped baths in figures 3.3.1 and 3.3.2, where $\mathcal{N}$ is larger and obtained within a shorter time for inhomogeneous baths. In the inhomogeneous limit, maximum information of the bath is returned to the system almost instantaneously due to its slow variation. As the correlation time of the bath decreases towards the homogeneous limit, more rapid dissipation of any information transferred from the system to the bath presents less opportunity for non-Markovian feedback, decreasing the measurable non-Markovianity. This therefore causes the system-bath interaction to become increasingly indistinguishable across the ensemble, such that it is fully Markovian in the homogeneous limit, with a flat spectral density and a correlation function which is a delta function of time.[149] This explains the dip in $\mathcal{N}$ observed on increasing the damping strength in figure 3.3.1, as $\mathcal{N}$ decreases from the underdamped to the homogeneous overdamped limit and then increases again from the homogeneous to the inhomogeneous overdamped limits. In identifying measurable non-Markovianity even as the damping approaches the homogeneous limit, these results demonstrate the superiority of HEOM methods in correctly accounting for coloured spectral densities and the resulting non-Markovian effects.[152,156]

Figure 3.3.4 shows 2D spectra for population times of $T = 0 - 300\,\mathrm{fs}$ for the $\tilde{\gamma} = 300\,\mathrm{cm}^{-1}$ underdamped bath, identified as $\gamma < \omega_0$, and the three overdamped baths, labelled with their $\Delta\tau_c$ values. For the underdamped bath,

the spectrum at $T = 0\,\mathrm{fs}$ shows a very intense, narrow peak which does not change as the population time increases. The overdamped spectra are much weaker, with significant broadening and demonstrate spectral diffusion as discussed for figure 3.2.3. For $T = 0\,\mathrm{fs}$, on increasing the damping from the more homogeneous bath with $\Delta\tau_c = 0.64$ to the more inhomogeneous bath with of $\Delta\tau_c = 3.00$, the diagonal peak width increases and the intensity decreases, reproducing the Lorentzian to Gaussian broadening observed in the linear spectra of figure 3.3.3. However, as in figure 3.2.3, the elongated diagonal width compared with the homogeneous anti-diagonal width identifies a degree of inhomogeneous broadening even in the $\Delta\tau_c = 0.64$ case, which is absent from the underdamped spectra. Elongation about the diagonal is visible for $T < \tau_c$, following the decay of the system-bath correlation function. The correlation times for each damping strength are included in table 3.2, with the ellipticity of the three overdamped baths, as defined in eq. 3.2.1, presented in figure 3.3.5.

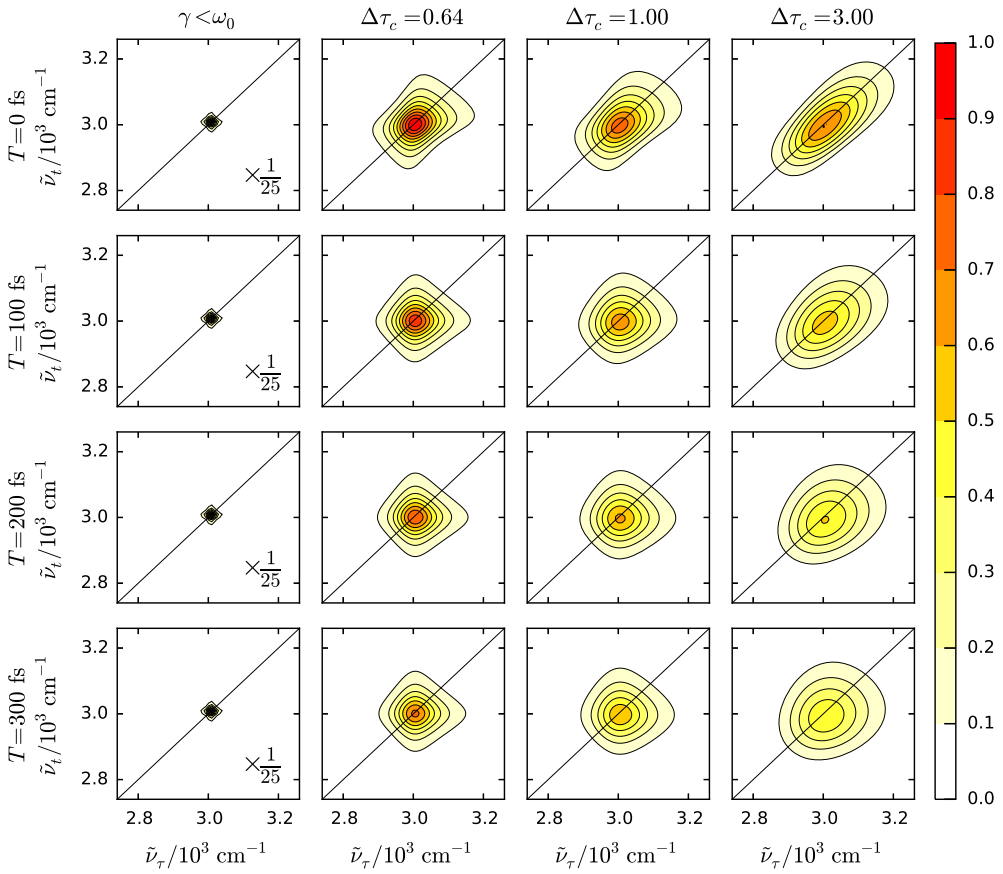

Figure 3.3.4: Absorptive 2D spectra for population times $T = 0 - 300\,\mathrm{fs}$ for the $\tilde{\gamma} = 300\,\mathrm{cm}^{-1}$ underdamped bath, labelled $\gamma < \omega_0$, and the three overdamped baths, identified by their $\Delta\tau_c$ values, as per table 3.1, normalised to the maximum of $\Delta\tau_c = 0.64$ at $T = 0\,\mathrm{fs}$. Reprinted from reference 194, with the permission of AIP Publishing.

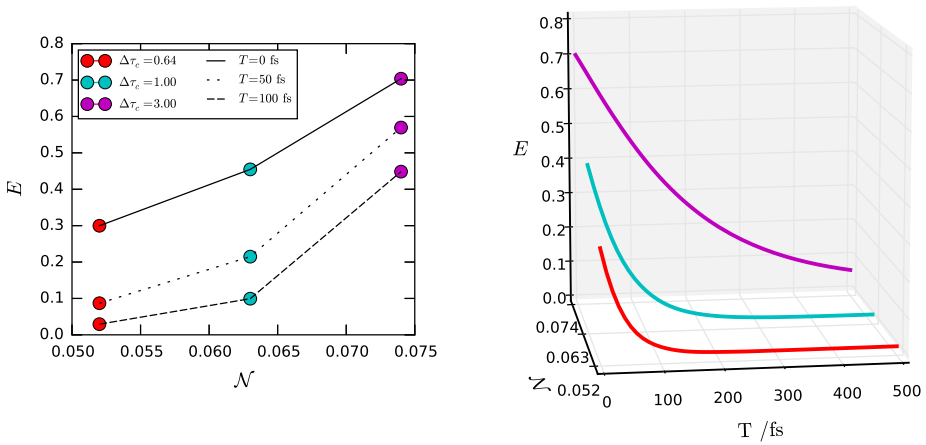

Figure 3.3.5: Ellipticity, E, of the absorptive 2D spectra against the measured non-Markovianity, $\mathcal{N}$, for the three overdamped baths, identified by their $\Delta\tau_c$ values, for (left) $T = 0, 50$ and $100\,\mathrm{fs}$ and (right) $T = 0 - 400\,\mathrm{fs}$, sampled at $10\,\mathrm{fs}$ intervals. Reprinted from reference 194, with the permission of AIP Publishing.

Figure 3.3.5 again shows an exponential decay in the ellipticity, but now demonstrates that the slower decay for the inhomogeneous baths is accompanied by an increase in the measurable non-Markovianity, $\mathcal{N}$. The short correlation time of the homogeneous bath with $\Delta\tau_c = 0.64$ produces the most rapid decay in ellipticity, such that in figure 3.3.4 any elongation of the 2D peak due to inhomogeneous broadening has depleted within $300\,\mathrm{fs}$, whilst the spectrum at this population time for the inhomogeneous bath with $\Delta\tau_c = 3.00$ remains slightly elongated due to the longer correlation time. Comparing the trends observed for $\mathcal{N}$ for the overdamped baths in figures 3.3.1 and 3.3.2 with the 2D spectra of figure 3.3.4 suggests that the 2D lineshape can be interpreted in an identical manner to the linear spectra. For inhomogeneous baths with long correlation times and slow diffusion, the increased non-Markovian feedback leads to significant elongation of the peak, representing the increased information obtained by the system from the bath regarding the Gaussian distribution of frequencies within the ensemble. Whereas, approaching the homogeneous limit, short correlation times and rapid dissipation reduce feedback from the bath to the system, limiting the elongation of peaks and causing swift diffusion. The greater initial elongation of the peak in the 2D spectrum, and thus larger E, at $T = 0\,\mathrm{fs}$ for $\Delta\tau_c = 3.00$ is therefore also related to the increased $\mathcal{N}$ for this bath compared with that of $\Delta\tau_c = 0.64$. Performing additional simulations where the parameters explore a greater range of damping strengths would further confirm these trends. However, numerical integration of the underdamped HEOM proved insufficiently stable to traverse the critical damping region between the underdamped and overdamped limits.

This is therefore left for future work, dependent on the development of improved dynamical methods.

To summarise, it has been shown that decreasing the damping strength for a Brownian oscillator of fixed mode frequency and reorganisation energy causes the maximum measurable non-Markovianity, $\mathcal{N}$, to be obtained more slowly, where this value is greatest for underdamped baths due to the non-monotonic, slowly decaying correlation function providing prolonged feedback from the bath to the system. Conversely, for overdamped baths, decreasing the damping strength from the inhomogeneous to the homogeneous limit leads to a decrease in $\mathcal{N}$, as a result of shorter correlation times increasing the rate of dissipation, such that the opportunity for non-Markovian feedback is reduced. This trend has then been correlated with the ellipticity of 2D spectra for equivalent overdamped baths such that an increase in $\mathcal{N}$ is directly related to increased inhomogeneous broadening. Such broadening should therefore be interpreted in terms of the information flow between the system and its environment, acknowledging that environmental signatures emerge in spectral lineshape as a result of the non-Markovian feedback of information from the bath to the system.

The results presented in this chapter demonstrate the capabilities of the underdamped and overdamped HEOM methods for modelling linear and 2D spectral lineshapes in a variety of bath conditions. Analysis of these lineshapes from the perspective of quantum information theory has then emphasised the role of non-Markovian effects in determining spectral broadening, demonstrating that spectral lineshape can be rationalised in terms of the flow of information between the system and bath. With the ability to interpret spectral lineshape in such depth, chapter 4 moves on to a discussion of the role of the laser spectrum, with chapter 5 applying the combined knowledge to more complex systems.

4 Spectral Filtering of a Vibronic Monomer

Each peak in a 2D spectrum results from a collection of Liouville pathways involving a particular pair of excitation and emission frequencies, as described in section 2.4. The intensity of peaks is related to the availability of photons at these frequencies, which is determined by the shape and strength of the laser spectrum. For complex systems with congested absorption spectra, careful tuning of the laser spectrum can therefore be used to isolate particular pathways.[86,87,101] Such an approach has recently been applied to the FMO complex to accentuate the role of ground state vibronic coherences.[127] However, unintentional filtering of Liouville pathways by the finite width of the laser spectrum can equally diminish spectral features, leading to the misinterpretation of spectra and the incorrect assignment of electronic and vibrational coherences. Camargo *et al.* have demonstrated experimentally that blue-shifting of the laser spectrum removes peaks from the 2D spectra of a 5,15-bisalkynyl zinc-porphyrin monomer due to the elimination of Liouville pathways.[22] In this chapter, these results are confirmed theoretically by modelling 2DES of the vibronic Q_x band of the zinc-porphyrin monomer, using the equation-of-motion phase-matching approach (EOM-PMA) to account for the finite width of the laser spectra. Parameters are determined by fitting of the model to the experimental linear absorption spectrum, where the vibronic system is coupled to separate overdamped baths for electronic dephasing and vibrational relaxation. Application of a third Fourier transform over the population time provides the *amplitude spectra* of the coupled vibrational mode, which are understood in terms of a detailed analysis of the Liouville pathways of a vibronic monomer. The results presented here feature improved fitting and analysis of the model compared with the original publication of this work in reference 186.

4.1 Zinc-Porphyrin Monomer and Laser Spectra

The molecular structure and linear absorption spectrum of the 5,15-bisalkynyl zinc-porphyrin monomer used by Camargo *et al.* are presented in figure 4.1.1, reproduced from references 22 and 186. Transitions of the ground state to three excited singlet states produce three distinct bands in the linear absorption spectrum. The Q band, for transitions to S_1, has a maximum at $15\,650\,\mathrm{cm}^{-1}$,

whilst the B band, to S_2, involves significantly more intense peaks in the region 21000 - 24 000 cm^{-1}. The N band at 28000 - 34 000 cm^{-1} is much weaker than the other bands, but very broad, corresponding to the quasi-continuum of S_3. Asymmetric substituents on the porphyrin macrocycle lower the symmetry of the molecule from D_{4h} to D_{2h}, separating the dipole moment into individual x and y contributions. The Q_x band features a vibronic progression with a frequency of 375 cm^{-1}, corresponding to a zinc-porphyrin breathing mode. Q_x overtones resulting from coupling to a higher energy vibrational mode of 1340 cm^{-1} produce a weaker peak at ca. 17 000 cm^{-1}, superimposed with the Q_y contributions.[105,233,240]

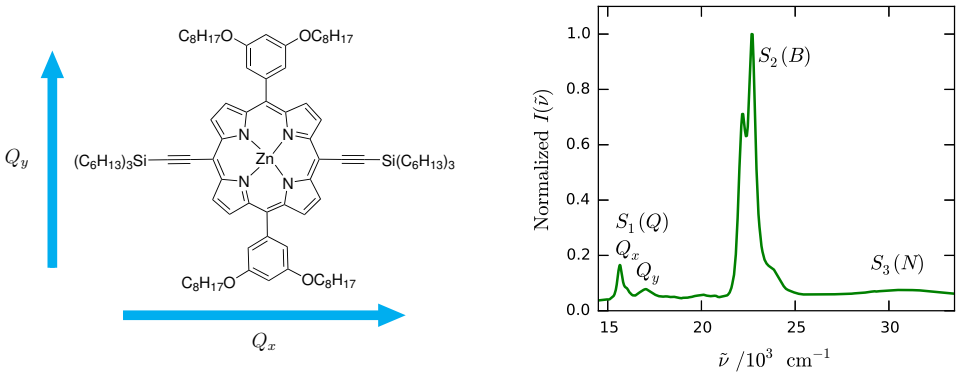

Figure 4.1.1: Molecular structure (left) and linear absorption spectrum (right) of the 5,15-bisalkynyl zinc-porphyrin monomer.

The vibronic progression of the Q_x band is modelled by defining the system Hamiltonian as a vibronic monomer, with $\mathsf{H}_\mathsf{S} = \mathsf{H}^V_\mathrm{M}$, where $\tilde{\omega}^0_{eg} = 15\,650\,\mathrm{cm}^{-1}$, $\tilde{\omega}_0 = 375\,\mathrm{cm}^{-1}$ and $\Delta_0 = 0.79$ such that $\tilde{\lambda}_0 = 117\,\mathrm{cm}^{-1}$. After diagonalization, the Hamiltonian is truncated to the first two vibronic levels, with $\nu_0 = 0, 1$ only. The dipole moment operator, $\hat{\mu} = \hat{\mu}^V_\mathrm{M}$, describes the transition dipole moment of magnitude $\mu_{eg} = 13\,\mathrm{D}$. The vibronic system is coupled to separate overdamped baths for electronic dephasing and vibrational relaxation as described in section 2.2.2.2, where $\mathsf{B}_1 = \mathsf{B}^V_{1,\mathrm{M}}$, with $\tilde{\eta}_1 = 29\,\mathrm{cm}^{-1}$, $\tilde{\Lambda}_1 = 20\,\mathrm{cm}^{-1}$, and $\mathsf{B}_2 = \mathsf{B}^V_{2,\mathrm{M}}$, with $\tilde{\eta}_2 = 29\,\mathrm{cm}^{-1}$, $\tilde{\Lambda}_2 = 20\,\mathrm{cm}^{-1}$. This places both baths within the inhomogeneous limit, $\Delta\tau_c = 5.5$, as discussed in chapter 3. The Markovian limit is set at $\xi = 10\Lambda_1$, producing an overdamped hierarchy with 1009 ADOs at 300 K, which simultaneously propagates both baths using eq. 2.3.18. Under these conditions, the calculated linear absorption spectrum, σ_A, in figure 4.1.2 shows excellent agreement with experimental results. For the analysis presented here, the model is restricted to the vibronic Q_x band, coupled to the 375 cm^{-1} mode only. As the maximum Q_y intensity is less than 30% of that of Q_x, the intensity of any vibronic progression for Q_y is similarly reduced. Also acknowledging that Q_y to Q_x relaxation occurs within 110 fs, any contribution from Q_y is assumed insignificant.[241]

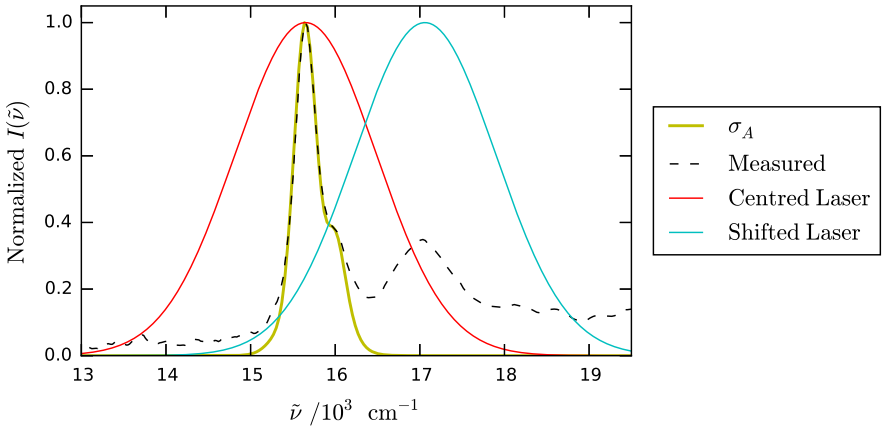

Figure 4.1.2: Calculated (σ_A) and experimental (Measured) linear absorption spectra with centred and shifted laser spectra.

To demonstrate the filtering of Liouville pathways by the laser spectrum, 2D spectra are calculated using the EOM-PMA, section 2.4.3.2, for two scenarios. Firstly, where the laser spectrum completely encompasses the Q_x band, centred at the fundamental transition frequency of the system with $\tilde{\omega}_m = 15\,650\,\mathrm{cm}^{-1}$ and a time full-width-half-maximum (FWHM) of $\tau_p = 15\,\mathrm{fs}$. Secondly, where the width of the laser spectrum is unchanged, but the frequency is blue-shifted to $\tilde{\omega}_m = 17\,060\,\mathrm{cm}^{-1}$, such that it provides greater intensity to the vibronic shoulder of the Q_x band than the fundamental transition, and any lower energy transitions are disregarded. Both laser spectra are also shown in figure 4.1.2, where the intensity of the electric field is $\chi_m = 10^7\,\mathrm{V\,m}^{-1}$ in both cases.

4.2 Liouville Pathway Analysis

For a vibronic monomer with two electronic states, each coupled to two vibrational levels, there are 32 double-sided Feynman diagrams that survive the rotating wave approximation. As discussed in section 2.4, these are distinguished into non-oscillatory population pathways, with equivalent ket and bra states, $|i\rangle\langle i|$, during t_2 and oscillatory coherence pathways, with different ket and bra states, $|i\rangle\langle j|$, $i \neq j$, during t_2. Using the 2DES convention, R_1 and R_4 pathways involve the sequence of field interactions which corresponds to the non-rephasing direction, whilst R_2 and R_3 are rephasing.

All 32 diagrams are presented in figures 4.2.1 - 4.2.4 in the usual manner, with the transition frequencies associated with each interaction written explicitly alongside the dashed lines. Here, the vibronic states are abbreviated in the style of Camargo *et al.* in ref. 22 as $|\alpha,\nu\rangle = |\alpha_\nu\rangle$. As $\hbar\omega_0 > k_\mathrm{B}T$, only pathways starting in the lowest vibrational level of the ground electronic state,

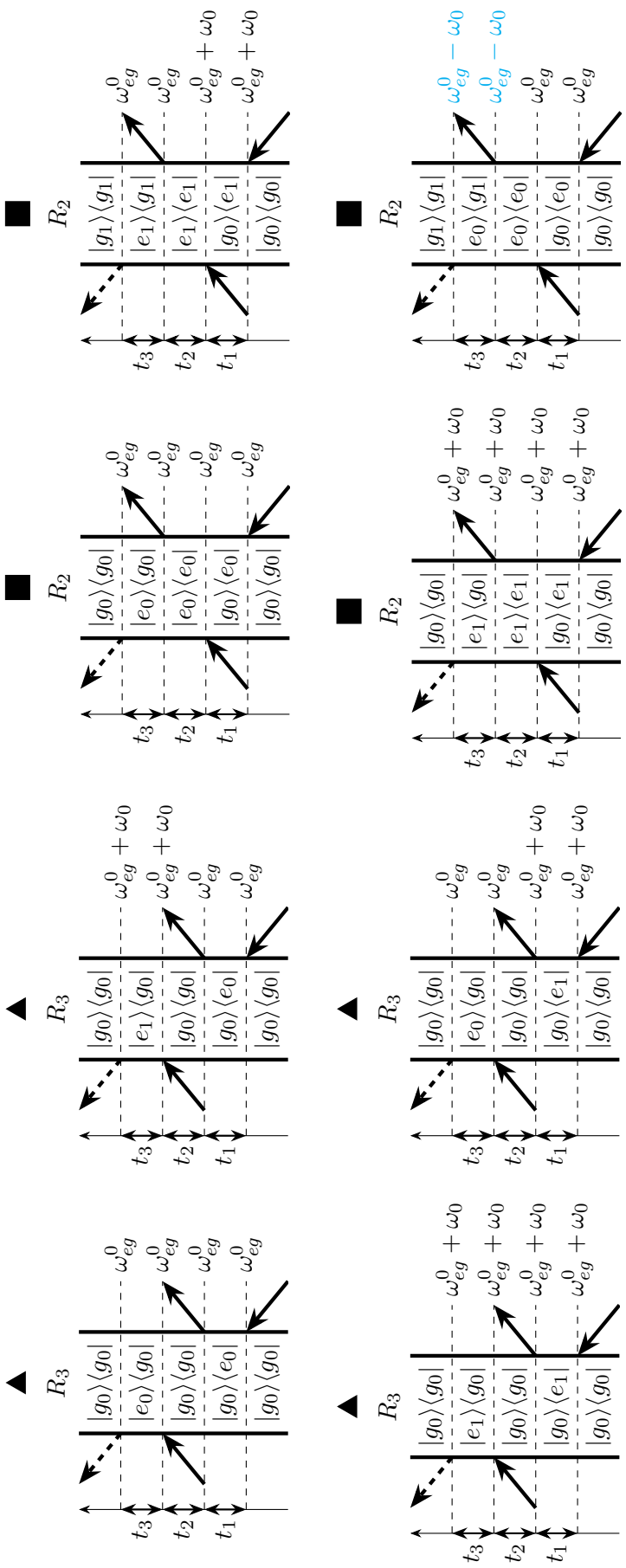

Figure 4.2.1: Rephasing population pathways, labelled as per table 4.1.

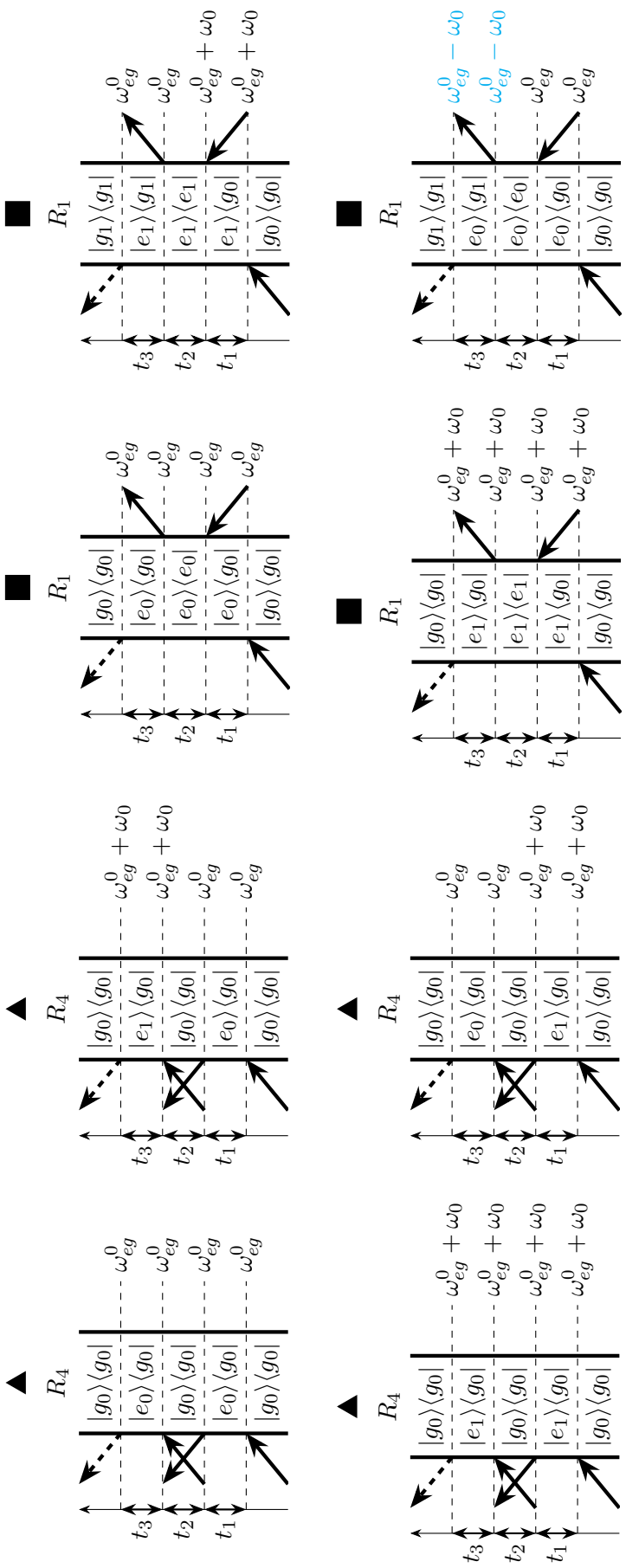

Figure 4.2.2: Non-rephasing population pathways, labelled as per table 4.1.

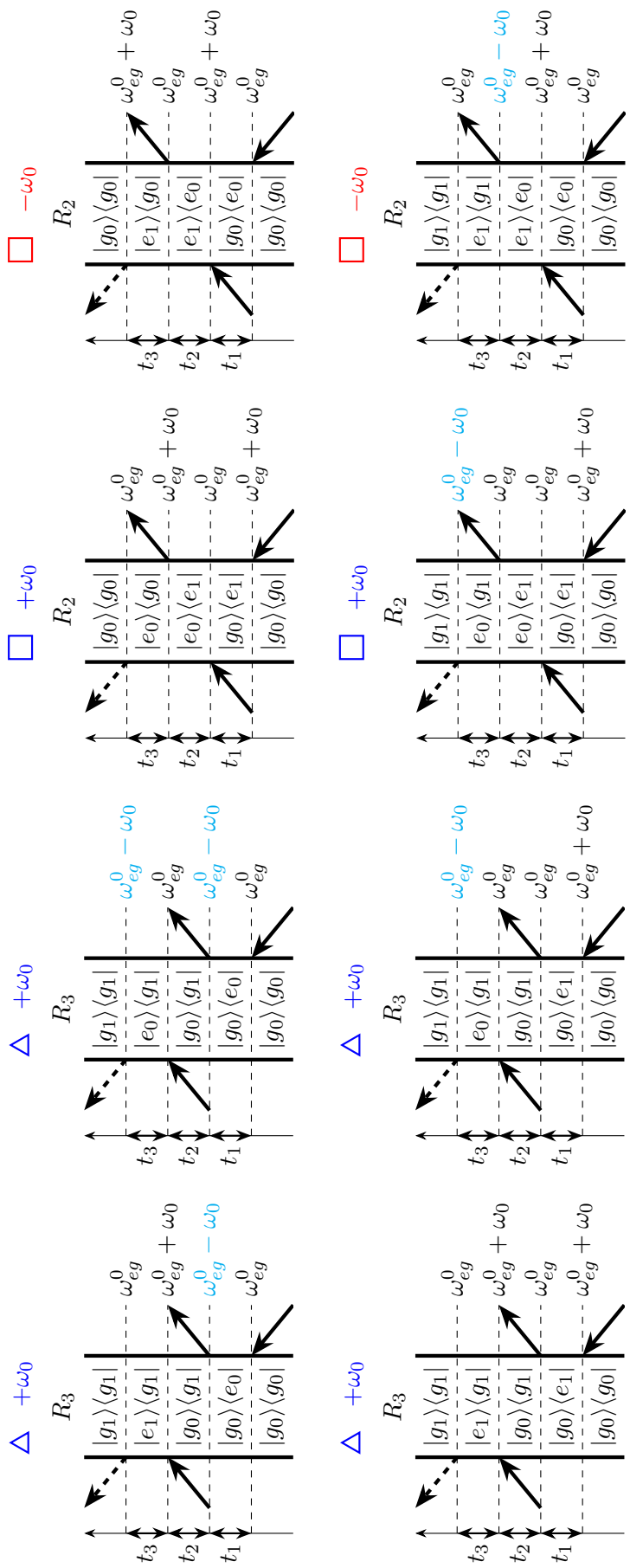

Figure 4.2.3: Rephasing coherence pathways, labelled as per table 4.1.

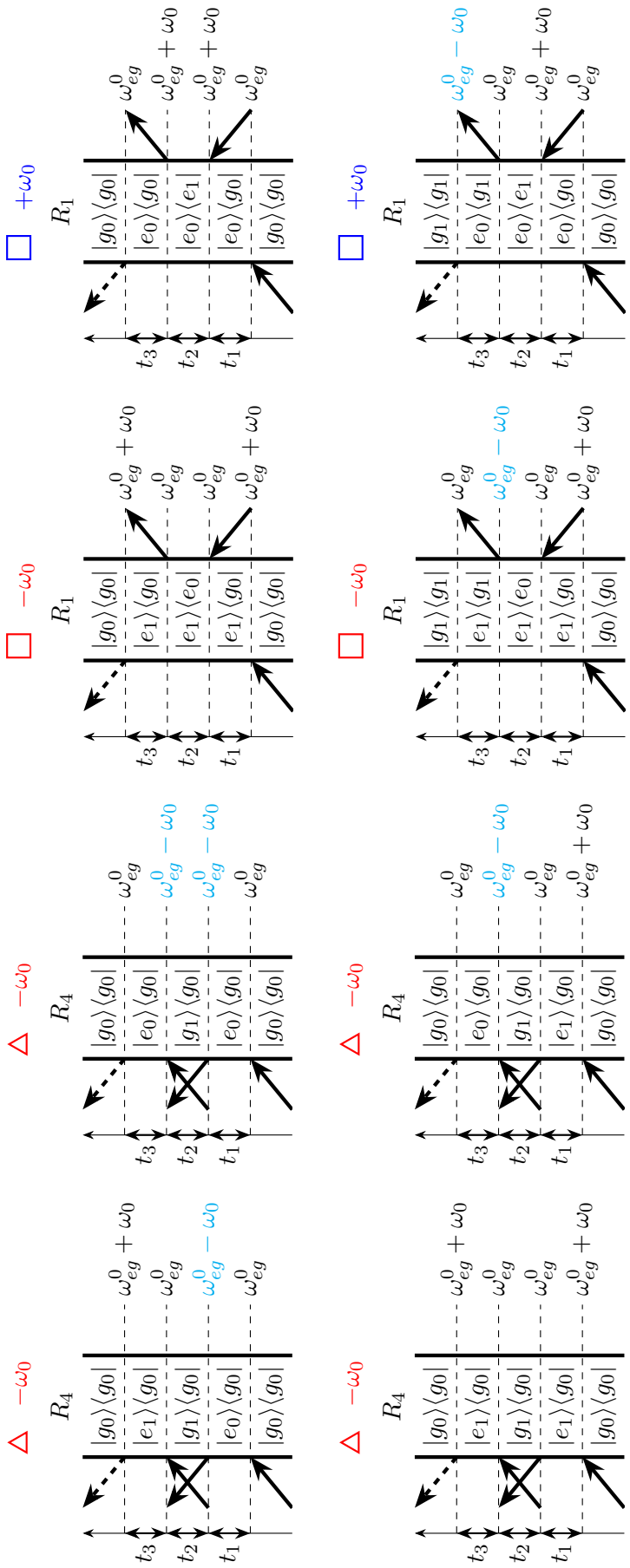

Figure 4.2.4: Non-rephasing coherence pathways, labelled as per table 4.1.

$|g_0\rangle\langle g_0|$, are considered. Population and coherence pathways for ground state bleach (GSB), R_3 and R_4, and stimulated emission (SE), R_1 and R_2, processes are labelled using colour-coded symbols, as defined in table 4.1. The oscillations of coherence pathways are either positive, $\propto \exp(+i\omega_0 t_2)$, or negative, $\propto \exp(-i\omega_0 t_2)$, dependent on the superposition involved, where here the adopted convention is such that,

$$|g_0\rangle\langle g_1| \propto \exp(+i\omega_0 t_2), \tag{4.2.1}$$

$$|g_1\rangle\langle g_0| \propto \exp(-i\omega_0 t_2). \tag{4.2.2}$$

Performing an additional Fourier transform over the population time separates the positive and negative oscillations, as discussed in section 4.3.

	Ground State Bleach	Stimulated Emission
Population	▲	■
Positive Coherence ($+\omega_0$)	△	□
Negative Coherence ($-\omega_0$)	△	□

Table 4.1: Symbol key for Liouville pathways.

These 32 pathways produce six peaks in the rephasing 2D spectra and five in the non-rephasing, as shown in the location key diagrams in figure 4.2.5.

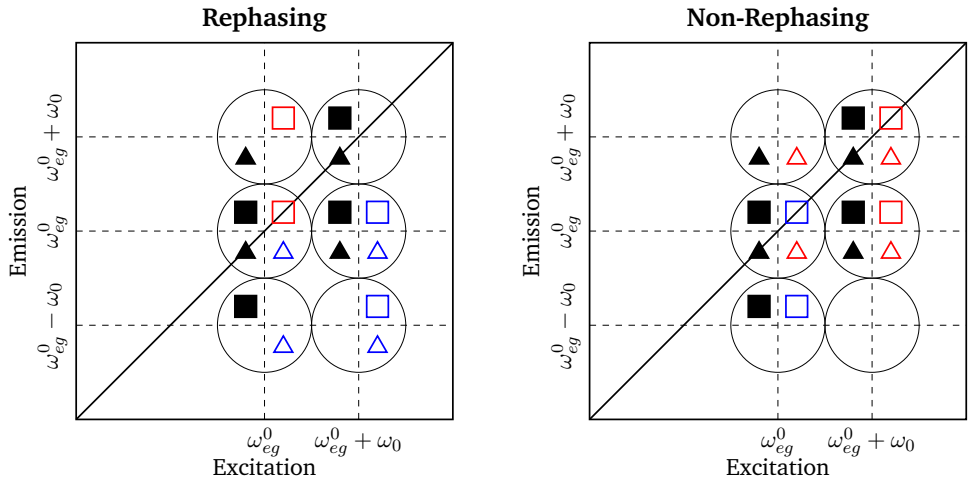

Figure 4.2.5: Unfiltered peak location key diagrams. The location of peaks corresponds to the centre of the circles, where the geometric shapes identify the contributing Liouville pathways.

On blue-shifting the laser spectrum as in figure 4.1.2, the intensity of pathways involving the $\omega_{eg}^0 - \omega_0$ transition frequency is significantly reduced, such that they are filtered from the 2D spectra. An example of a filtered pathway is presented in figure 4.2.6, where all filtered pathways are identified by the highlighted $\omega_{eg}^0 - \omega_0$ transition frequency in figures 4.2.1 - 4.2.4.

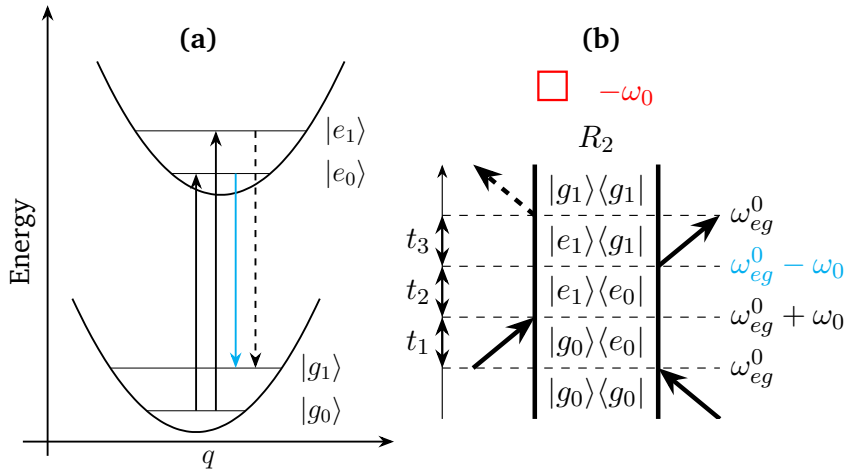

Figure 4.2.6: Example of a filtered pathway drawn on the vibronic PES and as a double-sided Feynman diagram. Reprinted with permission from reference 186. Copyright 2019 American Chemical Society.

Removing the contribution of these filtered pathways produces the location key diagrams in figure 4.2.7. These predict that blue-shifting the laser spectrum reduces the rephasing and non-rephasing 2D spectra to four peaks each, dominated by non-oscillatory population pathways, where the lower peaks with emission frequency of $\omega_{eg}^0 - \omega_0$ are completely removed. They also show that the remaining positive and negative coherence pathways contribute to separate peaks, which are off-diagonal in the rephasing spectrum and diagonal in the non-rephasing spectrum.

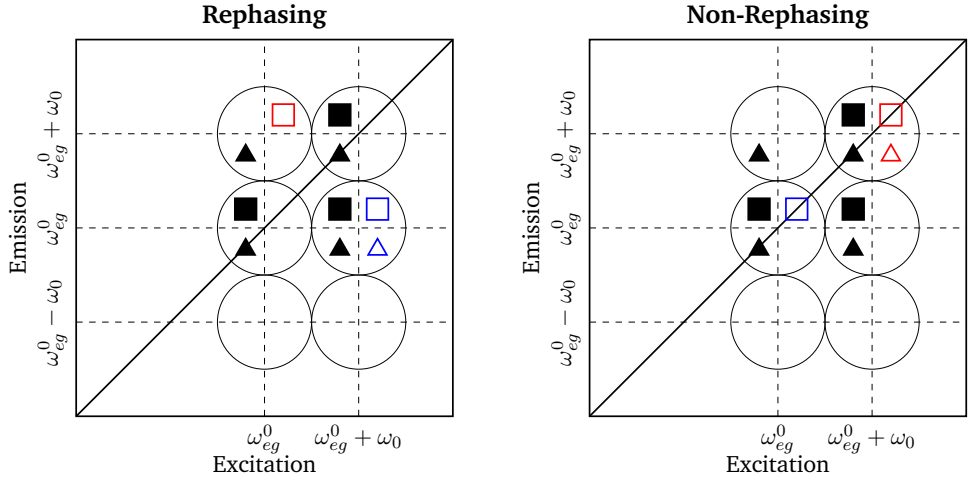

Figure 4.2.7: Filtered peak location key diagrams for the blue-shifted laser, as in figure 4.2.5.

4.3 Filtered Spectra

2D spectra were calculated for $T = 1\,\mathrm{ps}$ at intervals of $10\,\mathrm{fs}$ for the centred and blue-shifted laser spectra defined in section 4.1. A comparison of the rephasing and non-rephasing 2D spectra (real) for the centred and shifted laser at $T = 100,\ 200$ and $500\,\mathrm{fs}$ are shown in figures 4.3.1 and 4.3.2, respectively, normalised to the maximum achieved throughout the population time to demonstrate the oscillations in peak amplitude.

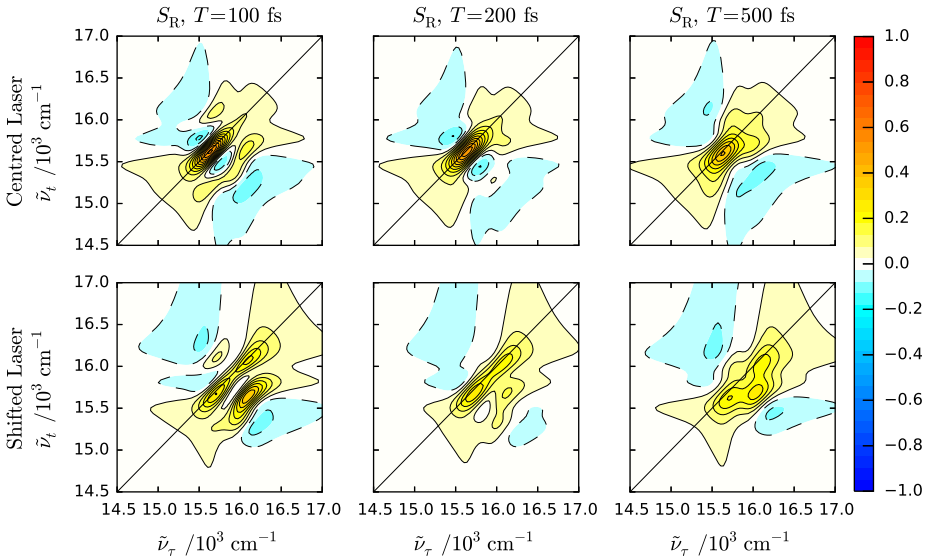

Figure 4.3.1: Rephasing spectra at $T = 100$, 200 and $500\,\mathrm{fs}$ for (top) centred and (bottom) blue-shifted laser spectra, each normalised to their maximum along the population time, T, respectively.

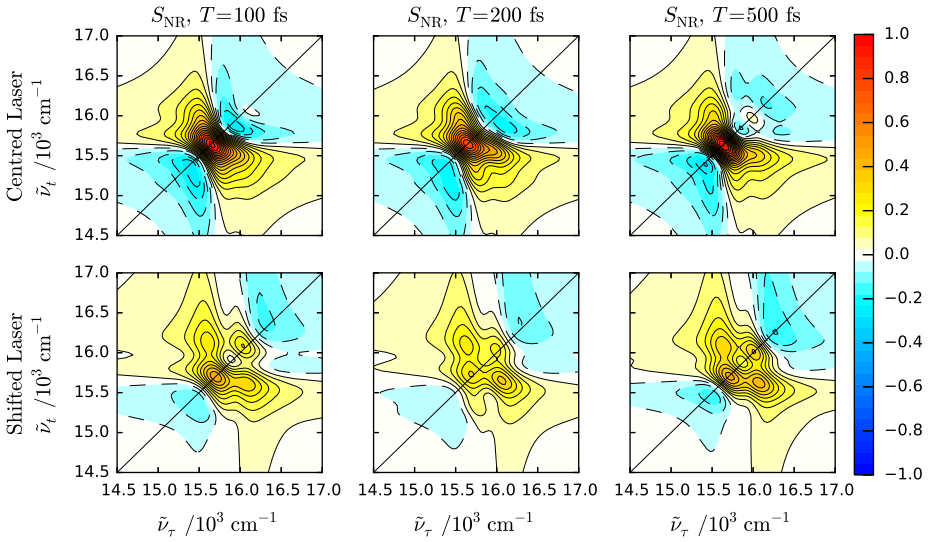

Figure 4.3.2: Non-rephasing spectra at $T = 100$, 200 and $500\,\mathrm{fs}$ for (top) centred and (bottom) blue-shifted laser spectra, each normalised to their maximum along the population time, T, respectively.

Both figures 4.3.1 and 4.3.2 show a loss of intensity at lower emission frequencies, $\tilde{\nu}_t$, on shifting the laser spectrum, as predicted by the Liouville pathway analysis in section 4.2. The rephasing spectra also show elongation of peaks along the diagonal due to inhomogeneous broadening by the environment, which diminishes with increasing population time, as discussed in chapter 3.

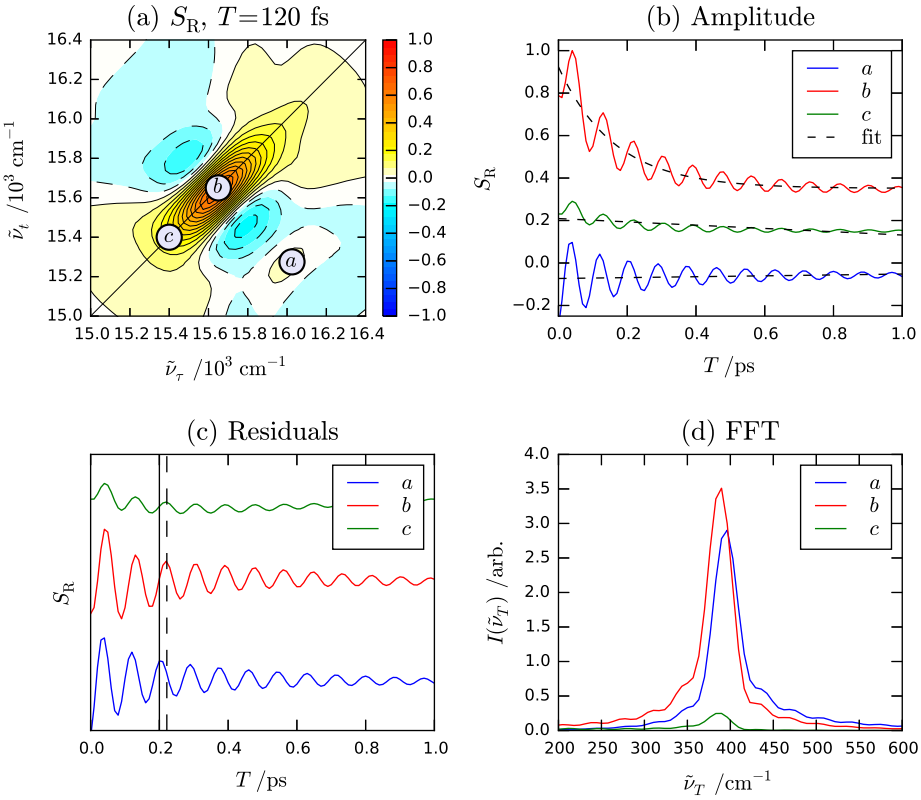

Figure 4.3.3: (a) Rephasing spectrum (real) at $T = 120\,\text{fs}$ for the centred laser spectrum, normalised to the maximum amplitude within the total $1\,\text{ps}$ of population time, with coordinates a, b and c labelled. (b) Trace of the rephasing (real) amplitude for the three coordinates in (a), including fit of an exponential decay for each. (c) Residual for each coordinate in (a) after subtraction of any exponential decay, with labelled phase shift between a and b/c, arbitrarily offset for clarity. (d) FFT spectra for the residuals in (c).

The vibronic coherence pathways cause the peak amplitude to oscillate at the mode frequency, as shown in figure 4.3.3. Figure 4.3.3 (b) shows the amplitude of the real component of the rephasing spectrum for the three coordinates identified in 4.3.3 (a), for the centred laser spectrum simulation. Coordinate b corresponds to the centre of the peak at $(\omega_{eg}^0, \omega_{eg}^0)$ in the location key diagram of figure 4.2.5, and shows a strong decaying oscillation in its amplitude due to the coherence pathways, superimposed on an exponential decay with a lifetime of $163\,\text{fs}$, caused by the dephasing and relaxation of the population pathways. Coordinate c, also on the diagonal of the spectrum, but slightly red-shifted from b, shows much weaker oscillations and decay, whilst coordinate a,

corresponding to the centre of the peak at ($\omega_{eg}^{0} + \omega_0$, $\omega_{eg}^{0} - \omega_0$) in figure 4.2.5, is the result of coherence pathways only and shows no exponential decay due to population pathways. Fitting and subtraction of a single exponential function to each of these traces yields the residuals in figure 4.3.3 (c), which corresponds to isolation of the coherence pathways and removal of the population pathways. In agreement with the experimental results of Camargo *et al.*, figure 4.3.3 (c) shows that the diagonal coordinates, b and c, oscillate in phase, and are both 90° out of phase with the off-diagonal coordinate, a.[105] This phase shift is also discussed by Butkus *et al.*, who showed that the phase of rephasing coherence pathways is constant along the diagonal lineshape, but varies along the anti-diagonal lineshape.[211,242] Fourier transform over the population time then produces the spectra in figure 4.3.3 (d), which identify the oscillations correspond to the mode frequency of the vibration included in the system Hamiltonian at $\tilde{\omega}_0 = 375\,\mathrm{cm}^{-1}$.

Repeating this procedure for the residuals of every (ω_τ, ω_t) coordinate produces a spectrum like 4.3.3 (d) for each coordinate. Plotting the amplitude at the frequency of $375\,\mathrm{cm}^{-1}$ then gives the *amplitude spectrum* of the vibrational mode. This shows the relative intensity of oscillations of that frequency across the 2D spectrum, identifying the locations of coherence pathways for that mode. For more complex systems with multiple vibrational modes producing multicomponent oscillations, this additional Fourier transform provides a means of isolating the coherence pathways for different modes. Fourier transform of the full complex rephasing or non-rephasing signal also produces separate amplitude spectra for the positively and negatively oscillating coherence pathways, enabling further distinction of the coherence pathways, as in the analysis of section 4.2.[48]

The calculated amplitude spectra for the $375\,\mathrm{cm}^{-1}$ mode using the centred laser spectrum are shown in figure 4.3.4, along with the experimental results presented in references 22 and 186.[a] In excellent agreement with the location key diagrams of figure 4.2.5, the positive rephasing amplitude spectra in figure 4.3.4 (1c) and (2c) show a square arrangement of four peaks below the diagonal, resulting from four GSB and two SE coherence pathways. A further two SE coherence pathways produce two peaks aligned along $\omega_\tau = \omega_{eg}^{0}$ in the negative rephasing amplitude spectra in figure 4.3.4 (1a) and (2a). Similarly, the positive non-rephasing amplitude spectra in figure 4.3.4 (1d) and (2d) show two peaks again aligned along $\omega_\tau = \omega_{eg}^{0}$ from two SE coherence pathways, whilst the negative non-rephasing in figure 4.3.4 (1b) and (2b) have a square arrangement of four peaks about the diagonal from the other two SE and all four GSB coherence pathways.

[a] Note that the calculated amplitude spectra are presented here as the power spectrum of the Fourier coefficients, $|F_{co}|^2$, in much better agreement with the experimental results than reported in reference 186, which mistakenly only presented the amplitude, $|F_{co}|$.

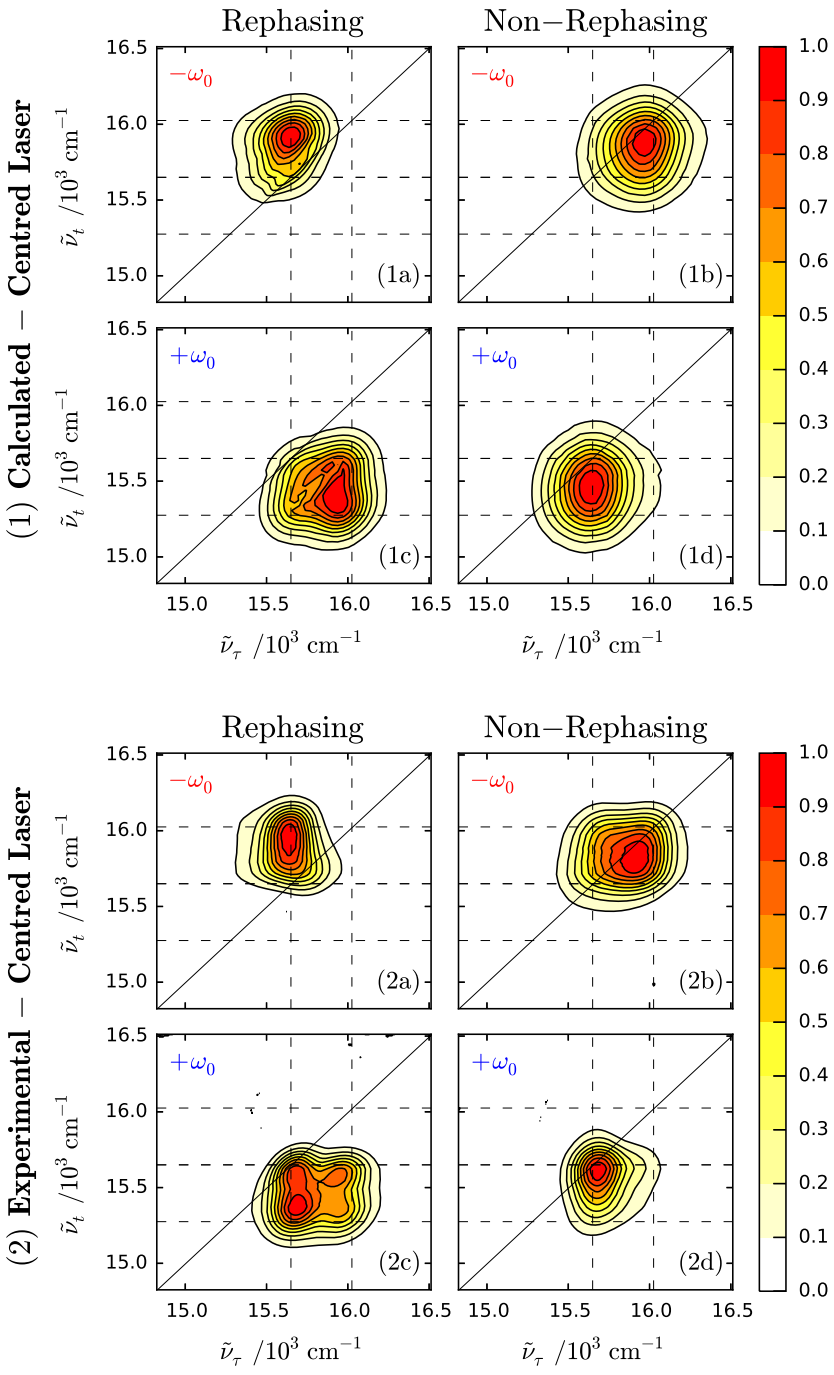

Figure 4.3.4: (1) Calculated and (2) experimental amplitude spectra for the centred laser spectrum. The dashed lines correspond to vibronic transition frequencies, as in the location key diagrams in figure 4.2.5. Experimental results reprinted (adapted) with permission from reference 186. Copyright 2019 American Chemical Society.

As shown in the location key diagram of figure 4.2.7, blue-shifting the laser spectrum eliminates most of the coherence pathways, leaving a single peak in each of the amplitude spectra. The calculated and experimental amplitude spectra for the blue-shifted laser spectrum are presented in figure 4.3.5. A single

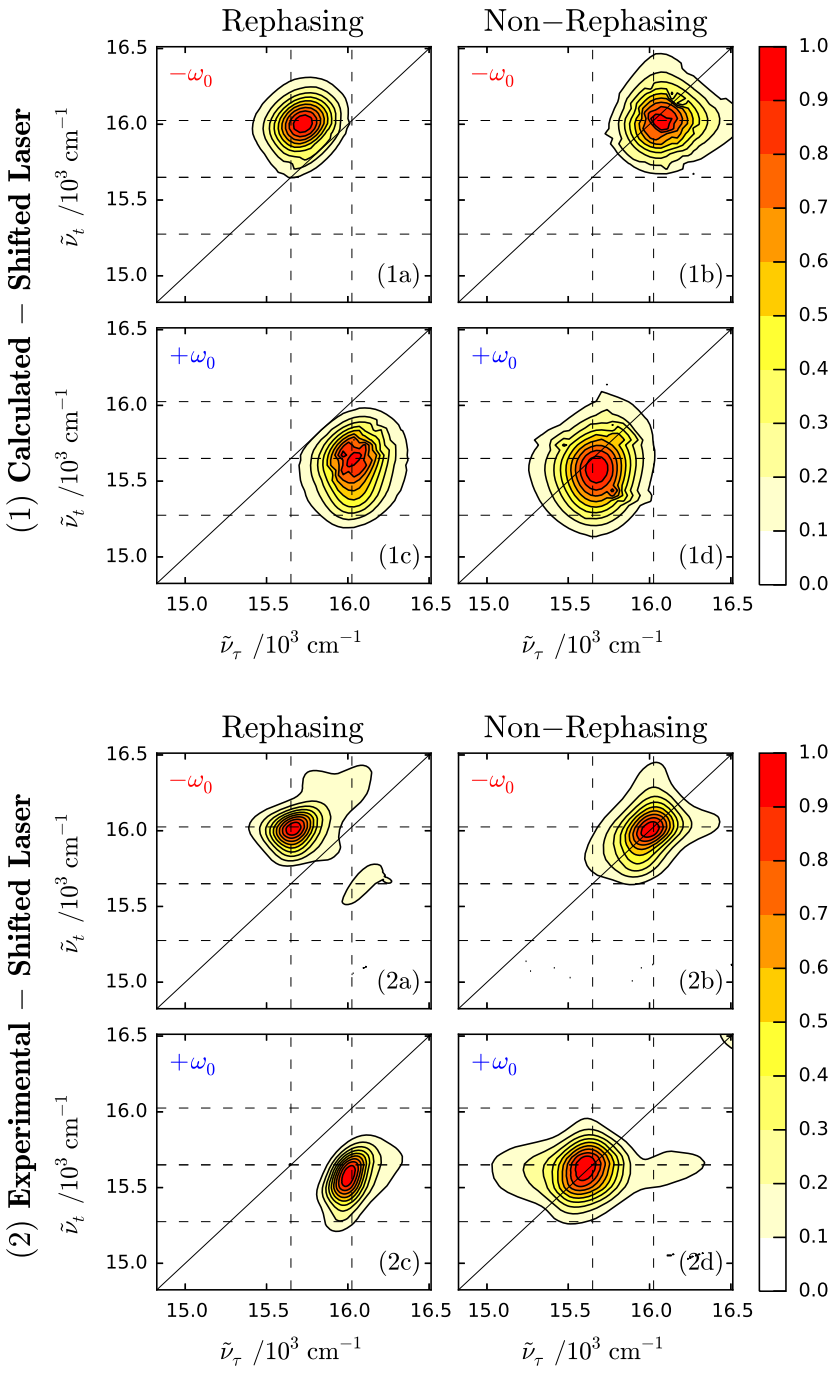

Figure 4.3.5: (1) Calculated and (2) experimental amplitude spectra for the blue-shifted laser spectrum. The dashed lines correspond to vibronic transition frequencies, as in the location key diagrams in figure 4.2.7. Experimental results reprinted (adapted) with permission from reference 186. Copyright 2019 American Chemical Society.

SE coherence pathway produces a peak above the diagonal in the negative rephasing amplitude spectrum in figure 4.3.5 (1a) and (2a), whilst one GSB and one SE coherence pathway produce a peak below the diagonal in figure 4.3.5 (1c) and (2c). For the non-rephasing amplitude spectra, both peaks appear on

the diagonal, where the peak in the positive amplitude spectrum from a single SE coherence pathway is centred at (ω_{eg}^0, ω_{eg}^0) in figure 4.3.5 (1d) and (2d), whilst the peak in the negative amplitude spectrum from one GSB and one SE coherence pathway is centred at ($\omega_{eg}^0 + \omega_0$, $\omega_{eg}^0 + \omega_0$) in figure 4.3.5 (1b) and (2b). The excellent agreement of the calculated amplitude spectra with both the experimental results and the Liouville pathway analysis of section 4.2 demonstrates the ability of the EOM-PMA to accurately account for the filtering of Liouville pathways caused by the finite width of the laser spectrum.

As the reduced number of Liouville pathways produce a single peak in each amplitude spectrum using the blue-shifted laser spectrum, the maximum intensity of each peak is centred at the intersection of the dashed lines in figure 4.3.5. In the amplitude spectra using the centred laser spectrum in figure 4.3.4, the summed amplitude of adjacent peaks causes the maximum intensity to appear between the dashed lines. For the centred laser spectrum, the Liouville pathway analysis predicts that twice as many coherence pathways contribute to peaks along $\omega_\tau = \omega_{eg}^0 + \omega_0$ than $\omega_\tau = \omega_{eg}^0$, for both the negative non-rephasing and positive rephasing amplitude spectra. This produces greater intensity at ca. $\tilde{\nu}_\tau = 16\,000\,\mathrm{cm}^{-1}$ compared with $\tilde{\nu}_\tau = 15\,650\,\mathrm{cm}^{-1}$ in figure 4.3.4 (1b) and (1c). However, this contrasts with the peak intensity in the experimental amplitude spectra in figure 4.3.4 (2b) and (2c), suggesting that a number of Liouville pathways are absent from the calculated spectra. These additional pathways likely involve overtones to higher vibrational levels ($\nu_0 = 2, 3, \ldots$), which are not accounted for within the truncated system Hamiltonian.

These results emphasise the role of the laser spectrum in determining the 2D spectral lineshape and the importance of a careful consideration of spectral filtering effects. But the filtering of Liouville pathways is not necessarily a negative result and can be employed as a tool for the study of a reduced set of pathways, where application of multicoloured pulses provides further control over the resulting spectra.[28,41,84] The simulations discussed in this chapter also demonstrate the ability of the vibronic model and non-Markovian HEOM dynamics to successfully reproduce experimental lineshapes in both the linear and 2D spectra, where combination with the EOM-PMA enables the study of spectral filtering effects. However, the amplitude spectra show that truncation of the quantum system within the model is a limiting factor on comparison with the experimental results, which always comprise the full degrees of freedom. This is explored further in chapter 5, where the models are applied to more complex vibronic dimer systems.

5 Application to Vibronic Dimers

Finally, this chapter discusses features of 2D spectra which demonstrate the formation of vibronic dimers. A general description regarding the coupling limits introduced in section 2.2.1.3 is followed by application of the model to a series of perylene bisimide homodimers, where the strength of the electronic coupling is decreased by increasing the separation distance between the monomers. Energy transfer between the coupled monomers is then demonstrated using a model heterodimer, where the finite width of the laser spectrum is used to preferentially excite one monomer, such that subsequent vibrational relaxation within the exciton manifold corresponds to transfer of the excited population to the other monomer.

5.1 Coupling Limits

The electronic coupling of monomers to form dimer species with delocalized exciton states was discussed in section 2.2.1.2, where section 2.2.1.3 further explained how the electronic coupling, J, is quenched by the vibronic coupling, with reorganisation energy $\hbar\lambda$, producing the strong and weak coupling limits. The transition between these limits is accompanied by pronounced differences in the potential energy surfaces of the exciton states. The harmonic potentials for the four electronic states in the composite site basis of the vibronic dimer are plotted in figure 5.1.1, where the contours for the two singly excited states are shown in relation to the separate monomer coordinates, $\mathrm{Q}_{j\mathrm{A}}$ and $\mathrm{Q}_{j\mathrm{B}}$, and in a rotated frame corresponding to symmetric $(+)$ and antisymmetric $(-)$ vibrational motion, respectively,

$$\mathrm{Q}_{j\pm} = \frac{\mathrm{Q}_{j\mathrm{A}} \pm \mathrm{Q}_{j\mathrm{B}}}{\sqrt{2}}. \tag{5.1.1}$$

The electronic coupling leads to nested potential energy surfaces for the two exciton states, $V^{\pm}$, which are calculated for a homodimer in terms of the transformed vibrational coordinate as,[110]

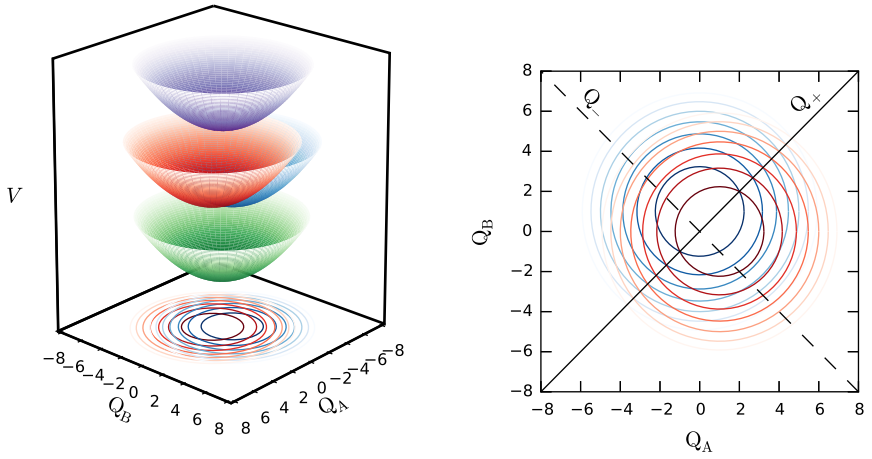

Figure 5.1.1: Site basis vibronic homodimer potential energy surface, showing V_{gg} (green), V_{eg} (red), V_{ge} (blue) and V_{ee} (purple).

$$V_j^{\pm} = \hbar\omega_{eg}^0 + \frac{\hbar\omega_j}{2}\left(\mathrm{Q}_{j+}^2 + \mathrm{Q}_{j-}^2\right) - \hbar\omega_j \frac{\Delta_j}{\sqrt{2}}\mathrm{Q}_{j+} \pm \sqrt{J^2 + \frac{\hbar^2\omega_j^2\Delta_j^2}{2}\mathrm{Q}_{j-}^2}. \quad (5.1.2)$$

For a H-aggregate in the strong coupling limit, when the reorganisation energy of the mode is less than the electronic coupling, $\hbar\lambda_j < J$, the two exciton states show only marginally distorted harmonic wells, whose minima are equidistant between monomers, as shown in figure 5.1.2. Whereas in the weak coupling limit, when the reorganisation energy of the mode is greater than the electronic coupling, $\hbar\lambda_j > J$, the lower antisymmetric potential, V^-, features a double minimum, as shown in figure 5.1.3, where the minima are found along the line,

$$\mathrm{Q}_{j+} = \frac{\Delta_j}{\sqrt{2}}, \qquad \mathrm{Q}_{j-} = \pm\sqrt{\frac{\Delta_j^2}{2} - \frac{2J^2}{\hbar^2\omega_j^2\Delta_j^2}}. \quad (5.1.3)$$

The potentials in figures 5.1.1 - 5.1.3 represent a homodimer where both monomers A and B correspond to the vibronic monomer used in section 3.1, with $\tilde{\omega}_{eg}^0 = 15\,000\,\mathrm{cm}^{-1}$, $\tilde{\omega}_0 = 600\,\mathrm{cm}^{-1}$ and $\Delta_0 = 1$ such that $\tilde{\lambda}_0 = 300\,\mathrm{cm}^{-1}$. Note that the subscript $j = 0$ has been neglected from the coordinates in these figures as each monomer is coupled to a single vibrational mode. With the transition dipole moment of strength $\mu_{eg} = 11\,\mathrm{D}$, the example strong coupling limit corresponds to a monomer separation distance of $R = 1.01\,\mathrm{nm}$ such that $J/hc = 500\,\mathrm{cm}^{-1}$, whilst the example weak coupling limit has a greater separation distance of $R = 1.72\,\mathrm{nm}$ such that $J/hc = 100\,\mathrm{cm}^{-1}$. For Förster coupling, eq. 2.2.26, J is inversely proportional to R^3 such that for a fixed reorganisation energy, an increase in the displacement of the two vibronic

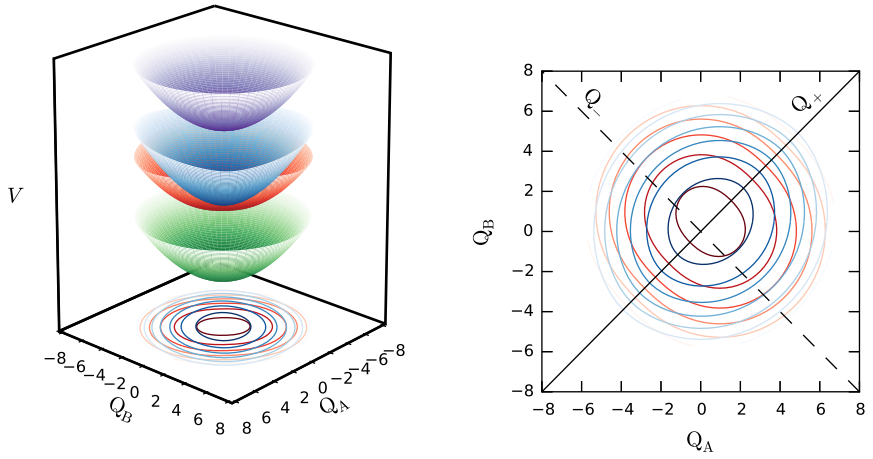

Figure 5.1.2: Exciton basis vibronic homodimer potential energy surface for a H-aggregate in the strong coupling limit, showing V_{gg} (green), V^- (red), V^+ (blue) and V_{ee} (purple).

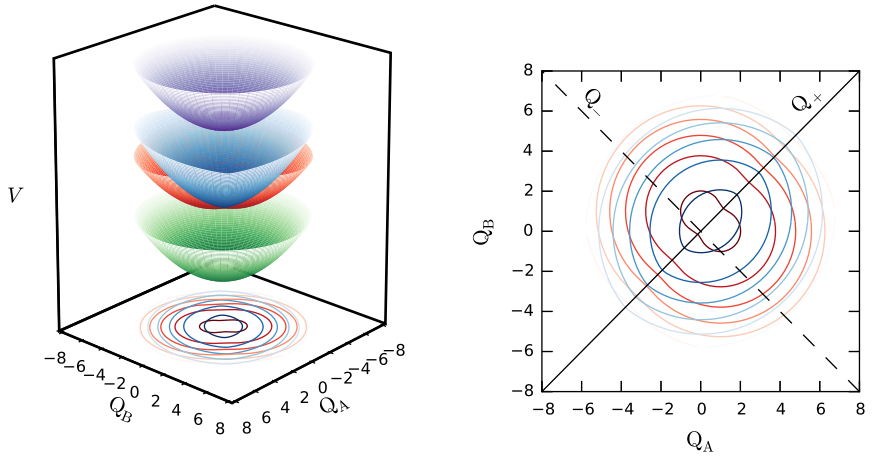

Figure 5.1.3: Exciton basis vibronic homodimer potential energy surface for a H-aggregate in the weak coupling limit, showing V_{gg} (green), V^- (red), V^+ (blue) and V_{ee} (purple).

monomers results in decreased electronic coupling, transitioning from the strong to weak coupling limits.

Switching to a collinear arrangement of transition dipole moments, such that the two monomers form a J-aggregate with $J < 0$, the linear and 2D spectra for the homodimer in the strong and weak coupling limits are shown in figure 5.1.4. These are calculated where the Hamiltonian for each monomer is truncated to the $\nu_0 = 0, 1$ vibrational levels only and the vibronic dimer system is coupled to a single bath for electronic dephasing with $\mathsf{B}_1 = \mathsf{B}^E_{1,\mathrm{D}}$, $\tilde{\eta}_1 = 20\,\mathrm{cm}^{-1}$, $\tilde{\Lambda}_1 = 40\,\mathrm{cm}^{-1}$ and $\xi = 10\Lambda_1$, such that there are 23 ADOs at $298\,\mathrm{K}$.

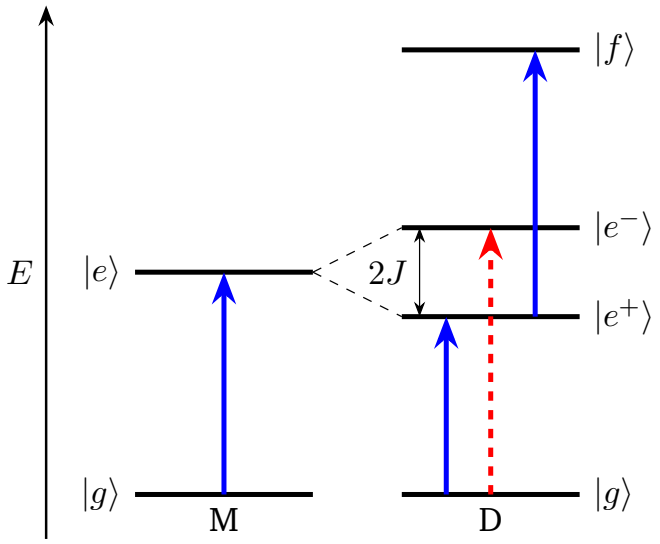

Figure 2.2.4: Energy level diagram for formation of a J-aggregate. *Repeated from page 38 for convenience.*

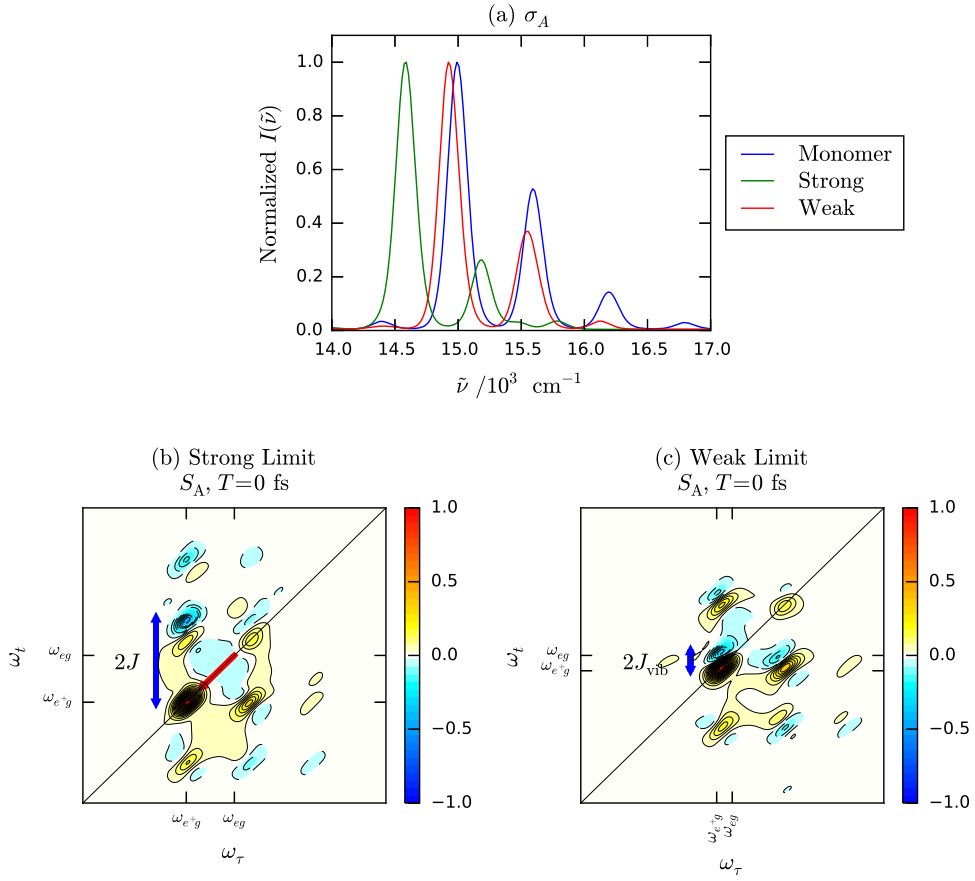

Figure 5.1.4: (a) Linear absorption spectra for J-aggregate homodimers in the strong and weak coupling limits as well as the monomer spectrum from figure 3.1.2 (a), and the corresponding absorptive 2D spectra at $T = 0\,\text{fs}$ for the homodimers in the (b) strong and (c) weak coupling limits.

Figure 5.1.4 (a) shows that the linear absorption spectrum of the homodimer in the strong coupling limit is significantly red-shifted compared with that of the vibronic monomer. This corresponds to the formation of exciton states in a J-aggregate, as in the energy level diagram of figure 2.2.4, where the fundamental peak now corresponds to a transition to the lower, symmetric exciton state with transition frequency ω_{e^+g}. In the absence of any vibronic coupling, $\Delta_j = 0$, the exciton states are split by $2J$ and the fundamental peak is red-shifted to $\omega_{e^+g} = \omega_{eg} - J/\hbar$. However, even in the strong coupling limit, with $\Delta_0 > 0$ the electronic coupling is quenched such that a smaller red-shift is observed. This is shown in figure 5.1.4 (a), which also demonstrates a significant decrease in the intensity of the vibronic peaks relative to the fundamental peak in the strong coupling limit. In the weak coupling limit, significant quenching of the already reduced electronic coupling produces a much smaller red-shift of the fundamental peak, and only a minor reduction in the intensity of the vibronic peaks.

The red-shift in the fundamental peak is also shown in the 2D spectra for the vibronic homodimers, accompanied by the appearance of strong negative peaks corresponding to excited state absorption (ESA) pathways involving the doubly excited state, introduced in section 2.4.3.1. As shown in figure 2.2.4, when $\Delta_j = 0$, $\omega_{fe^+} = \omega_{e^+g} + 2J/\hbar$, such that in the strong coupling limit, figure 5.1.4 (b), the positive GSB/SE peaks are well separated in emission frequency, ω_t, from the negative ESA peaks by ca. $2J$. In the weak coupling limit, figure 5.1.4 (c), the significantly quenched electronic coupling reduces the red-shift, as in the linear spectra, and keeps the negative ESA peaks closely paired with the positive peaks, separated in emission frequency by the much smaller $2J_{\text{vib}}$. The shift of the fundamental transition frequency and the appearance of ESA peaks in the 2D spectra are the main features which distinguish the vibronic dimer 2D spectra from that of the monomer, corresponding to significant changes in the electronic structure of the system. However, the environmental interaction is unchanged, such that inhomogeneous broadening in the monomer spectra in figure 3.1.3 (a) is again observed for the dimer spectra in figure 5.1.4 (b) and (c). The characterisation of vibronic dimers using these features is discussed in section 5.2 through application of the model to a series of perylene bisimide homodimers.

5.2 Perylene Bisimide Homodimers

Perylene bisimides are useful vibronic chromophores with broad application to studies of energy transfer,[243–245] electron transfer[246,247] and the development of optoelectronic devices.[248–250] In ref. 213, we used 2DES to demonstrate the formation of delocalized exciton states in two vibronic homodimers, where the

strength of the electronic coupling was controlled via the separation distance of the monomer units. In that work, experimental measurements were supported by theoretical calculations considering the electronic degrees of freedom only. Here, the models are improved by accounting for the vibronic coupling as well. The structure of the perylene bisimide (PBI) monomer is shown in figure 5.2.1 (left), where the transition dipole moment is directed along an axis connecting the two nitrogen atoms (blue spheres).[251] Long aliphatic chains included at the imide positions to aid solubility and prevent aggregation in the experimental measurements are omitted.[213]

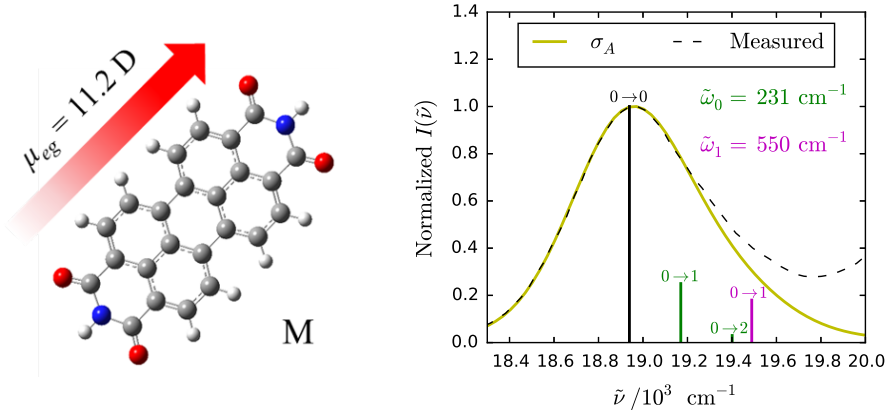

Figure 5.2.1: (Left) Structure of PBI monomer with transition dipole moment magnitude and orientation. (Right) Calculated (σ_A) and experimental (Measured) linear absorption spectra of the PBI monomer, also showing the relative intensity of the vibronic transitions contributing to the first peak.

The linear absorption spectrum of the PBI monomer has three broad peaks containing the vibronic progressions of several vibrational modes, including multiple overtones and combination bands. *Ab initio* calculations performed by Clark *et al.* show that the first peak is dominated by the vibronic progressions of two vibrational modes, with frequencies of $231\,\mathrm{cm}^{-1}$ and $550\,\mathrm{cm}^{-1}$.[252] Here, the PBI monomer is modelled as a two-mode vibronic monomer where $\mathsf{H}_\mathsf{S} = \mathsf{H}^V_\mathsf{M}$, $\tilde{\omega}^0_{eg} = 18\,939\,\mathrm{cm}^{-1}$, $\tilde{\omega}_0 = 231\,\mathrm{cm}^{-1}$ with $\Delta_0 = 0.7$, and $\tilde{\omega}_1 = 550\,\mathrm{cm}^{-1}$ with $\Delta_1 = 0.6$ such that the total reorganisation energy is $\tilde{\lambda} = 156\,\mathrm{cm}^{-1}$. The potential energy surface of the PBI monomer is presented in figure 5.2.2, which shows the displacement of the excited state potential for both modes, where the higher frequency mode produces a steeper parabolic potential in Q_1 than in Q_0. After diagonalization, the system Hamiltonian is truncated such that each electronic state is coupled to the lowest four vibronic states only, which correspond to $|n\rangle = |\nu_0, \nu_1\rangle = |0,0\rangle$, $|1,0\rangle$, $|2,0\rangle$ and $|0,1\rangle$, in order of increasing energy. The dipole moment operator $\hat{\mu} = \hat{\mu}^V_\mathsf{M}$ describes the transition dipole moment of magnitude $\mu_{eg} = 11.22\,\mathrm{D}$. The vibronic monomer system is coupled to a single overdamped bath for electronic dephasing where $\mathsf{B}_1 = \mathsf{B}^V_{1,\mathsf{M}}$, $\tilde{\eta}_1 = 160\,\mathrm{cm}^{-1}$ and $\tilde{\Lambda}_1 = 40\,\mathrm{cm}^{-1}$ such that $\Delta\tau_c = 6.44$ and there is substantial inhomogeneous broadening due to the large reorganisation energy of the bath.

The Markovian limit is set as $\tilde{\xi} = 1000\,\mathrm{cm}^{-1}$, producing an overdamped hierarchy of 51 ADOs at $298\,\mathrm{K}$. The calculated linear absorption spectrum, σ_A, is a superb fit to the first peak of the experimental spectrum from reference 213, measured in toluene, as shown in figure 5.2.1 (right). The frequency and normalised intensity of the vibronic transitions involved are also shown, calculated as the square of the corresponding transition dipole moment matrix elements. The increasing intensity of the experimental spectrum above $19\,500\,\mathrm{cm}^{-1}$ indicates the start of the second broad peak caused by higher frequency vibrational modes not included in the model.

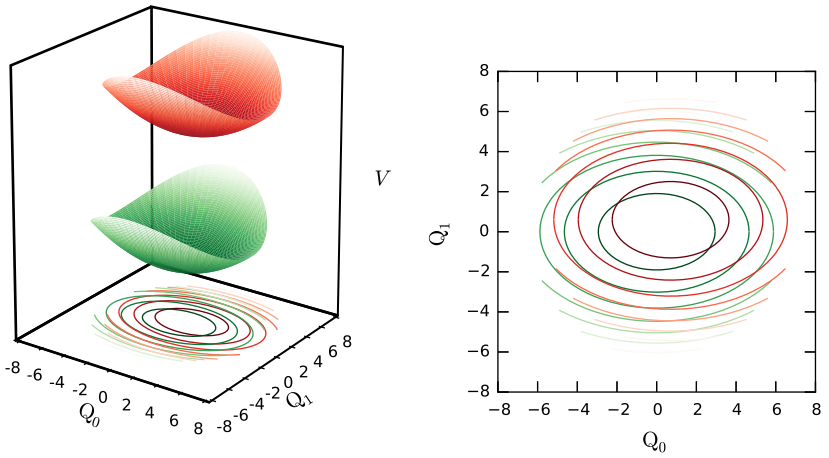

Figure 5.2.2: Potential energy surface of the two-mode PBI monomer, showing V_g (green) and V_e (red).

2D spectra for the two-mode PBI monomer under these conditions were calculated for $T = 1\,\mathrm{ps}$ at intervals of $5\,\mathrm{fs}$ in the impulsive limit, as described in section 2.4.3.1. Figure 5.2.3 shows the absorptive 2D spectra for the first $200\,\mathrm{fs}$ of population time at intervals of $50\,\mathrm{fs}$. The strong system-bath interaction via the large bath reorganisation energy again results in significant broadening such that all Liouville pathways are enveloped by a single peak. Note that as the monomer system only has two electronic states, ESA pathways are not involved in the monomer spectra and any negative intensity is an artefact of early population times, as discussed in section 3.1. However, the initial alignment and elongation of the peak about the diagonal at $T = 0\,\mathrm{fs}$, which diminishes with increasing population time into the uncorrelated peak at $T = 200\,\mathrm{fs}$, demonstrates the significant inhomogeneous broadening and timescale of spectral diffusion, as discussed in chapter 3.

Repeating the analysis of coherence pathways in section 4.3 for the two-mode PBI monomer produces residuals such as the example in figure 5.2.4 (a), for the $(\tilde{\nu}_\tau = 18\,939\,\mathrm{cm}^{-1}, \tilde{\nu}_t = 18\,939\,\mathrm{cm}^{-1})$ coordinate of the rephasing (real) spectra

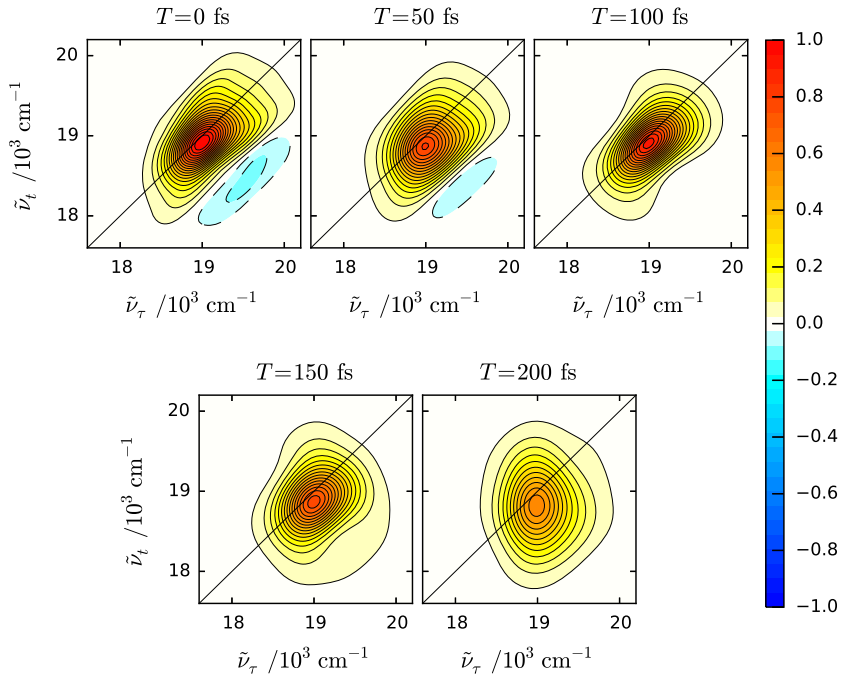

Figure 5.2.3: Absorptive 2D spectra of the two-mode PBI monomer for $T = 0 - 200\,\mathrm{fs}$ at intervals of $50\,\mathrm{fs}$, normalised to the maximum at $T = 0\,\mathrm{fs}$.

after subtraction of an exponential decay with a lifetime of $142\,\mathrm{fs}$. FFT of this residual gives the spectrum in figure 5.2.4 (b), identifying that the spectral amplitude oscillates as a result of two frequencies corresponding to the two vibrational modes with $\tilde{\omega}_0 = 231\,\mathrm{cm}^{-1}$ and $\tilde{\omega}_1 = 550\,\mathrm{cm}^{-1}$. Following the analysis of section 4.2, this means that coherence pathways for both modes contribute to the peak at $(\tilde{\nu}_\tau = 18\,939\,\mathrm{cm}^{-1}, \tilde{\nu}_t = 18\,939\,\mathrm{cm}^{-1})$.

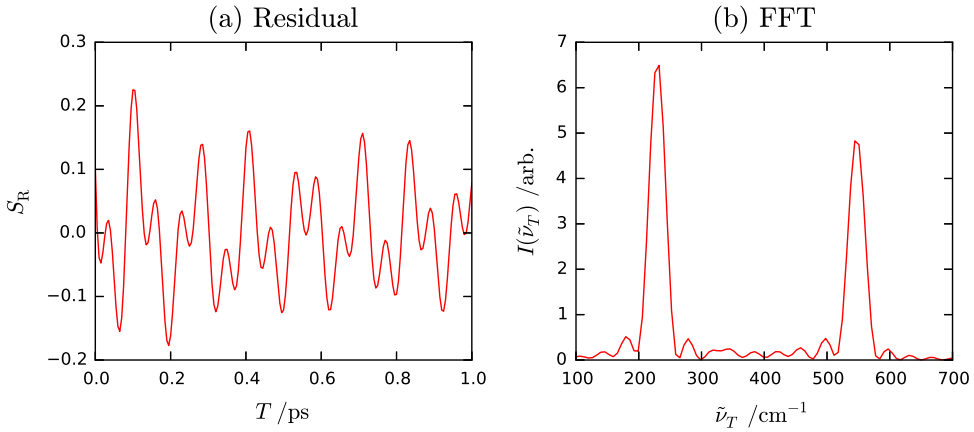

Figure 5.2.4: (a) Residual of the rephasing (real) amplitude for the coordinate $(\tilde{\nu}_\tau = 18\,939\,\mathrm{cm}^{-1}, \tilde{\nu}_t = 18\,939\,\mathrm{cm}^{-1})$, sampled every $5\,\mathrm{fs}$, after subtraction of an exponential decay with a lifetime of $142\,\mathrm{fs}$. (b) FFT power spectrum of the residual in (a), identifying peaks corresponding to ω_0 and ω_1.

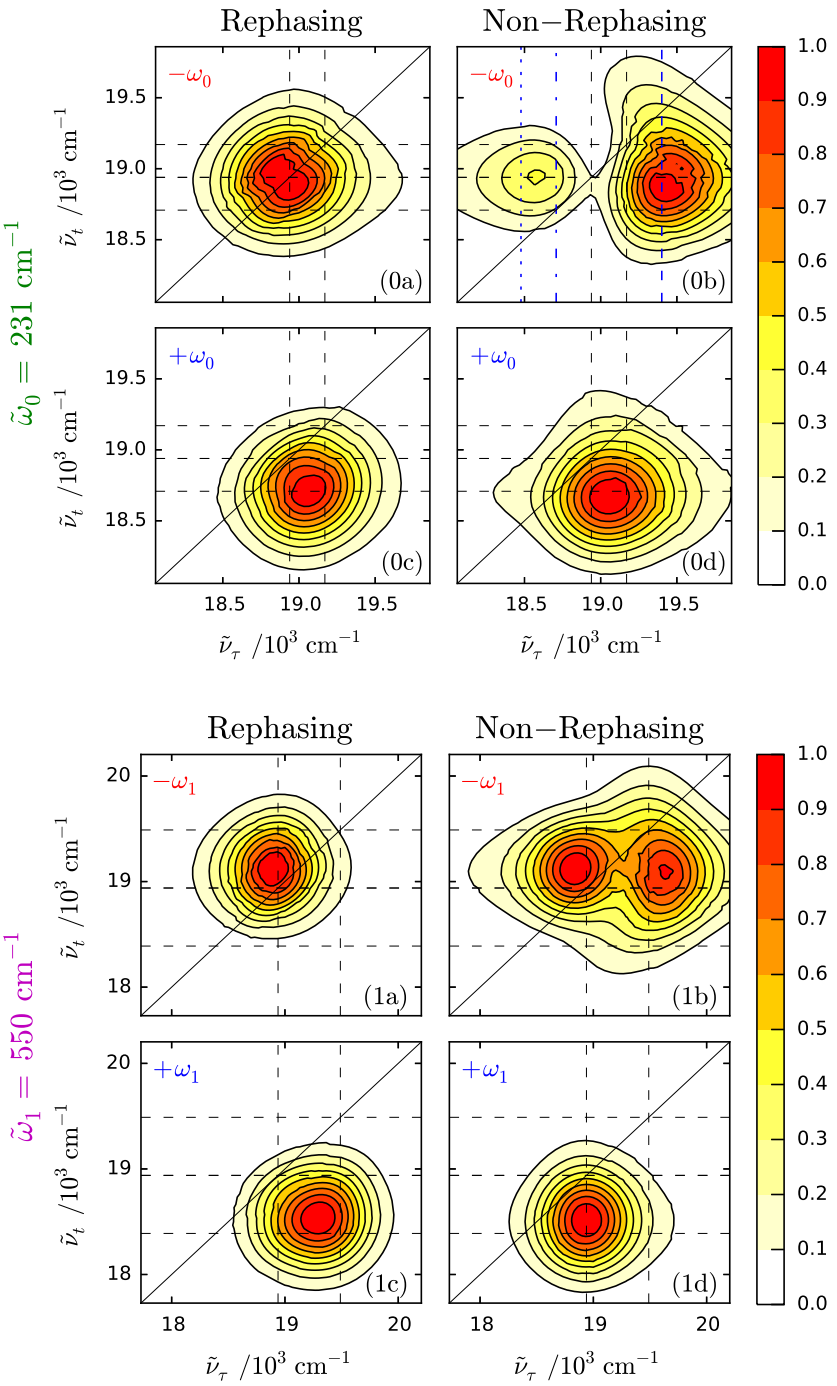

Figure 5.2.5: Amplitude spectra for the two-mode PBI monomer, where the black dashed lines correspond to the vibronic transitions in the location key diagrams of figure 4.2.5 and the patterned blue lines correspond to the excitation frequencies labelled in figure 5.2.6 (a).

Amplitude spectra for the ω_0 and ω_1 modes of the PBI monomer are shown in figure 5.2.5. As the $\tilde{\omega}_1 = 550\,\mathrm{cm}^{-1}$ mode is truncated to the $\nu_1 = 0, 1$ levels only, the amplitude spectra reproduce the arrangement of peaks observed for the unfiltered zinc-porphyrin monomer in figure 4.3.4. The appearance of peaks again matches the location key diagram of figure 4.2.5, where the important

vibronic transition frequencies are shown as dashed lines in figure 5.2.5. However, the much greater spectral broadening for the PBI monomer makes the assignment of peaks much more challenging for the $\tilde{\omega}_0 = 231\,\mathrm{cm}^{-1}$ mode amplitude spectra. Changes in the positions of maximum intensity in figure 5.2.5 (0a-d) compared with figure 4.3.4 (1a-d) suggest significant differences in the coherence pathways involved for this mode. In particular, the negative non-rephasing amplitude spectrum in figure 5.2.5 (0b) shows a split peak, with maximum intensity at a higher excitation frequency than is permitted by the analysis given in section 4.2, shown by the black dashed lines. This is a result of the additional $\nu_0 = 2$ vibrational level included in the system Hamiltonian for the $\tilde{\omega}_0 = 231\,\mathrm{cm}^{-1}$ mode adding coherence pathways into the model which involve an excitation frequency of $\omega_{eg}^0 + 2\omega_0$, shown by the blue dashed line in figure 5.2.5 (0b) and the energy level diagram in figure 5.2.6 (a). An example negative non-rephasing coherence pathway with an excitation frequency of $\omega_\tau = \omega_{eg}^0 + 2\omega_0$ and an emission frequency of $\omega_t = \omega_{eg}^0$ is given in figure 5.2.6 (b), corresponding to the position of maximum intensity in the amplitude spectrum of figure 5.2.5 (0b).

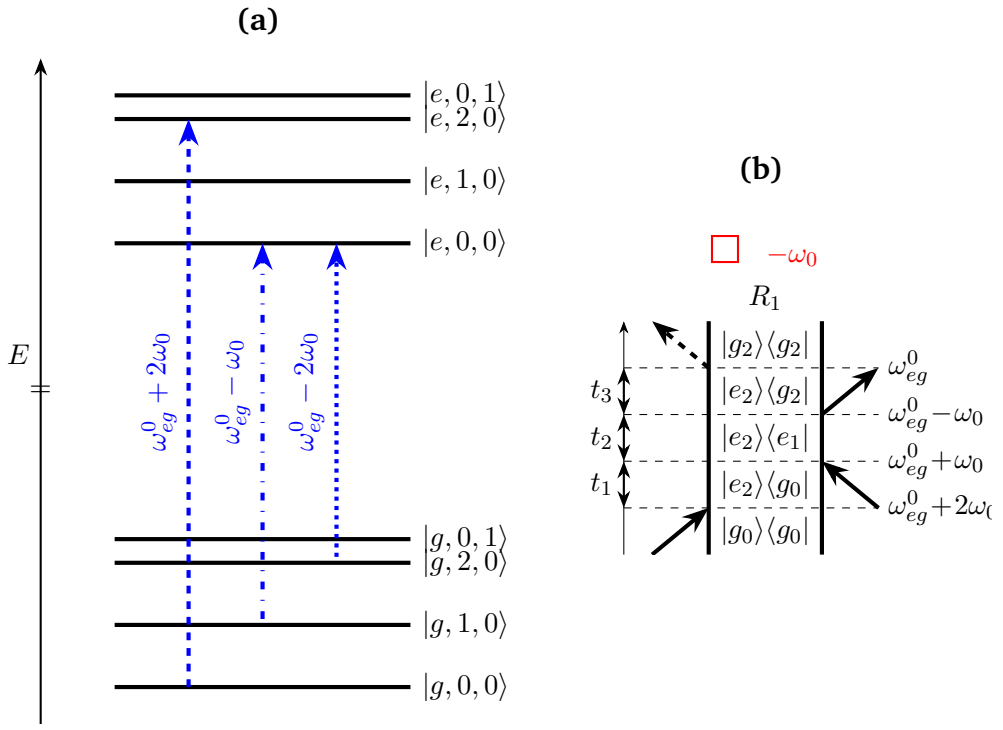

Figure 5.2.6: (a) Energy level diagram for the two-mode PBI monomer, showing the initial Boltzmann distribution for the population of the vibrational levels of the ground electronic state at 298 K in red, as well as the additional transition frequencies labelled in blue in figure 5.2.5 (0b). (b) Example negative non-rephasing coherence pathway contributing to the split peak in figure 5.2.5 (0b), where the states are abbreviated to show the quantum number of the $\tilde{\omega}_0 = 231\,\mathrm{cm}^{-1}$ mode only, as $|g_\nu\rangle = |g,\nu,0\rangle$.

Moreover, at $298\,\mathrm{K}$, the low frequency $\tilde{\omega}_0 = 231\,\mathrm{cm}^{-1}$ mode has a significant population in the excited vibrational levels of the ground electronic state, such that the assumption made in section 4.2, which limited the analysis to pathways starting from $|g,0\rangle\langle g,0|$ only, is no longer valid. The initial Boltzmann distribution amongst the vibrational levels of the ground electronic state is shown in red in figure 5.2.6 (a), where the width of each energy level corresponds to a population of unity. The hot populations introduce further Liouville pathways involving excitation frequencies red-shifted from the fundamental, including $\omega_{eg}^0 - \omega_0$ and $\omega_{eg}^0 - 2\omega_0$, shown as the dash-dotted and dotted blue lines, respectively, in figures 5.2.6 (a) and 5.2.5 (0b). These pathways, with lower excitation frequencies, produce the less intense portion of the split peak in the negative non-rephasing amplitude spectrum in figure 5.2.5 (0b). However, such splitting is unexpected in the negative non-rephasing amplitude spectrum for the $\tilde{\omega}_1 = 550\,\mathrm{cm}^{-1}$ mode in figure 5.2.5 (1b) and is not observed in the equivalent for a monomer coupled to the $550\,\mathrm{cm}^{-1}$ mode only, which shows the same lineshape as figure 4.3.4 (1b). Therefore, the splitting in figure 5.2.5 (1b) is likely an artefact resulting from the FFT of the bicomponent signal for the two-mode monomer, suggesting some interference between modes, but further analysis of the Liouville pathways is required. In order to focus on the formation of vibronic dimers, additional Liouville pathway analysis for such multimode vibronic monomers is left for future work. The results in figure 5.2.5 demonstrate that even a small increase in the dimensions of the quantum system produces significant additional complexity in the spectra, which is fully accounted for by the vibronic models developed in this thesis.

Covalent bonding of the PBI monomers at the imide position then produces a vibronic dimer with collinear transition dipole moments, such that a J-aggregate is formed. As described in ref. 213, connecting two PBI monomers with a N-N bond produces the D0 dimer, with a centre-to-centre separation distance of $1.27\,\mathrm{nm}$. Inserting a *p*-phenylene spacer between the nitrogen atoms then increases the separation distance to $1.7\,\mathrm{nm}$ in the D1 dimer. The structure of the two dimers and their experimental linear absorption spectra are shown in figure 5.2.7. The red-shift of the fundamental peak from $18\,939\,\mathrm{cm}^{-1}$ for the monomer, M, to $18\,657\,\mathrm{cm}^{-1}$ for D0, accompanied by the decrease in intensity of the second and third peaks relative to the fundamental peak, confirms formation of a J-aggregate, as discussed in section 5.1. But the increase in separation distance in D1 weakens the electronic coupling such that there is no red-shift and the linear absorption spectrum remains similar to that of the monomer. Note that the absorption spectra in figure 5.2.7 show all three broad peaks in the range 18 - $23 \times 10^3\,\mathrm{cm}^{-1}$, where figure 5.2.1 shows the first peak only, in the range 18 - $20 \times 10^3\,\mathrm{cm}^{-1}$.

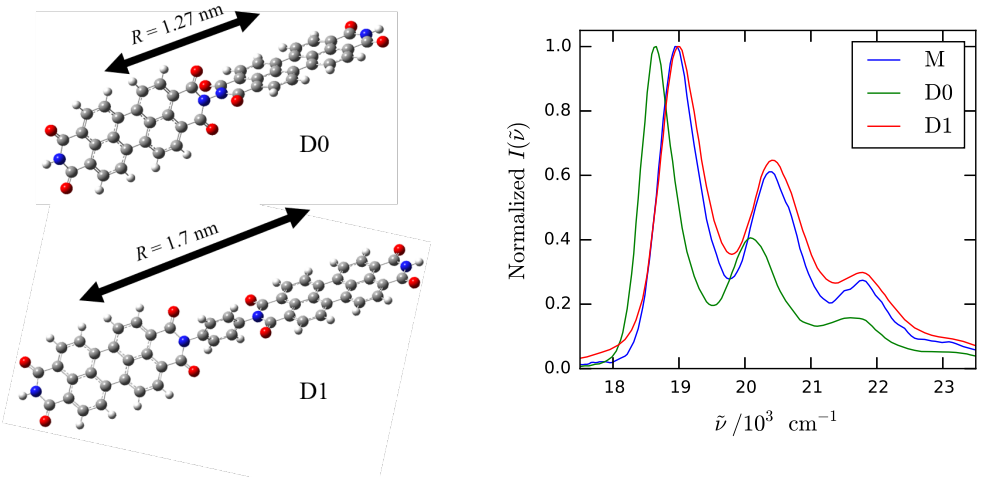

Figure 5.2.7: (Left) Molecular structure and monomer separation distance for the D0 and D1 dimers. (Right) Measured linear absorption spectra for M, D0 and D1, reproduced from reference 213.

Similarly, the formation of a J-aggregate is demonstrated in the 2D spectra for these systems. The experimental absorptive 2D spectra at $T = 100\,\mathrm{fs}$ are shown in figure 5.2.8 (top), for M (left), D0 (middle), and D1 (right), reprinted from ref. 213. The monomer spectrum demonstrates inhomogeneous broadening along the diagonal as well as elongation about the emission axis, $\tilde{\nu}_t = \tilde{\nu}_3$, as seen in the calculated spectra for the two-mode monomer in figure 5.2.3. The D0 spectrum then shows a red-shift in excitation frequency of the positive peak, as in the linear spectrum, accompanied by the appearance of a strong negative peak above the diagonal, corresponding to ESA from the lower, symmetric exciton state to the doubly excited state. The weaker electronic coupling in the D1 dimer causes no red-shift, where any ESA is obscured by the broader lineshape of the positive peak, resulting from the increased conformational freedom of the system.[213]

In ref. 213, the experimental measurements were supported by simple calculations which considered the electronic degrees of freedom only in the system Hamiltonian, following the Kasha model discussed in section 2.2.1.2. The electronic transition frequency of the monomer was determined from the experimental linear absorption spectrum as $\tilde{\omega}^0_{eg} = 18\,939\,\mathrm{cm}^{-1}$, and the magnitude of the monomer transition dipole moment was determined from the electronic coupling in the D0 dimer. As discussed in section 5.1, for a J-aggregate in the strong coupling limit, the maxima of the positive GSB/SE peak and the negative ESA peak are separated in emission frequency by $2J$, and thus can be used to determine the electronic coupling strength. In ref. 213, a vertical cut of the experimental D0 spectrum was taken at $\tilde{\nu}_\tau = 18\,682\,\mathrm{cm}^{-1}$, giving a difference in emission frequency of the positive and negative maxima of $2J/hc = 520\,\mathrm{cm}^{-1}$ such that $J/hc = -260\,\mathrm{cm}^{-1}$; where the minus is added in the knowledge that $J < 0$ for J-aggregates. For D0, with a separation distance of

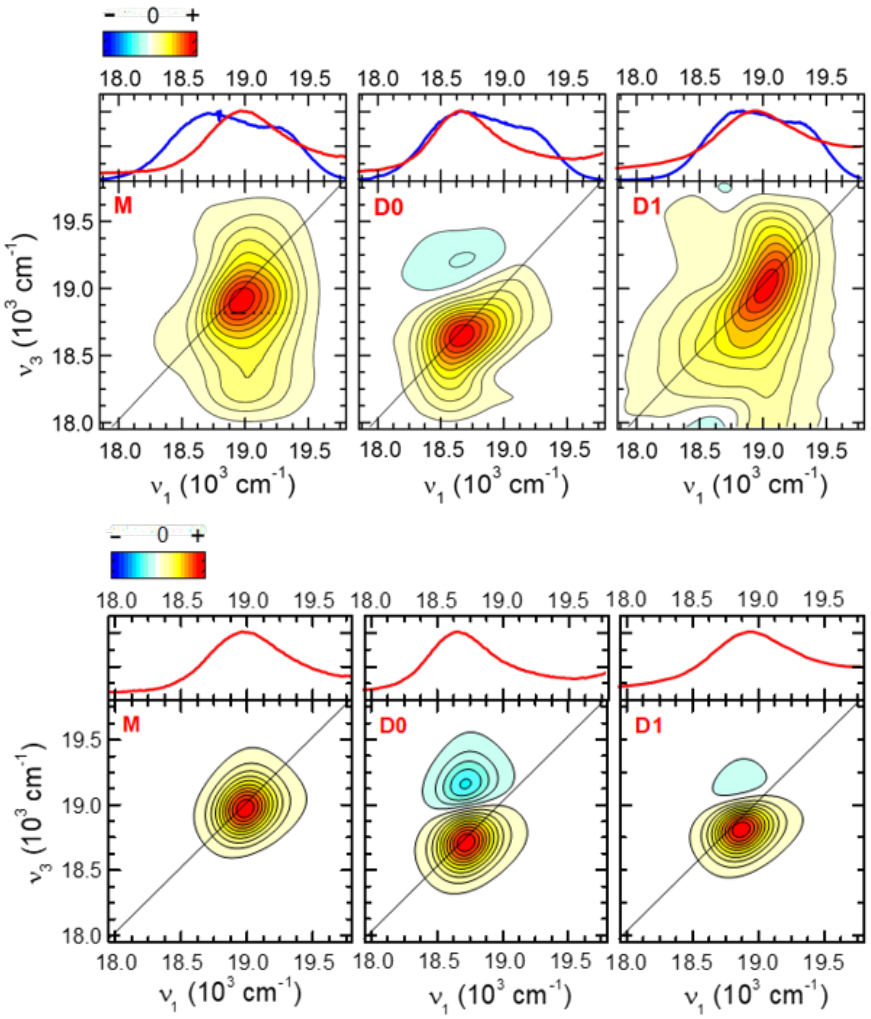

Figure 5.2.8: Experimental (top) and calculated (bottom) absorptive 2D spectra for M (left), D0 (middle) and D1 (right) at $T = 100\,\mathrm{fs}$, each normalised to their respective maxima. The top panels of each spectrum show the measured linear absorption spectra in red and the NOPA laser spectrum in blue for the experimental data. Reprinted (adapted) with permission from reference 213. Copyright 2019 American Chemical Society.

$R = 1.27\,\mathrm{nm}$, dissolved in toluene, where $\epsilon_r = 2.38$,[253] this corresponds to a monomer transition dipole moment of magnitude $\mu_{eg} = 11.22\,\mathrm{D}$, which is the value used in the improved vibronic model for the two-mode PBI monomer above. Keeping the monomer parameters fixed and increasing the separation distance to $R = 1.7\,\mathrm{nm}$ significantly reduces the electronic coupling strength in D1 to $J/hc = -108\,\mathrm{cm}^{-1}$, as expected from the $J \propto R^{-3}$ relationship in the Förster coupling equation. 2D spectra were then calculated using the EOM-PMA, coupling the electronic system to an overdamped bath where $\tilde{\eta}_1 = 20\,\mathrm{cm}^{-1}$ and $\tilde{\Lambda}_1 = 75\,\mathrm{cm}^{-1}$ such that $\Delta\tau_c = 1.21$ at $298\,\mathrm{K}$, with $\xi = 10\Lambda_1$ producing a hierarchy of 11 ADOs. The laser spectrum was centred at the electronic transition frequency of the monomer, $\omega_m = \omega^0_{eg}$, or the dimers, $\omega_m = \omega^0_{e^+g}$, with a FWHM nearing the impulsive limit of $\tau_p = 5\,\mathrm{fs}$ and

$\chi_m = 10^7\,\mathrm{V\,m^{-1}}$ in all cases.

The calculated absorptive 2D spectra at $T = 100\,\mathrm{fs}$ are shown in figure 5.2.8 (bottom), for M (left), D0 (middle), and D1 (right), reprinted from ref. 213. Without accounting for the system vibrational modes, the lineshape is significantly narrowed, where a small amount of inhomogeneous broadening provides a slight elongation about the diagonal. These calculated spectra clearly demonstrate the formation of a J-aggregate, showing a red-shift in excitation frequency of the positive peak and emergence of a strong ESA peak for D0, as seen in the experimental spectra. In this way, these PBI dimers clearly obey the Kasha model. However, in contrast to the experimental spectrum, ESA is observed in the calculated spectrum for D1 due to the reduced broadening, along with a minor red-shift of the positive peak compared with M. This is a result of the static disorder being kept constant for M, D0 and D1 to demonstrate the effect of reduced electronic coupling in the Kasha model. The poor fit to the experimental lineshape suggests the calculated spectra are overly simplified and a careful consideration of the vibrational degrees of freedom is required.

To go beyond the theoretical calculations presented in ref. 213, D0 and D1 are modelled as vibronic homodimers, constructed from the two-mode vibronic monomer defined above. Each dimer system, with $\mathsf{H_S} = \mathsf{H}_\mathrm{D}^E$ and $\hat{\mu} = \hat{\mu}_\mathrm{D}^E$, is coupled to a single overdamped bath for electronic dephasing through $\mathsf{B}_1 = \mathsf{B}_{1,\mathrm{D}}^E$. All monomer and bath parameters are defined as for the two-mode PBI monomer above, which produced the excellent fit in figure 5.2.1, assuming the excited state displacement and frequency of each mode is unchanged on dimer formation. Including the vibrational degrees of freedom for the $\tilde{\omega}_0 = 231\,\mathrm{cm^{-1}}$ and $\tilde{\omega}_1 = 550\,\mathrm{cm^{-1}}$ modes accounts for vibronic quenching of the electronic coupling strength and introduces a multitude of additional Liouville pathways into the calculations, improving the spectral lineshape. Note that both D0 and D1 dimers correspond to the strong coupling limit with respect to each vibrational mode, where the small displacements of $\Delta_0 = 0.7$ and $\Delta_1 = 0.6$ produce reorganisation energies of $\tilde{\lambda}_0 = 57\,\mathrm{cm^{-1}}$ and $\tilde{\lambda}_1 = 99\,\mathrm{cm^{-1}}$, respectively, which are less than the electronic coupling strengths of $|J|/hc = 260\,\mathrm{cm^{-1}}$ for D0 and $|J|/hc = 108\,\mathrm{cm^{-1}}$ for D1.

Figure 5.2.9 shows the calculated linear absorption spectra, σ_A, for the two-mode monomer and dimers, compared with the measured spectra for M and D0 from figure 5.2.7. Despite modelling D0 with the experimentally determined electronic coupling strength of $J/hc = -260\,\mathrm{cm^{-1}}$, the red-shift of the peak in the calculated spectrum for D0 compared with M is smaller than that of the measured spectra, demonstrating quenching of the electronic coupling on addition of the vibrational modes into the model. This suggests the value for the

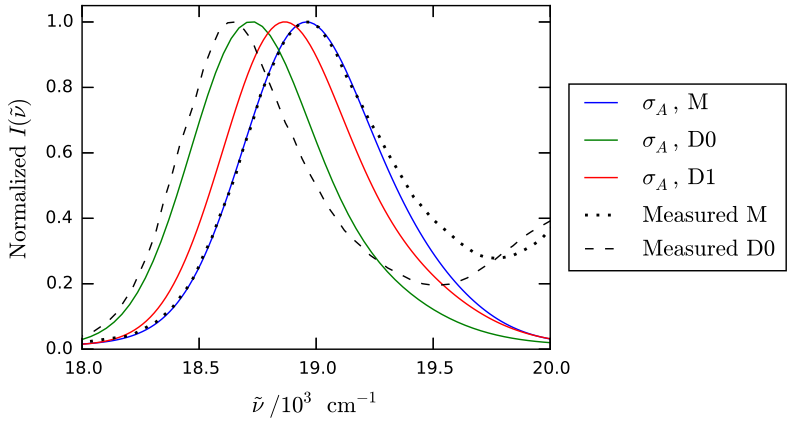

Figure 5.2.9: Calculated linear absorption spectra, σ_A, for two-mode M, D0 and D1 PBI systems, as well as the measured spectra for M and D0 from reference 213.

electronic coupling in D0 obtained from the experimental measurements in ref. 213 is too small and needs to be increased by ca. $80\,\mathrm{cm}^{-1}$ in order to counteract the vibronic quenching of the ω_0 and ω_1 modes. A further increase in the electronic coupling strength may be required on considering any additional quenching from other system modes. Furthermore, the calculated linear absorption spectrum for D1 in figure 5.2.7 shows a reduced red-shift due to the weaker electronic coupling, but the lack of any shift in the experimental spectrum for D1 in figure 5.2.7 suggests that the coupling remains insufficiently quenched in the current model. This implies that strong vibronic coupling to other system modes not modelled have a significant impact in the D1 dimer.

2D spectra for the improved vibronic D0 and D1 dimers were then calculated at intervals of $50\,\mathrm{fs}$ in the impulsive limit. Computational limitations due to the size of the system Hamiltonian permitted propagation to a maximum of $T = 100\,\mathrm{fs}$ only, where tensor product of the two-mode PBI monomers produces operators for the two-mode dimers with dimensions of 64x64 matrices. Therefore, 2D spectra were also calculated for dimers constructed from vibronic monomers coupled to either ω_0 or ω_1 only, to allow propagation up to $T = 200\,\mathrm{fs}$ and comparison with the two-mode monomer spectra in figure 5.2.3. The system Hamiltonians for the single-mode monomers were truncated to $\nu_j = 0, 1$ vibrational levels only, reducing the dimer Hamiltonian dimensions to a more manageable 16x16 matrix. This allows isolation of the contributions of each mode to the dimer spectra. However, it is important to note that the two-mode dimer spectra account for Liouville pathways simultaneously involving both modes and are therefore not equivalent to the sum of the single-mode spectra.

2D spectra for the single-mode D0 systems are presented in figure 5.2.10, and for the two-mode D0 dimer in figure 5.2.11. These figures again show the red-

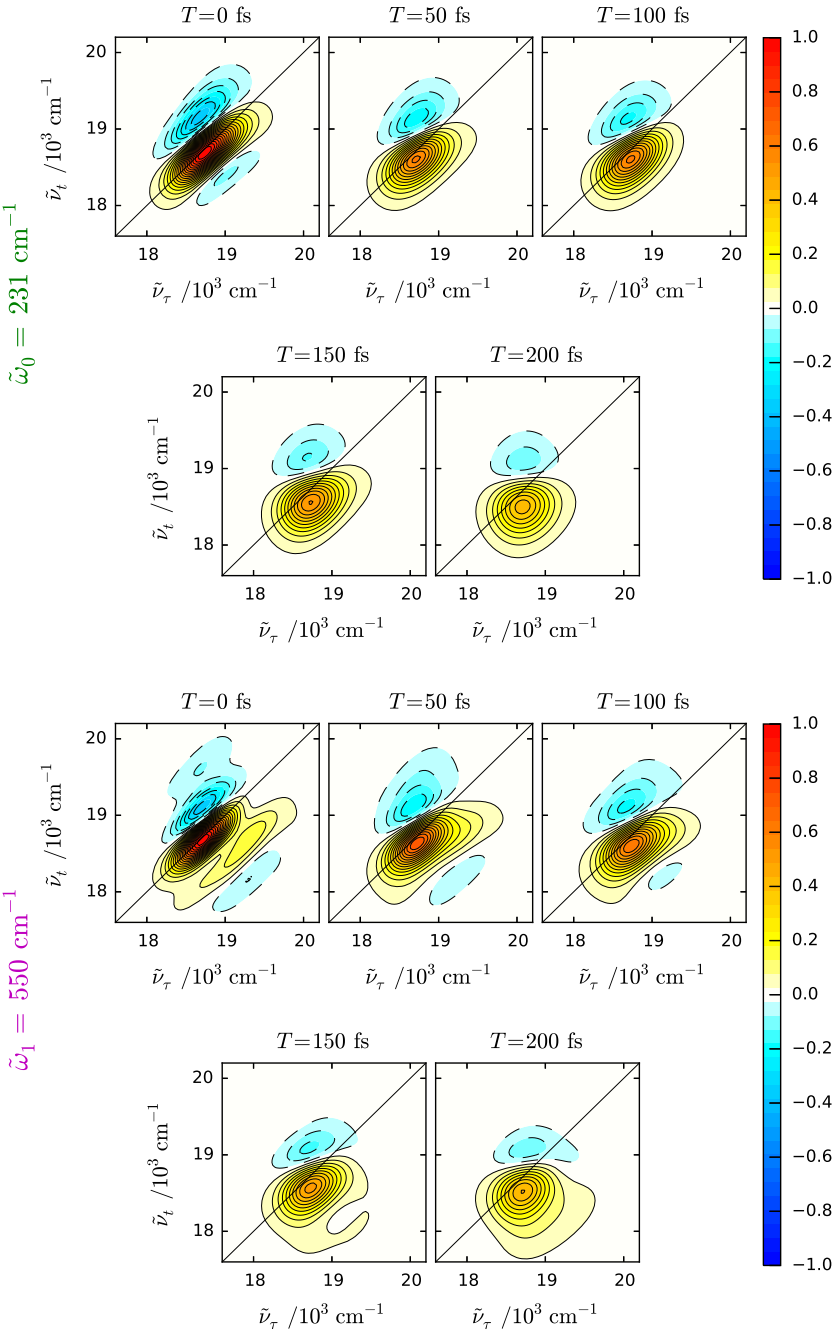

Figure 5.2.10: Absorptive 2D spectra for the D0 homodimer, where the constituent monomers are coupled to either the $\tilde{\omega}_0 = 231\,\mathrm{cm}^{-1}$ or $\tilde{\omega}_1 = 550\,\mathrm{cm}^{-1}$ vibrational mode only, for $T = 0 - 200\,\mathrm{fs}$ at intervals of $50\,\mathrm{fs}$, normalised to the maximum at $T = 0\,\mathrm{fs}$.

shift in the positive peak and the strong ESA peak above the diagonal observed in the spectra for the simplified D0 dimer in figure 5.2.8. But, the vibronic D0 spectra have a much improved lineshape, demonstrating that the ESA peak has contributions from both the ω_0 and ω_1 modes and endures up to a population time of at least $T = 200\,\mathrm{fs}$. The substantial inhomogeneous broadening of the PBI monomers produces clear elongation of the positive GSB/SE peak along the

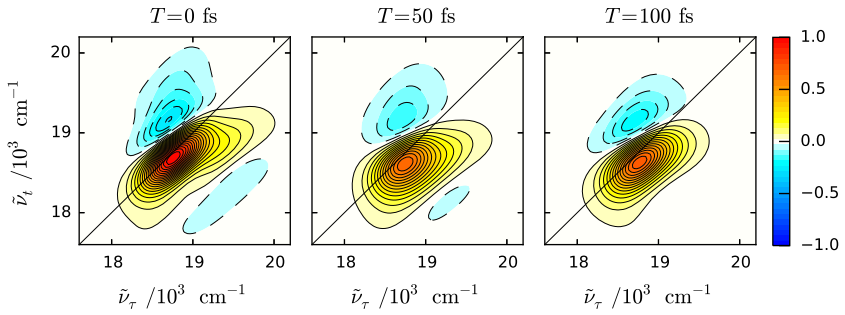

Figure 5.2.11: Absorptive 2D spectra for the two-mode D0 homodimer at $T = 0$, 50 and $100\,\mathrm{fs}$, normalised to the maximum at $T = 0\,\mathrm{fs}$.

diagonal, which diminishes due to spectral diffusion over the $200\,\mathrm{fs}$ of population time. For these dimer spectra, the decay in the system-bath correlation function is also visible in the decreasing gradient of the nodal line between the positive GSB/SE peak and negative ESA peak.[5,19] The spectra in figure 5.2.10 show that the gradient of the nodal line almost matches the diagonal of the spectra at $T = 0\,\mathrm{fs}$ and then decreases to approximately zero by $T = 200\,\mathrm{fs}$, where the nodal line follows the excitation axis, $\tilde{\nu}_\tau$. Furthermore, the nodal line in the two-mode D0 spectrum at $T = 100\,\mathrm{fs}$ in figure 5.2.11 shows good qualitative agreement with that of the experimental spectrum in figure 5.2.8 (top, middle). This suggests that the $\tilde{\Lambda}_1 = 40\,\mathrm{cm}^{-1}$ used to achieve an excellent fit of the linear absorption spectrum of the PBI monomer also provides a suitable correlation time for the system-bath interaction of the D0 dimer. Again, note that shallow blue regions below the diagonal in these spectra are an artefact of early population times and are not the result of ESA pathways.

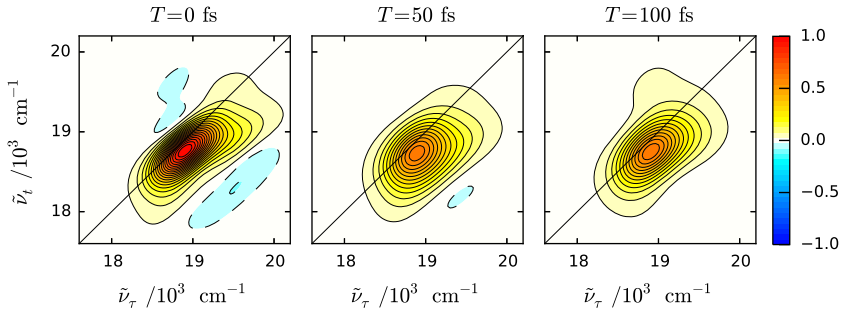

Figure 5.2.12: Absorptive 2D spectra for the two-mode D1 homodimer at $T = 0$, 50 and $100\,\mathrm{fs}$, normalised to the maximum at $T = 0\,\mathrm{fs}$.

In stark contrast to the calculated spectrum for the simplified D1 dimer in figure 5.2.8 (bottom, right), the two-mode D1 dimer spectra in figure 5.2.12 show that addition of the vibrational degrees of freedom into the D1 system suppresses the ESA peak, such that the weak negative peak above the diagonal visible at $T = 0\,\mathrm{fs}$ is absent within $T = 50\,\mathrm{fs}$. This is also observed for the single-mode D1 dimer systems in figure 5.2.13, where the ESA peak is removed within

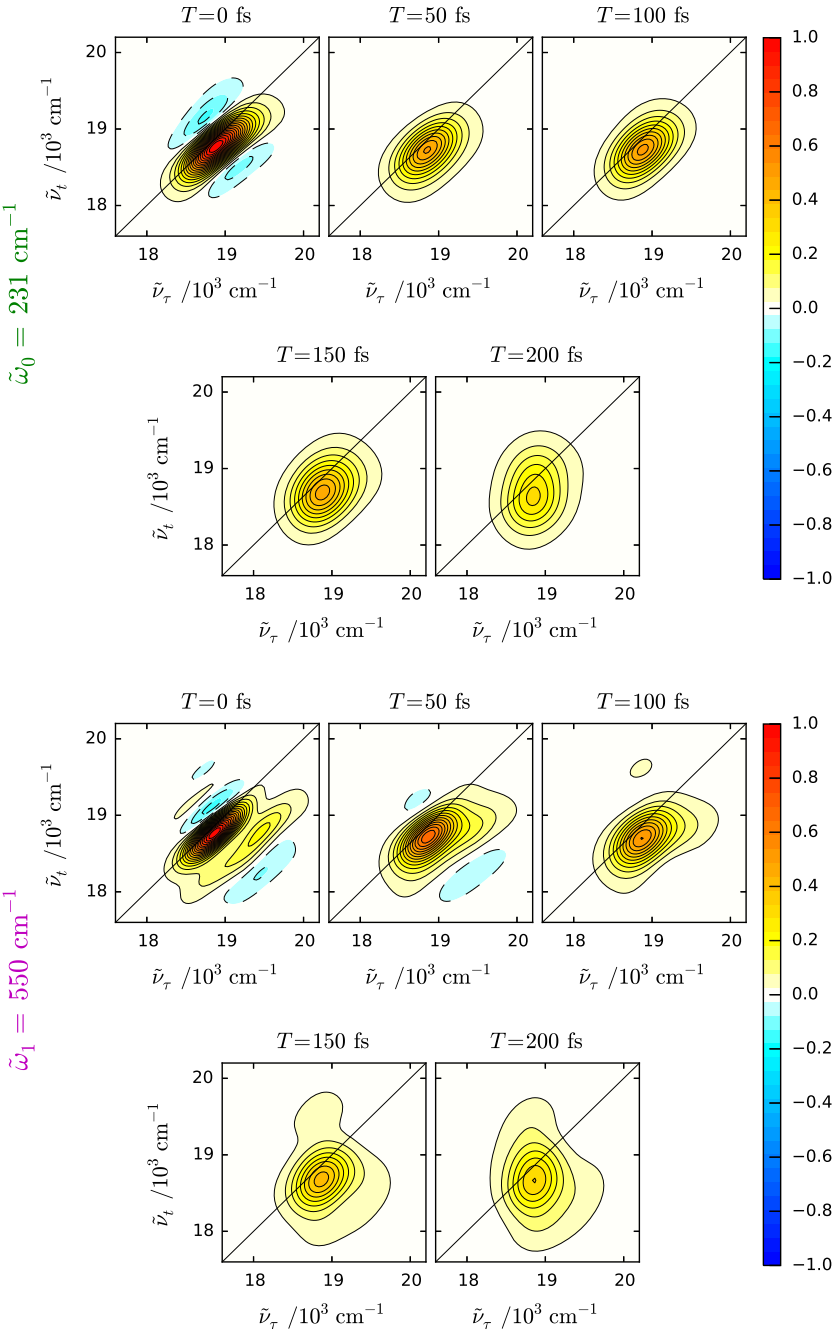

Figure 5.2.13: Absorptive 2D spectra for the D1 homodimer, where the constituent monomers are coupled to either the $\tilde{\omega}_0 = 231\,\mathrm{cm}^{-1}$ or $\tilde{\omega}_1 = 550\,\mathrm{cm}^{-1}$ vibrational mode only, for $T = 0 - 200\,\mathrm{fs}$ at intervals of $50\,\mathrm{fs}$, normalised to the maximum at $T = 0\,\mathrm{fs}$.

$T = 50\,\mathrm{fs}$ for D1 coupled to $\tilde{\omega}_0 = 231\,\mathrm{cm}^{-1}$ and within $T = 100\,\mathrm{fs}$ for D1 coupled to $\tilde{\omega}_1 = 550\,\mathrm{cm}^{-1}$. For both single-mode dimers, spectral diffusion produces an uncorrelated peak elongated about the emission axis at $T = 200\,\mathrm{fs}$, resembling the two-mode PBI monomer spectrum in figure 5.2.3. This suggests that the absence of a negative ESA peak in the experimental 2D spectrum for the D1 dimer in figure 5.2.8 (top, right) is not only caused by increased static disorder,

but also by the ESA peak becoming lost within the amplitude of the positive peak due to vibronic quenching of the electronic coupling. This demonstrates that a full understanding of the experimental 2D spectra of these dimer systems requires a detailed account of vibronic effects, beyond the Kasha model for the formation of exciton states.

In this section, the model has been tested through application of the vibronic dimer Hamiltonian of section 2.2.1.3 to two PBI homodimer species. This extends our results in ref. 213 by accounting for the vibronic coupling within the dimers, producing improved spectral lineshape and beginning an important discussion of vibronic quenching within these systems. Whilst the calculated spectra show excellent qualitative agreement with the experimental results, the size of the dimer Hamiltonian limits the population time for which spectra can be obtained, dependent on the computational resources available. Calculation of 2D spectra for a greater range of population times will enable a more thorough analysis of spectral broadening and the timescale of spectral diffusion, for comparison with the experimental results. The success of the model for the simple homodimer systems in this section is challenged in section 5.3, where the model is applied to a more complex vibronic heterodimer.

5.3 Energy Transfer in a Vibronic Heterodimer

Finally, the model is applied to a vibronic heterodimer to investigate excitation energy transfer (EET) driven by vibrational relaxation between vibronic exciton states. The dimer Hamiltonian has the usual form, $\mathsf{H}_\mathrm{S} = \mathsf{H}_\mathrm{D}^E$, but where monomer A has $\tilde{\omega}^0_{eg\mathrm{A}} = 15\,000\,\mathrm{cm}^{-1}$ and $\tilde{\omega}_{0\mathrm{A}} = 500\,\mathrm{cm}^{-1}$ with $\Delta_{0\mathrm{A}} = 1$ such that $\tilde{\lambda}_{0\mathrm{A}} = 250\,\mathrm{cm}^{-1}$, whilst monomer B has a lower transition frequency of $\tilde{\omega}^0_{eg\mathrm{B}} = 14\,800\,\mathrm{cm}^{-1}$ coupled to a lower frequency vibrational mode of $\tilde{\omega}_{0\mathrm{B}} = 350\,\mathrm{cm}^{-1}$ with $\Delta_{0\mathrm{B}} = 1$ such that $\tilde{\lambda}_{0\mathrm{B}} = 175\,\mathrm{cm}^{-1}$. After diagonalization, the exciton basis Hamiltonian is truncated to account for the $\nu_j = 0, 1$ vibrational levels of each monomer, such that the states $|\Psi^E_k\rangle$ where $k = 0 - 3$ correspond to the doubly ground states, $k = 4 - 11$ to the singly excited states and $k = 12 - 15$ to the doubly excited states. The dimer is again assumed to have a collinear arrangement of transition dipole moments, where both monomers have the same $\mu_{eg} = 13\,\mathrm{D}$ in $\hat{\mu} = \hat{\mu}^E_\mathrm{D}$, such that a separation distance of $R = 1.53\,\mathrm{nm}$ results in an electronic coupling of $J = -200\,\mathrm{cm}^{-1}$.

The singly excited states for this heterodimer in the composite site basis, $|\Psi^S_\mathrm{D}\rangle$, and in the exciton basis, $|\Psi^E_\mathrm{D}\rangle$, are shown in the energy level diagram of figure 5.3.1. The smaller electronic transition frequency and vibrational mode frequency of monomer B result in the composite site basis states where monomer B is in the electronic excited state, $|g, n_\mathrm{A}, e, n_\mathrm{B}\rangle$, being lower in energy

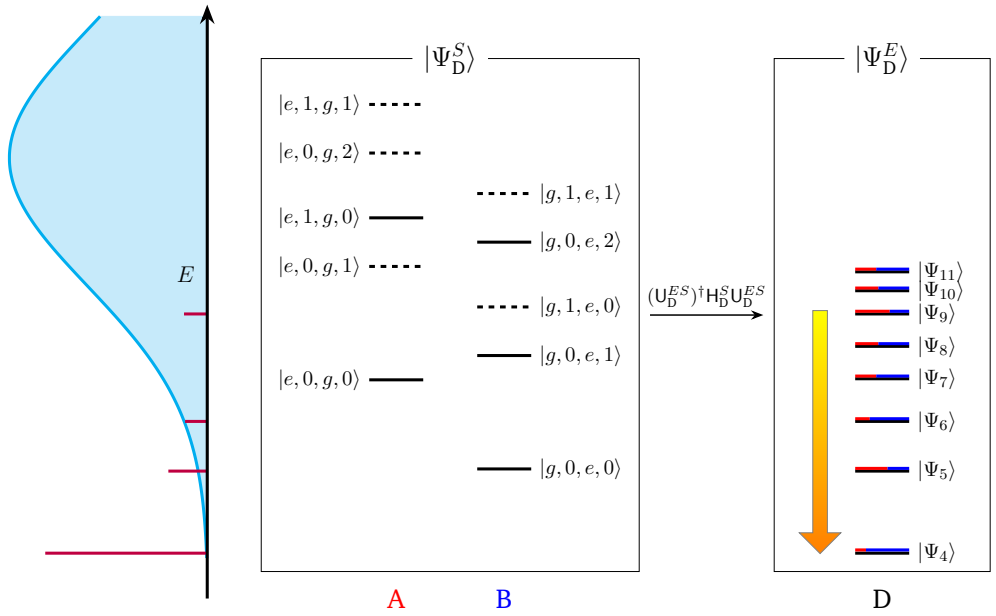

Figure 5.3.1: Energy level diagram showing the singly excited states of the vibronic heterodimer. In the composite site basis, $|\Psi_D^S\rangle$, the states are arranged into states where monomer A or B is excited, where states involving ground electronic states with excited vibrational levels are shown as dashed lines. In the exciton basis, $|\Psi_D^E\rangle$, the states are shaded in terms of the contributions of each monomer where A (B) is red (blue). The laser spectrum, adjusted relative to the ground state $|\Psi_0^E\rangle = |g,0,g,0\rangle$, is also shown (light blue, shaded), as well as the stick spectrum corresponding to the transition dipole moment matrix elements squared for transitions from the ground state to the singly excited exciton states (purple). The orange arrow indicates vibrational relaxation.

than the equivalent states for monomer A, $|e,n_A,g,n_B\rangle$. Diagonalization of the site basis Hamiltonian then produces a manifold of exciton states delocalized across the two monomers. The contribution of monomer A to each exciton state, the eigenstates of H_D^S, is calculated by summing the square of the coefficients which correspond to A being in the electronic excited state whilst B is in the ground state, $|e,n_A,g,n_B\rangle$, and presenting this sum as a fraction of the total. The contribution of monomer B is similarly calculated. In figure 5.3.1, the exciton states are shaded with the contribution of A in red and B in blue. Unlike in a homodimer, where each monomer contributes equally to each exciton state, in this heterodimer, the lowest exciton state, $|\Psi_4\rangle$, is 80% monomer B, whilst the higher energy state $|\Psi_9\rangle$ is 64% monomer A. Therefore, relaxation of a population in $|\Psi_9\rangle$ to $|\Psi_4\rangle$ corresponds to a decrease in the proportion of excitation energy localised on monomer A, accompanied by an increase in the proportion localised on monomer B. In this way, relaxation in the exciton basis corresponds to the transfer of excitation energy in the site basis, which is the essence of excitation energy transfer (EET) in excitonic light-harvesting systems.[82]

In order to demonstrate evidence for such EET in 2DES, the EOM-PMA is employed to selectively excite the higher energy exciton states of the vibronic heterodimer. 2D spectra at increasing population times are then used to monitor the transfer of population to lower exciton states via rapid vibrational relaxation, caused by coupling to a homogeneous overdamped bath. The laser spectrum is centred at $\tilde{\omega}_m = 16\,000\,\mathrm{cm}^{-1}$, with $\chi_m = 10^7\,\mathrm{V\,m}^{-1}$ and a long pulse duration of $\tau_p = 30\,\mathrm{fs}$, which produces a much narrower spectrum than used in chapter 4. The laser spectrum is included in figure 5.3.1, adjusted relative to the energy of the ground electronic state, $|\Psi_0^E\rangle = |g,0,g,0\rangle$, to show the preferential excitation of higher energy exciton levels. The square of the transition dipole moment matrix elements describing transitions from the ground electronic state to the singly excited exciton states are also shown in purple. The laser spectrum is therefore designed to preferentially induce transitions to exciton state $|\Psi_9\rangle$, with no intensity at the transition frequency for the lowest exciton state, ω_{40}. The heterodimer is coupled to two overdamped baths, one for electronic dephasing where $\mathsf{B}_1 = \mathsf{B}_{1,\mathrm{D}}^E$, with $\tilde{\eta}_1 = 20\,\mathrm{cm}^{-1}$ and $\tilde{\Lambda}_1 = 250\,\mathrm{cm}^{-1}$, and a second for vibrational relaxation where $\mathsf{B}_2 = \mathsf{B}_{2,\mathrm{D}}^E$, with $\tilde{\eta}_2 = 20\,\mathrm{cm}^{-1}$ and $\tilde{\Lambda}_2 = 250\,\mathrm{cm}^{-1}$. Both baths correspond to the homogeneous limit, with $\Delta\tau_c = 0.36$, such that dephasing/relaxation is rapid and approximately Markovian. Calculations are completed at $298\,\mathrm{K}$, with $\tilde{\xi} = 1000\,\mathrm{cm}^{-1}$ such that an overdamped hierarchy of 51 ADOs accounts for both baths simultaneously.

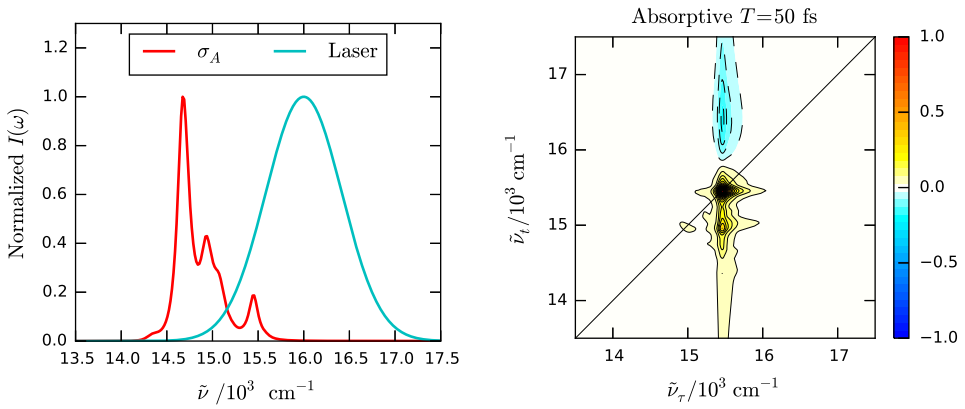

Figure 5.3.2: (Left) Calculated linear absorption spectrum, σ_A, of the vibronic heterodimer with laser spectrum overlaid. (Right) Normalised absorptive 2D spectrum at $T = 50\,\mathrm{fs}$.

The linear absorption spectrum and laser spectrum are shown in figure 5.3.2 (left). The homogeneous bath results in a narrow linewidth for each of the transitions identified in purple in figure 5.3.1, where the narrow laser spectrum focuses on the peak at ca. $15\,460\,\mathrm{cm}^{-1}$, corresponding to transitions from $|\Psi_0^E\rangle$ to $|\Psi_9^E\rangle$ as discussed above. Figure 5.3.2 (right) shows the absorptive 2D spectrum at $T = 50\,\mathrm{fs}$. The spectrum is dominated by peaks with an excitation frequency of ca. $15\,460\,\mathrm{cm}^{-1}$ due to spectral filtering, where the homogeneous

baths produce Lorentzian lineshapes for each peak. At this excitation frequency, positive peaks have emission frequencies corresponding to each of the peaks in the linear absorption spectrum and the negative ESA peak above the diagonal again demonstrates the formation of a J-aggregate as in section 5.2. Extension of the negative ESA peak to higher $\tilde{\nu}_t$ and the positive GSB/SE peaks to lower $\tilde{\nu}_t$ is a result of using the particularly narrow laser spectrum within the EOM-PMA; an effect which requires further investigation, not included here.

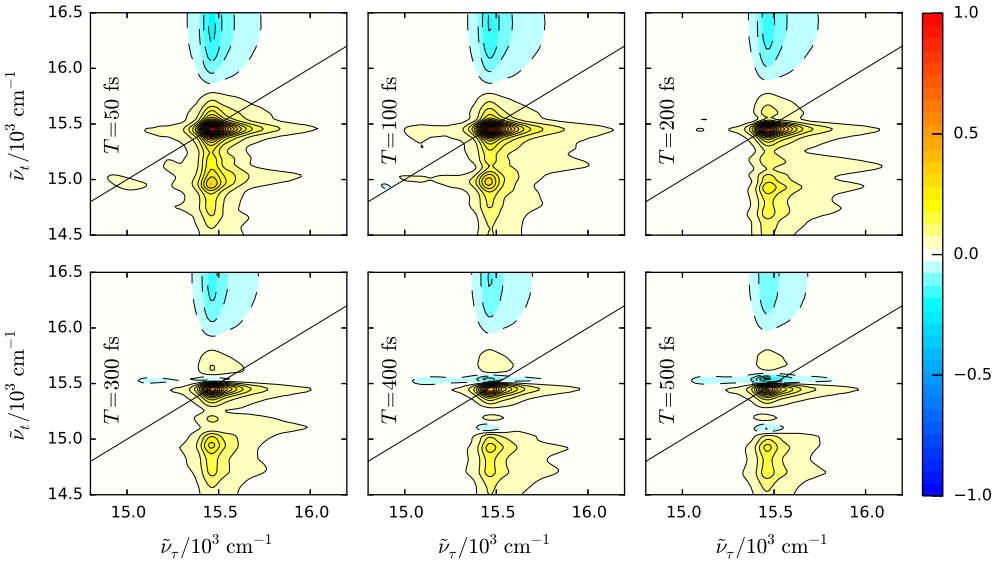

Figure 5.3.3: Absorptive 2D spectra for the vibronic heterodimer at $T = 50,\ 100,\ 200,\ 300,\ 400$ and $500\,\mathrm{fs}$, normalised to the maximum along the population time, T.

Figure 5.3.3 shows absorptive 2D spectra of the heterodimer up to $T = 500\,\mathrm{fs}$ in the region of the main peaks, with an excitation frequency of ca. $15\,460\,\mathrm{cm}^{-1}$ and emission frequencies in the range $14\,500$ - $16\,500\,\mathrm{cm}^{-1}$. As the population time increases, additional negative ESA peaks appear at this excitation frequency and grow in intensity, diminishing the neighbouring positive peaks. First, an ESA peak at ca. ($\tilde{\nu}_\tau = 15\,460\,\mathrm{cm}^{-1}$, $\tilde{\nu}_t = 15\,540\,\mathrm{cm}^{-1}$), with a very narrow width in $\tilde{\nu}_t$ but broad width in $\tilde{\nu}_\tau$, emerges at $T = 300\,\mathrm{fs}$, with a second, smaller peak at ca. ($\tilde{\nu}_\tau = 15\,460\,\mathrm{cm}^{-1}$, $\tilde{\nu}_t = 15\,100\,\mathrm{cm}^{-1}$) appearing within $T = 400\,\mathrm{fs}$.

The appearance of additional ESA peaks at progressively lower emission frequencies demonstrates vibrational relaxation during the population time, associated with EET between monomers. To illustrate this, the exciton basis density operator for the vibronic heterodimer is initialised with the entire population in $|\Psi_9^E\rangle\langle\Psi_9^E|$, assuming selective excitation by the laser spectrum in figure 5.3.2. Propagation of the heterodimer in the same bath conditions used to produce the spectra in figure 5.3.3 then yields the results in figure 5.3.4. The exciton basis populations in figure 5.3.4 (a) show the dissipation of energy from the excited heterodimer into the phonon bath and the relaxation of the system

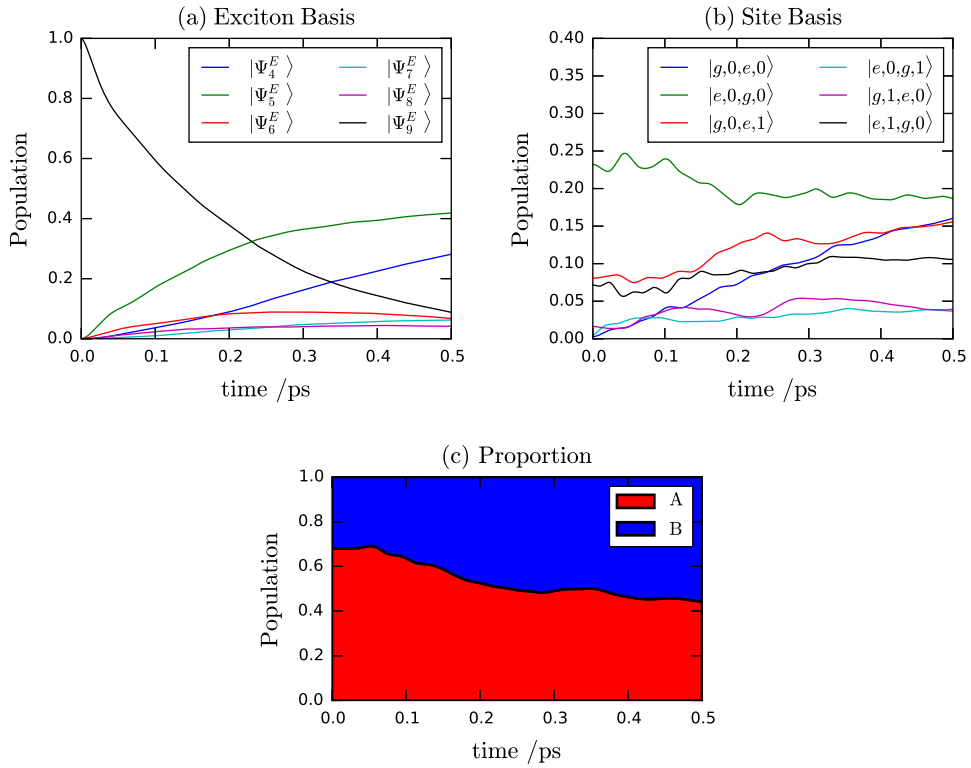

Figure 5.3.4: (a) Exciton basis and (b) equivalent composite site basis state populations for the vibronic heterodimer initialised with the entire population in $|\Psi_9^E\rangle$. (c) Summing the site basis populations corresponding to excitation of monomer A versus B demonstrates ca. 20% excitation energy transfer from A to B over $500\,\mathrm{fs}$.

from $|\Psi_9^E\rangle$ to the lowest vibronic level of the singly excited states, $|\Psi_4^E\rangle$. Initially, population transfers from $|\Psi_9^E\rangle$ to the lower energy $|\Psi_5^E\rangle$ as these exciton states are both predominantly localised to monomer A; see figure 5.3.1. Subsequent relaxation then results in the steady increase in population of $|\Psi_4^E\rangle$. Figure 5.3.4 (b) shows the same relaxation of the system in terms of the composite site basis populations, obtained by a reverse transformation of the exciton basis density operator. The initial superposition of states and relatively minor changes in site basis populations demonstrate the extent of delocalization of the exciton states across the two monomers. However, the significant increase in population of $|g,0,e,0\rangle$ (blue) and $|g,0,e,1\rangle$ (red) over $500\,\mathrm{fs}$, compared with the majority initial population in $|e,0,g,0\rangle$ (green), shows the transfer of excitation energy from monomer A to B. Plotting the total population of site basis states where A is excited versus where B is excited, as defined in figure 5.3.1, against propagation time produces figure 5.3.4 (c). This shows that, under these conditions, vibrational relaxation between the exciton states corresponds to ca. 20% transfer of excitation energy from monomer A to B over $500\,\mathrm{fs}$.

The selective excitation of the laser spectrum to state $|\Psi_9^E\rangle$ means the exciton populations in figure 5.3.4 (a) can be directly related to vibrational relaxation

during increasing population time, T, for the 2D spectra in figure 5.3.3. Between $T = 200\,\mathrm{fs}$ and $T = 300\,\mathrm{fs}$, the population of $|\Psi_9^E\rangle$ drops below that of $|\Psi_5^E\rangle$ and Liouville pathways involving ESA from $|\Psi_5^E\rangle$ become more prominent. The drop in energy to $|\Psi_5^E\rangle$ produces an equivalent decrease in emission frequency for the corresponding ESA pathways, resulting in the appearance of the additional negative peak at ca. ($\tilde{\nu}_\tau = 15\,460\,\mathrm{cm}^{-1}$, $\tilde{\nu}_t = 15\,540\,\mathrm{cm}^{-1}$) in the 2D spectrum at $T = 300\,\mathrm{fs}$. The continued increase in population of $|\Psi_5^E\rangle$ thus results in the increasing intensity of this peak for longer population times. Similarly, figure 5.3.4 (a) shows that by $T = 400\,\mathrm{fs}$, the population of $|\Psi_9^E\rangle$ drops below that of $|\Psi_4^E\rangle$, and the second ESA peak at ($\tilde{\nu}_\tau = 15\,460\,\mathrm{cm}^{-1}$, $\tilde{\nu}_t = 15\,100\,\mathrm{cm}^{-1}$) corresponds to ESA pathways involving $|\Psi_4^E\rangle$ becoming a more prominent feature of the 2D spectrum.

These results show an example of how 2DES is used to monitor EET within excitonic molecular aggregates. Although the amount of energy transfer in this model is relatively small, considering the timescales involved and the more specialised design of natural light-harvesting complexes, it is easy to imagine how the concepts demonstrated here can quickly scale up to significant light-harvesting capabilities. Further analysis of the spectral lineshape and Liouville pathways is required, but the results presented here demonstrate the capability of the model for the study of EET within vibronic heterodimers, relating 2D spectral lineshape to population dynamics in both the exciton and site basis perspectives. This section presents the full functionality of the model developed in this thesis, combining the vibronic dimer Hamiltonian with the spectral filtering effects of the EOM-PMA and the non-Markovian HEOM dynamics for vibrational relaxation and dephasing. The flexibility of such an approach provides immense potential for the investigation of vibronic effects in systems with functionalised energy transfer, but this combination of methods is computationally demanding and efficiency needs to be improved before larger systems are modelled.

6 Conclusion

Open quantum system models for the 2DES of vibronic systems have been described, using the HEOM to account for non-Markovian effects within the bath dynamics and the EOM-PMA to account for finite pulse effects. Separate HEOM methods are applied to the overdamped and underdamped limits, each efficiently terminated with a Markovian convergence parameter. The models have been used to recreate experimental spectra for monomers coupled to multiple vibrational modes and the formation of dimer systems via electronic coupling, based upon the Kasha model. The modular design of the bespoke software used in this research enables a wide variety of simulations to be performed, producing spectra using the EOM-PMA or in the impulsive limit, with underdamped or overdamped HEOM dynamics, for vibronic monomers, homodimers or heterodimers, interchangeably. However, the efficiency of the simulations is limited by the size of the system Hamiltonian, which increases rapidly on dimer formation, and the number of ADOs involved in the hierarchy. Dependent on the computational resources available, achieving suitable resolution for the 2D spectra requires a delicate balance between the degrees of freedom of the system and the number of baths which can be included with sufficient ADOs to achieve the appropriate Markovian limit. Further developments regarding the software include improving algorithmic efficiency to alleviate this issue, reducing the substantial requirements of memory and computation time, where a useful feature would be to enable the combination of underdamped and overdamped terms within the propagation of a single hierarchy, as used by Tanimura.[159]

Chapter 3 presented a discussion of the linear and 2D spectral lineshapes for a vibronic monomer coupled to an overdamped bath, compared with an equivalent two-level-system, where the strongly coupled vibration is transformed into the bath degrees of freedom as an underdamped Brownian oscillator. Clear vibronic peaks are observed in the spectra of both systems, but with fundamental differences in the broadening observed. An analysis of the linear spectra for a range of damping strengths and temperatures demonstrated that coupling to an overdamped bath applies a broadening to each vibronic peak individually, whilst for the underdamped bath, the damping strength controls the intensity of vibronic peaks. The homogeneous and inhomogeneous limits of

the overdamped bath were then examined via the decay of the ellipticity of the 2D lineshape, which reveals the correlation time of the system-bath correlation function. A study using the BLP measure, $\mathcal{N}$, to quantify the degree of non-Markovianity on transitioning from the underdamped to overdamped limits then identified that $\mathcal{N}$ is greater for underdamped baths, but that the total effect accumulates over a prolonged period of feedback. This contrasts with the rapid return of information from the bath to the system observed for overdamped baths. Furthermore, for overdamped baths, $\mathcal{N}$ increases as the damping strength increases from the homogeneous to the inhomogeneous limits, where the slower bath motion enables greater feedback of information. Using these results, the linear and 2D spectral lineshapes under equivalent bath conditions were then interpreted in terms of the information flow between the system and the environment. The correlation of the ellipticity of overdamped 2D spectra with $\mathcal{N}$ demonstrates that environmental signatures such as inhomogeneous broadening should be interpreted as a result of non-Markovian feedback effects. This links the theory of spectral lineshape with quantum information theory, demonstrating the ability of non-Markovian HEOM dynamics to produce realistic spectral lineshapes and thus the importance of non-Markovian effects. Further comparison of spectral lineshapes with metrics from quantum information theory will provide greater insight into the origins of spectral broadening, particularly if measurements can be obtained closer to the critical damping region. But the issue of instability in this region requires further development of the HEOM, perhaps using the ASD-HEOM. The results of the ASD-HEOM presented in section 3.2 hint at its usefulness for investigating fundamental theory, but its application more generally in these models is prevented by the severe computational demands.

The role of the laser spectrum in determining 2D spectral lineshape was then demonstrated in chapter 4, where the disappearance of peaks on blue-shifting the laser spectrum was reconciled with the filtering of Liouville pathways. Successful reproduction of the vibronic progression in the Q_x band of the linear absorption spectrum of a zinc-porphyrin monomer was achieved by modelling the vibronic monomer coupled to separate overdamped baths for electronic dephasing and vibrational relaxation. Calculation of the amplitude spectra for the $375\,\mathrm{cm}^{-1}$ mode confirmed the Liouville pathway analysis presented by Camargo *et al.* in reference 22. This demonstrates the ability of the model to reproduce a specific experimental scenario, including finite pulse effects via the EOM-PMA. But, small differences in the intensities of the calculated and experimental amplitude spectra for the centred laser simulation suggest that the experimental spectra involve Liouville pathways excluded from the model by truncation of the system Hamiltonian. As the locations of peaks in the calculated and experimental amplitude spectra are consistent, this does not affect the analysis. However, it implies that agreement between the calculated and

experimental results can be improved by incorporation of a greater number of vibrational levels into the system Hamiltonian, accompanied by an extension of the Liouville pathway analysis. This is left for future work. Similarly, additional pulse effects such as chirp, resulting from unwanted phase differences in the field interactions, can also be incorporated into the EOM-PMA through addition of a phase factor into eq. 2.2.56.[254,255] However, as this was an unnecessary complication for the Gaussian pulses used in chapter 4, this is left as a possible extension.

The model was then applied to more demanding vibronic dimer systems in chapter 5. For reference, 2D spectra for the strong and weak coupling limits of J-aggregate homodimers were presented. These identified a red-shift in the positive peaks compared with the monomer spectra and the appearance of negative ESA peaks as the primary signatures of dimer formation in 2D spectra. These features were then discussed in greater detail by modelling a series of PBI homodimers, where the electronic coupling strength is decreased by increasing the separation of the monomers. Spectra for the PBI monomer and homodimers showed excellent qualitative agreement with the experimental results of Bressan *et al.* in reference 213, in terms of broadening and spectral diffusion. Analysis of the PBI monomer results produced amplitude spectra for each of the two vibrational modes included in the system Hamiltonian, where the negative non-rephasing amplitude spectrum for the $\tilde{\omega}_0 = 231\,\mathrm{cm}^{-1}$ mode showed significant differences from the results of chapter 4. These were attributed to inclusion of the $\nu_0 = 2$ level and a significant excited population in the vibrational levels of the ground electronic state at $298\,\mathrm{K}$. The dimensions of the two-mode dimer Hamiltonian strained the available computational resources, such that single-mode homodimers were also modelled to obtain spectra at longer population times. The smaller red-shifts in the calculated homodimer spectra compared with the experimental results suggest that the electronic coupling strength of D0 presented by Bressan *et al.* is likely underestimated. The inclusion of vibrational modes into the improved dimer model in section 5.2 suggests that an increase in electronic coupling is required to compensate for vibronic quenching. These results demonstrate the ability of the model to simulate 2DES of vibronic dimer systems, where the main limitation is the size of the system Hamiltonian. The current focus on qualitative features completes the initial development, where the model is now ready for thorough quantitative comparisons with experimental results, in terms of broadening and the timescale of spectral diffusion.

Finally, section 5.3 presented an example of EET in a vibronic heterodimer system, employing the finite width of the laser spectrum in the EOM-PMA to preferentially excite monomer A. The appearance of extra ESA peaks with lower emission frequencies for increasing population times then demonstrated

vibrational relaxation between exciton states, resulting in an increased population of the electronic excited state of monomer B, corresponding to the transfer of excitation energy. This is a simple demonstration of the potential of such vibronic models for the study of EET in molecular aggregates and light-harvesting complexes. Here, the heterodimer featured different electronic transition frequencies and different mode frequencies for each monomer for contrast with the homodimer systems. Other interesting studies could involve further distinction of the monomers via changing the arrangement of transition dipole moments, perhaps including one optically dark monomer to provide even stronger evidence of EET.[103] The versatility of the model regarding the structure of the dimer system, the bath dynamics and finite pulse effects presents exciting opportunities for application to the forefront of research in this field. But the demanding calculations and the difficulties in reconciling the results in terms of the exciton and site basis perspectives present significant obstacles to a complete understanding of the dynamics of these systems.

In summary, a multipurpose model for the 2DES of vibronic systems has been developed, which correctly accounts for vibronic quenching of the electronic coupling in dimer systems, essential non-Markovian effects within the bath dynamics and the spectral filtering of Liouville pathways from 2D spectra due to the finite width of the laser spectrum. Each component of the model has been tested, applied to the reproduction of experimental results or to investigations of the theoretical origins of spectral features. Given sufficient computational resources and time, such models provide valuable insight into the dynamics of vibronic molecular aggregates to supplement and enhance experimental results. It is through the combined effort of experimental and theoretical methods that important design principles will be identified for the development of novel technologies tasked with resolving contemporary issues, such as the efficient harvesting of solar energy. The model developed in this research is now ready for broader application and testing, with a series of expansion projects already underway. These include further application of quantum information theory to the interpretation of spectral lineshape, the implementation of multicoloured laser pulses into the EOM-PMA to enable two-colour 2DES as well as 2DEV simulations, and a comparison of the differences in efficiency and broadening achieved when dimer systems have coupled vibrational modes defined within the system versus the bath degrees of freedom.

A Notation and Symbols

For reference, table A.1 contains the conventions of mathematical notation used in this thesis, whilst table A.2 reviews the physical meaning of all the parameters involved.

Notation	Meaning
$\|\Psi\rangle$	Dirac ket vector
$\langle\Psi\|$	Dirac bra vector
$\|\alpha\rangle \otimes \|n\rangle$	Tensor product of $\|\alpha\rangle$ and $\|n\rangle$
$\|\alpha\rangle \|n\rangle = \|\alpha, n\rangle$	Abbreviated notation for $\|\alpha\rangle \otimes \|n\rangle$
A^*	Complex conjugate of operator A
$\mathsf{A}^\dagger$	Hermitian conjugate (adjoint) of operator A
$+c.c.$	Abbreviation for complex conjugate of preceding term
$\mathbf{Tr}(\mathsf{A}) = \langle\mathsf{A}\rangle$	Trace of the operator A
$\mathbf{Tr}_m(\mathsf{A})$	Partial trace of the operator A over subsystem m
$\mathsf{A}^\times\rho = [\mathsf{A}, \rho]$	Commutator; $[\mathsf{A}, \rho] = \mathsf{A}\rho - \rho\mathsf{A}$
$\mathsf{A}^\circ\rho = \{\mathsf{A}, \rho\}$	Anti-commutator; $\{\mathsf{A}, \rho\} = \mathsf{A}\rho + \rho\mathsf{A}$
$\mathbf{r} = r\hat{\mathbf{r}}$	Vector quantity of magnitude $\|\mathbf{r}\| = r$
$\hat{\mathbf{r}}$	Unit vector
r_k	kth element of vector $\mathbf{r}$
$\mathbf{k} \cdot \mathbf{r}$	Scalar (dot) product of two vectors
I_m	Identity matrix over subsystem m
$\mathbf{Re}(z)$	Real component of the complex number z
$\mathbf{Im}(z)$	Imaginary component of the complex number z
$\|z\|$	Modulus of complex number z
A	Font reserved for operators
A	Font reserved for matrices
$\sigma_x, \sigma_y, \sigma_z$	Standard Pauli matrices

Table A.1: Summary of mathematical notation.

Symbol	Physical Meaning	Section
$\mathsf{H}_{\mathsf{S}}^{B}$	System Hamiltonian, S $\in \{\mathrm{M}, \mathrm{D}\}$, in basis $B \in \{S, V, E\}$.	2.2.1
$\omega_{eg}^{(0)}$	Fundamental electronic transition frequency for transitions equivalent to $\|g,0\rangle \rightarrow \|e,0\rangle$.	2.2.1.1
ω_j	Frequency of vibrational mode j (mode in system).	2.2.1.1
Δ_j	Dimensionless excited state displacement of vibrational mode j (mode in system).	2.2.1.1
$\hbar\lambda$	Total reorganisation energy of system vibrational modes.	2.2.1.1
μ_{eg}	Magnitude of transition dipole moment, $\boldsymbol{\mu}_{eg}$.	2.2.3.2
J	Electronic coupling strength.	2.2.1.2
R	Magnitude of dimer displacement vector, $\mathbf{R}$.	2.2.1.2
$\mathsf{B}_{n,\mathsf{S}}^{B}$	System-bath coupling operator for bath n, coupled to system S $\in \{\mathrm{M}, \mathrm{D}\}$, in basis $B \in \{S, V, E\}$.	2.2.2.1
$\hbar\eta_n$	Total reorganisation energy of bath n.	2.2.2.1
Δ	Fluctuation amplitude.	2.2.2.3
τ_c	Correlation time.	2.2.2.3
Λ_n	Rate of dephasing/dissipation (τ_c^{-1}) for bath n.	2.2.2.3
ω_{0n}	Frequency of underdamped vibrational mode in bath n (mode in bath).	2.2.2.3
γ_n	Damping rate of bath n.	2.2.2.3
ξ	HEOM convergence parameter, assigned as the Markovian limit.	2.3.2.1
χ_m	Electric field strength of laser pulse.	2.2.3.1
τ_p	Time domain FWHM of field envelope, $E'(t-\tau_m)$.	2.2.3.1
ν_m	Laser frequency.	2.2.3.1

Table A.2: Review of parameters.

B Further Theory

B.1 Wavepacket Projection

For a vibronic monomer, any superposition of site basis states results in an oscillating wavepacket, unless the superposition corresponds to population of a single vibronic state, which is a stationary eigenstate of the monomer Hamiltonian. This is shown in figure 2.2.2, where an arbitrary vibronic monomer with $\Delta_0 > 0$ is evolved as a closed system using the Liouville-von Neumann equation. When $\rho(t = 0) = |e,0\rangle\langle e,0|$, the vibronic coupling delocalizes the population across the vibrational levels, resulting in an oscillating wavepacket. But when ρ is initialised in a vibronic state, reverse transformation to the site basis, $\rho^S = \mathsf{U}^{VS}\rho^V(\mathsf{U}^{VS})^\dagger$, shows a superposition of site basis states at $t = 0$ which does not change over time. The site basis density matrix is converted from the energy to position representation via,

$$\rho(\mathsf{Q},\mathsf{Q}';t) = \sum_{\nu,\nu'} \psi_\nu(\mathsf{Q})\rho_{\nu,\nu'}(t)\psi_{\nu'}(\mathsf{Q}'), \tag{B.1.1}$$

where ψ_ν are the vibrational wavefunctions and the diagonal elements of $\rho(\mathsf{Q},\mathsf{Q}';t)$ are the probability density of finding the mode at position Q at time t.[103,256] The vibrational wavefunctions are assumed to be that of a harmonic oscillator such that,

$$\psi_\nu(\mathsf{Q}) = \left(\frac{\alpha}{\pi}\right)^{\frac{1}{4}} \frac{H_\nu(\mathsf{Q})}{\sqrt{2^\nu \nu!}} \exp\left(-\frac{\mathsf{Q}^2}{2}\right), \tag{B.1.2}$$

where $\alpha = m\omega/\hbar$, $\mathsf{Q} = \sqrt{\alpha}\mathsf{q}$ and $H_\nu(\mathsf{Q})$ are the Hermite polynomials.[257]

B.2 Site Basis Vibronic Dimer Hamiltonian

Below is the matrix form of the site basis Hamiltonian for a vibronic homodimer where the monomer Hamiltonian is that of eq. 2.2.22. The diagonal energies have been replaced with their corresponding state labels for easier identification of the states associated with the off-diagonal couplings.

$$
H_D^S = \begin{pmatrix}
 & |g,0,g,0\rangle & |g,0,g,1\rangle & |g,0,e,0\rangle & |g,0,e,1\rangle & |g,1,g,0\rangle & |g,1,g,1\rangle & |g,1,e,0\rangle & |g,1,e,1\rangle & |e,0,g,0\rangle & |e,0,g,1\rangle & |e,0,e,0\rangle & |e,0,e,1\rangle & |e,1,g,0\rangle & |e,1,g,1\rangle & |e,1,e,0\rangle & |e,1,e,1\rangle \\
|g,0,g,0\rangle & 0 & 0 & 0 & 0 & 0 & 0 & 0 & 0 & 0 & 0 & 0 & 0 & 0 & 0 & 0 & 0 \\
|g,0,g,1\rangle & 0 & 0 & 0 & -\hbar\omega_0\frac{\Delta}{\sqrt{2}} & 0 & 0 & 0 & -\hbar\omega_0\frac{\Delta}{\sqrt{2}} & 0 & 0 & 0 & 0 & 0 & 0 & 0 & 0 \\
|g,0,e,0\rangle & 0 & 0 & 0 & 0 & 0 & 0 & 0 & 0 & J & 0 & 0 & 0 & 0 & 0 & 0 & 0 \\
|g,0,e,1\rangle & 0 & -\hbar\omega_0\frac{\Delta}{\sqrt{2}} & 0 & 0 & 0 & 0 & 0 & 0 & 0 & J & 0 & 0 & 0 & 0 & 0 & 0 \\
|g,1,g,0\rangle & 0 & 0 & 0 & 0 & 0 & 0 & 0 & 0 & 0 & 0 & 0 & 0 & 0 & 0 & 0 & 0 \\
|g,1,g,1\rangle & 0 & 0 & 0 & 0 & 0 & 0 & 0 & 0 & 0 & 0 & 0 & 0 & 0 & 0 & 0 & 0 \\
|g,1,e,0\rangle & 0 & 0 & 0 & 0 & 0 & 0 & 0 & -\hbar\omega_0\frac{\Delta}{\sqrt{2}} & 0 & 0 & 0 & 0 & J & 0 & 0 & 0 \\
|g,1,e,1\rangle & 0 & 0 & 0 & 0 & 0 & 0 & -\hbar\omega_0\frac{\Delta}{\sqrt{2}} & 0 & 0 & 0 & 0 & 0 & 0 & J & 0 & 0 \\
|e,0,g,0\rangle & 0 & 0 & J & 0 & 0 & 0 & 0 & 0 & 0 & 0 & 0 & -\hbar\omega_0\frac{\Delta}{\sqrt{2}} & 0 & 0 & 0 & 0 \\
|e,0,g,1\rangle & 0 & 0 & 0 & J & 0 & 0 & 0 & 0 & 0 & 0 & -\hbar\omega_0\frac{\Delta}{\sqrt{2}} & 0 & 0 & 0 & 0 & -\hbar\omega_0\frac{\Delta}{\sqrt{2}} \\
|e,0,e,0\rangle & 0 & 0 & 0 & 0 & 0 & 0 & 0 & 0 & 0 & -\hbar\omega_0\frac{\Delta}{\sqrt{2}} & 0 & 0 & 0 & 0 & -\hbar\omega_0\frac{\Delta}{\sqrt{2}} & 0 \\
|e,0,e,1\rangle & 0 & 0 & 0 & 0 & 0 & 0 & 0 & 0 & -\hbar\omega_0\frac{\Delta}{\sqrt{2}} & 0 & 0 & 0 & 0 & 0 & 0 & -\hbar\omega_0\frac{\Delta}{\sqrt{2}} \\
|e,1,g,0\rangle & 0 & 0 & 0 & 0 & 0 & 0 & 0 & 0 & 0 & 0 & 0 & 0 & 0 & 0 & 0 & 0 \\
|e,1,g,1\rangle & 0 & 0 & 0 & 0 & 0 & 0 & 0 & 0 & 0 & 0 & 0 & 0 & 0 & 0 & 0 & 0 \\
|e,1,e,0\rangle & 0 & 0 & 0 & 0 & 0 & 0 & 0 & 0 & 0 & 0 & 0 & 0 & 0 & 0 & 0 & -\hbar\omega_0\frac{\Delta}{\sqrt{2}} \\
|e,1,e,1\rangle & 0 & 0 & 0 & 0 & 0 & 0 & 0 & 0 & 0 & 0 & 0 & 0 & 0 & 0 & -\hbar\omega_0\frac{\Delta}{\sqrt{2}} & 0
\end{pmatrix} \tag{B.2.1}
$$

B.3 EOM-PMA Generating Functions

As described by Gelin *et al.* in reference 175, the Liouville pathway generating function $\rho_1(\lambda_1, \lambda_2, \lambda_3; t)$ is expanded as a Taylor series with respect to each of the three field interactions as,

$$\rho_1(\lambda_1, \lambda_2, \lambda_3; t) = \sum_{i,j,k=0}^{\infty} \lambda_1^i \lambda_2^j \lambda_3^k \rho_1^{i,j,k}(t). \tag{B.3.1}$$

The rephasing and non-rephasing pathways correspond to $\rho_1^{111}(t)$, which is one of the contributions to $\rho_1(\lambda_1, \lambda_2, \lambda_3; t)$,

$$\begin{aligned}
\rho_1(\lambda_1, \lambda_2, \lambda_3; t) &= \sum_{i,j,k=0}^{\infty} \lambda_1^i \lambda_2^j \lambda_3^k \rho_1^{i,j,k}(t) \\
&= \rho_1^{000}(t) + \lambda_1 \rho_1^{100}(t) + \lambda_2 \rho_1^{010}(t) + \lambda_3 \rho_1^{001}(t) + \lambda_1 \lambda_2 \rho_1^{110}(t) \\
&\quad + \lambda_1 \lambda_3 \rho_1^{101}(t) + \lambda_2 \lambda_3 \rho_1^{011}(t) + \lambda_1 \lambda_2 \lambda_3 \rho_1^{111}(t) + \lambda_1^2 \rho_1^{200}(t) \\
&\quad + \lambda_2^2 \rho_1^{020}(t) + \lambda_3^2 \rho_1^{002}(t) + \lambda_1^2 \lambda_2 \rho_1^{210}(t) + \lambda_1^2 \lambda_3 \rho_1^{201}(t) \\
&\quad + \lambda_1 \lambda_2^2 \rho_1^{120}(t) + \lambda_2^2 \lambda_3 \rho_1^{021}(t) + \lambda_1 \lambda_3^2 \rho_1^{102}(t) + \lambda_2 \lambda_3^2 \rho_1^{012}(t) \\
&\quad + \lambda_1^3 \rho_1^{300}(t) + \lambda_2^3 \rho_1^{030}(t) + \lambda_3^3 \rho_1^{003}(t) \\
&\quad + O(\lambda_1^i \lambda_2^j \lambda_3^k),\ i + j + k > 3.
\end{aligned} \tag{B.3.2}$$

On comparison with other generating functions with different combinations of field interactions,

$$\begin{aligned}
\rho_1(\lambda_1, \lambda_2, 0; t) &= \sum_{i,j=0}^{\infty} \lambda_1^i \lambda_2^j \lambda_3^0 \rho_1^{i,j,0}(t) \\
&= \rho_1^{000}(t) + \lambda_1 \rho_1^{100}(t) + \lambda_2 \rho_1^{010}(t) + \lambda_1 \lambda_2 \rho_1^{110}(t) + \lambda_1^2 \rho_1^{200}(t) \\
&\quad + \lambda_2^2 \rho_1^{020}(t) + \lambda_1^2 \lambda_2 \rho_1^{210}(t) + \lambda_1 \lambda_2^2 \rho_1^{120}(t) + \lambda_1^3 \rho_1^{300}(t) \\
&\quad + \lambda_2^3 \rho_1^{030}(t) + O(\lambda_1^i \lambda_2^j),\ i + j > 3,
\end{aligned} \tag{B.3.3}$$

$$\begin{aligned}
\rho_1(0, \lambda_2, \lambda_3; t) &= \sum_{j,k=0}^{\infty} \lambda_1^0 \lambda_2^j \lambda_3^k \rho_1^{0,j,k}(t) \\
&= \rho_1^{000}(t) + \lambda_2 \rho_1^{010}(t) + \lambda_3 \rho_1^{001}(t) + \lambda_2 \lambda_3 \rho_1^{011}(t) + \lambda_2^2 \rho_1^{020}(t) \\
&\quad + \lambda_3^2 \rho_1^{002}(t) + \lambda_2^2 \lambda_3 \rho_1^{021}(t) + \lambda_2 \lambda_3^2 \rho_1^{012}(t) + \lambda_2^3 \rho_1^{030}(t) \\
&\quad + \lambda_3^3 \rho_1^{003}(t) + O(\lambda_2^j \lambda_3^k),\ j + k > 3,
\end{aligned} \tag{B.3.4}$$

$$\begin{aligned}\rho_1(\lambda_1,0,\lambda_3;t) &= \sum_{i,k=0}^{\infty}\lambda_1^i\lambda_2^0\lambda_3^k\rho_1^{i,0,k}(t)\\ &= \rho_1^{000}(t)+\lambda_1\rho_1^{100}(t)+\lambda_3\rho_1^{001}(t)+\lambda_1\lambda_3\rho_1^{101}(t)+\lambda_1^2\rho_1^{200}(t)\\ &\quad+\lambda_3^2\rho_1^{002}(t)+\lambda_1^2\lambda_3\rho_1^{201}(t)+\lambda_1\lambda_3^2\rho_1^{102}(t)+\lambda_1^3\rho_1^{300}(t)\\ &\quad+\lambda_3^3\rho_1^{003}(t)+O(\lambda_1^i\lambda_3^k),\ i+k>3, \qquad \text{(B.3.5)}\end{aligned}$$

$$\begin{aligned}\rho_1(\lambda_1,0,0;t) &= \sum_{i=0}^{\infty}\lambda_1^i\lambda_2^0\lambda_3^0\rho_1^{i,0,0}(t)\\ &= \rho_1^{000}(t)+\lambda_1\rho_1^{100}(t)+\lambda_1^2\rho_1^{200}(t)+\lambda_1^3\rho_1^{300}(t)\\ &\quad+O(\lambda_1^i),\ i>3, \qquad \text{(B.3.6)}\end{aligned}$$

$$\begin{aligned}\rho_1(0,\lambda_2,0;t) &= \sum_{j=0}^{\infty}\lambda_1^0\lambda_2^j\lambda_3^0\rho_1^{0,j,0}(t)\\ &= \rho_1^{000}(t)+\lambda_2\rho_1^{010}(t)+\lambda_2^2\rho_1^{020}(t)+\lambda_2^3\rho_1^{030}(t)\\ &\quad+O(\lambda_2^j),\ j>3, \qquad \text{(B.3.7)}\end{aligned}$$

$$\begin{aligned}\rho_1(0,0,\lambda_3;t) &= \sum_{k=0}^{\infty}\lambda_1^0\lambda_2^0\lambda_3^j\rho_1^{0,0,k}(t)\\ &= \rho_1^{000}(t)+\lambda_3\rho_1^{001}(t)+\lambda_3^2\rho_1^{002}(t)+\lambda_3^3\rho_1^{003}(t)\\ &\quad+O(\lambda_3^k),\ k>3, \qquad \text{(B.3.8)}\end{aligned}$$

$$\rho_1(0,0,0;t)=\rho_1^{000}(t), \qquad \text{(B.3.9)}$$

it is clear that $\lambda_1\lambda_2\lambda_3\rho_1^{111}(t)$ can be isolated by combining all of these permutations,

$$\begin{aligned}\lambda_1\lambda_2\lambda_3\rho_1^{111}(t) &= \rho_1(\lambda_1,\lambda_2,\lambda_3;t)+\rho_1(\lambda_1,0,0;t)-\rho_1(\lambda_1,0,\lambda_3;t)\\ &\quad-\rho_1(\lambda_1,\lambda_2,0;t)-\rho_1(0,\lambda_2,\lambda_3;t)-\rho_1(0,0,0;t)\\ &\quad+\rho_1(0,0,\lambda_3;t)+\rho_1(0,\lambda_2,0;t)\\ &\quad+O(\lambda_1^i\lambda_2^j\lambda_3^k),\quad i+j+k>3, \qquad \text{(B.3.10)}\end{aligned}$$

as all other terms, and thus Liouville pathways, cancel,

$$
\begin{aligned}
\lambda_1\lambda_2\lambda_3\rho_1^{111}(t) \quad = \quad & \rho_1^{000}(t) + \rho_1^{000}(t) - \rho_1^{000}(t) - \rho_1^{000}(t) - \rho_1^{000}(t) \\
& -\rho_1^{000}(t) + \rho_1^{000}(t) + \rho_1^{000}(t) \\
& +\lambda_1\rho_1^{100}(t) + \lambda_1\rho_1^{100}(t) - \lambda_1\rho_1^{100}(t) - \lambda_1\rho_1^{100}(t) \\
& +\lambda_2\rho_1^{010}(t) - \lambda_2\rho_1^{010}(t) - \lambda_2\rho_1^{010}(t) + \lambda_2\rho_1^{010}(t) \\
& +\lambda_3\rho_1^{001}(t) - \lambda_3\rho_1^{001}(t) - \lambda_3\rho_1^{001}(t) + \lambda_3\rho_1^{001}(t) \\
& +\lambda_1\lambda_2\rho_1^{110}(t) - \lambda_1\lambda_2\rho_1^{110}(t) \\
& +\lambda_1\lambda_3\rho_1^{101}(t) - \lambda_1\lambda_3\rho_1^{101}(t) \\
& +\lambda_2\lambda_3\rho_1^{011}(t) - \lambda_2\lambda_3\rho_1^{011}(t) \\
& +\lambda_1\lambda_2\lambda_3\rho_1^{111}(t) \\
& +\lambda_1^2\rho_1^{200}(t) + \lambda_1^2\rho_1^{200}(t) - \lambda_1^2\rho_1^{200}(t) - \lambda_1^2\rho_1^{200}(t) \\
& +\lambda_2^2\rho_1^{020}(t) - \lambda_2^2\rho_1^{020}(t) - \lambda_2^2\rho_1^{020}(t) + \lambda_2^2\rho_1^{020}(t) \\
& +\lambda_3^2\rho_1^{002}(t) - \lambda_3^2\rho_1^{002}(t) - \lambda_3^2\rho_1^{002}(t) + \lambda_3^2\rho_1^{002}(t) \\
& +\lambda_1^2\lambda_2\rho_1^{210}(t) - \lambda_1^2\lambda_2\rho_1^{210}(t) \\
& +\lambda_1^2\lambda_3\rho_1^{201}(t) - \lambda_1^2\lambda_3\rho_1^{201}(t) \\
& +\lambda_1\lambda_2^2\rho_1^{120}(t) - \lambda_1\lambda_2^2\rho_1^{120}(t) \\
& +\lambda_2^2\lambda_3\rho_1^{021}(t) - \lambda_2^2\lambda_3\rho_1^{021}(t) \\
& +\lambda_1\lambda_3^2\rho_1^{102}(t) - \lambda_1\lambda_3^2\rho_1^{102}(t) \\
& +\lambda_2\lambda_3^2\rho_1^{012}(t) - \lambda_2\lambda_3^2\rho_1^{012}(t) \\
& +\lambda_1^3\rho_1^{300}(t) + \lambda_1^3\rho_1^{300}(t) - \lambda_1^3\rho_1^{300}(t) - \lambda_1^3\rho_1^{300}(t) \\
& +\lambda_2^3\rho_1^{030}(t) - \lambda_2^3\rho_1^{030}(t) - \lambda_2^3\rho_1^{030}(t) + \lambda_2^3\rho_1^{030}(t) \\
& +\lambda_3^3\rho_1^{003}(t) - \lambda_3^3\rho_1^{003}(t) - \lambda_3^3\rho_1^{003}(t) + \lambda_3^3\rho_1^{003}(t) \\
& +O(\lambda_1^i\lambda_2^j\lambda_3^k), \quad i+j+k > 3. \qquad \text{(B.3.11)}
\end{aligned}
$$

C Computational Implementation

The principal result of this research is the software produced. The HEOM dynamics are separated into a series of importable Python classes, which feed into a larger piece of software for the 2D spectroscopy calculations. The main software features a sophisticated graphical user interface (GUI) which manages a database of experiments and integrates with the LSF batch system of the High Performance Computing (HPC) cluster at UEA. All software is written in FORTRAN90 and Python 3,[258] using open source packages including NumPy,[259] SciPy,[260,261] Matplotlib,[262] F2PY[263] and the Quantum Toolbox in Python (QuTiP).[264,265]

C.1 HEOM Dynamics Packages

Separate Python classes have been written for the propagation of overdamped and underdamped HEOM dynamics, adapted from the work of Dr. A. G. Dijkstra. Using the F2PY package, fast FORTRAN algorithms for the creation of the hierarchy and numerical integration of the equations of motion are seamlessly integrated into Python objects, which handle the data and communicate with the wider software. These generalised classes have been designed for use in a variety of quantum dynamical simulations, not limited to 2D spectroscopy calculations. The main functionality is described by the flowchart in figure C.1.1.

The main Python script passes the system parameters in simple wavenumber units to the HEOMsolve class, which converts these to the necessary radians per second and prepares the timeline for the propagation. Note that all the calculations involved in this thesis are completed in SI units. The HEOMsolve class then generates the hierarchy of ADOs using a FORTRAN search algorithm which adopts a recursive method to explore each Matsubara axis until the Markovian limit is reached and the terminating ADOs are identified. Finally, the propagation of the system density matrix is completed using RK4 integration, with each step completed using fast FORTRAN subroutines. The HEOMsolve class then returns the resulting states to the main script for further calculations and plotting, along with the full set of ADOs if the propagation of system-bath

correlations is required.

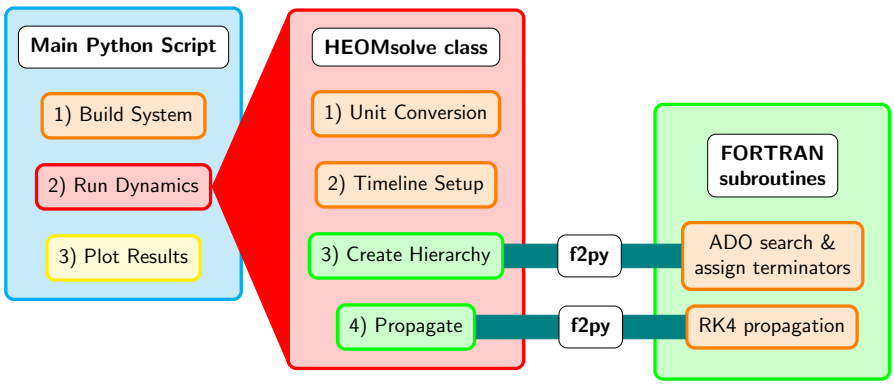

Figure C.1.1: Flowchart for HEOM dynamics packages.

The Python class for the ASD-HEOM is designed in much the same way, where the number of layers involved is predefined such that no search is involved and the RK4 progresses sequentially from the lowest (second) layer for each of k_{1-4}.

C.2 2D Spectroscopy Software

The main software controls a database of simulations via a GUI, where each 2D spectroscopy calculation is distinguished into an *experiment* with a unique ID number. The experiment class contains methods for construction of the different systems defined in section 2.2 and calculation of their linear and 2D spectra, using the HEOM dynamics classes, as described in section 2.4. The parameters and results of the calculations are stored as attributes of the experiment object, such that simulations are easily compared and archived. Each stage of the calculations updates a status system which works in unison with the database so that the GUI cannot interrupt calculations in progress and can access the results on completion. Figure C.2.1 shows the main windows involved in the software, with the standardised calculation procedure described by the flowchart in figure C.2.2.

The home window displays the current status of experiments, from which the results can be viewed or new experiments can be submitted. After entering all of the system, bath and laser parameters into the new experiment window, there are two methods available to calculate 2D spectra. The *response function* method corresponds to the impulsive limit, ignoring any of the entered laser parameters, whilst the *EOM-PMA* method undertakes the full equation-of-motion phase-matching approach calculation for finite laser pulses. Selection of either method initiates a new job on a fresh compute node, where the GUI integrates

with the LSF batch system of the HPC cluster via automatic submission of shell commands.

(a) Home

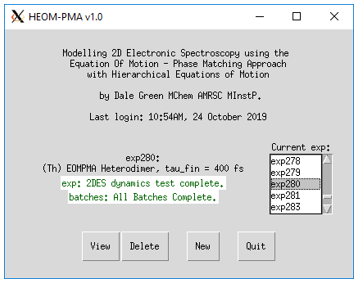

(b) New Experiment

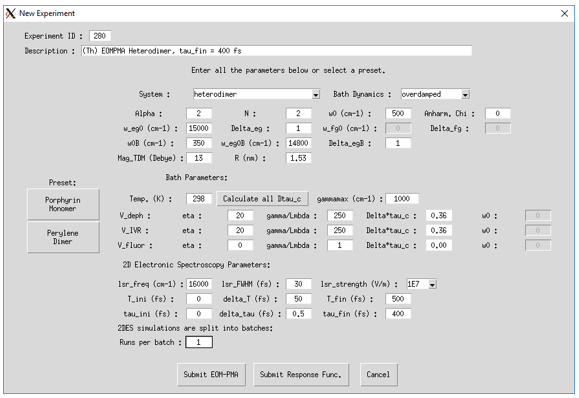

(c) Main Results

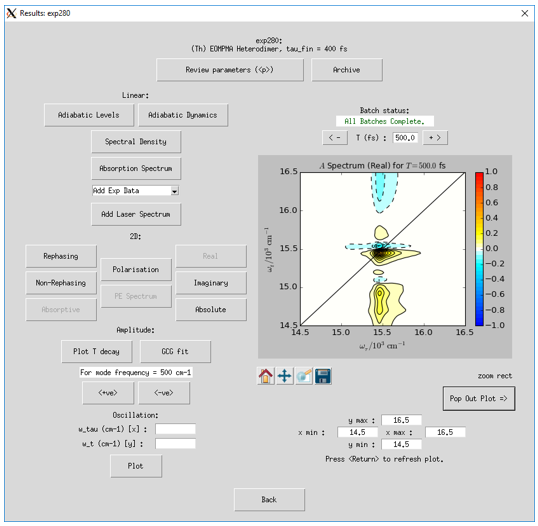

(d) Separate Plot

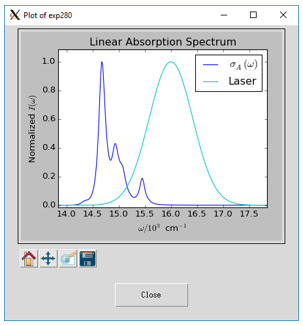

(e) Parameter Review

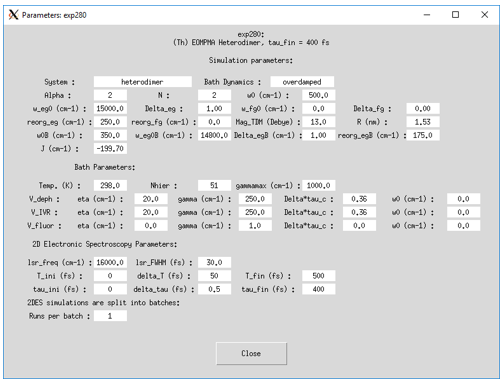

Figure C.2.1: Main windows of the 2D spectroscopy software.

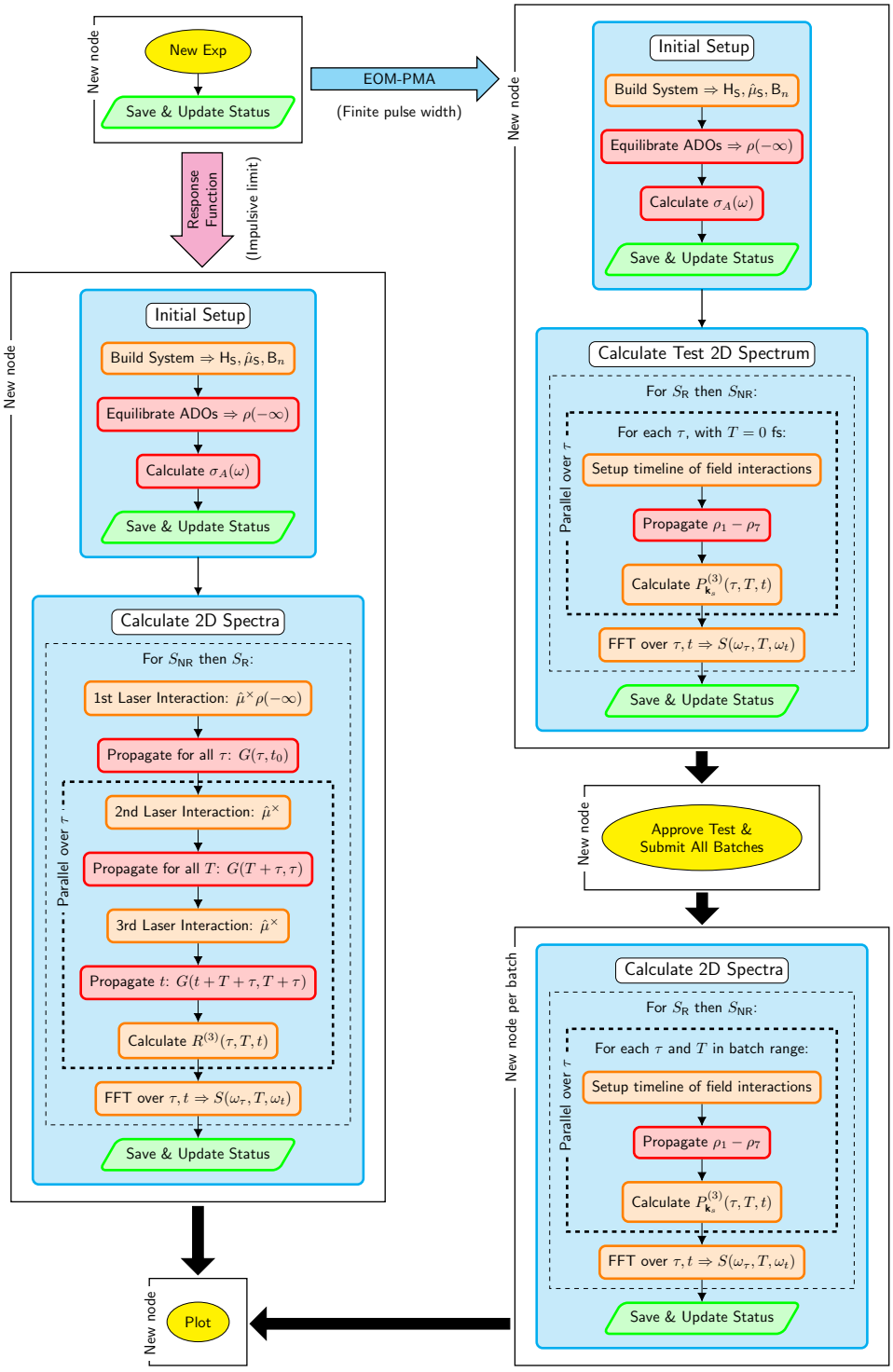

Figure C.2.2: Flowchart for 2D spectroscopy calculations.

As shown in figure C.2.2, both methods begin with an initial setup involving construction of the system operators for any of the preset system types (i.e. single and multimode monomers and dimers) and diagonalization to the adiabatic vibronic/exciton basis. All calculations are performed in the adiabatic basis so that the system dimensions can be reduced to a manageable size after

incorporating the vibronic coupling of a large number of vibrational levels, reducing truncation errors. The dynamics are then tested by equilibrating the HEOM for a few picoseconds to setup initial correlations. The linear absorption spectrum is then calculated and the results saved, before the 2D calculations begin. For the *response function* method, the calculations launch straight into generation of the third order polarization. After the initial $P^{(3)}_{\mathbf{k}_s}(\tau, T = 0, t = 0)$ propagation, the calculation is parallelized over the τ axis using all available cores on the compute node. Fourier transform of the 3D polarization matrix with respect to τ and t then produces 2D spectra for each population time. This process is completed for both the rephasing and non-rephasing signals. For the significantly more intensive *EOM-PMA* calculations, initially only the $T = 0\,\mathrm{fs}$ spectrum is calculated, where again the calculation is parallelized over the τ axis. The user must then approve the rephasing and non-rephasing $T = 0\,\mathrm{fs}$ spectrum before the remaining spectra are calculated sequentially for each population time, in a series of batches, where each batch begins a new job on a fresh compute node. The direct *response function* calculations typically complete within minutes, whilst the intensive *EOM-PMA* calculations can easily take days, dependent on the size of the system and the number of ADOs in the hierarchy.

On completion of the calculations, all of the results are viewed in the results window. Buttons are included to plot the energy levels of the system and the corresponding transition frequencies, the change in state populations during the equilibration dynamics, the linear absorption spectrum with overlaid laser spectrum, and the 2D polarization and photon echo spectra for both rephasing and non-rephasing as well as absorptive signals as the real, imaginary or absolute component. Further analysis is then completed with buttons which plot the trace over the population time for a particular coordinate and its Fourier transform, as well as the amplitude spectra for a particular mode frequency. Together with a separate window for reviewing the parameters and the ability to produce additional plot windows, this creates a fully functional working environment for the analysis and interpretation of 2D spectra. Additional functionality on key presses is also included to save spectra in alternative formats, useful for construction of figures for publications *et cetera*.

Production of the results for this thesis corresponds to extensive testing of the software, however, there remains many features which would benefit from further development.

C.3 Fourth Order Runge-Kutta Integration

Integration of the equations of motion is completed using the Fourth Order Runge-Kutta (RK4) algorithm within the FORTRAN portion of the software.[266]

For an unknown function $y(t)$, with known $y(t_0) = y_0$ and known $\frac{dy}{dt} = f(t, y)$, RK4 approximates $y(t_{n+1}) = y_{n+1}$ using the weighted average of four possible steps with step-size h, as,

$$k_1 = f(t_n, y_n), \tag{C.3.1}$$

$$k_2 = f(t_n + \tfrac{1}{2}h, y_n + \tfrac{1}{2}hk_1), \tag{C.3.2}$$

$$k_3 = f(t_n + \tfrac{1}{2}h, y_n + \tfrac{1}{2}hk_2), \tag{C.3.3}$$

$$k_4 = f(t_n + h, y_n + hk_3), \tag{C.3.4}$$

$$y_{n+1} = y_n + \frac{h}{6}(k_1 + 2k_2 + 2k_3 + k_4) + O(h^5). \tag{C.3.5}$$

C.4 Fourier Transform and Normalisation Procedures

Following the procedure of Hamm and Zanni in reference 26, 2D Fourier transform of the third order polarization is completed by halving the values of $P^{(3)}_{\mathbf{k}_s}(\tau = 0, T, t)$ and $P^{(3)}_{\mathbf{k}_s}(\tau, T, t = 0)$, followed by sequential FFT with respect to τ then t. Both transforms are zero-padded multiple times to improve resolution. It is important to note that the forwards and inverse FFT used in the literature are defined as the opposite of those in the default Python `numpy.fft.fft` package. Hence all forwards transformations, from the time to frequency domain, are performed using `np.fft.ifft()` and vice versa.

All 2D spectra are normalised such that the origin is unaffected. Unless stated otherwise, normalisation of 2D spectra is completed with respect to the maximum along the entire axis of population times, T, such that oscillations in peak amplitude are clearly visible. Normalisation along the axis of population times also improves the fitting of exponential functions involved in calculation of the amplitude spectra.

Acronyms

2DES 2D electronic spectroscopy.

2DEV 2D electronic-vibrational spectroscopy.

2DIR 2D infrared spectroscopy.

2DOS 2D optical spectroscopy.

2DVE 2D vibrational-electronic spectroscopy.

ADO auxiliary density operator.

ASD-HEOM HEOM for an arbitrary spectral density.

BLP Breuer, Laine and Piilo.

EET excitation energy transfer.

EOM-PMA equation-of-motion phase-matching approach.

ESA excited state absorption.

FFT Fast Fourier Transform.

FMO Fenna-Mathews-Olson.

FWHM full-width-half-maximum.

GSB ground state bleach.

GUI graphical user interface.

HEOM hierarchical equations of motion.

HPC High Performance Computing.

IVR intramolecular vibrational relaxation.

LO Local Oscillator.

MBO multimode Brownian oscillator.

PBI perylene bisimide.

PES potential energy surface.

QED quantum electrodynamics.

RK4 Fourth Order Runge-Kutta.

RWA rotating wave approximation.

SE stimulated emission.

TLS two-level-system.

UEA University of East Anglia.

Bibliography

[1] S. Mukamel, *Principles of Nonlinear Optical Spectroscopy*, Oxford University Press, New York, 1995.

[2] R. Borrego-Varillas et al., Chem. Sci. **10**, 9907 (2019).

[3] A. Gelzinis, R. Augulis, V. Butkus, B. Robert, and L. Valkunas, Biochim. Biophys. Acta, Bioenerg. **1860**, 271 (2019).

[4] M. Khalil, N. Demirdöven, and A. Tokmakoff, J. Phys. Chem. A **107**, 5258 (2003).

[5] Y. Tanimura and A. Ishizaki, Acc. Chem. Res. **42**, 1270 (2009).

[6] E.-M. Laine, J. Piilo, and H.-P. Breuer, Phys. Rev. A **81**, 062115 (2010).

[7] H.-P. Breuer, E.-M. Laine, J. Piilo, and B. Vacchini, Rev. Mod. Phys. **88**, 021002 (2016).

[8] H.-P. Breuer and F. Petruccione, *The Theory of Open Quantum Systems*, Oxford University Press, New York, 2007.

[9] I. de Vega and D. Alonso, Rev. Mod. Phys. **89**, 015001 (2017).

[10] D. M. Jonas, Annu. Rev. Phys. Chem. **54**, 425 (2003).

[11] N. S. Ginsberg, Y.-C. Cheng, and G. R. Fleming, Acc. Chem. Res. **42**, 1352 (2009).

[12] G. S. Schlau-Cohen, A. Ishizaki, and G. R. Fleming, Chem. Phys. **386**, 1 (2011).

[13] M. K. Petti, J. P. Lomont, M. Maj, and M. T. Zanni, J. Phys. Chem. B **122**, 1771 (2018).

[14] C. C. Jumper, S. Rafiq, S. Wang, and G. D. Scholes, Curr. Opin. Chem. Biol. **47**, 39 (2018).

[15] J. D. Hybl, A. W. Albrecht, S. M. Gallagher Faeder, and D. M. Jonas, Chem. Phys. Lett. **297**, 307 (1998).

[16] J. C. Dean and G. D. Scholes, Acc. Chem. Res. **50**, 2746 (2017).

[17] G. D. Scholes et al., Nature **543**, 647 (2017).

[18] G. D. Scholes, J. Phys. Chem. Lett. **9**, 1568 (2018).

[19] T. A. A. Oliver, R. Soc. Open Sci. **5**, 171425 (2018).

[20] A. Tokmakoff, J. Phys. Chem. A **104**, 4247 (2000).

[21] S. M. Gallagher Faeder and D. M. Jonas, J. Phys. Chem. A **103**, 10489 (1999).

[22] F. V. A. Camargo, L. Grimmelsmann, H. L. Anderson, S. R. Meech, and I. A. Heisler, Phys. Rev. Lett. **118**, 033001 (2017).

[23] P. J. Nowakowski, M. F. Khyasudeen, and H.-S. Tan, Chem. Phys. **515**, 214 (2018).

[24] D. Paleček, P. Edlund, E. Gustavsson, S. Westenhoff, and D. Zigmantas, J. Chem. Phys. **151**, 024201 (2019).

[25] Y. Song et al., Rev. Sci. Instrum. **90**, 013108 (2019).

[26] P. Hamm and M. Zanni, *Concepts and Methods of 2D Infrared Spectroscopy*, Cambridge University Press, Cambridge, 2011.

[27] M. Cho, Chem. Rev. **108**, 1331 (2008).

[28] S. S. Senlik, V. R. Policht, and J. P. Ogilvie, J. Phys. Chem. Lett. **6**, 2413 (2015).

[29] A. Konar et al., J. Phys. Chem. Lett. **9**, 5219 (2018).

[30] G. H. Richards, K. E. Wilk, P. M. G. Curmi, and J. A. Davis, J. Phys. Chem. Lett. **5**, 43 (2014).

[31] V. P. Singh et al., J. Chem. Phys. **142**, 212446 (2015).

[32] Y. Song et al., Chem. Sci. **10**, 8143 (2019).

[33] A. F. Fidler, V. P. Singh, P. D. Long, P. D. Dahlberg, and G. S. Engel, Nat. Commun. **5**, 1 (2014).

[34] T. L. Courtney, Z. W. Fox, K. M. Slenkamp, and M. Khalil, J. Chem. Phys. **143**, 154201 (2015).

[35] J. D. Gaynor and M. Khalil, J. Chem. Phys. **147**, 094202 (2017).

[36] N. H. C. Lewis et al., J. Phys. Chem. Lett. **7**, 4197 (2016).

[37] E. C. Wu, E. A. Arsenault, P. Bhattacharyya, N. H. C. Lewis, and G. R. Fleming, Faraday Discuss. **216**, 116 (2019).

[38] P. Bhattacharyya and G. R. Fleming, J. Phys. Chem. Lett. **10**, 2081 (2019).

[39] H. Dong, N. H. C. Lewis, T. A. A. Oliver, and G. R. Fleming, J. Chem. Phys. **142**, 174201 (2015).

[40] N. H. C. Lewis, H. Dong, T. A. A. Oliver, and G. R. Fleming, J. Chem. Phys. **142**, 174202 (2015).

[41] J. O. Tollerud, C. R. Hall, and J. A. Davis, Opt. Express **22**, 6719 (2014).

[42] J. O. Tollerud, S. T. Cundiff, and J. A. Davis, Phys. Rev. Lett. **117**, 097401 (2016).

[43] K. W. Stone et al., Science **324**, 1169 (2009).

[44] E. Harel, S. M. Rupich, R. D. Schaller, D. V. Talapin, and G. S. Engel, Phys. Rev. B **86**, 075412 (2012).

[45] B. P. Fingerhut, M. Richter, J.-W. Luo, A. Zunger, and S. Mukamel, Ann. Phys. (Berlin, Ger.) **525**, 31 (2013).

[46] M. Righetto et al., Phys. Chem. Chem. Phys. **20**, 18176 (2018).

[47] J. Seibt, T. Hansen, and T. Pullerits, J. Phys. Chem. B **117**, 11124 (2013).

[48] J. Seibt and T. Pullerits, J. Phys. Chem. C **117**, 18728 (2013).

[49] A. A. Bakulin et al., Nat. Chem. **8**, 16 (2016).

[50] B. Fresch, D. Hiluf, E. Collini, R. D. Levine, and F. Remacle, Proc. Natl. Acad. Sci. U. S. A. **110**, 17183 (2013).

[51] B. Fresch et al., J. Phys. Chem. Lett. **6**, 1714 (2015).

[52] M. Kullmann, S. Ruetzel, J. Buback, P. Nuernberger, and T. Brixner, J. Am. Chem. Soc. **133**, 13074 (2011).

[53] J. M. Anna, C. R. Baiz, M. R. Ross, R. McCanne, and K. J. Kubarych, Int. Rev. Phys. Chem. **31**, 367 (2012).

[54] S. Ruetzel, M. Kullmann, J. Buback, P. Nuernberger, and T. Brixner, Phys. Rev. Lett. **110**, 148305 (2013).

[55] S. Ruetzel et al., Proc. Natl. Acad. Sci. U. S. A. **111**, 4764 (2014).

[56] L. M. Kiefer, J. T. King, and K. J. Kubarych, Acc. Chem. Res. **48**, 1123 (2015).

[57] P. Nuernberger, S. Ruetzel, and T. Brixner, Angew. Chem., Int. Ed. **54**, 11368 (2015).

[58] L. A. Bizimana, J. Epstein, J. Brazard, and D. B. Turner, J. Phys. Chem. B **121**, 2622 (2017).

[59] L. Bolzonello et al., J. Phys. Chem. Lett. **9**, 1079 (2018).

[60] G. S. Schlau-Cohen et al., J. Phys. Chem. B **113**, 15352 (2009).

[61] H. Scheer, Acta Phys. Pol., A **122**, 247 (2012).

[62] S. J. Jang and B. Mennucci, Rev. Mod. Phys. **90**, 035003 (2018).

[63] T. Brixner et al., Nature **434**, 625 (2005).

[64] D. Hayes and G. S. Engel, Biophys. J. **100**, 2043 (2011).

[65] C. Y. Wong et al., Nat. Chem. **4**, 396 (2012).

[66] C. Smyth, F. Fassioli, and G. D. Scholes, Philos. Trans. R. Soc., A **370**, 3728 (2012).

[67] J. M. Anna, G. D. Scholes, and R. van Grondelle, BioScience **64**, 14 (2014).

[68] F. Levi, S. Mostarda, F. Rao, and F. Mintert, Rep. Prog. Phys. **78**, 082001 (2015).

[69] E. Romero, V. I. Novoderezhkin, and R. van Grondelle, Nature **543**, 355 (2017).

[70] A. Marais et al., J. R. Soc., Interface **15**, 20180640 (2018).

[71] G. S. Engel et al., Nature **446**, 782 (2007).

[72] E. Collini et al., Nature **463**, 644 (2010).

[73] G. Panitchayangkoon et al., Proc. Natl. Acad. Sci. U. S. A. **107**, 12766 (2010).

[74] E. L. Read et al., Proc. Natl. Acad. Sci. U. S. A. **104**, 14203 (2007).

[75] S. Westenhoff, D. Paleček, P. Edlund, P. Smith, and D. Zigmantas, J. Am. Chem. Soc. **134**, 16484 (2012).

[76] D. B. Turner, K. E. Wilk, P. M. G. Curmi, and G. D. Scholes, J. Phys. Chem. Lett. **2**, 1904 (2011).

[77] D. B. Turner et al., Phys. Chem. Chem. Phys. **14**, 4857 (2012).

[78] E. Meneghin et al., Nat. Commun. **9**, 3160 (2018).

[79] F. Fassioli, R. Dinshaw, P. C. Arpin, and G. D. Scholes, J. R. Soc., Interface **11**, 20130901 (2013).

[80] V. Tiwari, W. K. Peters, and D. M. Jonas, Nat. Chem. **6**, 173 (2014).

[81] E. Romero et al., Nat. Phys. **10**, 676 (2014).

[82] A. Chenu and G. D. Scholes, Annu. Rev. Phys. Chem. **66**, 69 (2015).

[83] H.-G. Duan et al., J. Phys. Chem. B **119**, 12017 (2015).

[84] F. Novelli et al., J. Phys. Chem. Lett. **6**, 4573 (2015).

[85] F. Ma, E. Romero, M. R. Jones, V. I. Novoderezhkin, and R. van Grondelle, Nat. Commun. **10**, 933 (2019).

[86] J. C. Dean, T. Mirkovic, Z. S. Toa, D. G. Oblinsky, and G. D. Scholes, Chem **1**, 858 (2016).

[87] K. L. Wells, P. H. Lambrev, Z. Zhang, G. Garab, and H.-S. Tan, Phys. Chem. Chem. Phys. **16**, 11640 (2014).

[88] A. Ishizaki and G. R. Fleming, Proc. Natl. Acad. Sci. U. S. A. **106**, 17255 (2009).

[89] N. Christensson et al., J. Phys. Chem. B **115**, 5383 (2011).

[90] N. Christensson, H. F. Kauffmann, T. Pullerits, and T. Mančal, J. Phys. Chem. B **116**, 7449 (2012).

[91] T. Mančal et al., J. Phys. Chem. Lett. **3**, 1497 (2012).

[92] K.-H. Song et al., J. Phys. Chem. Lett. **6**, 4314 (2015).

[93] S. Polyutov, O. Kühn, and T. Pullerits, Chem. Phys. **394**, 21 (2012).

[94] D. Hayes, G. B. Griffin, and G. S. Engel, Science **340**, 1431 (2013).

[95] A. Halpin et al., Nat. Chem. **6**, 196 (2014).

[96] V. Butkus, L. Valkunas, and D. Abramavicius, J. Chem. Phys. **140**, 034306 (2014).

[97] J. Lim et al., Nat. Commun. **6**, 7755 (2015).

[98] H.-G. Duan, P. Nalbach, V. I. Prokhorenko, S. Mukamel, and M. Thorwart, New J. Phys. **17**, 072002 (2015).

[99] F. V. A. Camargo, H. L. Anderson, S. R. Meech, and I. A. Heisler, J. Phys. Chem. B **119**, 14660 (2015).

[100] L. Bolzonello, F. Fassioli, and E. Collini, J. Phys. Chem. Lett. **7**, 4996 (2016).

[101] M. Cipolloni et al., Phys. Chem. Chem. Phys. **19**, 23043 (2017).

[102] L. Wang et al., Nat. Chem. **9**, 219 (2017).

[103] A. De Sio, X. T. Nguyen, and C. Lienau, Zeitschrift für Naturforschung A **74**, 721 (2019).

[104] R. Tempelaar et al., J. Phys. Chem. A **120**, 3042 (2016).

[105] F. V. A. Camargo, H. L. Anderson, S. R. Meech, and I. A. Heisler, J. Phys. Chem. A **119**, 95 (2015).

[106] R. Moca, S. R. Meech, and I. A. Heisler, J. Phys. Chem. B **119**, 8623 (2015).

[107] E. Meneghin, C. Leonardo, A. Volpato, L. Bolzonello, and E. Collini, Sci. Rep. **7**, 11389 (2017).

[108] S. Kopec, P. Ottiger, S. Leutwyler, and H. Köppel, J. Chem. Phys. **137**, 184312 (2012).

[109] P. Ottiger, S. Leutwyler, and H. Köppel, J. Chem. Phys. **136**, 174308 (2012).

[110] P. Ottiger, H. Köppel, and S. Leutwyler, Chem. Sci. **6**, 6059 (2015).

[111] V. Tiwari, W. K. Peters, and D. M. Jonas, Proc. Natl. Acad. Sci. U. S. A. **110**, 1203 (2013).

[112] V. Tiwari, W. K. Peters, and D. M. Jonas, J. Chem. Phys. **147**, 154308 (2017).

[113] V. Tiwari and D. M. Jonas, J. Chem. Phys. **148**, 084308 (2018).

[114] A. Chenu, N. Christensson, H. F. Kauffmann, and T. Mančal, Sci. Rep. **3**, 2029 (2013).

[115] V. I. Novoderezhkin, E. Romero, and R. van Grondelle, Phys. Chem. Chem. Phys. **17**, 30828 (2015).

[116] V. Perlík et al., J. Chem. Phys. **142**, 212434 (2015).

[117] P. Malý, O. J. G. Somsen, V. I. Novoderezhkin, T. Mančal, and R. van Grondelle, ChemPhysChem **17**, 1356 (2016).

[118] M. H. Lee and A. Troisi, J. Chem. Phys. **146**, 075101 (2017).

[119] V. Butkus, H. Dong, G. R. Fleming, D. Abramavicius, and L. Valkunas, J. Phys. Chem. Lett. **7**, 277 (2016).

[120] Y. Fujihashi, G. R. Fleming, and A. Ishizaki, J. Chem. Phys. **142**, 212403 (2015).

[121] D. M. Monahan, L. Whaley-Mayda, A. Ishizaki, and G. R. Fleming, J. Chem. Phys. **143**, 065101 (2015).

[122] H.-G. Duan, M. Thorwart, and R. J. D. Miller, J. Chem. Phys. **151**, 114115 (2019).

[123] P. Kjellberg, B. Brüggemann, and T. Pullerits, Phys. Rev. B **74**, 024303 (2006).

[124] B. Brüggemann, P. Kjellberg, and T. Pullerits, Chem. Phys. Lett. **444**, 192 (2007).

[125] H.-G. Duan et al., Proc. Natl. Acad. Sci. U. S. A. **114**, 8493 (2017).

[126] E. Thyrhaug et al., Nat. Chem. **10**, 780 (2018).

[127] M. Maiuri, E. E. Ostroumov, R. G. Saer, R. E. Blankenship, and G. D. Scholes, Nat. Chem. **10**, 177 (2018).

[128] D. M. Jonas, Annu. Rev. Phys. Chem. **69**, 327 (2018).

[129] S. M. Blau, D. I. G. Bennett, C. Kreisbeck, G. D. Scholes, and A. Aspuru-Guzik, Proc. Natl. Acad. Sci. U. S. A. **115**, E3342 (2018).

[130] D. I. G. Bennett, P. Malý, C. Kreisbeck, R. van Grondelle, and A. Aspuru-Guzik, J. Phys. Chem. Lett. **9**, 2665 (2018).

[131] B. S. Rolczynski et al., Chem **4**, 138 (2018).

[132] J. D. Roscioli, S. Ghosh, A. M. LaFountain, H. A. Frank, and W. F. Beck, J. Phys. Chem. Lett. **9**, 5071 (2018).

[133] M. F. Gelin, R. Borrelli, and W. Domcke, J. Phys. Chem. Lett. **10**, 2806 (2019).

[134] U. Weiss, *Quantum Dissipative Systems*, World Scientific, 4th edition, 2012.

[135] T. Joo, Y. Jia, J. Yu, M. J. Lang, and G. R. Fleming, J. Chem. Phys. **104**, 6089 (1996).

[136] W. P. de Boeij, M. S. Pshenichnikov, and D. A. Wiersma, J. Phys. Chem. **100**, 11806 (1996).

[137] J. Sue, Y. J. Yan, and S. Mukamel, J. Chem. Phys. **85**, 462 (1986).

[138] Y. Zhao and R. S. Knox, J. Phys. Chem. A **104**, 7751 (2000).

[139] J. Sung and R. J. Silbey, J. Chem. Phys. **118**, 2443 (2003).

[140] S. Mukamel and D. Abramavicius, Chem. Rev. **104**, 2073 (2004).

[141] T. Brixner, T. Mančal, I. V. Stiopkin, and G. R. Fleming, J. Chem. Phys. **121**, 4221 (2004).

[142] Y.-C. Cheng, H. Lee, and G. R. Fleming, J. Phys. Chem. A **111**, 9499 (2007).

[143] A. Caldeira and A. Leggett, Phys. A **121**, 587 (1983).

[144] E. Cortés, B. J. West, and K. Lindenberg, J. Chem. Phys. **82**, 2708 (1985).

[145] J. I. Jiménez-Aquino and R. M. Velasco, Entropy **16**, 1917 (2014).

[146] C. Meier and D. J. Tannor, J. Chem. Phys. **111**, 3365 (1999).

[147] D. Chruściński and A. Kossakowski, Phys. Rev. Lett. **104**, 070406 (2010).

[148] D. Egorova, M. Thoss, W. Domcke, and H. Wang, J. Chem. Phys. **119**, 2761 (2003).

[149] Y. Tanimura, J. Phys. Soc. Jpn. **75**, 082001 (2006).

[150] Y. Tanimura and R. Kubo, J. Phys. Soc. Jpn. **58**, 101 (1989).

[151] Y. Tanimura, Phys. Rev. A **41**, 6676 (1990).

[152] A. Ishizaki and Y. Tanimura, J. Phys. Soc. Jpn. **74**, 3131 (2005).

[153] Y. Tanimura, J. Chem. Phys. **141**, 044114 (2014).

[154] Y. Tanimura, J. Chem. Phys. **142**, 144110 (2015).

[155] H. Liu, L. Zhu, S. Bai, and Q. Shi, J. Chem. Phys. **140**, 134106 (2014).

[156] A. Ishizaki and Y. Tanimura, Chem. Phys. **347**, 185 (2008).

[157] L. Chen, R. Zheng, Q. Shi, and Y. Yan, J. Chem. Phys. **131**, 094502 (2009).

[158] A. G. Dijkstra and Y. Tanimura, J. Chem. Phys. **142**, 212423 (2015).

[159] Y. Tanimura, J. Chem. Phys. **137**, 22A550 (2012).

[160] A. Ishizaki and Y. Tanimura, J. Chem. Phys. **123**, 014503 (2005).

[161] A. Ishizaki and Y. Tanimura, J. Phys. Chem. A **111**, 9269 (2007).

[162] M. Tanaka and Y. Tanimura, J. Phys. Soc. Jpn. **78**, 073802 (2009).

[163] A. G. Dijkstra and Y. Tanimura, Phys. Rev. Lett. **104**, 250401 (2010).

[164] A. G. Dijkstra and Y. Tanimura, Phil. Trans. R. Soc. A **370**, 3658 (2012).

[165] J. Strümpfer and K. Schulten, J. Chem. Phys. **131**, 225101 (2009).

[166] C. Kreisbeck, T. Kramer, and A. Aspuru-Guzik, J. Chem. Theory Comput. **10**, 4045 (2014).

[167] M. Schröter, T. Pullerits, and O. Kühn, Ann. Phys. (Berlin, Ger.) **527**, 536 (2015).

[168] A. Chin, E. Mangaud, V. Chevet, O. Atabek, and M. Desouter-Lecomte, Chem. Phys. **525**, 110392 (2019).

[169] S.-H. Yeh, R. D. Hoehn, M. A. Allodi, G. S. Engel, and S. Kais, Proc. Natl. Acad. Sci. U. S. A. **116**, 18263 (2019).

[170] V. Butkus, L. Valkunas, and D. Abramavicius, J. Chem. Phys. **137**, 44513 (2012).

[171] T. Mančal, A. V. Pisliakov, and G. R. Fleming, J. Chem. Phys. **124**, 234504 (2006).

[172] L. Seidner, G. Stock, and W. Domcke, J. Chem. Phys. **103**, 3998 (1995).

[173] S. Meyer and V. Engel, Appl. Phys. B: Lasers Opt. **71**, 293 (2000).

[174] M. F. Gelin, D. Egorova, and W. Domcke, Acc. Chem. Res. **42**, 1290 (2009).

[175] M. F. Gelin, D. Egorova, and W. Domcke, J. Chem. Phys. **123**, 164112 (2005).

[176] M. F. Gelin, D. Egorova, and W. Domcke, J. Chem. Phys. **131**, 194103 (2009).

[177] J. Krčmář, M. F. Gelin, and W. Domcke, Chem. Phys. **422**, 53 (2013).

[178] L. Z. Sharp, D. Egorova, and W. Domcke, J. Chem. Phys. **132**, 014501 (2010).

[179] M. Sala and D. Egorova, Chem. Phys. **481**, 206 (2016).

[180] D. Egorova, M. F. Gelin, and W. Domcke, J. Chem. Phys. **126**, 074314 (2007).

[181] D. Egorova, J. Chem. Phys. **140**, 034314 (2014).

[182] Y.-C. Cheng, G. S. Engel, and G. R. Fleming, Chem. Phys. **341**, 285 (2007).

[183] Y.-C. Cheng and G. R. Fleming, J. Phys. Chem. A **112**, 4254 (2008).

[184] X. Leng, S. Yue, Y.-X. Weng, K. Song, and Q. Shi, Chem. Phys. Lett. **667**, 79 (2017).

[185] X. Leng et al., J. Phys. Chem. B **122**, 4642 (2018).

[186] D. Green, F. V. A. Camargo, I. A. Heisler, A. G. Dijkstra, and G. A. Jones, J. Phys. Chem. A **122**, 6206 (2018).

[187] M. A. Nielsen and I. L. Chuang, *Quantum Computation and Quantum Information*, Cambridge University Press, Cambridge, 2010.

[188] M. M. Wolf, J. Eisert, T. S. Cubitt, and J. I. Cirac, Phys. Rev. Lett. **101**, 150402 (2008).

[189] F. Bloch, Phys. Rev. **70**, 460 (1946).

[190] H.-P. Breuer, E.-M. Laine, and J. Piilo, Phys. Rev. Lett. **103**, 210401 (2009).

[191] Á. Rivas, S. F. Huelga, and M. B. Plenio, Rep. Prog. Phys. **77**, 094001 (2014).

[192] A. Wehrl, Rev. Mod. Phys. **50**, 221 (1978).

[193] P. M. Poggi, F. C. Lombardo, and D. A. Wisniacki, EPL **118**, 20005 (2017).

[194] D. Green, B. S. Humphries, A. G. Dijkstra, and G. A. Jones, J. Chem. Phys. **151**, 174112 (2019).

[195] X.-M. Lu, X. Wang, and C. P. Sun, Phys. Rev. A **82**, 042103 (2010).

[196] H.-S. Zeng, N. Tang, Y.-P. Zheng, and G.-Y. Wang, Phys. Rev. A **84**, 032118 (2011).

[197] B. Witt, L. Rudnicki, Y. Tanimura, and F. Mintert, New J. Phys. **19**, 013007 (2017).

[198] D. P. Craig and T. Thirunamachandran, *Molecular Quantum Electrodynamics: An Introduction to Radiation-Molecule Interactions*, Courier Corporation, London, 1984.

[199] R. Louden, *The Quantum Theory of Light*, Oxford University Press, Oxford, 3rd edition, 2000.

[200] M. Maiuri, M. Garavelli, and G. Cerullo, J. Am. Chem. Soc. **142**, 3 (2020).

[201] L. A. Nafie, J. Chem. Phys. **79**, 4950 (1983).

[202] L. D. Smith and A. G. Dijkstra, J. Chem. Phys. **151**, 164109 (2019).

[203] K. F. Riley, M. P. Hobson, and S. J. Bence, *Mathematical Methods for Physics and Engineering*, Cambridge University Press, Cambridge, 3rd edition, 2006.

[204] J. E. Frost and G. A. Jones, New J. Phys. **16**, 113067 (2014).

[205] N. J. Hestand and F. C. Spano, Acc. Chem. Res. **50**, 341 (2017).

[206] N. J. Hestand and F. C. Spano, Chem. Rev. **118**, 7069 (2018).

[207] T. Förster, Ann. Phys. **437**, 55 (1948).

[208] J. S. Briggs and A. Eisfeld, Phys. Rev. E **83**, 051911 (2011).

[209] T. Mančal, Chem. Phys. **532**, 110663 (2020).

[210] M. Kasha, Radiat. Res. **20**, 55 (1963).

[211] V. Butkus, D. Zigmantas, D. Abramavicius, and L. Valkunas, Chem. Phys. Lett. **587**, 93 (2013).

[212] H. Fidder, J. Knoester, and D. A. Wiersma, Chem. Phys. Lett. **171**, 529 (1990).

[213] G. Bressan et al., J. Phys. Chem. A **123**, 1594 (2019).

[214] F. P. Diehl et al., J. Phys. Chem. Lett. **5**, 262 (2014).

[215] P. Vöhringer, D. C. Arnett, R. A. Westervelt, M. J. Feldstein, and N. F. Scherer, J. Chem. Phys. **102**, 4027 (1995).

[216] A. G. Dijkstra and V. I. Prokhorenko, J. Chem. Phys. **147**, 064102 (2017).

[217] A. S. Bondarenko, J. Knoester, and T. L. Jansen, Chem. Phys. **529**, 110478 (2020).

[218] Á. Rivas, S. F. Huelga, and M. B. Plenio, Phys. Rev. Lett. **105**, 050403 (2010).

[219] S. Mukamel, Annu. Rev. Phys. Chem. **41**, 647 (1990).

[220] J. Iles-Smith, A. G. Dijkstra, N. Lambert, and A. Nazir, J. Chem. Phys. **144**, 044110 (2016).

[221] J. Sung and R. J. Silbey, J. Chem. Phys. **115**, 9266 (2001).

[222] T. N. Do, M. F. Gelin, and H.-S. Tan, J. Chem. Phys. **147**, 144103 (2017).

[223] C. A. Brasil, F. F. Fanchini, and R. d. J. Napolitano, Rev. Bras. Ensino Fis. **35**, 1303 (2013).

[224] F. Fassioli and A. Olaya-Castro, New J. Phys. **12**, 085006 (2010).

[225] O. Linden and V. May, Eur. Phys. J. D **12**, 473 (2000).

[226] A. Strathearn, P. Kirton, D. Kilda, J. Keeling, and B. W. Lovett, Nat. Commun. **9**, 3322 (2018).

[227] A. Jain, A. S. Petit, J. M. Anna, and J. E. Subotnik, J. Phys. Chem. B **123**, 1602 (2019).

[228] Y. Tanimura and R. Kubo, J. Phys. Soc. Jpn. **58**, 1199 (1989).

[229] R. P. Feynman and A. R. Hibbs, *Quantum Mechanics and Path Integrals*, McGraw-Hill Companies, Inc., New York, 1965.

[230] M. Cho, N. F. Scherer, G. R. Fleming, and S. Mukamel, J. Chem. Phys. **96**, 5618 (1992).

[231] M. H. Farag, T. l. C. Jansen, and J. Knoester, Phys. Chem. Chem. Phys. **20**, 12746 (2018).

[232] A. Mandal et al., J. Phys. Chem. Lett. **10**, 3509 (2019).

[233] F. V. A. Camargo, *Unravelling Vibrational and Electronic Coherences via Two-Dimensional Electronic Spectroscopy of Zinc-Porphyrins*, PhD thesis, University of East Anglia, 2017.

[234] S. T. Roberts, J. J. Loparo, and A. Tokmakoff, J. Chem. Phys. **125**, 084502 (2006).

[235] E. K. Irish, R. Gómez-Bombarelli, and B. W. Lovett, Phys. Rev. A **90**, 012510 (2014).

[236] H. Mustroph et al., ChemPhysChem **10**, 835 (2009).

[237] F. Šanda, V. Perlík, C. N. Lincoln, and J. Hauer, J. Phys. Chem. A **119**, 10893 (2015).

[238] K. Lazonder, M. S. Pshenichnikov, and D. A. Wiersma, Opt. Lett. **31**, 3354 (2006).

[239] O. Kühn, V. Rupasov, and S. Mukamel, J. Chem. Phys. **104**, 5821 (1996).

[240] M. Drobizhev et al., J. Phys. Chem. B **109**, 7223 (2005).

[241] S. Y. Kim and T. Joo, J. Phys. Chem. Lett. **6**, 2993 (2015).

[242] V. Butkus, D. Zigmantas, L. Valkunas, and D. Abramavicius, Chem. Phys. Lett. **545**, 40 (2012).

[243] M. R. Wasielewski, Acc. Chem. Res. **42**, 1910 (2009).

[244] C. Hippius, F. Schlosser, M. O. Vysotsky, V. Böhmer, and F. Würthner, J. Am. Chem. Soc. **128**, 3870 (2006).

[245] R. Pandya, R. W. MacQueen, A. Rao, and N. J. L. K. Davis, J. Phys. Chem. C **122**, 22330 (2018).

[246] L. Zang, R. Liu, M. W. Holman, K. T. Nguyen, and D. M. Adams, J. Am. Chem. Soc. **124**, 10640 (2002).

[247] T. Takada et al., Chem. - Eur. J. **24**, 8228 (2018).

[248] X. Feng, Y. An, Z. Yao, C. Li, and G. Shi, ACS Appl. Mater. Interfaces **4**, 614 (2012).

[249] B. Wang and C. Yu, Angew. Chem., Int. Ed. **49**, 1485 (2010).

[250] K. Sugiyasu, N. Fujita, and S. Shinkai, Angew. Chem., Int. Ed. **43**, 1229 (2004).

[251] U. Selig et al., ChemPhysChem **14**, 1413 (2013).

[252] A. E. Clark, C. Qin, and A. D. Q. Li, J. Am. Chem. Soc. **129**, 7586 (2007).

[253] D. R. Lide, *CRC Handbook of Chemistry and Physics*, CRC Press, New York, 85th edition, 2004.

[254] P. F. Tekavec, J. A. Myers, K. L. M. Lewis, F. D. Fuller, and J. P. Ogilvie, Opt. Express **18**, 11015 (2010).

[255] N. Christensson et al., J. Chem. Phys. **132**, 174508 (2010).

[256] R. Schneider, W. Domcke, and H. Köppel, J. Chem. Phys. **92**, 1045 (1990).

[257] P. Atkins and R. Friedman, *Molecular Quantum Mechanics*, Oxford University Press, Oxford, 5th edition, 2011.

[258] M. Lutz, *Programming Python*, O'Reilly Media, 4th edition, 2010.

[259] S. Van Der Walt, S. C. Colbert, and G. Varoquaux, Comput. Sci. Eng. **13**, 22 (2011).

[260] K. J. Millman and M. Aivazis, Comput. Sci. Eng. **13**, 9 (2011).

[261] P. Virtanen et al., arXiv:1907.10121 [cs.MS] , 1 (2019).

[262] J. D. Hunter, Comput. Sci. Eng. **9**, 90 (2007).

[263] P. Peterson, Int. J. Comput. Sci. Eng. **4**, 296 (2009).

[264] J. Johansson, P. Nation, and F. Nori, Comput. Phys. Commun. **183**, 1760 (2012).

[265] J. Johansson, P. Nation, and F. Nori, Comput. Phys. Commun. **184**, 1234 (2013).

[266] W. H. Press, S. A. Teukolsky, W. T. Vetterling, and B. P. Flannery, *Numerical Recipes 3rd Edition: The Art of Scientific Computing*, volume 1, Cambridge University Press, Cambridge, 3rd edition, 2007.